An investigation of self-assembled nanostructured protein-based therapeutic approaches in Breast Cancer

A THESIS SUBMITTED FOR AWARD OF THE DEGREE OF

DOCTOR OF PHILOSOPHY

IN

BIOTECHNOLOGY AND MEDICAL ENGINEERING

Submitted by

Sailendra Kumar Mahanta

(Roll No: 510BM101)

Under the guidance of

Dr. Subhankar Paul

Department of Biotechnology & Medical Engineering

National Institute of Technology

Rourkela-769008, Orissa, India

2015

National Institute of Technology Rourkela
Department of Biotechnology and Medical Engineering
769008, Odisha, India

Dr. Subhankar Paul
Associate Professor
Phone: +0661-2462284
Fax: +0661-2462281
Email: spaul@nitrkl.ac.in

Date: Dec-08, 2015

Certificate

This is to certify that the thesis entitled **"An investigation of self-assembled nanostructured protein based therapeutic approaches in Breast Cancer"** submitted by **Mr. Sailendra Kumar Mahanta (Roll No. 510BM101)** to National Institute of Technology, Rourkela towards partial fulfillment of the requirements for the award of the **Doctor of Philosophy** degree in **Biotechnology and Medical Engineering**, is a bonafide record of his work carried out under my supervision.

Place: Rourkela
Date: 08-12-2015.

(Dr. Subhankar Paul)
Associate Professor
Dept. of Biotechnology & Medical
Engineering, NIT Rourkela.

ACKNOWLEDGEMENT

This research was supported by the Department of Biotechnology and Medical Engineering, National Institute of Technology, Rourkela, India. During the last five years, I have gained one of the most valuable experience of my life. At this juncture, I would like to express my appreciation to one and all who have contributed to successfully complete the work.

I owe my sincere gratitude to my supervisor Prof. Subhankar Paul, for his continuous encouragement of my research instincts and for allowing me to grow as a researcher. His advice on both research as well as on my career has been priceless.

My special thanks are due to Prof. S. K. Sarangi, Director, National Institute of Technology, Rourkela for all the facilities provided to successfully complete this work.

I am also very thankful to all the members of my doctoral scrutiny committee Prof. R. K. Patel, Prof. S. Mishra, Prof. N. Sarkar and Prof. K. Pramanik for their thoughtful suggestions, inspiration and continuous encouragement throughout the research work. I take this opportunity to thank Prof. M. K. Gupta, Prof. P. Balasubramaniam, Prof. S. K. Patra, Prof. S. K. Bhutia, Prof. S. Paria, Prof. S. Jha, Prof. S. K. Pratihar and the supporting staff members of the Department of Biotechnology and Medical Engineering for their timely co-operation and support at various phases of experimental work.

I would like to extend a special thanks to my dear friends Deependra Kumar Ban, Arun Wamankar, Astik Biswas, Akalabya Bissoyi, Niladrinath Panda, Smita Pilla, Manoranjan Arakha and my brother-in-law Abinash for their valuable suggestions and encouragement.

I am also grateful to my beloved wife Priyanka, who had always been very supportive through this venture.

I will be failing in my duty if I do not acknowledge the constant cooperation and support of my parents and in-laws who have always been a source of inspiration for me.

Above all, I would like to thank the Almighty for his enormous blessings and guiding me in the right direction in life.

LIST OF FIGURES

Figure 2.1 Cancer statistics between the period 1990-2013 (A) Incidences of Breast cancer is on the rise from 1990 to 2013, (B) Percentage change in incidence rate due to population growth (35%), due to change in age structure (38%) and due to change in incidence rates (26%).. 12

Figure 2.2 Current statistics for Age-standardized incidence rates (ASIR) of Breast cancer (Fitzmaurice et al., 2015). 13

Figure 2.3 Current statistics for ASIR of disease assisted life years (DALY) for Breast cancer (Fitzmaurice et al., 2015)................................... 14

Figure 2.4 Prevalence of various forms of cancers among 188 countries based on incidence rates of the year 2013 (Fitzmaurice et al., 2015). 14

Figure 2.5 Mortality due to various forms of cancers among 188 countries based on mortality rates for the year 2013 (Fitzmaurice et al., 2015). 15

Figure 4.1 Schematic representation of preparation of snLYZ/snBLA and its conjugates with Tamoxifen (TAM) and activated Folic Acid (FAa). 44

Figure 4.2 Characterization of size and shape of snLYZ. (A) Field emission scanning electron microscopy (FESEM) of snLYZ. (B) AFM image of snLYZ (C) Hydrodynamic diameter of snLYZ obtained by DLS particle size analysis. The overall nanostructure size was found to 300 nm. 45

Figure 4.3 Characterization of size and shape of snBLA. (A) Field emission scanning electron microscopy (FESEM) of snBLA. (B) AFM image of snBLA (C) Hydrodynamic diameter of snBLA. The overall nanostructure size was found to be 300 nm. 46

Figure 4.4 FTIR spectra analysis of Amide I and Amide II band between 1500cm^{-1} – 1725 cm^{-1}. (A) nmLYZ and snLYZ (B). nmBLA and snBLA. In both the protein nanostructures a peak shift in Amide I and II peaks was observed. 47

Figure 4.5 Characterization of nmLYZ and snLYZ with respect to its conformational state. (A) Circular dichroism spectra of nmLYZ and snLYZ. (B) Trp fluorescence emission spectra of native lysozyme and snLYZ. All data were expressed as the mean of three readouts generated from the instrument. 48

Figure 4.6 Characterization of snLYZ and snBLA with respect to its conformational state. (A) Circular dichroism spectra of native BLA and snBLA (B) Trp fluorescence emission spectra of nmBLA and snBLA. All data were expressed as the mean of three readouts generated from the instrument 50

Figure 4.7 Thermal stability analysis of (A) native lysozyme (nmLYZ), (B) self-assembled nanostructured lysozyme (snLYZ) by CD spectroscopy. (C) Comparison of the change in molar ellipticity of nmLYZ and snLYZ at 222nm (α-helix). All data were expressed as the mean of three readouts generated from the instrument.. 52

Figure 4.8 Thermal stability analysis of (A) native bovine α-lactalbumin (nmBLA), (B) self-assembled nanostructured bovine α-lactalbumin (snBLA) by CD spectroscopy. (C) Comparison of the change in molar ellipticity of nmBLA and snBLA at 222 nm (α-helix). All data were expressed as the mean of three readouts generated from the instrument... 53

Figure 4.9 Thermal stability analysis of (A) native lysozyme (nmLYZ), (B) self-assembled nanostructured lysozyme (snLYZ) by Tryptophan (Trp) fluorescence spectroscopy. (C) Comparison of the change in Trp fluorescence of nmLYZ and snLYZ. All data were expressed as the mean of three readouts generated from the instrument... 54

Figure 4.10 Thermal stability analysis of (A) native bovine α-lactalbumin (nmBLA), (B) self-assembled nanostructured bovine α-lactalbumin (snBLA) by Tryptophan (Trp) fluorescence spectroscopy. (C) Comparison of the change in Trp fluorescence of nmBLA and snBLA. All data were expressed as the mean of three readouts generated from the instrument. 55

Figure 4.11 Thermal stability analysis of (A) native Lysozyme (nmLYZ), (B) self-assembled nanostructured lysozyme (snLYZ) by ANS fluorescence spectroscopy and (C) Comparison of the change in ANS fluorescence of nmLYZ and snLYZ. All data were expressed as the mean of three readouts generated from the instrument. 57

Figure 4.12 Thermal stability analysis of (A) native bovine α-lactalbumin (nmBLA), (B) self-assembled nanostructured bovine α-lactalbumin (snBLA) by ANS fluorescence spectroscopy. (C) Comparison of the change in ANS fluorescence of nmBLA and snBLA. All data were expressed as the mean of three readouts generated from the instrument. 58

Figure 4.13 pH stability analysis of (A) native lysozyme (nmLYZ), (B) self-assembled nanostructured lysozyme (snLYZ) by Circular dichroism (CD) spectroscopy. (C) Comparison of the change in the structure of nmBLA and snBLA by measuring the CD signal at 222 nm. All data were expressed as the mean of three readouts generated from the instrument. 59

Figure 4.14 pH stability analysis of (A) native bovine α-lactalbumin (nmBLA), (B) self-assembled nanostructured bovine α-lactalbumin (snBLA) by CD spectroscopy. (C) Comparison of the change in the structure of protein nanostructures by CD spectroscopy @ 222 nm. All data were expressed as the mean of three readouts generated from the instrument. 60

Figure 4.15 pH stability analysis of (A) native lysozyme (nmLYZ), (B) self-assembled nanostructured lysozyme (snLYZ) by Trp fluorescence spectroscopy. (C) Comparison of the change in protein bound Trp fluorescence of nmBLA and snBLA. All data were expressed as the mean of three readouts generated from the instrument. 61

Figure 4.16 pH stability analysis of (A) native bovine α-lactalbumin (nmBLA), (B) self-assembled nanostructured bovine α-lactalbumin (snBLA) by Trp fluorescence spectroscopy. (C) Comparison of the change in protein bound Trp fluorescence of nmBLA and snBLA. All data were expressed as the mean of three readouts generated from the instrument. 62

Figure 4.17 pH stability analysis of (A) native lysozyme (nmLYZ), (B) self-assembled nanostructured lysozyme (snLYZ) by ANS fluorescence spectroscopy. (C) Comparison of the change in protein bound ANS fluorescence of nmLYZ and snLYZ. All data were expressed as the mean of three readouts generated from the instrument. 63

Figure 4.18 pH stability analysis of (A) native bovine α-lactalbumin (nmBLA), (B) self-assembled nanostructured bovine α-lactalbumin (snBLA) by ANS fluorescence spectroscopy. (C) Comparison of the change in protein bound ANS fluorescence of nmBLA and snBLA. All data were expressed as the mean of three readouts generated from the instrument. 64

Figure 4.19 UV-Vis spectroscopic measurement of nmBLA and snBLA before and after treatment with 3 μM Proteinase K (PK). The protein nanostructures resist Proteinase K related stress. All data were expressed as the mean of three readouts generated from the instrument. 66

Figure 4.20 Plot of the biological activity of LYZ in nmLYZ and snLYZ at various pH (5-9) by *Micrococcus lysodekticus* assay. The protein nanostructure snLYZ retains its activity. All data are expressed as Mean ± S.E.M, n = 3. 67

Figure 4.21 Surface hydrophobicity assessment of protein nanostructures using ANS Fluorescence spectra. (A) snLYZ and (B) snBLA. Surface hydrophobicity of snLYZ was found to increase whereas snBLA was found decreased. All data are expressed as a mean of three readouts generated from the instrument. 68

Figure 4.22 Thioflavin T assay for the assessment of the presence of amyloid in the protein nanostructures (A) snLYZ and (B) snBLA. The presence of amyloid produces a very intense peak at 490 nm. All data are expressed as a mean of three readouts generated from the instrument. 70

Figure 5.1 Dose-dependent cytotoxic effect of (A) snLYZ and (B) snBLA on the MCF-7 cell viability at the end of 24 h. Statistically significant vs control group, *** $p < 0.001$ by One way

ANOVA and post Tukey test. All data are expressed as Mean ± S.E.M, n = 3. 77

Figure 5.2 Dose-dependent cytotoxic effect of (A) snLYZ and (B) snBLA on the MCF-7 cell viability at the end of 48 h. Statistically significant vs control group, *** $p < 0.001$ by One way ANOVA and post Tukey test. All data are expressed as Mean ± S.E.M, n = 3. 78

Figure 5.3 Dose-dependent cytotoxic effect of (A) snLYZ and (B) snBLA on the MDAMB-231 cell viability at the end of 24 h. Statistically significant vs control group, *** $p < 0.001$ by One way ANOVA and post Tukey test. All data are expressed as Mean ± S.E.M, n = 3. 79

Figure 5.4 Dose-dependent cytotoxic effect of (A) snLYZ and (B) snBLA on the MDAMB-231 cell viability at the end of 48 h. Statistically significant vs control group, *** $p < 0.001$ by One way ANOVA and post Tukey test. All data are expressed as Mean ± S.E.M, n = 3. 80

Figure 5.5 Comparison of the IC_{50} values of snLYZ and snBLA on MCF-7 cells at the end of 24 and 48h. 81

Figure 5.6 Cell viability assay of protein nanoassembly in 3T3 (mouse fibroblast cells) cells (A) snLYZ and (B) snBLA. snLYZ and snBLA did not have any cytotoxic effect in normal cells. All data are expressed as Mean ± S.E.M, n = 3. 82

Figure 5.7 Cell viability assay of protein nanoassembly in HaCaT (human keratinocyte) cells (A) snLYZ and (B) snBLA. snLYZ and snBLA did not have any cytotoxic effect in normal cells. All data are expressed as Mean ± S.E.M, n = 3. 82

Figure 5.8 Dose-dependent cytotoxic effect of Tamoxifen citrate on the MCF-7 cell viability at the end of 24 h. statistically significant vs control group, *** $p < 0.001$ by One way ANOVA and post Tukey test. All data are expressed as Mean ± S.E.M, n = 3. 83

Figure 5.9 Cell viability assay of snLYZ-FAa in MCF-7 cells at 24 h post administration. Folic acid conjugation enhances cytotoxicity in MCF-7 cells. Statistically significant vs control group, *** $p < 0.001$ by One way ANOVA and post Tukey test. All data are expressed as Mean ± S.E.M, n = 3... 85

Figure 5.10 Cell viability assay of snLYZ-FAa in MCF-7 cells at 48 h post administration. Folic acid conjugation enhances cytotoxicity in MCF-7 cells. Statistically significant vs control group, *** $p < 0.001$ by One way ANOVA and post Tukey test. All data are expressed as Mean ± S.E.M, n = 3... 86

Figure 5.11 Cell viability assay of snLYZ and snLYZ-FAa in A549 cells measured by MTT assay. Folic acid conjugation did not affect the cytotoxicity in A549 cells. Statistically significant vs control group, *** $p < 0.001$ by One way ANOVA and post Tukey test. All data are expressed as Mean ± S.E.M, n =3. 87

Figure 5.12 Cell viability assay of snBLA-FAa in MDAMB-231 cells at 24 h post administration. Folic acid conjugation enhances cytotoxicity in MDAMB-231cells. Statistically significant vs control group, *** p < 0.001 by One way ANOVA and post Tukey test. All data are expressed as Mean ± S.E.M, n = 3. 88

Figure 5.13 Cell viability assay of snBLA-FAa in MDAMB-231 cells at 48 h post administration. Statistically significant vs control group, *** p < 0.001 by One way ANOVA and post Tukey test. All data are expressed as Mean ± S.E.M, n = 3. 88

Figure 5.14 Cell viability assay of FAa-conjugated snBLA (A) MDAMB-231 cells and A549 cells. (B) Inset shows the percentage of cell viability of A549 and MDAMB-231 cells treated with snBLA and snBLA-FAa at a dose of 133.33 µg/ml. Folic acid conjugation enhances cytotoxicity in MDAMB-231cells. Statistically significant vs. control group, ***p< 0.001 by One way ANOVA and post Tukey test. All data are expressed as Mean ± S.E.M, n = 3. 89

Figure 5.15 Comparison of cytotoxic effect of snLYZ, snLYZ-FAa in MCF-7 cells and snBLA, snBLA-FAa in MDAMB-231 cells by MTT cell viability assay at 24 h post administration. All data are expressed as Mean ± S.E.M, n = 3. 91

Figure 5.16 Fluorescent images of MCF-7 cancer cells showing internalization of acridine orange tagged snLYZ. (A) Control, administered with none; (B) Cell images after administration of acridine orange tagged snLYZ uptake for 1 h; (C) Acridine orange tagged snLYZ uptake at 3 h; (D) acridine orange tagged snLYZ uptake at 6 h; (E) Acridine Orange tagged snLYZ uptake at 12 h. 92

Figure 5.17 Fluorescence microscopic image of MCF-7 cells at (A) 0, (B) 3, (C) 6 and (D) 12 h post administration of snBLA conjugated with acridine orange. The orange fluorescence emitted by the particles inside the cytoplasm are due to the internalised snBLA. The internalization of snBLA was observed within 3 h of administration. 94

Figure 5.18 Cell viability assay of snLYZ in the presence and absence of NAC at 24 h post administration in MCF-7 cells. Statistically significant vs control group, *** p <0.001 by One way ANOVA and post Tukey test. All data are expressed as Mean ± S.E.M, n = 3. 95

Figure 5.19 Cell viability assay of snBLA in the presence and absence of NAC at 24 h post administration in MCF-7 cells. The presence of NAC reversed the cytotoxicity indicating a ROS based mechanism. Statistically significant vs control group, *** p < 0.001 by One way ANOVA and post Tukey test. All data are expressed as Mean ± S.E.M, n = 3. 96

Figure 5.20 Comparison of cell viability in MCF-7 cells at doses of snLYZ and snBLA inducing maximum cytotoxic effects in the presence and absence of NAC at 24 h post administration. All data are expressed as Mean ± S.E.M, n = 3. 97

Figure 5.21 Comparison of cell viability in MCF-7 and MDAMB-231 cells at 24 h post administration of snBLA and BAMLET in a dose range of 16.66 - 333.33 µg/ml. snBLA was found to have a better cytotoxic profile than BAMLET. All data are expressed as Mean ± S.E.M, n = 3. 98

Figure 5.22 Comparison of cell viability of snBLA and BAMLET in (A) HeLa and (B) A549 cells at 24 h post administration. snBLA was found to have a better cytotoxic profile than BAMLET. All data are expressed as Mean ± S.E.M, n = 3. 99

Figure 5.23 Comparison of cell viability of snBLA and BAMLET in (A) HaCaT and (B) 3T3 cells at 24 h post administration. snBLA was found to have a better cytotoxic profile than BAMLET. All data are expressed as Mean ± S.E.M, n = 3. 100

Figure 5.24 Comparison of cytotoxic effects of snBLA and BAMLET due to ROS generation in MCF-7 cells at 24 h post administration. The presence of NAC reversed the cytotoxicity indicating a ROS based mechanism in snBLA, however, the presence of NAC partially reversed the cytotoxicity indicating a partial contribution of a ROS based mechanism. All data are expressed as Mean ± S.E.M, n = 3. 101

Figure 5.25 Comparison of cytotoxic effects of snBLA and BAMLET due to ROS generation in MDAMB-231 cells at 24 h post administration. The presence of NAC reversed the cytotoxicity indicating a ROS based mechanism in snBLA, however, the presence of NAC partially reversed the cytotoxicity indicating a partial contribution of a ROS based mechanism. All data are expressed as Mean ± S.E.M, n = 3. 101

Figure 5.26 MTT assay of snBLA in MDAMB-231 cells both treated in the presence and absence Caspase-3 inhibitor, Gallic acid (GA), C (Caspase inhibitor) at the end of 24h. Statistically significant vs control group, ***p< 0.001 by One way ANOVA and post Tukey test. All data are expressed as Mean ± S.E.M, n = 3. 103

Figure 5.27 Western blot analysis of Caspase 3 and Hsp90 expression in MDAMB-231 cells treated with snBLA and BAMLET. The expression of Hsp 90, Caspase 3 is observed in the samples labelled vertically, Lane 1 (control), Lane 2 (nmBLA), Lane 3 (snBLA) and Lane 4 (BAMLET). β- actin is used as a loading control. 104

Figure 5.28 Hemolysis assay results of various samples. (A) nmLYZ and 0.1% GTD, (B) snLYZ, (C) Tamoxifen. Appropriate (-ve) control RBC and (+ve) control TritonX was used. All data are expressed as Mean ± S.E.M, n = 3. 105

Figure 5.29 Hemolysis assay results of the samples. (A) nmBLA, (B) snBLA,(C) BAMLET and (D) Oleic acid. Appropriate (-ve) control RBC and (+ve) control Triton X was used. All data are expressed as Mean ± S.E.M, n = 3. 106

Figure 5.30 Proposed model of how nanoassembly proteins (snLYZ and snBLA) and snLYZ/snBLA-FAa and cause cell death in cancer cell. (A) In normal cells, (B) In cancer cells. 108

Figure 6.1 Estimation of the maximum loading capacity of the protein nanoassembly, snLYZ. All data are expressed as Mean ± S.E.M, n = 3. 118

Figure 6.2 Estimation of the maximum loading capacity of the protein nanoassembly, snLYZ. All data are expressed as Mean ± S.E.M, n = 3. 120

Figure 6.3 Percentage release of TAM from snLYZ-TAM conjugate at various pH with time till 12 h. A pH dependent increase in drug release was observed in snLYZ-TAM conjugate. All data are expressed as Mean ± S.E.M, n = 3. 121

Figure 6.4 Percentage non-cumulative release of TAM from snLYZ-TAM conjugate at pH 6.0 with time till 30 h. No further release of drug was observed beyond 24 h indicating the maximum possible release of the drug. All data are expressed as Mean ± S.E.M, n = 3. 122

Figure 6.5 Percentage cumulative release of TAM from snBLA-TAM conjugate at various pH (3-7.4) with time till 12 h. A pH dependent increase in drug release was observed in snLYZ-TAM conjugate. All data are expressed as Mean ± S.E.M, n = 3... 123

Figure 6.6 Percentage non-cumulative release of TAM from snBLA-TAM conjugate at pH 6.0 with time till 30 h. No further release of drug was observed beyond 24 h indicating the maximum possible release of the drug. All data are expressed as Mean ± S.E.M, n = 3. 124

Figure 6.7 LYZ activity of various states of LYZ in snLYZ measured by Micrococcus lysodekticus assay. Both snLYZ and 'reconstituted snLYZ' retain partial LYZ activity. All data are expressed as Mean ± S.E.M, n = 3... 125

Figure 6.8 Tryptophan fluorescence spectra of nmLYZ, snLYZ, snLYZ-TAM and 'reconstituted snLYZ' recorded between 300–400 nm. The drop in fluorescence intensity of snLYZ, snLYZ-TAM and 'reconstituted snLYZ' indicates probable translocation of Trp residues to the surface of the protein structure or to a more hydrophobic region. All data were expressed as the mean of three readouts generated from the instrument.............................. 126

Figure 6.9 Protein bound ANS fluorescence spectra of nmLYZ, snLYZ, snLYZ-TAM and 'reconstituted snLYZ'. The surface hydrophobicity of samples increased in the following order, snLYZ < snLYZ-TAM < 'reconstituted snLYZ'. Some of the Trp residues on the surface of the 'reconstituted snLYZ' got exposed to ANS after the drug release from snLYZ, hence an increase in fluorescence intensity. All data were expressed as the mean of three readouts generated from the instrument. 128

Figure 6.10 Tryptophan fluorescence spectra of nmBLA, snBLA, snBLA-TAM and reconstituted snLYZ. The drop in intensity of snLYZ, snLYZ-TAM and reconstituted snLYZ indicates translocation of Trp residues to a more hydrophobic region. All data were expressed as the mean of three readouts generated from the instrument. 129

Figure 6.11 ANS fluorescence spectra of nmBLA, snBLA, snBLA-TAM and reconstituted snBLA. The surface hydrophobicity increased in the following order, nmBLA < snBLA-TAM < 'reconstituted snBLA'< snBLA. All data were expressed as the mean of three readouts generated from the instrument. 130

Figure 6.12 Cell viability assay of free TAM, nmLYZ, snLYZ and snLYZ-TAM conjugates in MCF-7 cells. Three different snLYZ concentration (A) 60, (B) 100 and (C) 200 µg/ml along with TAM (15, 25, 50 µg/ml) were used with protein: TAM and maintained at 4:1 ratio. The increased amount of TAM in the conjugate increased the cytotoxicity in MCF-7 cancer cells. Statistically significant vs control group, ***p< 0.001,*p<0.05 by One way ANOVA and post Tukey test. All data are expressed as Mean ± S.E.M, n = 3. 131

Figure 6.13 Effect of reconstituted samples of snLYZ on the cell viability of MCF-7 cells and comparison of their cytotoxic effect with other formulations. The presence of NAC reversed the cytotoxicity of snLYZ in cancer cells, however, in case of snLYZ-TAM it was however, in case of snLYZ-TAM it was observed to be partially reversed. All the data are expressed as Mean ± S.E.M, n = 3. 132

Figure 6.14 MTT based cell viability assay of snBLA, snBLA-TAM and TAM in MCF-7 cells at 24 h post administration. The ratio of snBLA: TAM used is 1:1 (w/w). The loading of the drug TAM in snLYZ increased the cytotoxicity at all doses. All data are expressed as Mean ± S.E.M, n = 3. 134

Figure 6.15 MTT based cell viability assay of various formulations of snBLA-TAM in MCF-7 cells at 24 h post administration. snBLA-TAM formulations having snBLA: TAM ratios of 1:1, 4:1 and 10:1 were administered in MCF-7 cells. snBLA-TAM (4:1) maximum cytotoxic effect. All data are expressed as Mean ± S.E.M, n = 3. 136

Figure 6.16 MTT based cell viability assay of various reconstituted forms of snBLA-TAM in MCF-7 breast cancer cells. The various ratios of the snBLA: TAM used were 1:1, 4:1 and 10:1 (w/w). The reconstituted snBLA-TAM (4:1) demonstrated maximum cytotoxic effect. All data are expressed as Mean ± S.E.M, n = 3.. 137

Figure 6.17 MTT assay based assessment of ROS mediated cell killing induced by various formulations of snBLA. (A) snBLA:TAM (1:1, 4:1 and 10:1). (B) Reconstituted snBLA (1:1, 4:1 and 10:1). The reconstituted snBLA demonstrated to snBLA alone. Statistically significant vs control group, ***p< 0.001 by One way ANOVA and post Tukey test. All data are expressed as Mean ± S.E.M, n = 3. 139

Figure 7.1 Different steps in the preparation of (A) graphene oxide nanosheets (GOns) using controlled pyrolysis of citric acid. (B) GOns functionalization method. 146

Figure 7.2 Characterization of GOns based on UV-Vis and fluorescence spectroscopy (A) UV-Vis absorption and fluorescence spectra of GOns synthesized using controlled pyrolysis of citric acid. Both excitation and emission slit widths for fluorescence spectroscopy measurement were used as 10 nm each. (B) The photoluminescence spectra of GOns at various excitation wavelengths. All data are expressed as mean of three readouts generated from the instrument. 147

Figure 7.3 Characterization of GO nanosheet (GOns) by AFM imaging. (A) AFM image of GOns. (B) 3D surface morphology of GO nanosheets. 149

Figure 7.4 Characterization of GO nanosheet (GOns) by FESEM imaging (A) FESEM image of GO sheet. (B) FESEM images of functionalized GOns (FGOns) inset shows the magnified image of FGOns. 149

Figure 7.5 Characterization of GO nanosheet (GOns) by (A) Raman spectra of GOns; the G peak at 1580 cm^{-1} and the D peak at 1350 cm^{-1}. (B) XRD analysis of GOns; the sharp diffraction peak for GOns was observed at $2\theta = 10.80^0$. 150

Figure 7.6 Distribution of hydrodynamic diameter analysed by DLS particle size analyser of (A) GOns (122-190 nm), (B) FGOns (141-458 nm). 151

Figure 7.7 FTIR analysis based characterization of GOns, BLA and FGOns (BLA cross-linked GOns). The characteristics peaks for GOns, BLA and FGOns are observed. 152

Figure 7.8 Circular Dichroism based spectroscopy of (A) FGOns and (B) interaction of native BLA with GOns. Significant change in secondary structure was observed in FGOns and nmBLA treated with GOns. All data were expressed as the mean of three readouts generated from the instrument. 154

Figure 7.9 Tryptophan fluorescence measurement of (A) FGOns, and (B) The solution of native BLA with increasing concentrations of GOns. The drop in fluorescence intensity was due to translocation of Trp residues to a more hydrophobic region. All data were expressed as the mean of three readouts generated from the instrument. 156

Figure 7.10 (A) Optimization of ANS concentration for fluorescence spectra of native BLA, and FGOns, and (B) Protein bound ANS fluorescence spectra of native BLA and FGOns. Small drop in surface hydrophobicity was observed in case of FGOns. All data were expressed as the mean of three readouts generated from the instrument. 157

Figure 8.1 Characterization of size and shape using FESEM images of (A) ZnONP, (B) FZnONP conjugates 164

Figure 8.2 AFM image of ZnONP, inset shows the 3D morphology of ZnONP. 164

Figure 8.3 DLS particle size analysis of various samples in suspension (A) ZnONP and (B) FZnONP. 165

Figure 8.4 FTIR spectrum of Native BLA, FZnONP and ZnONP. Inset shows the spectra between 1400 – 1800 cm^{-1} highlighting the Amide I and Amide II peaks. 165

Figure 8.5 Characterization of nmBLA and FZnONP with respect to its conformational state analyzed by the CD spectra of nmBLA and FZnONP. Significant change in the secondary structure was observed for FZnONP. All data were expressed as the mean of three readouts generated from the instrument................ 166

Figure 8.6 Trp fluorescence spectra of BLA and FZnONP. The drop in fluorescence intensity of FZnONP was due to translocation of Trp residues from the surface of the protein to the core of the protein or to a more hydrophobic region. All data were expressed as the mean of three readouts generated from the instrument. 167

Figure 8.7 ANS fluorescence spectra of nmBLA and FZnONP. The surface hydrophobicity of FZnONP was reduced compared to nmBLA indicated a structural change at the surface. All data were expressed as the mean of three readouts generated from the instrument. 168

Figure 8.8 Thermal stability analysis by CD spectroscopy of (A) native bovine α-lactalbumin (nmBLA), (B) Functionalized Zinc oxide nanoparticle (FZnONP) and (C) Comparison of the change in molar ellipticity of nmBLA and FZnONP at 222nm (α-helix). All data were expressed as the mean of three readouts generated from the instrument. 169

Figure 8.9 Thermal stability analysis by measurement of Trp fluorescence spectroscopy of (A) native bovine α-lactalbumin (nmBLA), (B) Functionalized Zinc oxide nanoparticle (FZnONP) and (C) Comparison of the change in Trp fluorescence of nmBLA and FZnONP. All data were expressed as the mean of three readouts generated from the instrument....................................... 171

Figure 8.10 Thermal stability analysis by measurement of ANS fluorescence spectroscopy of (A) native bovine α-lactalbumin (nmBLA), (B) Functionalized Zinc oxide nanoparticle (FZnONP) and (C) Comparison of the change in Trp fluorescence of nmBLA and FZnONP. All data were expressed as the mean of three readouts generated from the instrument. 172

Figure 8.11 pH stability analysis by CD spectroscopy of (A) native bovine α-lactalbumin (nmBLA), (B) Functionalized Zinc oxide nanoparticle (FZnONP) and (C) Comparison of the change in molar ellipticity of nmBLA and FZnONP at 222nm (α-helix). All data were expressed as the mean of three readouts generated from the instrument. 174

Figure 8.12 pH stability analysis by measurement of Trp fluorescence spectroscopy of (A) native bovine α-lactalbumin (nmBLA), (B) Functionalized Zinc oxide nanoparticle (FZnONP) and (C) Comparison of the change in Trp fluorescence of nmBLA and FZnONP. All data were expressed as the mean of three readouts generated from the instrument....................................... 175

Figure 8.13 pH stability analysis by measurement of ANS fluorescence spectroscopy of (A) native bovine α-lactalbumin (nmBLA), (B) Functionalized Zinc oxide nanoparticle (FZnONP) and (C) Comparison of the change in Trp fluorescence of nmBLA and FZnONP. All data were expressed as the mean of three readouts generated from the instrument....................................... 176

Figure 9.1 Hemolysis assay of (A) GOns and (B) FGOns. FGOns demonstrates excellent hemocompatibility compared to GOns. All data were expressed as Mean ± S.E.M, n = 3. 182

Figure 9.2 FESEM images of erythrocytes treated with various samples. (A) Control; erythrocytes administered with none. Administered with (B) 15µg/ml of GOns (C) administered with 15µg/ml of FGOns (GOns and BLA was 1:1 w/w). (D) 66 µg/ml FGOns, (E) 133 µg/ml FGOns and (F) 333 µg/ml FGOns. FGOns demonstrates excellent hemocompatibility compared to GOns. 183

Figure 9.3 Microscope images of human erythrocytes exposed to GOns (15 µg/ml) at different time points. (A) Control at 0 min, (B) 15min, (C) 30 min and (D) 60 min. Magnification is (800X). GOns induces visible damage to human erythrocytes. 184

Figure 9.4 Schematic representation of the interaction of GOns and FGOns with human erythrocytes: Step (1) GOns come in contact with erythrocytes. Step (2) GOns attach on the surface of erythrocytes and cause haemolysis if the concentration of GOns is greater than 30 µg/ml. Step (3) GOns attach on the surface of erythrocytes and do not cause haemolysis if the concentration of GOns is less than 30µg/ml. Step (4) FGOns nanosheets do not interact with RBC's hence, insignificant haemolysis... 185

Figure 9.5 Hemolysis assay of (A) ZnONP, (B) FZnONP. FZnONP shows enhanced hemocompatibility compared to ZnONP alone. All data were expressed as Mean ± S.E.M, n = 3. 186

Figure 9.6 Imaging of MCF-7 cells at 12 h post administration of FGOns. (A) Phase contrast image (B) Cells stained with fluorescein di-acetate (green fluorescence) highlighting cytoplasmic boundary (C) Cells stained with DAPI (blue fluorescence) highlighting the intact nucleus (D) Acridine orange cross-linked FGOns (E) Merged images of A–D. Confocal microscopy images of cellular uptake (12h post administration) of GOns and FGOns cross-linked with acridine orange (F) Merged Phase contrast image showing the degraded cytoplasmic regions treated with GOns.(G) The image highlighting the cellular uptake of GOns (H) merged phase contrast image showing a comparatively intact cytoplasmic boundary of the MCF-7 cells treated with FGOns.(I) The image shows the cellular uptake of FGOns.......... 188

Figure 9.7 Relative cytotoxicity of GOns and FGOns in various cancer. (A) and (B) MCF-7 cells; (C) and (D) MDAMB-231 cells. The cell cytotoxicity was presented as the percentage of mean value. Statistically significant vs. control group, *** p < 0. 001 by One way ANOVA and post Tukey test. All the data were expressed as Mean ± S.E.M, n = 3... 190

Figure 9.8 Relative cytotoxicity of GOns and FGOns in various cancer and normal cells. (A) and (B) HaCaT cells (C) and (D) 3T3 cells. The cell cytotoxicity was presented as the percentage of mean value. Statistically significant vs. control group, *** p < 0.001 by One way ANOVA and post Tukey test. All the data were expressed as Mean ± S.E.M, n = 3... 191

Figure 9.9 MTT assay of ZnONP in breast cancer cells, both in the presence and absence of NAC, (A) MDAMB-231 cells and (B) MCF-7 cells. ZnONP shows a dose dependent increase in cytotoxicity and acts by a ROS dependent mechanism. All the data were expressed as Mean ± S.E.M, n = 3. 193

Figure 9.10 MTT assay of FZnONP in breast cancer cells, both in the presence and absence of NAC, (A) MDAMB-231 cells and (B) MCF-7 cells. ZnONP shows a dose dependent increase in cytotoxicity and acts by a ROS dependent mechanism. All the data were expressed as Mean ± S.E.M, n = 3. 194

Figure 9.11 MTT assay of ZnONP in HaCaT cells, both in the presence and absence of NAC. ZnONP shows a dose dependent increase in cytotoxicity and acts by a ROS dependent mechanism. All the data were expressed as Mean ± S.E.M, n = 3. 195

Figure 9.12 MTT assay of FZnONP in HaCaT cells, both in the presence and absence of NAC. FZnONP did not show any cytotoxicity in HaCaT cells. All the data were expressed as Mean ± S.E.M, n = 3. 195

LIST OF TABLES

Table 2.1 Global Rankings of various Cancers for both sexes based on absolute years of life lost (YLLs) between the year 1990 and 2013.......... 12

Table 2.2 Few key applications of self-assembled proteins in bio-nanotechnology related applications.......... 27

Table 4.1 Percentage of secondary structural components of the native protein and the protein self-assembly. 49

Table 5.1 Comparison of IC_{50} values of snLYZ, snBLA and TAM in MCF-7 cells. 84

Table 6.1 In vitro drug loading of Tamoxifen (TAM) on snLYZ and its release at pH 5.0 and 6.0. The duration of drug loading was 8 h.......... 118

Table 6.2 In vitro drug loading of Tamoxifen (TAM) on snBLA and its release at pH 6.0. The duration of drug loading was 8 h. 119

Table 7.1 The change of BLA secondary structural components in FGOns samples measured by CD spectroscopy.......... 154

Table 7.2 The change of BLA secondary structural components during interaction with GOns measured by CD spectroscopy. 155

LIST OF ABBREVIATIONS

AFM	Atomic force microscopy
AGE	Advanced glycation end products
ANS	1-anilinonapthalene-8-sulfonic acid
ASIRs	Age standardized incidence rates
BAMLET	Bovine α-lactalbumin made lethal to tumor cells
BLA	Bovine α-lactalbumin
CD	Circular dichroism
DA	Dopamine
DALY’s	Disease assisted life years
DHFR	Dihydrofolate reductase
DLS	Dynamic light scattering
DMEM	Dulbecco’s Minimum Essential Medium
DPDIM	2, 2'-diphenyl-3, 3'-diindolylmethane
ER	Estrogen receptor
ET	Endocrine therapy
FA	Folic acid
FBS	Fetal bovine serum
FESEM	Field emission scanning electron microscopy
FR	Folic acid receptor
GA	Gallic acid
GO	Graphene oxide
GOns	Graphene oxide nanosheets
GST	Glutathione S-transferase
GTD	Glutaraldehyde
HAMLET	Human α-lactalbumin made lethal to tumor cells
HSA	Human serum albumin
LYZ	Hen egg white lysozyme
NAC	N-acetylcysteine

NHS	N-hydroxysuccinimide
nmBLA	Native bovine α-lactalbumin
nmLYZ	Native hen egg white lysozyme
PK	Proteinase K
PMSF	Phenylmethanesulfonyl fluoride
ROS	Reactive oxygen species
SERM	Selective estrogen receptor modulator
snBLA	Self-assembled nanostructured bovine α-lactalbumin
snLYZ	Self-assembled nanostructured lysozyme
SOD	Superoxide dismutase
TAM	Tamoxifen
TBSV	Tomato bushy stunt virus
TEM	Transmission electron microscopy
ThT	Thioflavin-T
Trp	Tryptophan
XRD	X-ray Diffraction
YLLs	Years of life lost
ZnONP	Zinc Oxide nanoparticle

TABLE OF CONTENTS

ACKNOWLEDGEMENT........i

LIST OF FIGURES........iii

LIST OF TABLES........xxix

LIST OF ABBREVIATIONS........xxxi

TABLE OF CONTENTS........xxxiii

ABSTRACT........1

CHAPTER 1 INTRODUCTION........5

CHAPTER 2 LITERATURE REVIEW........11

CHAPTER 3 OBJECTIVES AND SCOPE........33

CHAPTER 4 PREPARATION AND CHARACTERIZATION OF PROTEIN NANOSTRUCTURES........35

4.1 MATERIALS AND METHODS........35

4.1.1 Materials........35

4.1.2 Methods........36

4.1.2.1 Preparation of self-assembled nanostructured lysozyme (snLYZ) and bovine α-lactalbumin (snBLA)........36

4.1.2.2 Folic acid conjugation of snLYZ and snBLA........37

4.1.2.3 Characterization of snLYZ and snBLA........37

4.1.2.3.1 Field emission scanning electron microscopy (FESEM)........37

4.1.2.3.2 Atomic force microscopy (AFM)........38

4.1.2.3.3 Dynamic light scattering (DLS) particle size analysis and zeta-potential analysis 38

4.1.2.3.4 FTIR analysis of snLYZ and snBLA 39

4.1.2.3.5 Circular Dichroism (CD) spectroscopy 39

4.1.2.3.6 Tryptophan (Trp) fluorescence measurement 40

4.1.2.4 Stability analysis 40

4.1.2.4.1 Stability of snLYZ and snBLA across various temperature and pH 40

4.1.2.4.2 Proteinase K (PK) assay 41

4.1.2.4.3 Lysozyme activity of snLYZ 41

4.1.2.4.4 Surface hydrophobicity of snLYZ and snBLA 42

4.1.2.4.5 Thioflavin T assay for detection of amyloid formation 43

4.2 RESULTS AND DISCUSSION 43

4.2.1 Preparation and Characterization of snLYZ and snBLA 43

4.2.2 Stability analysis 51

4.2.2.1 Thermal stability of snLYZ and snBLA 51

4.2.2.2 Stability of snLYZ and snBLA against varying pH 59

4.2.2.3 Thioflavin T (ThT) assay 69

CHAPTER 5 PROTEIN NANOASSEMBLY MEDIATED CYTOTOXICITY, MECHANISMS AND TARGETING OF CANCER CELLS 71

5.1 MATERIALS AND METHODS 71

5.1.1 Materials 71

5.1.2 Methods 72

5.1.2.1 Preparation and Characterization of BAMLET (Bovine α-lactalbumin made lethal to tumor cells) 72

5.1.2.2 Cell viability assay..72

5.1.2.3 Folate conjugation for targeting cancer cells..73

5.1.2.4 Cellular Uptake of snBLA/snLYZ in MCF-7 cells 74

5.1.2.5 Reactive oxygen species (ROS) mediated cell death 74

5.1.2.6 Role of Caspase 3 mediated apoptotic cell death 74

5.1.2.7 Hemocompatibility assay 75

5.2 RESULTS AND DISCUSSION 76

5.2.1 Preparation and Characterization of BAMLET...76

5.2.2 Cytotoxicity study of snLYZ and snBLA..76

5.2.3 Folate conjugation for targeting cancer cells...85

5.2.4 Cellular uptake of snLYZ/snBLA in MCF-7 cells 91

5.2.5 Reactive oxygen species (ROS) mediated cell death 95

5.2.6 Role of Caspase-3 mediated apoptotic cell death......................................103

5.2.7 Hemolysis assay: 105

CHAPTER 6 IN-VITRO DRUG LOADING, RELEASE STUDIES AND EVALUATION OF THEIR CYTOTOXICITY 111

6.1 MATERIALS AND METHODS..111

6.1.1 Materials 111

6.1.2 Methods 111

6.1.2.1 Preparation of self-assembled protein and Tamoxifen conjugate 111

6.1.2.2 Drug loading study 112

6.1.2.3 pH-responsive drug release studies 113

6.1.2.4 Preparation of reconstituted protein nanoassembly................................114

6.1.2.5 Characterization of ‘reconstituted snLYZ’ 114

6.1.2.6 Activity assay of nmLYZ and snLYZ 114

6.1.2.7 Cell viability assay of various formulations of snLYZ/snBLA-TAM conjugates containing different ratios of snLYZ/snBLA:TAM and their reconstituted forms..115

6.1.2.8 Evaluation of the mechanism of toxicity of snLYZ/snBLA and snLYZ/snBLA-TAM conjugates 116

6.1.2.9 Hemolysis assay of snLYZ/snBLA and snLYZ/snBLA-TAM conjugates ………………………………………………………………………..116

6.2 RESULTS AND DISCUSSION 117

6.2.1 Preparation of snLYZ/snBLA-TAM conjugates 117

6.2.2 Drug loading efficiency...117

6.2.3 In vitro pH-dependent release...120

6.2.4 Activity assay of LYZ in reconstituted snLYZ-TAM.............................125

6.2.5 Cytotoxicity study of snLYZ-TAM...130

6.2.6 snBLA-TAM based design of various formulations 134

6.2.7 Mechanism of cytotoxicity of reconstituted snBLA.................................138

CHAPTER 7 PREPARATION AND CHARACTERIZATION OF GOns AND BLA FUNCTIONALIZED GOns...141

7.1 MATERIALS AND METHODS..141

7.1.1 Materials 141

7.1.2 Methods 141

7.1.2.1 Preparation of graphene oxide nanosheets (GOns) by pyrolysis of citric acid………………………………………………………………………..141

7.1.2.2 Preparation of BLA functionalized GOns (FGOns) 142

7.1.2.3 Preparation of acridine orange conjugated GOns and FGOns for observing the cellular uptake in cancer cells………...…………………..142

7.1.2.3.4 Characterization of GOns and FGOns 143
- 7.1.2.3.4.1 Electron Microscope analysis 143
- 7.1.2.3.4.2 Atomic Force Microscopy 143
- 7.1.2.3.4.3 X-ray diffraction (XRD) and Raman spectra analysis 144
- 7.1.2.3.4.4 DLS particle size and zeta-potential analysis 144
- 7.1.2.3.4.5 Fourier Transform Infra-red (IR) spectroscopy 144
- 7.1.2.3.4.6 Circular Dichroism (CD) and fluorescence measurement 145

7.5 RESULTS AND DISCUSSION 146
- 7.5.1 Synthesis of GOns and functionalized GOns (FGOns) 146
- 7.5.2 Preparation of Acridine orange conjugated GOns and FGOns for observing the cellular uptake in cancer cells. 147
- 7.5.3 UV absorbance, photoluminescence and fluorescence spectroscopy 147
- 7.5.4 AFM, FESEM imaging, XRD, Raman scattering DLS size distribution and zeta-potential measurement 148
- 7.5.5 FTIR analysis of GOns and FGOns 151
- 7.5.6 Circular dichroism (CD) and Trp fluorescence spectroscopy of BLA in FGOns 153

CHAPTER 8 PREPARATION AND CHARACTERIZATION OF ZnO NANOPARTICLES AND THEIR FUNCTIONALIZATION WITH BLA 159

8.1 MATERIALS AND METHODS 159

8.1.1 MATERIALS 159
- 8.1.2 Methods 159
- 8.1.2.1 Preparation of ZnO (ZnONP): 159

8.1.2.2 Preparation of Bovine α-lactalbumin conjugated ZnO nanoparticles i.e., Functionalized Zinc oxide nanoparticles (FZnONP):................................160
8.1.2.3 Characterization of ZnONP and FZnONP by FESEM analysis............160
8.1.2.3.1 DLS particle size analysis and zeta-potential analysis.......................161
8.1.2.3.2 FTIR analysis..161
8.1.2.3.3 Circular Dichroism (CD), Tryptophan fluorescence (Trp) and ANS fluorescence measurement..161
8.1.2.4 Stability analysis under varying conditions of temperature and pH:......162
8.2 RESULTS AND DISCUSSION:..163
8.2.1 Preparation and Characterization of ZnO nanoparticles (ZnONP) and FZnONP:...163
8.2.2 DLS particle size and Zeta potential analysis..164
8.2.3 FTIR analysis:...165
8.2.4 Circular Dichroism (CD), Trp fluorescence and ANS fluorescence measurement:..166
8.2.5 Stability Analysis due to varying temperature and pH.............................169
8.2.5.1 Thermal Stability...169
8.2.5.2 Stability against varying pH..173
CHAPTER 9 BIOCOMPATIBILITY AND CELL VIABILITY ASSAYS OF GRAPHENE OXIDE NANOSHEETS (GOns) AND ZINC OXIDE NANOPARTICLE (ZnONP)...179
9.1 MATERIALS AND METHODS...179
9.1.1 MATERIALS...179
9.1.2 METHODS...179
9.1.1 Hemolysis assay..179

9.1.2 Cellular uptake of GOns and FGOns..180

9.1.2 Cytotoxicity study...180

9.2 RESULTS AND DISCUSSION 181

9.2.1 Hemolysis assay for GOns, FGOns, ZnONP and FZnONP......................181

9.2.2 Cellular Uptake of GOns and FGOns...187

9.2.2 Cytotoxicity study of GOns, FGOns, ZnONP and FZnONP 189

CHAPTER 10 CONCLUSION..197

CHAPTER 11 FUTURE WORK 201

APPENDIX: SUPPLEMENTARY FIGURES...203

REFERENCES..221

CURRICULUM VITAE...251

ABSTRACT

Development of various therapeutic approaches for the treatment of breast cancer is on the rise. Among them, chemotherapy has been widely practised for the treatment of breast cancer. However, the approach exposes the patient to various kinds of side effects caused by the drugs. Although gene therapy finds a decent approach but it is expensive and associated with delivery problems. In order to avoid the side effects of chemotherapeutic drugs and achieve a cheap and toxicity free therapeutics, the focus has been gradually shifting towards biomolecule-based therapeutics like gene, peptide and proteins as an alternate therapeutic strategy.

In our present investigation, we have developed protein-based various therapeutic strategies in breast cancer which includes two proteins, bovine α-lactalbumin (BLA) and hen egg white lysozyme (LYZ). Both of them are already reported to have antitumor and anticancer activity. However no detail investigation was performed in breast cancer. Moreover, it was also reported for BLA that the specific structural state is responsible for its antitumor or anticancer activity. Here both the proteins were transformed into their self-assembled nanostructure state using simple desolvation technique through the chemical crosslinking process. Both the nanoassembly were characterized in details and their anti-proliferative activity in breast cancer cells was evaluated.

The nanostructures were characterized using FESEM (Field Emission Scanning Electron Microscopy), AFM (Atomic Force Microscopy) and DLS (Dynamic Light Scattering) analysis for size and shape, FTIR (Fourier Transform Infrared

Spectroscopy for bonds involved in nanoassembly), Circular dichroism and Fluorescence spectroscopy and conformational change of proteins. Microscopy and DLS analysis confirmed their average size as 300 nm. The stability of both the self-assembled nanostructures of lysozyme (snLYZ) and α-lactalbumin (snBLA) were examined against thermal, pH and protease stress and found to be highly stable. Moreover, both of them demonstrated excellent hemocompatibility in human erythrocytes as well as cytocompatibility in normal human cells like HaCaT and mouse cells like 3T3.

When the nanoassemblies were applied to breast cancer cells MCF-7 and MDA-MB231, they demonstrated high (> 90%) cell death at 24 h and almost complete cell death after 48 h of administration. The microscopic images confirmed that the internalization of protein assemblies by MCF-7 cancer cells was the major cause of such cell death. Further, the investigation also confirmed that such death was mediated by reactive oxygen species (ROS) generation.The microscopic image and western blotting results confirmed that apoptosis had no role in cell death mechanism.

The cytotoxic behaviour of snBLA was compared with a well reported anti-cancer agent BAMLET (bovine α-lactalbumin made lethal to tumor cells) in four different cancer cell lines including two breast cancer cell lines MCF-7 and MDA-MB-231. Our synthesized snBLA demonstrated better cell killing potential than BAMLET with much higher hemocompatibility.

Both the nanoassembly demonstrated high Tamoxifen loading (124%) through chemical crosslinking process and release of drug efficiently in a pH-responsive

manner. Furthermore the drug release process was completely regulated by conformational change of the protein in nanoassembly.

In our next step we attempted to develop Graphene oxide nanosheets (GOns) and Zinc oxide nanoparticle (ZnONP) based therapeutic strategy in breast cancer to compare with our protein-based therapeutic approach.

Graphene oxide nanosheets (GOns) and Zinc oxide nanoparticles (ZnONP) are being developed as drug carriers, however, such an approach was plagued with problems such as hemotoxicity and cellular biocompatibility. Hence, we made an attempt to develop a therapeutic strategy based on ZnONP and GOns by functionalizing them with BLA protein. The surface functionalization with BLA improved their hemocompatibility in human erythrocytes and cytocompatibility in normal human cells. They also demonstrated high anti-proliferative activity in breast cancer cells via the ROS-based mechanism of cell death. However, considering the consequence like protein degradation in cells and subsequent exposure of GOns and ZnONP to cells may lead to their accumulation in normal cells and tissues that might limit their use as a rational approach.

Therefore, in our present study, we concluded that our developed stable self-assembled nanostructured lysozyme and α-lactalbumin can be used as a rational therapeutic strategy in breast cancer.

KEYWORDS: Breast Cancer; lysozyme; bovine α-lactalbumin; self-assembly; graphene oxide nanosheet; zinc oxide nanoparticles; drug loading and release; reactive oxygen species; cellular uptake; biocompatibility.

Chapter 1

Introduction

According to GLOBOCAN 2008, the second most commonly diagnosed cancers worldwide is breast cancer that is associated with 10.9% of the global cancer incidences (Ferlay et al., 2010). Recently documented statistics about breast cancer in the year 2013, reveal 1.8 million incidences of breast cancer and 4,64,000 deaths. As a result of breast cancer, 13.1 million people had disease assisted life years (DALY's) in 2013 with the developing and developed countries contributing 63% and 37% respectively (Fitzmaurice et al., 2015).

As far as the cancer therapy is concerned there have been ample ways to treat breast cancer and chemotherapy is the most common among them. Numerous chemotherapeutic drugs such as paclitaxel, tamoxifen, cisplatin, 17-DMAG are widely used for the treatment of breast cancer (Andey et al., 2015; Zhou et al., 2002). Many new compounds such as 2, 2'-diphenyl-3, 3'-diindolylmethane (DPDIM) are being also pursued recently as potential anti-breast cancer agents in breast cancertherapy (Bhowmik et al., 2013). These compounds, however, inflict serious side effects that sometimes limit their use beyond a certain dose in patients. Gene therapy is a promising and expensive approach, but it is plagued with problems with site specific delivery. While metal/non-metal nanoparticles such as Fe_2O_3, Ag, Au, TiO_2 , ZnO have shown a lot of promise in targeted drug delivery system against cancers, their accumulation in body tissues and cells and their subsequent detrimental side effects have raised further concerns about their future applications (Baek et al., 2012; Balasubramanian et al., 2010; Banerjee, 2011; Chakraborti et al., 2009; Iversen et al., 2013; Khandelia et al., 2014; Scown et al., 2009).

Due to the problems mentioned above, the attention is shifting gradually towards protein-based therapeutics. A small protein, lysozyme has already been reported for possessing anti-tumorigenic potential (Caseli and Schumacher, 1955; Guo et al., 2007; Ye et al., 2008). Another protein bovine α-lactalbumin (BLA) is also reported to possess anti-cancer activity (Lin et al., 2008; Sternhagen and Allen, 2001; Thompson et al., 1992; Xu et al., 2005) and cancer-preventing potential (Parodi, 2007). A suitable cancer drug or vehicle should not only be target specific, but it must be biocompatible and biodegradable so that its existence after its desired action should not bring harmful effect on healthy cells and tissues. Protein-based drugs have been proposed to be a new generation therapeutic agent in many diseases including cancer which not only acts as a therapeutic agent without causing any cytotoxicity but can also be used as drug carrier with targeted therapy.

Proteins are normally extremely sensitive to various kinds of external stress because of their intimate link between their unique 3-D structure and biological function (Hegyi and Gerstein, 1999; Martin et al., 1998; Thornton et al., 1999). They can change their secondary as well as tertiary structure depending on the external chemical environments and surface properties proteins can be modulated by external means (Neklesa et al., 2011). Proteins also possess unique properties to form self-assembled nanostructures. They form disordered as well as ordered aggregates (sometimes known as amyloid) in cells and in many cases that may cause number of lethal diseases (Aguzzi and O'Connor, 2010; Ciryam et al., 2013; Jucker and Walker, 2013; Ross and Poirier, 2004). However, protein and their self-assembled structure can be externally driven in-vitro and this has recently been explored towards many applications in biology and medicine (Gangar et al., 2013; Jabbari, 2009; Li et al., 2008; Liu et al., 2011; Panda et al., 2013; Xu et al., 2014; Zhang, 2003; Zhu et al., 2013).

Biological molecules including proteins, peptides, nucleic acids and lipids have inherent properties for self-assembling into the fundamental biological unit, known as the cell. Cellular events like amyloid fibril formation, antigen-antibody recognition, chromatin assembly, and phospholipid membrane self-assembly are excellent examples of molecular self-assembly.

Recently small proteins such as bovine and human α-lactalbumin were also reported to be made lethal against number of tumor cells where a specific conformational state of the protein was responsible for forming the conjugate known as BAMLET (Bovine α-lactalbumin made lethal to tumor cells) or HAMLET (Human α-lactalbumin made lethal to tumor cells) with oleic acid to cause tumor cell death (Rammer et al., 2010; Zhang et al., 2009).The hydrophobic cores present in HAMLET and BAMLET are structurally distinct from their native forms (Mok et al., 2007).

The idea behind using LYZ to develop its self-assembled nanostructure for cancer therapy was originated from its earlier reports of its anti-tumorigenic and anti-cancer potential.

However, besides cancer cells, in most of these cases proteins have been used as conjugates with either chemotherapeutic drugs (Ma et al., 2007; Niidome et al., 2014) or oleic acid which showed various levels of toxicity to healthy cells as well. However, if protein alone acts as a therapeutic agent or can be made lethal against cancer cells without conjugating with other molecules like chemotherapeutic drugs, the post-administration side effect could be avoided.

In our present investigation, we have used hen egg white Lysozyme (LYZ) having a molecular mass of 14.4 kDa and bovine α-lactalbumin (BLA) having molecular mass of 14.17 kDa for the preparation of self-assembled nanostructured particle and applied in breast cancer cells to examine its anticancer effect.

The anticancer potential of exogenous native LYZ was reviewed exhaustively in 1989 by Sava et al where he reviewed various models and mechanism of action of LYZ-mediated cancer cell death (Sava et al., 1989). Lysozyme was used earlier for antitumor activity in many in vivo model systems of animal tumors (Fukawa et al., 1982; Sava, 1989; Sava et al., 1988; Sava et al., 1986). However, after 1989, except the report on the anti-proliferative effect of recombinant human lysozyme in gastric cancer cells (Guo et al., 2007), no significant progress was made towards LYZ- based therapeutic approach in cancer. Recently lysozyme extracted from a marine bacterium has been found to inhibit angiogenesis and tumor growth in mice (Ye et al., 2008).

In our present investigation we have prepared a structurally stable self-assembled nanostructured lysozyme (snLYZ) and bovine α-lactalbumin (snBLA) synthesized using a simple desolvation technique. Further, we characterized the nanoassemblies for their shape and size using Field Emission Scanning Electron microscopy (FESEM), Atomic force microscopy (AFM) and Dynamic light scattering (DLS) particle size analysis. The conformational state of the protein self-assembly was characterized using Circular Dichroism (CD), Tryptophan and ANS fluorescence spectroscopy. Using these techniques the stability studies of the protein nanoassemblies were performed against varying temperature, pH and protease related stress.

These protein nanoassemblies were evaluated for their anticancer activity in breast cancer cells using the MTT assay and the cellular uptake study was also performed. Moreover, we also conjugated the nanoassemblies with activated folic acid to observe the enhancement in uptake in breast cancer cells. The drug loading and pH responsive drug (Tamoxifen) release potential were also studied. The hemocompatibility assays for the above mentioned protein nanoassemblies along with the drug loaded state were also performed. We also attempted to develop graphene oxide nanosheet (GOns) and zinc oxide nanoparticles (ZnONP)-based therapeutic approach in breast cancer for a comparative reason with our protein based approach.

In addition to the above, we have also synthesized graphene oxide nanosheets (GOns) and Zinc oxide nanoparticles (ZnONP's) by modifying the standard synthesis procedures. The anticancer activity of GOns and ZnONP were evaluated in breast cancer cells. Both these nanostructures were functionalized with bovine α-lactalbumin and their anticancer activity were evaluated in breast cancer cells. The GOns and ZnONP nanostructures along with their protein functionalized states were also evaluated for their hemocompatibility. Overall, the thesis contains a detailed study on the development of two small protein based therapeutic option for breast cancer and an approach to establish a realistic strategy for future implementation.

Chapter 2

Literature Review

Cancer is one of the leading causes of death worldwide which figured out to be 7.6 million deaths (approximately 13% of all deaths) in 2008 and the death projection is on the rise. Breast cancer is the most common types of cancer and responsible for majority of cancer death among females, accounting for 23% of all cancer cases and 14% of all cancer-related deaths (Ferlay et al., 2010).

Breast cancer is still the foremost cause behind cancer death among females in economically developing countries, toppling cervical cancer from the top position, which was the leading cause of cancer death a decade ago (Jemal et al., 2011). Recently documented statistics about breast cancer in the year 2013, reveal 1.8 million incident cases of breast cancer and 4,64,000 deaths. Breast cancer resulted in 13.1 million people leading disease assisted life years (DALY's) in 2013 with the contribution from developing and developed countries being 63% and 37%, respectively (Fitzmaurice et al., 2015).

More alarming findings reported are as follows (Fitzmaurice et al., 2015):

1. Every woman among 18 women developed breast cancer after birth till 79 years.
2. Breast cancer had the highest incidence among women in 161 countries and is the most common cause for cancer deaths in women in 98 countries.
3. The ranking for breast cancer moved from sixth in the year 1990 to fifth in the year 2013 (see Table 2.1).

4. The number of breast cancer incidence rates in the year 2013 increased by 8,98,000 (99% increase) compared to the year 1990 (see Fig.2.1A).

Table 2.1 Global Rankings of various Cancers for both sexes based on absolute years of life lost (YLLs) between the year 1990 and 2013.

Rankings	1990	Rankings	2013
1	Tracheal, bronchus and lung cancer	1	Tracheal, bronchus and lung cancer
2	Stomach Cancer	2	Liver Cancer
3	Liver Cancer	3	Stomach Cancer
4	Colon and rectum cancer	4	Colon and rectum cancer
5	Leukemia	5	Breast cancer
6	Breast cancer	6	Esophageal Cancer
7	Esophageal Cancer	7	Leukemia
8	Cervical Cancer	8	Pancreatic Cancer
9	Brain and Nervous system Cancer	9	Cervical Cancer
10	Non-Hodgkin lymphoma	10	Brain and Nervous system Cancer

5. The breast cancer incidence rates would have increased by 38% with a stable population and age. However, with aging population with unchanged incidence rates would have pushed the breast cancer incidence rates to 35% and 26% respectively (see Fig.2.1B).

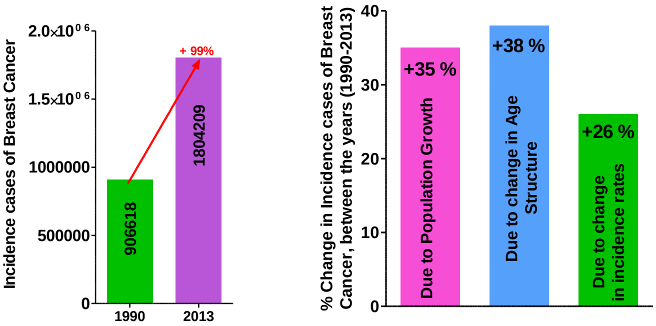

(A)

(B)

Figure 2.1 Cancer statistics between the period 1990-2013 (A) Incidences of breast cancer is on the rise from 1990 to 2013, (B) Percentage change in incidence rate due to population growth (35%), due to change in age structure (38%) and due to change in incidence rates (26%).

6. Eventhough female breast cancer incidence is lower in developing countries, it is increasing rapidly compared to developing countries where rates have been stable to declining since the early 2000s.
7. Between 1990 and 2013, age standardized incidence rates (ASIRs) per 100,000 have increased by 17% globaly (44.36 to 51.73), 46% in developing countries (22.74 to 40.40) and 8% in developed countries (69.75 to 74.98) (see Fig.2.2).

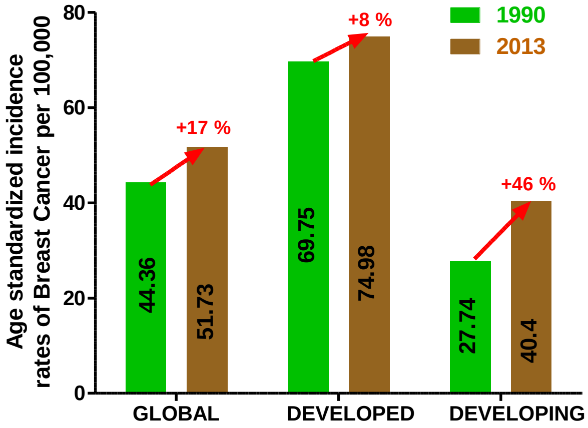

Figure 2.2 Current statistics for Age-standardized incidence rates (ASIR) of Breast cancer (Fitzmaurice et al., 2015).

8. Age-standardized disability assisted life years (DALY) during the period between 1990-2013 have decreased at the global level by 17%, for developed countries by 25% and 3% for developing countries see Fig.2.3.

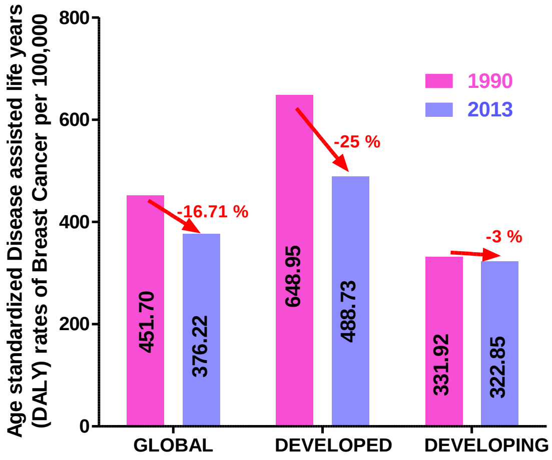

Figure 2.3 Current statistics for ASIR of disease assisted life years (DALY) for Breast cancer (Fitzmaurice et al., 2015).

The incidence rates of breast cancer (Ranks first in 37% of the countries among 188 countries) is a major concern world-wide. Breast cancer (37%) contributes to the major chunk of the cancer burden, closely followed by prostate cancer (29%) (see Fig.2.4).

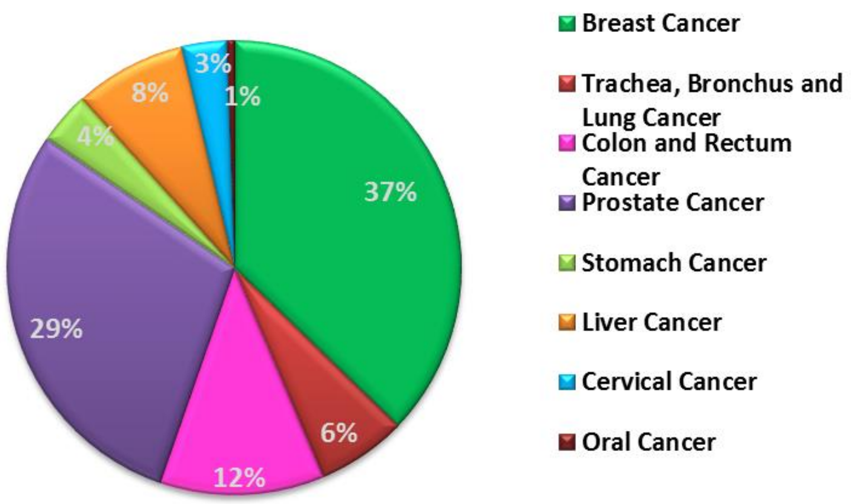

Figure 2.4 Prevalence of various forms of cancers among 188 countries based on incidence rates of the year 2013 (Fitzmaurice et al., 2015).

The factors that result in the international variation in incidence rates of breast cancers largely arise from changes in the reproductive and hormonal behavior of females world-wide (Jemal et al., 2010). Reproductive factors that contribute to the risk of breast cancer include a prolonged menstrual history, obesity, nulliparity, postmenopausal hormone therapy, oral contraceptives, and late onset of pregnancy (Hulka and Moorman, 2001). Apart from the above mentioned reproductive factors increased alcohol consumption, observed in many western countries also increases the chances of breast cancer (Baan et al., 2007; Key et al., 2006).

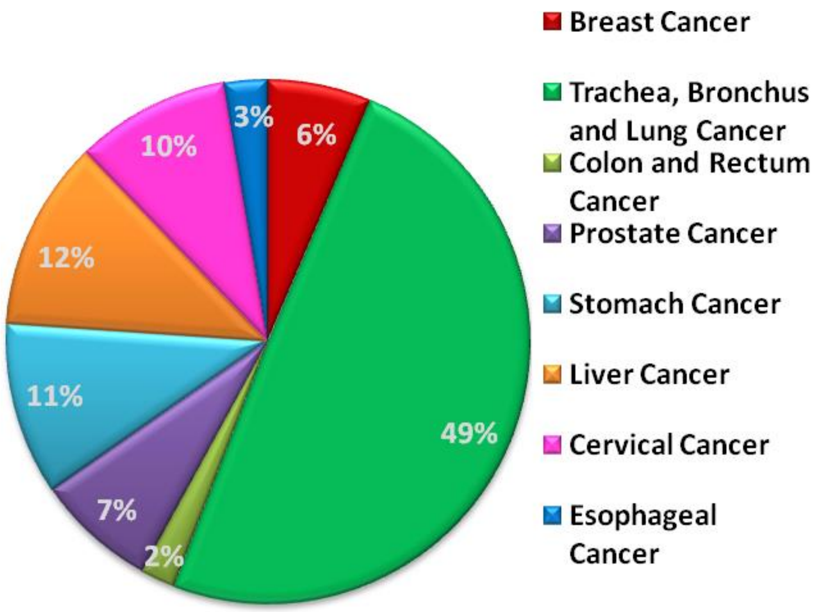

Figure 2.5 Mortality due to various forms of cancers among 188 countries based on mortality rates for the year 2013 (Fitzmaurice et al., 2015).

Breast cancer is the most common malignancy type diagnosed in women in developed countries and developing countries (Fitzmaurice et al., 2015). The incidences of breast cancer have reached alarming proportions and is a major health problem in India (Yeole et al, 2003). As per the survey carried out by Indian Council of Medical

Research (ICMR) in the metropolitan cities such as Delhi, Mumbai, Chennai and Bangalore, during the period between 1982 to 2005, the incidences of breast cancer have increased two-fold. There has been a steady increase in the incidences of breast cancer in India and approximately 100,000 new patients are being diagnosed with breast cancer every year (Yip et al., 2006; Michael et al., 2003). A 12% increase in breast cancer incidences have been recorded in cancer registries during the period 1985 to 2001, which accounts for 57% increase in the cancer burden of India (Yip et al., 2006; Hadjiiski et al., 2006). The total cancer cases in India are likely rise from 979,786 cases in the year 2010 to 1,148,757 cases in 2020. Breast cancer of males and females in India, alone is expected to cross the figure of 100,000 by the year 2020 (Takiar et al., 2010).

Cancer cells possess self-sufficiency in growth signals, insensitive to antigrowth signals, limitless replicative capability, prolonged angiogenesis, apoptosis evading potential, tissue invasion and metastasis potential (Hanahan and Weinberg, 2000) and due to the above mentioned characteristics of cancer cells, targeting cancer cells has been an uphill task. A number of oncogenes and tumor suppressor genes are found mutated in cancer (Stehr et al., 2011).

Estrogen receptor (ER) expression is the key indicator for potential responses to endocrine therapy (ET). Around 70% of all breast cancers are hormone responsive and ER-positive (Lumachi et al., 2013). The introduction of Tamoxifen therapy led to a significant increase in post-surgical survival and a decrease in relapse, particularly in women in early stages of breast cancer and those having ER+ve tumors.

Tamoxifen binds to the estrogen receptors in breast cancer cells and stops estrogen from binding to them and prevents estrogen mediated stimulation of growth and cell proliferation. Tamoxifen acts as an anti-estrogenic agent in breast cells, whereas it acts as an estrogen mimetic in tissues, such as the uterus and bones. Since, it acts like estrogen in some tissues and as an anti-estrogen in others, it is popularly known as selective estrogen receptor modulator (SERM).

For women with ER receptor-positive invasive breast cancer, tamoxifen can be given for five years after surgery to avoid relapse (Koberle and Thurlimann, 2005). It also reduces the risk of development of a new breast cancer in the contralateral breast. For early stage breast cancer, this drug is mainly used for women who have not yet gone through menopause. Tamoxifen can also stop the growth and even shrink tumors in women with metastatic breast cancer. It can also be used to reduce the risk of developing breast cancer in women at high risk (Hu et al., 2015). Tamoxifen has a lot of other advantages. It improves the lipid profile and bone mineral density in post-menopausal patients, however it also suffers from disadvantages such as thromboembolic disorders, uterine disorders and other malignancies (Munshi and Singh, 2008).

A lot of other chemotherapeutic agents have been developed after the synthesis of Tamoxifen which includes paclitaxel, doxorubicin, gemcitabine, cisplatin and Abraxane. Side effects of paclitaxel induces bone marrow suppression, hypersensitivity reactions, cardiovascular problems, neurotoxicity, mucositis, hepatic, renal and dermatological problems (Cella et al., 2003). Doxorubicin causes myelosuppression and cardiac arrhythmias (Tacar et al., 2013). Pulmonary and neurological toxicity is associated with Gemcitabine (Gupta et al., 2002). Cardiovascular disorders are associated with cisplatin-based therapy (Uner, 1993). Conventional treatment such as chemotherapy is plagued with problems related to site-specific drug delivery, drug resistance and recurrence of cancer. Hence, new and more evolved forms of treatment procedures are required for the treatment of cancer.

Due to the above pitfalls associated with chemotherapy, gradually the focus is shifting towards protein-based therapeutics. Commercially, for example, albumin-bound Paclitaxel (Abraxane) was the first protein-nanoparticle formulation that was approved on January 2005, by US-FDA for treating metastatic Breast cancer (Miele et al., 2009). Abraxane consists of nanoparticles of paclitaxel, stabilized with the protein human albumin through hydrophobic interactions and have a particle size of 130 nm. Albumin has a number of advantages that make it an attractive choice for drug vehicle in cancer. It is a natural transporter of endogenous molecules such as vitamins and hormones having non-covalent interactions (Hawkins et al., 2008; Purcell et al., 2000). Moreover albumin facilitates endothelial transcytosis through glycoprotein (gp60) receptor (albondin) (Miele et al., 2009).

A small protein, lysozyme has already been reported for possessing anti-tumorigenic potential (Caseli and Schumacher, 1955; Guo et al., 2007; Ye et al., 2008). The mature hen egg white LYZ is composed of 129 amino acids (Canfield, 1963) and the structure of lysozyme is consistent under a variety of conditions, making it an ideal choice for crystallography studies. The active site of lysozyme contains a deep crevice, which divides the protein into two separate domains linked by an α helix. The first domain (residues 40 to 85) consists mostly of β-sheet structure, whereas the second domain (residues 89-99) is more helical in nature (Strynadka and James, 1991). Lysozyme is a basic protein having a molecular weight of 14.4 kDa with its isoelectric point in the range of 10.5-11.5 (Carr, 1953). Lysozyme acts as a natural bacteriostatic and bactericidal agent by degrading the poly-saccharide (N-acetyl glucosamine (NAG) and N-acetylmuramic acid) that is present in the cell walls of many bacteria. The bacterial polysaccharide consists of long chains of alternating amino sugars: N-acetylglucosamine (NAG) and N-acetylmuramic acid (NAM). It is widely distributed in various physiological fluids and such as human colostrum, milk, blood, tears, saliva, nasal mucus and in cells of the immune system (Cegielska-Radziejewska et al., 2008). Lysozyme is stable under a wide range of conditions, and hence, used as a food preservative for meat, seafood, fruits, vegetables and dairy products (Touch et al., 2009). Lysozyme is used to treat ulcers, infections and neoplastic diseases, and as a component in ophthalmologic preparations (Gasior-Chrzan, 1988; Permanetter and Meister, 1984; Rubio, 2014). Moreover, lysozyme plays an important role in the immune system response of organisms in response to infections and inflammation (Thompson et al., 1990). Due to the aggregation propensity of lysozyme, it can be used for designing protein assemblies for the delivery of drugs and nutraceuticals (Diarrassouba et al., 2015; Price et al., 1999).

The first report on antitumorigenic activity of native lysozyme (nmLYZ) was documented by Caselli and Schumacher (Caseli and Schumacher, 1955). During the period between 1955 and 1989, several studies on antitumorigenic and anticancer effect of nmLYZ on the immunogenic response on various in vivo models were reported by few groups. Two remarkable studies performed by Babudieri-Callerio and Callerio (Callerio-Babudieri and Callerio, 1963; Callerio, 1959) where they demonstrated that the effect of LYZ on H.S 1 (mesenchymal origin), Hep2 (epithelial nature) strains and HeLa cells produced irregular granular structures in the cytoplasm.

Bovine α-lactalbumin (BLA) is another such protein present in the whey fraction of bovine milk and reported to possess anti-cancer activity (Lin et al., 2008; Sternhagen and Allen, 2001; Thompson et al., 1992; Xu et al., 2005) and cancer-preventing potential (Parodi, 2007). The structure of α-lactalbumin is well known and is composed of 123 amino acids and 4 disulfide bridges. The molecular weight is 14.17 kDa, and the isoelectric point lies close to 4.2 (Bramaud et al., 1997). The α-lactalbumin content in human milk and bovine milk is 28 and 3% respectively. Both the human and bovine α-lactalbumin variants share a 72% similarity in amino acid sequence. Both human and bovine α-lactalbumin contains 6, 5 and 0.9% (wt/wt) of tryptophan, cysteine and methionine respectively. Therefore, the only difference in the amino acid compositions of bovine and human milks is mainly attributed to their α-lactalbumin content (Heine et al., 1991). The protein has a distinct binding site for calcium and zinc ions. The binding of calcium increases the stability of the protein and known as holo α-lactalbumin. The calcium depleted state of the protein is known as apo α-lactalbumin. It mainly functions as a modifier protein in lactose biosynthesis (Brodbeck et al., 1967). Moreover due to the aggregation propensity of α-lactalbumin, it can be used for the preparation of protein self-assemblies for delivery of bioactive substances (Livney, 2010). Incidentally, both the above mentioned proteins are monomeric and low molecular weight proteins (14 kDa approx.) having closely similar aminoacid sequences and Ca^{2+} binding pockets.

Recently small proteins such as bovine and human α-lactalbumin have also been reported to be made lethal against number of tumor cells where a specific conformational state of the protein was responsible for forming the conjugate known as BAMLET (Bovine α-lactalbumin made lethal to tumor cells) or HAMLET (Human α-lactalbumin made lethal to tumor cells) with oleic acid to cause cell death (Rammer et al., 2010; Zhang et al., 2009). The hydrophobic cores present in HAMLET and BAMLET are structurally distinct from their native forms (Mok et al., 2007).

However, in most of these cases proteins have been used as conjugates with either chemotherapeutic drugs (Ma et al., 2007; Niidome et al., 2014) or oleic acid which showed various levels of toxicity to healthy cells as well. However, if protein alone acts as a therapeutic agent or can be made lethal against cancer cells without conjugating with other molecules, the post-administration side effects could be avoided.

A suitable cancer drug or vehicle should not only be target specific, but it must be biocompatible and biodegradable so that its existence after its desired action should not bring harmful effect on healthy cells and tissues. Protein-based drugs have been proposed to be a new generation therapeutic agent in many diseases including cancer which not only acts as a therapeutic agent without causing any cytotoxicity but can also be used as drug carrier with targeted therapy.

Proteins are normally extremely sensitive to various kinds of external stress because of their intimate link between their unique 3-D structure and biological function (Hegyi and Gerstein, 1999; Martin et al., 1998; Thornton et al., 1999). They can change their secondary as well as tertiary structure depending on the external chemical environments (Neklesa et al., 2011). Proteins also possess unique properties to form self-assembled nanostructures that can be externally driven in-vitro and this has recently been explored towards many applications in biology and medicine (Gangar et al., 2013; Jabbari, 2009; Li et al., 2008; Liu et al., 2011; Panda et al., 2013; Xu et al., 2014; Zhang, 2003; Zhu et al., 2013).

There are certain advantages of using self-assembled protein nanostructures in biology and medicines, like 1) They are normally nontoxic, non-immunogenic, biocompatible and biodegradable (natural proteins); 2) They are good candidates for conjugation with drug molecules 3) They are structurally and functionally modifiable to make them fit for loading various compounds like anti-cancer drugs and hence, can be used in targeted drug delivery. Nanoparticles developed from natural proteins are usually biodegradable, easy to metabolize, and surface modifications can easily be done for efficient attachment of drugs (Weber et al., 2000). Nanoparticles from various proteins have been developed including bovine and human serum albumin, zein and gliadin (Weber et al., 2000).

Self-assembly is the inherent property of numerous multimeric biological structures to assemble from their respective parts through the random arrangement of molecules and due to the weak formation of chemical bonds between the surfaces (Hosseinkhani et al., 2013). Molecular self-assembly is a powerful tool for scientists fabricating and developing novel supramolecular architectures and spontaneous assembly of molecules into structurally well-defined and stable arrangements through noncovalent and covalent interactions (Duval-Terri et al., 2003; Grill et al., 2007).

In most of the cases, molecular self-assembly relies on chemical and structural compatibility (Whitesides and Grzybowski, 2002). Electrostatic, hydrogen bond, hydrophobic or hydrophilic and van der Waals interactions are involved in such chemical processes. Such collective interactions can produce molecules that are structurally and chemically stable (Hosseinkhani et al., 2013). Molecular components require inherently compatible properties such as specific surface characteristics, surface charge, and polarizability, mass and surface functionalities to self-assemble into different physiological forms (Whitesides and Grzybowski, 2002). Biological molecules including proteins, peptides, nucleic acids and lipids have inherent properties that facilitate self-assembling into the cell. Events such as amyloid fibril formation, antigen-antibody recognition, and chromatin as well as phospholipid membrane self-assembly are excellent examples of molecular self-assembly.

Many artificial bio-nanostructures have been developed by programming specific molecular self-assemblies based on the combination of multiple hydrogen bonds and coordination bonds (Conn and Rebek, 1997; Philp and Stoddart, 1996; Rebek, 1996; Sanders, 1995; Sun et al., 2002).

In biological systems, many types of cellular and sub-cellular structures, such as microtubule network, actin filaments, flagella, clathrin lattices, viruses and chromatins are generated spontaneously by self-assembly of various biomolecules, including nucleicacids, lipids and proteins. Microtubules are naturally occurring nanotubes having a diameter of 24 nm formed by self-assembly of α-tubulin and β proteins, in the presence of GTP, which actively participates in intracellular transport and the development of cytoskeletal components (Mandelkow and Mandelkow, 1994). The clathrin lattice has a diameter of approximately 100nm and is a polyhedral structure developed due to self-assembly of clathrin triskeleton comprising of three proteins along with Mg^{2+} ion, that is involved in receptor-mediated endocytosis (Fotin et al., 2004; Kirchhausen and Harrison, 1984).

The virus is also a good example of a naturally formed supramolecular assembly having a discrete size and possess a rod-like or spherical morphology of approximate diameter of 18–100 nm (Matsuurua, 2014). Such assemblies comprise of genomic nucleic acids encapsulated in an outer protein case known as the capsid. Most spherical viruses developed from the self-assembly of proteins, possessing an icosahedral symmetry involving C5, C3, and C2-symmetric axes.

The satellite tobacco necrosis virus is the smallest virus having a diameter of 18 nm and is formed due to the self-assembly of 60 protein subunits. Tomato bushy stunt virus (TBSV, the diameter of 33 nm) is another instance where the virus formed from 180 quasi-equivalent protein subunits (Branden, 1999; Olson et al., 1983).

Various amphiphilic strategies have been used to develop and design protein/peptide assemblies. Self-assembly of peptide nanofibers have been developed from amphiphilic peptides (Cui et al., 2010; Palmer and Stupp, 2008). Boerakker et al. developed a "giant amphiphile" consisting of an apo-protein of horseradish peroxidase (HRP) and heme-modified polystyrene, which self-assembled to form a protein vesicle (Boerakker et al., 2002). Although simple, the giant amphiphile approach suffers from various disadvantages, such as the broad size distribution of the nanocapsules ranging from 100–1000 nm and very low enzyme activity.

Recently, Kimizuka et al. also reported the development of protein microcapsules by cross-linking proteins at water interface (Morikawa et al., 2012). Protein microcapsules and nanotubes can also prepared by layer-by-layer adsorption of proteins (Komatsu, 2012; Tong et al., 2008) but, such artificial protein assemblies created through hydrophobic effects , electrostatic interactions, lack of precision and discreteness when compared with natural biomolecular assemblies created through specific interactions (Matsuurua, 2014).

Linear self-assembly of protein

Hemoproteins, such as hemoglobin, myoglobin, cytochromes, and peroxidases, can disassemble into heme (cofactor) and apoprotein, and reconstitution can create various artificial hemoproteins (Hayashi and Hisaeda, 2002).Hayashi et al. developed a liner assembly of hemoprotein by successive inter protein heme–heme pocket interactions (Kitagishi et al., 2007).

Barrel / tubeself-assembled structure of proteins

In 1993, pioneering work on the tubular hollow assembly of peptides was reported by Ghadiri (Ghadiri et al., 1993). The peptide nanotubes were formed by self-assembly of cyclic D, L-peptides composed of alternating D- and L-amino acids. The internal diameter was regulated by the structure of cyclic peptides. Self-assembled nanotubes from cyclic peptides containing hydrophobic side chains were applied to transmembrane ion channels (Bong and Ghadiri, 2001; Brea et al., 2010).

Gazit et al. found that the simple dipeptide L-phenylaranyl-L-phenylalanine (FF), which is the hydrophobic core motif of ß-amyloid, self-assembled into stiff nanotubes (Cherny and Gazit, 2008; Gazit, 2007; Reches and Gazit, 2003). When a concentrated solution of FF in hexafluoroisopropanol was diluted by water, ordered semi-crystalline structures were formed. Transmission electron microscopy (TEM) images showed well-ordered tubular assemblies formed having a diameter of 100 nm. The authors also suggested that discrete silver nanowires can be synthesized by reduction of silver ions within nanotubes used as a template, followed by enzymatic digestion of the peptide. The dipeptide FF can form vertically aligned nanotubes by self-assembly on siliconized glass plates (Reches and Gazit, 2006).

Kruif et al. found self-assembled α-lactalbumin into protein nanotubes in the presence of Ca^{2+} ion after partial hydrolysis by a protease (Graveland-Bikker et al., 2009). The protein nanotubes were proposed to consist of dimeric building blocks, which self-assemble through β-sheet stacking.

Ring shaped self-assembly of protein

Closed ring-shaped self-assemblies of proteins can be developed by specific interactions between the ligand dimer and the receptor protein dimer under proper conditions. Wagner et al. reported that two dihydrofolate reductase (DHFR) proteins can be linked by a suitable peptide linker in the presence of bis-methotrexate spontaneously forming cyclic structures with diameters ranging from 8 to 20 nm (Carlson et al., 2006). The authors are also developed enzyme nano-rings (10–70 nm) by self-assembly of DHFR–human histidine triad nucleotide binding 1 (hHint1) protein with bis-methotrexate. The size of the nanoring regulated the enzymatic activity of hHint1 (Chou et al., 2008). Therefore, such enzyme activity can be regulated by designing similar kind of ring-shaped assemblies.

Sphere, cage and polyhedral assemblies

An artificial C3-symmetric peptide conjugatecontaining three β-sheet forming peptides (trigonal-(FKFE)2) self-assembled to form spherical assemblies having a diameter of 19 ± 4nm (Matsuura et al., 2005). Similarly C3-symmetric peptide conjugates having three tryptophan zipper-forming peptides (CKTWTWTE) demonstrated pH-responsive changes in the secondary structure of nanoassembly in the presence of water as a solvent.

The conjugate self-assembled nanospheres are having a diameter of 30 nm by forming a tryptophan zipper at pH 7 and was also converted into a mixture of nanofibers and nanospheres through the formation of β-sheets at pH 11. The conjugate was converted to irregular aggregates mediated by random coil structure at pH 3 (Matsuura et al., 2011).

The design of artificial protein subunits, which form symmetrically arranged protein oligomers, result in the formation of three-dimensional protein cage assemblies that may reduce the loss in entropy of the self-assembly process in water. In 2001, Yeates et al. designed 16 nm tetrahedral protein cages by the self-assembly of a fusion protein of bromo-peroxidase together along with the M1 matrix protein of the influenza virus linked with a nine-residue helical linker (Lai et al., 2012; Lai et al., 2013; Padilla et al., 2001).

Hydrogels based on protein self-assembly

Wang et al. designed artificial proteins that could self-assemble to form hydrogels (Wang et al., 2005).The group designed artificial proteins with an ionic self-complementary peptide group with the polar and nonpolar peptide molecules arranged alternately. Stable β-sheet structures were formed from these peptides that self-assembled to form nanofibers. The interwoven network of these nanofibres that provided the scaffold hydrogel with high water retaining capacity and responds to changes in pH in its environment. These protein hydrogels can be used for facilitating wound closure and tissue repair. These protein hydrogels are biodegradable and find applications in drug delivery systems, which deliver drug-protein complexes in the treatment of cancer.

Adams et al. designed peptide nanotubes from surfactant-like peptides (Adams et al., 2007). Such peptide nanotubes can be used as frames for generation of metal nanocrystals and fabrication of nanowires. Peptide nanotubes can also perform as ion channels when introduced in the phospholipid bilayer present on the cell membrane. Recent reports show protein structures and peptides can form complexes with various metals and semiconducting elements. Surface-binding peptides can bind covalently with the metal surfaces such as gold (McMillan et al., 2001). These properties can find various applications in design and fabricate nanobiosensors. Various applications of self-assembly of protein architectures are shown in Table 2.2.

Table 2.2 Few key applications of self-assembled proteins in bio-nanotechnology related applications.

Applications	References
Self-assembly of amphiphilic peptides to nanoscale fibers for designing nanostructured fibrous scaffold that resembles extracellular matrix	(Hartgerink et al., 2001)
Formation of various nanostructures like nanofibers, nanotubes, vesicles, helical ribbons, and fibrous scaffolds for biomedical applications.	(Zhang et al., 2002)
Artificial proteins can self-assemble to form hydrogels in response to pH and environmental changes. Such protein hydrogels can be used for advanced wound closure and tissue repair in regenerative medicine and tissue engineering. Peptide nanofibers may be used as drug delivery systems with better biocompatibility.	(Niece et al., 2003)
Nanoengineering of molecular design frames and supramolecular structures	(Chung et al., 2011)

A lot of recent progress has been made in the construction of artificial nano-and micro-sized protein/peptide architectures. Peptide nanofibers were fabricated by the self-assembly of coiled-coil-forming and β-sheet-generating peptides. Interprotein heme–hemepocket interactions resulted in the formation of nanotubes. Specific interactions between ligands and receptors provided ring-shaped protein assemblies. The self-assembly of fusion proteins resulted in the construction of protein cages. The generation of artificial nano and micro-structures from protein/peptide conjugates allows new avenues for improvisation in bio-nanotechnology. The protein/peptide nano-architectures may be explored for their effects in various diseases such as cancer since, it has observed that the change in secondary structures may add new properties like specific toxicity towards cancer cells.

Breast cancer is the disease having the greatest presence of nanotechnological therapeutic agents in the clinic. The pegylated form of liposomally encapsulated doxorubicin is currently used for the treatment of metastatic cancer, and albumin-paclitaxel nanostructures commercially known as Abraxane is currently under use for the treatment of breast cancer. More than 150 clinical trials are currently using these drugs in combination with biological therapeutics. Despite these advancements, breast cancer morbidity and mortality is unacceptably high. Nanotechnology offers potential solutions to the historical challenge that has rendered breast cancer so difficult to contain and eradicate. Apart from these protein self-assemblies, there are other non-protein materials such as zinc oxide nanoparticles and graphene oxide nanosheets that are also being used for studies involving drug delivery and therapy in cancer.

Zinc oxide (ZnO) is a common nanomaterial and has a wide range of applications (Fan and Lu, 2005). ZnO acts as a photocatalyst, and it helps in the degradation of environmental pollutants (Xu et al., 2007; Yeber et al., 2000). ZnO nanoparticles (ZnONPs) find use in cosmetics, paints, and medical products. They are also used as antibacterial agents and its application on the surface prevents microorganism growth(Jones et al., 2008). ZnONPs are also used as ingredients in dietary supplements as it stimulates the immune system and acts as an anti-inflammatory agent(Prasad, 2008; Rincker et al., 2005).

Various in-vitro studies demonstrated increased toxicity of ZnO-NPs towards mammalian cells (Jeng and Swanson, 2006; Lai et al., 2008). Brunner et al.(Brunner et al., 2006) showed increased toxicity of ZnONPs (19 nm) towards human mesothelioma and rodent fibroblast cells causing DNA and mitochondrial damages. ZnO also shows increased toxicity towards cancer cells (Sahu et al., 2013). ZnO mediated toxicity towards HaCaT and A549 cells was found to be inhibited when the surface of ZnO was coated with foetal bovine serum (Horie et al., 2009). However the specific serum components were not identified which provided the protection against ZnO mediated cytotoxicity. Hence, surface functionalization aspects of ZnONP may be explored further for cancer therapy.

Graphene oxide (GO) is a graphene derivative having covalent bonds between carbon and oxygen (Dreyer et al., 2010). The continuous increasing interest of researchers for graphene oxide (GO) has been primarily attributed due to its excellent material characteristics, such as superior optical, electronic, chemical as well as mechanical properties (Dong et al., 2012). GO is used as an essential component of biological sensors for the detection of dopamine (DA) (Ponnusamy et al., 2014), glucose (Unnikrishnan et al., 2013), sildenafil (Li et al., 2013), folic acid (Ren et al., 2011), ATP, GTP (Wang et al., 2014), DNA fluorosensing (Zhang et al., 2014b) and protein detection (Lin et al., 2014).Moreover, the good surface functional properties of GO finds applications in targeted hydrophobic drug delivery applications and helps in targeting cancer cells by the folic acid functionalization and near infrared photothermal therapy (Qin et al., 2013). GO has already been explored in tissue engineering (Erika et al., 2014; Kang et al., 2015; Ku and Park, 2013; Lee et al., 2011), as an antibacterial agent (Chen et al., 2014; Gurunathan et al., 2012) and shown promising results against liver (Corr et al., 2013; Lammel et al., 2013), lung (Chang et al., 2010) and breast cancer cells experimentally (Liu et al., 2008).

Although GO nanosheet (GOns) shows wide applications in various kinds of biomedical sciences, its biocompatibility has been a great concern (Liao et al., 2011; Singh et al., 2012; Wang et al., 2012). Since most of the biological and medical applications expose GOns to cells and tissues, biocompatibility of GOns has become a major issue to be considered. Recently, Liao et al. have demonstrated increased hemolysis with the decrease in GOns size. However, the GOns had a broad size distribution with an extremely irregular shape (Liao et al., 2011). Since the cytotoxicity of a nanomaterial depends on its shape and size, it is essential to understand the exact mechanism behind such cytotoxicity.

In an another study, coating of GOns with chitosan led to the elimination of toxicity associated with GOns (Liao et al., 2011). Similarly, coating of GOns with polyethylene glycol increases its biocompatibility and stability in various biological solutions. GOns is also a material suitable for the attachment of hydrophobic drugs with a high level of aqueous solubility (Jabbari, 2009; Liang et al., 2013). In a very recent finding, Wang et al. demonstrated a dose-dependent GOns toxicity towards human fibroblast cells where GOns showed to cause toxicity at a dose higher than 50 µg/ml. In contrary, Ryoo et al. reported that GOns was highly biocompatible with improved gene transfection efficacy in NIH-3T3 fibroblasts (Ryoo et al., 2010). Moreover, GOns in many cases has recently been reported biocompatible and a potential candidate for biological applications, such as drug delivery and carriers in cancer therapy (Zhang et al., 2014a).

Therefore, the apparent connection between GOns and the toxicity produced by them has yet not been established. GOns with various shape and size have their varying effect on the biological system, and hence they differ in biocompatibility. In a recent report, Shen and the group have documented the preparation and characterization of bovine serum albumin (BSA) functionalized GOns (Shen et al., 2010). However, the average size (length) of GOns was close to 1.0 µM, and the BSA protein was comparatively large (Molecular mass is 66 kDa).

Large protein can limit the effective functionalization of GO surface, as they cannot bind entire surface homogeneously. In other findings, Mu and the group (Mu et al., 2012) reported on the preparation of protein-coated GOns and its size-dependent cellular uptake. Although, in the same study, the GOns used were heterogeneous in shape, the protein, BSA was coated based on the strong protein binding capacity of GOns. However, such binding may not be strong enough to withstand the stress associated with prolonged circulation in the blood for biomedical applications. Hence, conjugating GOns with a protein or protein assembly having therapeutic properties will not only increase the biocompatibility but also improve its therapeutic application.

Chapter 3

OBJECTIVES AND SCOPE

The main aim of the current research work was the development of suitable therapeutic strategies using self-assembled protein nanostructures in breast cancer.

The specific objective of the present thesis consists of the following:

1. Synthesis of self-assembled nanostructures of hen egg-white lysozyme (snLYZ) and bovine α lactalbumin (snBLA) and their detailed characterization in terms of size, shape, function, homogeneity, stability, and conformation.
2. Evaluation of their anti-proliferative potential in breast cancer cells such as MCF-7 and MDAMB-231, the mechanism of their cytotoxicity as well as cell death by studying Hsp90 and Caspase 3 expression.
3. Evaluation of hemocompatibility and cytocompatibility of snLYZ and snBLA in normal cells.
4. Synthesize graphene oxide nanosheets (GOns) and Zinc oxide nanoparticles (ZnONP) and develop their therapeutic approach in breast cancer using bovine α-lactalbumin-mediated surface functionalization and comparison with protein nanostructure based approach.
5. Study of drug loading, pH-responsive drug release in vitro and design of suitable formulation using protein nanoassembly and drug to develop the dual therapeutic approach in breast cancer.

Scope of the work:

There are numerous ways for the treatment of breast cancer, and chemotherapy is the most common among them. For the treatment of breast cancer various chemotherapeutic drugs such as paclitaxel, tamoxifen, cisplatin, 17-DMAG are used, however, administration of these compounds induce serious side effects. Hence, the focus has shifted to protein-based therapeutics that are highly biocompatible and efficacious.

The current research work on the self-assembly of protein nanostructures has wider applications for cancer therapy. The previously known applications of protein nanostructures have been limited to drug delivery e.g. Abraxane, where the human serum albumin protein was used for preparing protein nanoparticles for paclitaxel delivery. However, the anti-proliferative activity of the protein was never been investigated. In the current investigation, we have developed self-assembled protein nanostructures that possess anti-cancer activity apart from their drug carrying abilities. The protein nanostructures were found to be highly stable against temperature, pH and protease related stress. The synthesized protein nanostructures can be used to provide a dual therapeutic approach for the treatment of cancer. The acidic environment of cancer cells can be exploited to use these protein nanostructures as a therapeutic agent and as a carrier for the drug. These protein nanostructures, when loaded with the drug Tamoxifen, have demonstrated excellent drug loading and delivery capabilities in response to pH. Hence, these protein nanostructures have a wide scope of usage, by loading of various other anti-cancer agents

Chapter 4

Preparation and Characterization of Protein Nanostructures

4.1 Materials and Methods

4.1.1 Materials

N-acetylcysteine (NAC), Glutaraldehyde (GTD) (25%), Tamoxifen citrate (TAM), N-hydroxysuccinimide (NHS), and Whatman filter paper were purchased from Sigma-Aldrich, India. Lysozyme, Bovine α-lactalbumin, Folic acid (FA), MTT assay kit, Ethanol, DMEM, Fetal bovine serum (FBS), antibiotics, DAPI, acridine orange, Fluorescein diacetate, Phenylmethanesulfonyl fluoride (PMSF), Proteinase K (PK), Sodium cacodylate, Sodium phosphate buffer, 1-anilinonapthalene-8-sulfonic acid (ANS) and Disodium EDTA were purchased from HiMedia India Pvt. Ltd. Milli-Q water was used in all the experiments.

T-25 flasks, 96 well plates and all other plasticwares were purchased from Tarsons Pvt. Ltd., 3T3 (murine fibroblast cell line), HaCaT (human keratinocyte cell line), A549 (human lung adenocarcinoma epithelial cell line) MDAMB-231 and MCF-7 (Breast cancer cell line) cells were procured from NCCS, Pune, India.

Triton-X was purchased from Calbiochem, India. Human blood (B $^{+ve}$) was freshly obtained from the donor before the experiments. All the glasswares used in the study were purchased from Borosil, India. All other reagents were of analytical grade.

4.1.2 Methods

4.1.2.1 Preparation of self-assembled nanostructured bovine α-lactalbumin (snBLA) and lysozyme (snLYZ)

Native protein (10 mg) of LYZ or BLA was taken in a beaker and 2 ml of Milli-Q water was added. The contents were stirred at 500 rpm for 5 min. Ethanol was added dropwise at the rate of 1ml/min and results in the change of colour into turbid white. The cross linker Glutaraldehyde (GTD) was added to achieve a final concentration of 0.1%.The contents were stirred at 500 rpm, for 8 h followed by five cycles of centrifugation (25000g, 30 min, 4^0C). The pellet was resuspended in 2 ml of Milli-Q water and stored for further use at 4^0C. The frequent washing and five cycles of centrifugation were carried out, in order to remove the residual GTD from the formulation.

During the process of optimization, snLYZ was prepared using various concentrations of GTD such as 0.1, 0.3, 1 and 3%. The biological activity assay of LYZ (see section 4.1.2.2.1) (see Supplementary Figure S1), Field emission scanning electron microscopy (FESEM) imaging (see section 4.1.2.2.4) (see Supplementary Figure S3), Circular dichroism (CD) and tryptophan (Trp) Fluorescence spectroscopy (see section 3.2.4) (see Supplementary Figure S2) were performed for the optimization of GTD concentration. Although, the various concentrations of GTD were used in the preparation of snLYZ, the optimized GTD concentration, i.e., 0.1% was used in the preparation of snLYZ and subsequent experiments.

Protein (BLA) amount of 1, 3, 5, 10 and 20 mg were used as the starting material for optimizing the synthesis of self-assembly (see Supplementary Figure S4). The rest of the procedure remains same as mentioned above. After optimization of protein concentration, we also crosschecked the use of GTD concentration along with its effect on the zeta potential of the particles (see Supplementary Figure S5 and S6). Moreover, we also optimized the effect of duration of crosslinking on the particle size of the self-assembly by increasing the duration of cross-linking from 3-8 h (see Supplementary Figure S7).

4.1.2.2 Folic acid conjugation of snLYZ and snBLA

We prepared the snLYZ/snBLA-folic acid (snLYZ-FA) conjugates with the aim of increasing the specificity of snLYZ for cancer cells (Lale et al., 2015). For the preparation of snLYZ/snBLA-FA conjugate, the prepared snLYZ/snBLA was suspended in 5 ml of Milli-Q water, followed by the addition of 25µl of 2 mg/ml stock solution of NHS-activated FA. NHS-activated FA was prepared as reported by Kouchakzadeh and colleagues (Kouchakzadeh et al., 2015). The carboxylic functional groups of the NHS folate were conjugated with the amino groups of the snBLA and snLYZ under alkaline conditions. NHS folate (2.5 mg) was dissolved in 1 mL of 0.1 M bicarbonate buffer (pH 10), and slowly added to the stirring solution of snBLA/snLYZ. The reaction was allowed to continue for 45 min at ambient temperature. The contents were centrifuged at 25000 g for 10 min at 4^0C. The process was repeated five times to remove any residual unreacted NHS-FA.

4.1.2.3 Characterization of snLYZ and snBLA

4.1.2.3.1 Field emission scanning electron microscopy (FESEM)

For capturing high-resolution images of various self-assembled nanostructured samples, FESEM study was performed. A volume of 10 µl of protein assembly (2 mg/ml) was spread on a glass slide and allowed to dry in a desiccator. The glass slides with the samples were fixedon a carbon tape attached to the aluminium stub. The aluminium stub was placed in a gold sputtering unit for 30 s. The samples were subsequently placed in the FESEM (NOVA NANO SEM 450) sample chamber and images were captured at a voltage of 5 kV.

4.1.2.3.2 Atomic force microscopy (AFM)

AFM imaging and measurements were performed using Bioscope Catalyst AFM (Bruker Corporation, Billerica, MA) with silicon probes. A volume of 10 µl of protein assembly (2 mg/ml) was placed on a freshly peeled mica surface followed by drying under a continuous flow of nitrogen gas. The mica discs were gently washed with 200 µl of Milli-Q water.

The mica discs were allowed to dry in a desiccator overnight. The standard tapping mode was used for capturing images of different samples at room temperature in the presence of air. The nominal spring constant of the cantilever used was 20-80 N/m. A standard scan rate of 0.5 Hz with 512 samples per line was used for imaging the samples. AFM image of the snLYZ/snBLA sample was captured the next day.

4.1.2.3.3 Dynamic light scattering (DLS) particle size analysis and zeta-potential analysis

The average particle size analysis and ζ-potential measurement of the aqueous suspensions of protein assembly were performed on a Malvern Zetasizer Nano-ZS DLS analyzer. A sample volume of 10 µl of snLYZ and snBLA (2 mg/ml) was taken and diluted with 1990 µl of deionized water and applied to DLS instrument for sizeand ζ potential analysis.

4.1.2.3.4 FTIR analysis of snLYZ and snBLA

A sample volume of 100 µl (1 mg/ml) of snLYZ and snBLA was used for analysis. The samples were analysed at pH 7.0 in ATR mode. The spectral range was used between 4000 $cm^{-1}$and 500 cm^{-1} with a resolution of 2 cm^{-1} and 25 scans per spectrum in absorbance mode.

4.1.2.3.5 Circular Dichroism (CD) spectroscopy

CD spectra of native lysozyme (nmLYZ), native BLA (nmBLA) , snLYZ and snBLA (200 µg/ml) was recorded using a JASCO J-815 CD polarimeter. Sodium cacodylate (20 mM) at pH 7.4 was used as a buffer for measuring the CD spectra. All the measurements were carried out at physiological temperature (37ºC) and a constant flow of N_2gas.

Each spectrum represented the average of three accumulations recorded between wavelengths of 200-250 nm, with a 0.2 nm resolution, and a bandwidth of 1.0 nm. A scan speed of 100 nm/min and a standard sensitivity was set using a cuvette of path length of 0.1 cm. Appropriate buffer contribution was subtracted from every measurement. The percentage of the secondary structures (α-helix and β-sheet) was calculated using the software provided along with the instrument. The CD signal in mdeg was converted to molar residue ellipticity (θ) [$deg.cm^2.dmol^{-1}$] using Eqn.4.1 (Sohl et al., 2008).

$$[\theta] = 100 \text{ x } (\text{signal}) / C \text{ x } n \text{ x } l \text{ ---------------------------} (4.1)$$

The signal is in mdeg; C represents the protein concentration in mM, ‘n’ represents number of amino acid residues in the protein, ‘l’ represents the path length in cm.

4.1.2.3.6 Tryptophan (Trp) fluorescence measurement

For Trp fluorescence measurement, 20 mM sodium phosphate buffer was used at pH 7.4. The Trp fluorescence spectra were measured with a Perkin-Elmer LS-55 Luminescence spectrometer. Samples of nmLYZ, snLYZ (28 µg/ml), BLA and snBLA (60µg/ml) were incubated, and spectra were measured at 37°C. An excitation wavelength of 290 nm was used, and Trp fluorescence emission spectrum (represents the average of three accumulations recorded) was recorded in the range of 300 to 400 nm. The excitation and emission slit widths were set at 5 and 10 nm, respectively. Background corrections were made with buffer without protein in all cases.

4.1.2.4 Stability analysis

4.1.2.4.1 Stability of snLYZ and snBLA across various temperature and pH

Both snLYZ and snBLA were exposed to a temperature range of 20-80 ºC using the peltier accessory and their CD spectra were generated. The concentration of protein used for generating CD spectra of snLYZ and snBLA was 300 µg/ml. The Trp fluorescence spectra of snLYZ (28 µg/ml) and snBLA (60 µg/ml) was also measured in the temperature range of 20-80 ºC.

The CD spectrum of snLYZ was also recorded by varying the pH of the buffer in the pH range of 5-10.The Trp fluorescence of snLYZ and snBLA was measured in a pH range of 3.0 to 7.4 for snLYZ and 5-10 for snBLA respectively.

For ANS-based fluorescence study, the ANS concentration was optimized by incubating the native protein with varying concentrations of ANS ranging from 10 – 150 µM ANS for 30 min at 25°C. ANS bound fluorescence emission spectra were measured at 25°C at an excitation wavelength of 350 nm. The slit width of 5 nm and 10 nm were used for excitation and emission band pass, respectively with a scan rate of 240 nm/min. The optimized ANS concentration was added to snBLA solution in 20 mM phosphate buffer, pH 7.4. Solutions were incubated at various pH for 30 min at 25°C. Protein-bound ANS fluorescence was measured at 20-80°C and with varying pH (5-10) at an excitation wavelength of 350 nm with a slit width of 5 nm and 10 nm for excitation and emission bandpass, respectively.

4.1.2.4.2 Proteinase K (PK) assay

The stability of snLYZ and snBLA was evaluated by analyzing the proteolytic susceptibilities of both solutions. PK (3 µM) was applied to both the solution (200 µg/ml) and incubated for 10 min at pH 7.4. The reaction was quenched by the addition of 1 mM PMSF (PK inhibitor). The absorbance of both the samples was recorded in a wavelength range of 250-305 nm and necessary baseline corrections were made. The absorbance of the control sample, i.e., PK solution was also measured and deducted. The extent of degradation of the snLYZ, snBLA and their native forms were measured from the drop in absorbance.

4.1.2.4.3 Lysozyme activity of snLYZ

Cells of *Micrococcus lysodekticus* (9 mg) were suspended in 30 ml of 100 mM sodium phosphate buffer, pH 7.4, shortly before the assay. Each of the microplate wells contained 50 µl samples and 200 µl of micrococcus cell suspension. The plate was gently shaken for 1.0 min in a microplate reader (iMark, Bio-Rad) followed by measurement of absorbance at 450 nm and continued for 10 min at 1 min interval.

To observe the effect of pH on the lytic activity of LYZ in snLYZ, the pH of the sodium phosphate buffer was varied from 3 to 7.4 with the addition of 1N HCl.

Lysozyme activity (Ng et al., 2013) was measured by measuring the change in OD over a period of 10 min and is represented by the following formula.

$$\text{Lys activity (Change in O.D)} = \text{O.D}_{\text{initial}} - \text{O.D}_{\text{10 min}} \text{-----------------(4.2)}$$

4.1.2.4.4 Surface hydrophobicity of snLYZ and snBLA

An increase in the surface hydrophobic character of a protein has been shown to provide stability to proteins from thermal stress (Gromiha et al., 2013; Pace et al., 2011). Hence, estimation of surface hydrophobic character of the protein surface will provide an indirect measurement of thermal stability of the protein.

8-Anilinonaphthalene-1-sulfonic acid (ANS) is a common extrinsic fluorescence probe usually used to determine the hydrophobic character of the protein surface. Here, snLYZ/snBLA-bound ANS fluorescence was used to determine the surface hydrophobic character of the protein. ANS concentration of 110 µM was added to 6.0 µM nmLYZ, nmBLA, snLYZ and snBLA solution prepared in 20 mM phosphate buffer, pH 7.4.

Solutions were incubated for 30 min at 25°C. Fluorescence spectra were measured with a PerkinElmer LS 55 spectrofluorimeter at 25°C. The excitation wavelength was fixed at 350 nm with slit width 5 nm, 10 nm for excitation and emission bandpass, respectively and at a scan rate of 240 nm/min.The fluorescence emission range was kept at 360-650 nm.

4.1.2.4.5 Thioflavin T assay for detection of amyloid formation

Thioflavin-T (ThT) is a benzothiazole salt used as a dye for the visualization and quantification of fibrillar and misfolded protein aggregates or amyloid both in-vitro and in-vivo (Hawe et al., 2008). ThT upon binding with the amyloid fibrils causes a peak-shift from 450 to 490 nm. Normally when excited at 440 nm, the ThT bound amyloid fibrils show an intense peak at 490 nm (Hudson et al., 2009).

ThT (20µM) bound protein fluorescence was recorded to monitor the presence of amyloid fibrils in snLYZ and snBLA. Both snLYZ and snBLA solutions were incubated with ThT (20µM) for 20 min at room temperature. After incubation, the nmLYZ and snLYZ samples were excited at 440 nm and the emission fluorescence was measured within an emission range of 450 nm and 600 nm used for the ThT assay.

4.2 Results and Discussion

4.2.1 Preparation and Characterization of snLYZ and snBLA

The preparation method for snLYZ/snBLA and its conjugates is given schematically in Fig.4.1. The details are provided in the "Materials and Methods Section". The prepared snLYZ was characterized using Field emission scanning electron microscopy (FESEM) (see Fig 4.2 A), Atomic force microscopy (AFM) (see Fig 4.2 B), DLS particle size analyser (see Fig 4.2 C). The synthesized snLYZ demonstrated a particle size of 300nm as evidenced from FESEM image, AFM image and DLS particle size analysis.

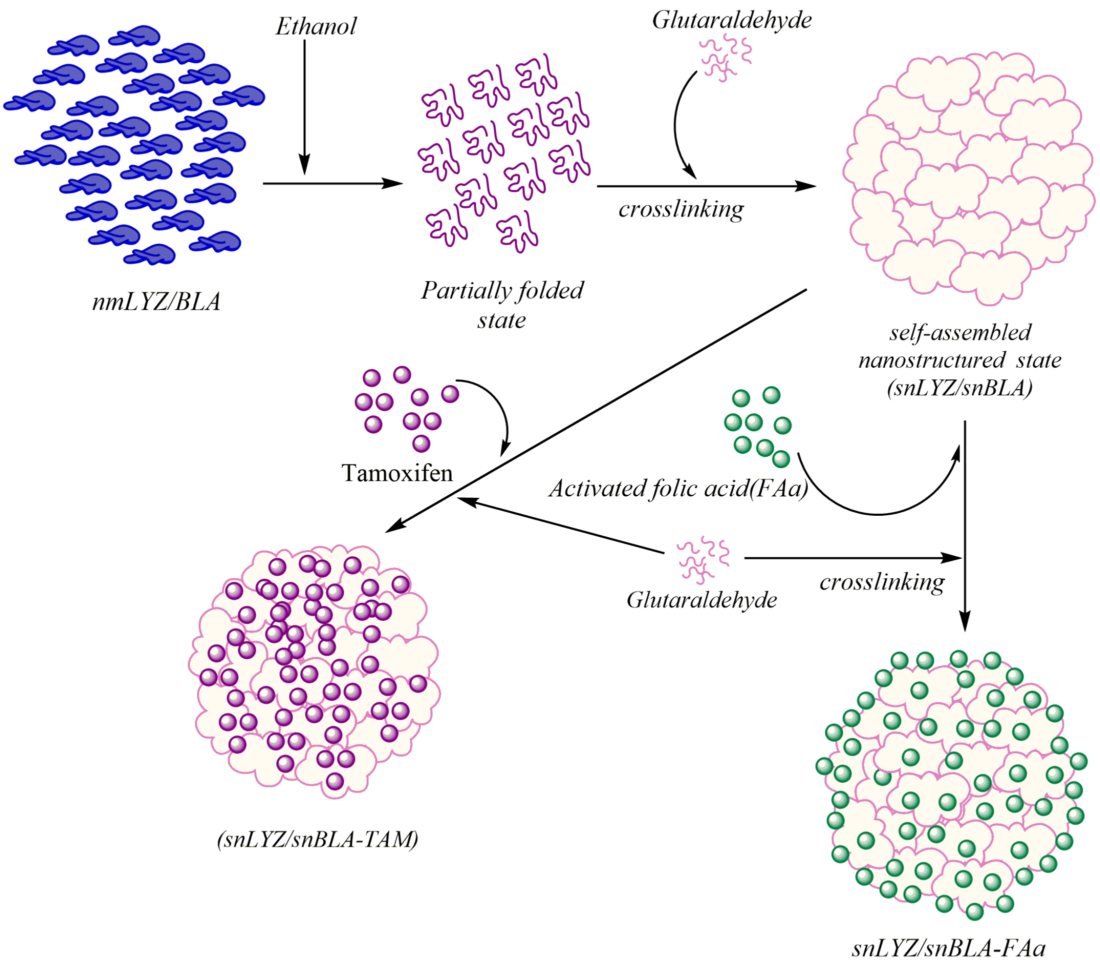

Figure 4.1 Schematic representation of preparation of snLYZ/snBLA and its conjugates with Tamoxifen (TAM) and activated Folic Acid (FAa).

The prepared snBLA was characterized using Field emission scanning electron microscopy (FESEM) (see Fig 4.3 A), Atomic force microscopy (AFM) (see Fig 4.3 B), DLS particle size analyser (see Fig 4.3 C). The synthesized snLYZ demonstrated a particle size of 300 nm as observed from FESEM image, AFM image and DLS particle size analysis. Moreover, one of the most important aspects of our result was the shape of snLYZ and snBLA particles, which was clearly observed to be spherical. However, both protein nanoassemblies were found remain stable for a period of 3 months at a pH of 7.4 and a temperature of 4^0C.

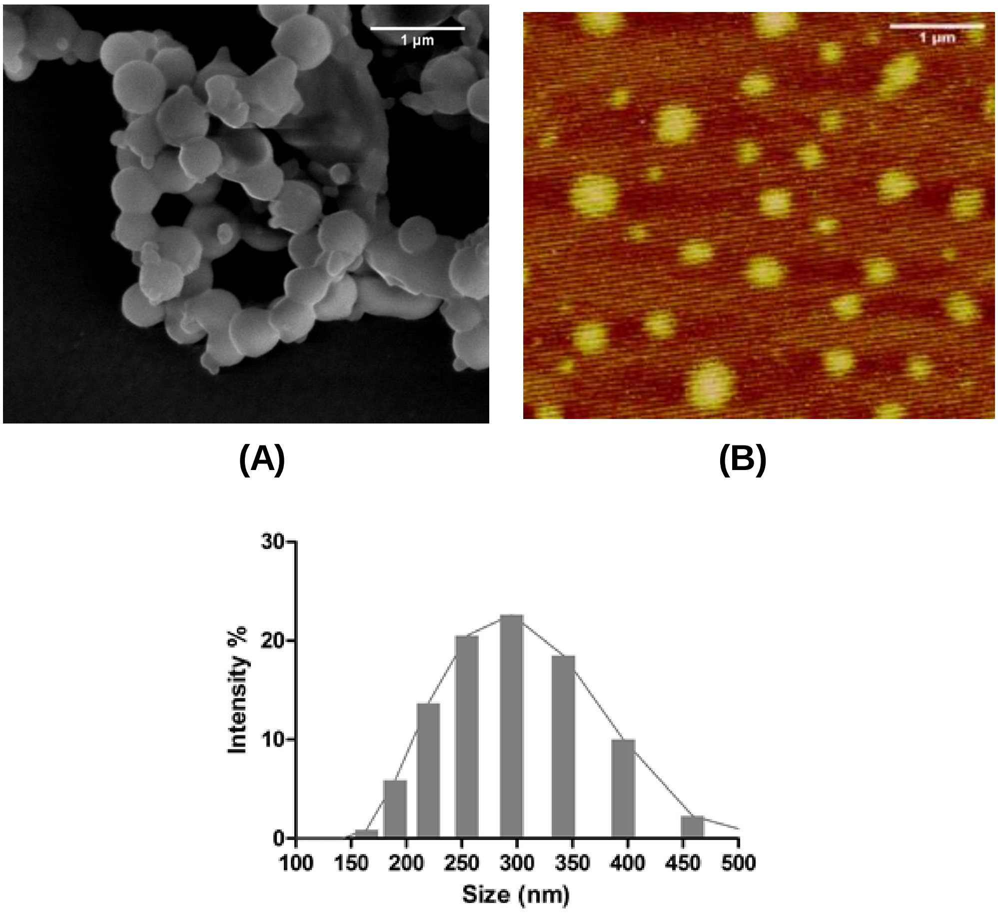

(A)

(B)

(C)

Figure 4.2 Characterization of size and shape of snLYZ. (A) Field emission scanning electron microscopy (FESEM) of snLYZ. (B) AFM image of snLYZ (C) Hydrodynamic diameter of snLYZ obtained by DLS particle size analysis. The overall nanostructure size was found to 300 nm.

Such a spherical shape offers the least resistance against the flow and achieves maximum penetration potential across cell membranes.The zeta potential of snLYZ and snBLA was found to be -39.1 mV and +40 mV respectively.

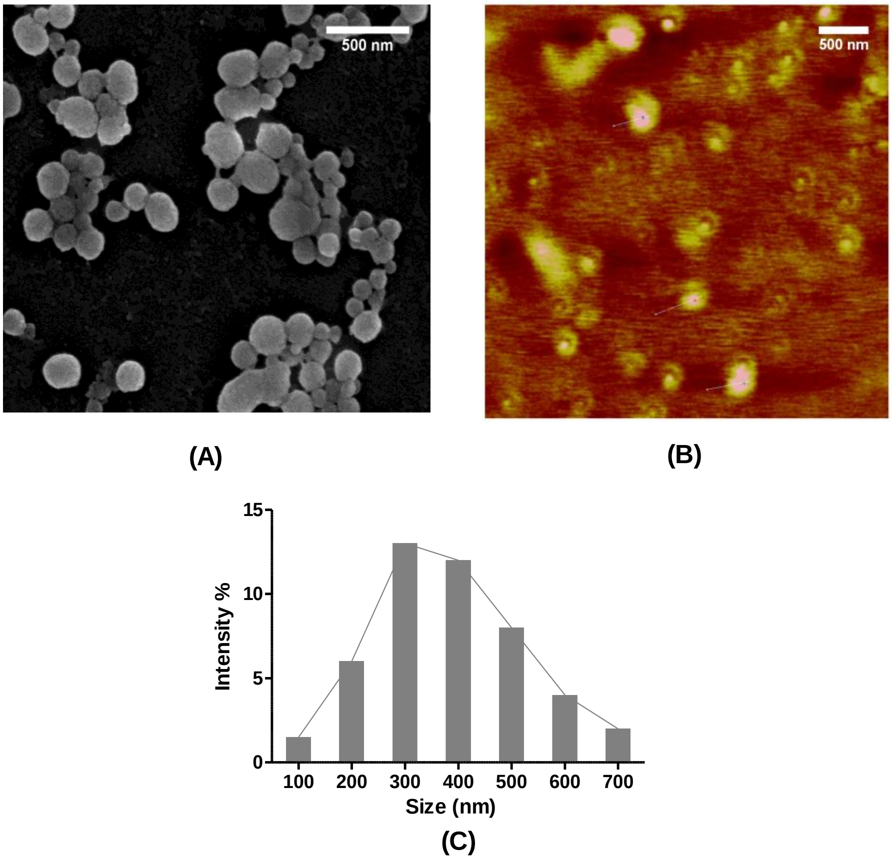

Figure 4.3 Characterization of size and shape of snBLA. (A) Field emission scanning electron microscopy (FESEM) of snBLA. (B) AFM image of snBLA (C) Hydrodynamic diameter of snBLA. The overall nanostructure size was found to be 300 nm.

Zeta potential usually measures the electrostatic potential at the surface of the particle. Normally ±30 mV suggests that the particles in suspension are highly stable and less susceptible to agglomeration. Hence, the snLYZ and snBLA particles are highly stable in suspension without forming aggregates or agglomerated particles.

FTIR analysis clearly revealed the presence of amide I and amide II for nmBLA and nmLYZ respectively(see Fig. 4.4 A and B).

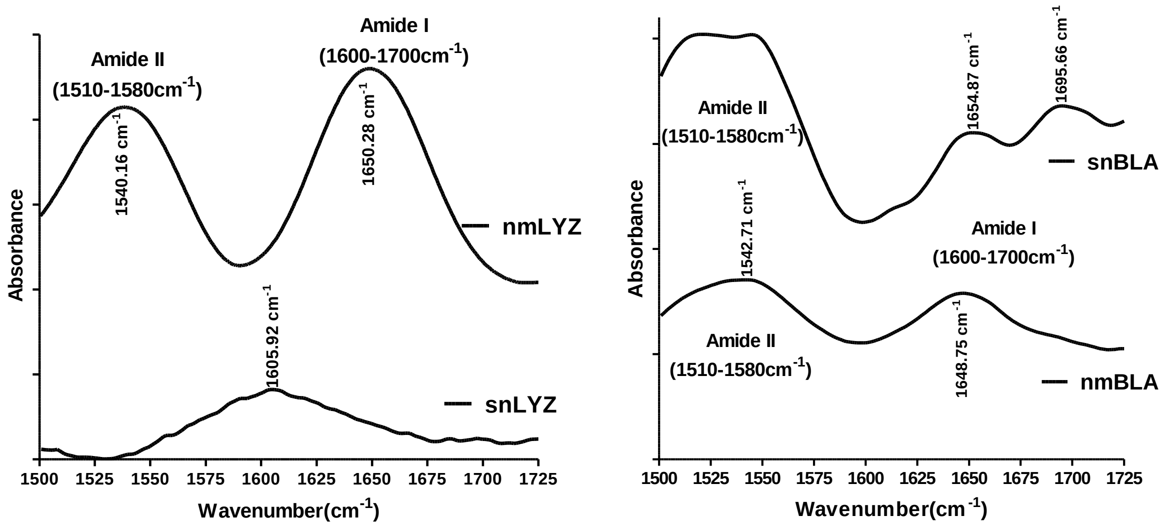

(A) **(B)**

Figure 4.4 FTIR spectra analysis of Amide I and Amide II band between 1500cm^{-1} – 1725 cm^{-1}. (A) nmLYZ and snLYZ (B). nmBLA and snBLA. In both the protein nanostructures a peak shift in Amide I and II peaks was observed.

From Fig. 4.4A, the amide I and amide II peaks and formation of a single peak at 1605.92 cm^{-1} for snLYZ is due to the crosslinking of GTD. On the otherhand snBLA showed a clear change in both shape of spectra and peak position of amide I and amide II, which indicates a change in the secondary structure of the BLA in the conjugates (see Fig. 4.4 B).

The native BLA shows the distinct peak for the amide I and amide II band, however, the amide I band shows a slight right shift in snBLA, indicating a structural change.Moreover, the amide I band in snBLA is split into two peaks at 1654.87 and 1695.66 cm^{-1}, which is also a clear indication of structural change due to the formation of the crosslink with GTD. The Amide II band in snBLA appears to be flattened and broad compared to native BLA, which may be due to interaction with GTD.

The characterization of the secondary structural state of snLYZ and snBLA was carried out using circular dichroism (CD) and fluorescence spectroscopy. The CD and Tryptophan (Trp) fluorescence spectroscopy were performed as per the protocol mentioned in Materials and Methods section.

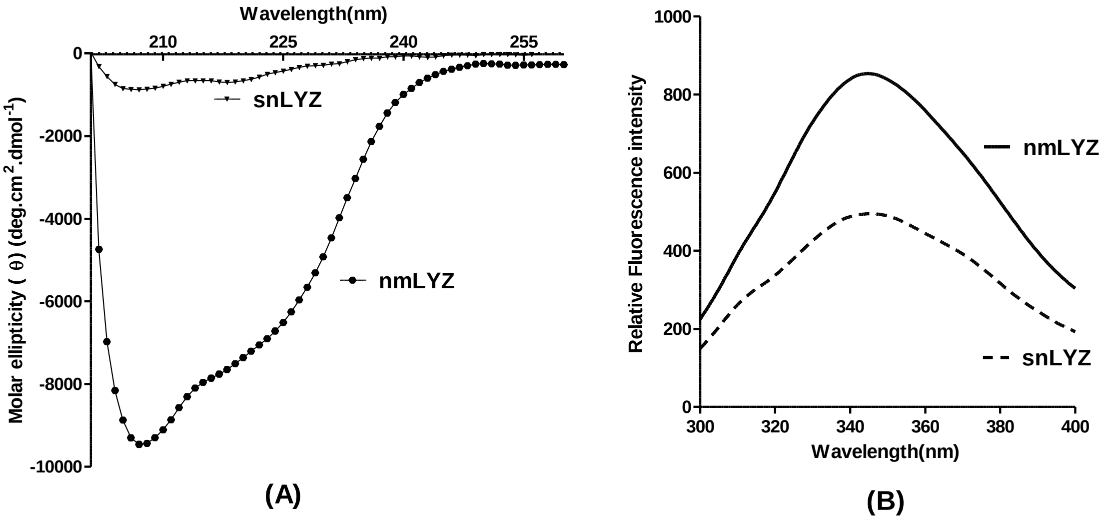

Figure 4.5 Characterization of nmLYZ and snLYZ with respect to its conformational state. (A) Circular dichroism spectra of nmLYZ and snLYZ. (B) Trp fluorescence emission spectra of native lysozyme and snLYZ. All data were expressed as the mean of three readouts generated from the instrument.

From the change in intensity of CD signal for secondary structural components such as α-helix and β-sheet we can estimate the extent of structural change in the protein nanostructures. The change in fluorescence intensity of tryptophan (Trp) is also an indicative of the structural change associated with the position of the Trp residues present in the protein nanostructures.

We observed a huge drop in the CD signal of snLYZ compared to nmLYZ (see Fig.4.5 A). Such a change was inflicted upon snLYZ due to the structural change that occurred while preparing the snLYZ nanoparticles. The percentage of secondary structural components were generated by the software associated with the CD spectrometer and recorded in Table 4.1.

Table 4.1 Percentage of secondary structural components of the native protein and the protein self-assembly.

Protein / Protein assembly	**α- helix content (%)**	**β- sheet content (%)**
nmLYZ	16.9	20.4
snLYZ	32.1	37.7
nmBLA	22.9	21.2
snBLA	25.5	28.5

We observed a similar kind of drop in the CD signal of snBLA compared to nmBLA. Such a change was induced on snBLA due to the structural change that occurred while preparing the snBLA nanoparticles. The percentage of secondary structural components are shown in Table 4.1.

The CD spectra of both snLYZ and snBLA showed a prominent change in the secondary structure (see Fig.4.4 A and Fig.4.5 A) as reflected from the percentage of secondary structural components (see Table 4.1).

We observed an increase in the α- helix (16.9 - 32.1 %) and β-sheet content (20.4 - 37.7 %) by almost two folds in the snLYZ nanostructure. However we observed a significant increase in the β-sheet content (21.2 - 28.5 %) of snBLA with minimal change in the α- helix (22.9 – 25.5 %). Such, a change in the secondary structural components is bound to induce a change in Trp fluorescence intensity. We observed a clear drop in the Trp fluorescence intensity of snLYZ and snBLA (see Fig.4.5 B and Fig.4.6 B).

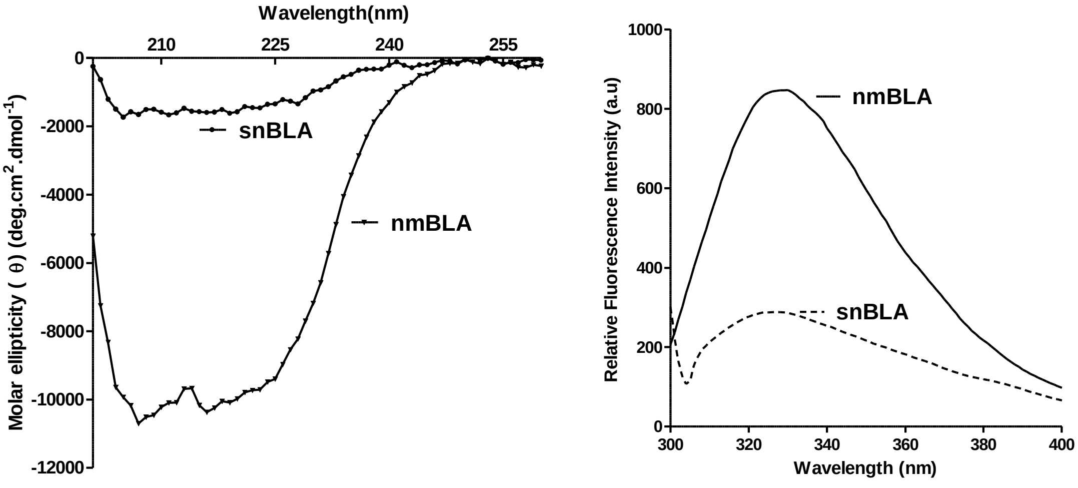

(A) (B)

Figure 4.6 Characterization of snLYZ and snBLA with respect to its conformational state. (A) Circular dichroism spectra of native BLA and snBLA (B) Trp fluorescence emission spectra of nmBLA and snBLA. All data were expressed as the mean of three readouts generated from the instrument

The drop in the Trp fluorescence intensity of snLYZ and snBLA was due to the translocation of the Trp residues present on the surface of the nanostructure to the more hydrophobic regions of the protein nanostructure. Since, the Trp fluorescence recorded is due to the Trp residues present on the surface of the protein , any alteration or shift in the location of Trp residues from periphery, to the more hydrophobic regions or the inner core of the protein is bound to reduce the overall Trp fluorescence.

4.2.2 Stability analysis

Stability of the protein nanostructures was assessed by exposing the protein nanostructures to varying temperature, pH and protease mediated stress. Stability against increased temperature related stress is a major issue (Kaushik and Bhat, 1999). The thermal stability of proteins can be analyzed using CD spectroscopy (Sujak et al., 2007). The stability of a protein structure under varying conditions of change in pH can also be studied using CD spectroscopy (Kwaambwa and Maikokera, 2008). Apart from analyzing the stability of protein nanostructures using CD spectroscopy, Trp fluorescence spectroscopy and ANS fluorescence spectroscopy also can be used for analyzing the stability of protein nanostructures(Kwaambwa and Maikokera, 2007; Yamamoto et al., 2006).

4.2.2.1 Thermal stability of snLYZ and snBLA

The thermal stability analysis of both snLYZ and snBLA across a temperature range of 20-80^{0}C was performed in a CD spectrometer. The temperature related stress may cause a change in the overall structure of the protein nanostructure. Hence, to study the secondary structural change in the protein nanostructure due to increased thermal stress, CD spectroscopy was performed.

The CD signal remained stable for both snLYZ (Fig. 4.7A, B and C) and snBLA (Fig. 4.8A, B and C) in a temperature range of 20-80 ^{0}C indicating increased stability compared to their native forms where we observed a clear variation in the CD signal indicating instability. The native proteins change their structure in response to thermal stress so that they can maintain their stability, however beyond a certain level of thermal stress the protein suddenly deviates from the natural CD signal as observed in nmLYZ (see Fig.4.7 A and C).The overall change in the CD signal at 222 nm is shown in Fig.4.7 C. We have plotted the CD signal at 222 nm for comparison between nmLYZ and snLYZ since, it represents the signal from the α- helix region. Moreover, the region around the α- helix shows a visible change in signal intensity which can be extrapolated to obtain a line graph between Temperature and CD signal.

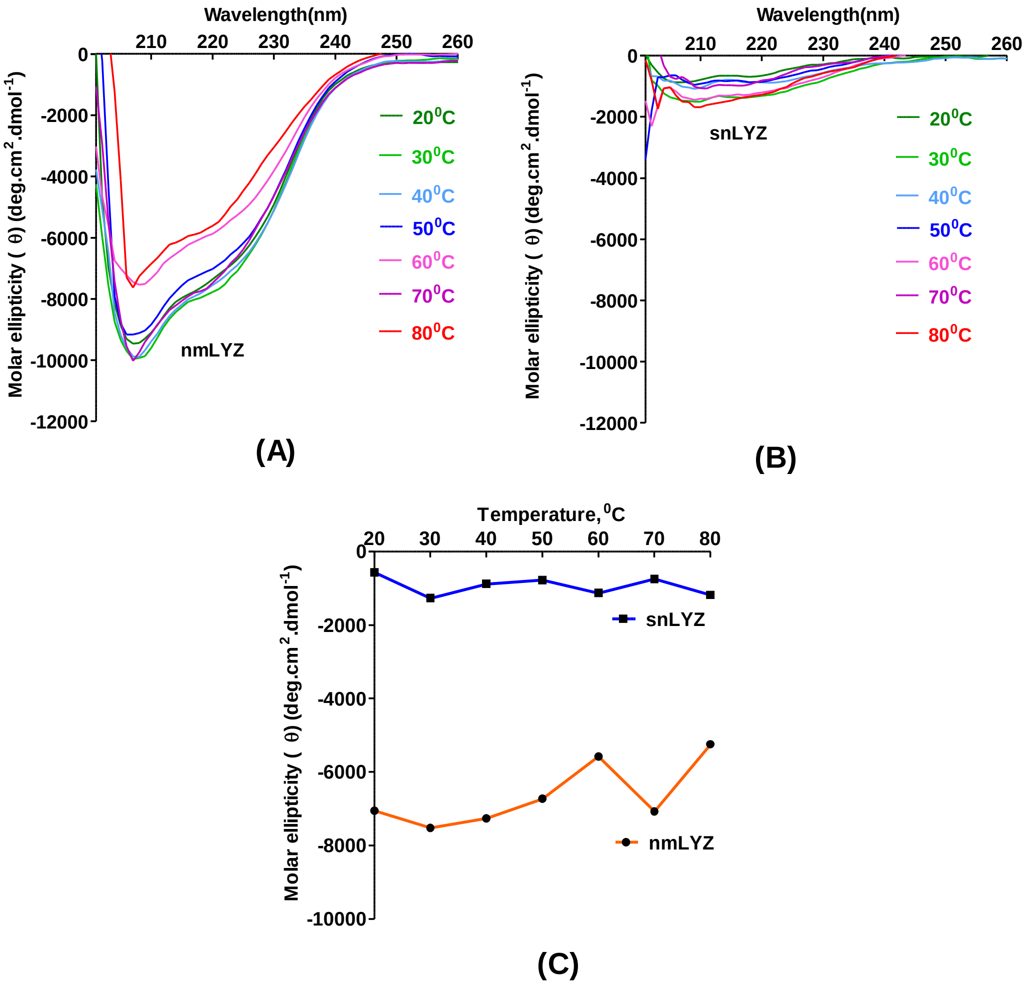

Figure 4.7 Thermal stability analysis of (A) native lysozyme (nmLYZ), (B) self-assembled nanostructured lysozyme (snLYZ) by CD spectroscopy. (C) Comparison of the change in molar ellipticity of nmLYZ and snLYZ at 222nm (α-helix). All data were expressed as the mean of three readouts generated from the instrument.

The CD signal from nmLYZ showed maximum variation beyond 60^{0}C (Fig. 4.7A and C) indicating structural changes in the native lysozyme. This wasbecause at higher temperatures the strength of the hydrogen bonds present in the protein decreases.

The same reason may be ascribed to the constant variation in CD signal with an increase in temperature for nmBLA (Fig. 4.8A and C) indicating thermal instability.The CD signal from snBLA remains stable indicating the stability of snBLA.The CD signal measures the change in secondary structural components in a protein structure. A fairly consistent CD signal indicates that no significant structural change has occurred.

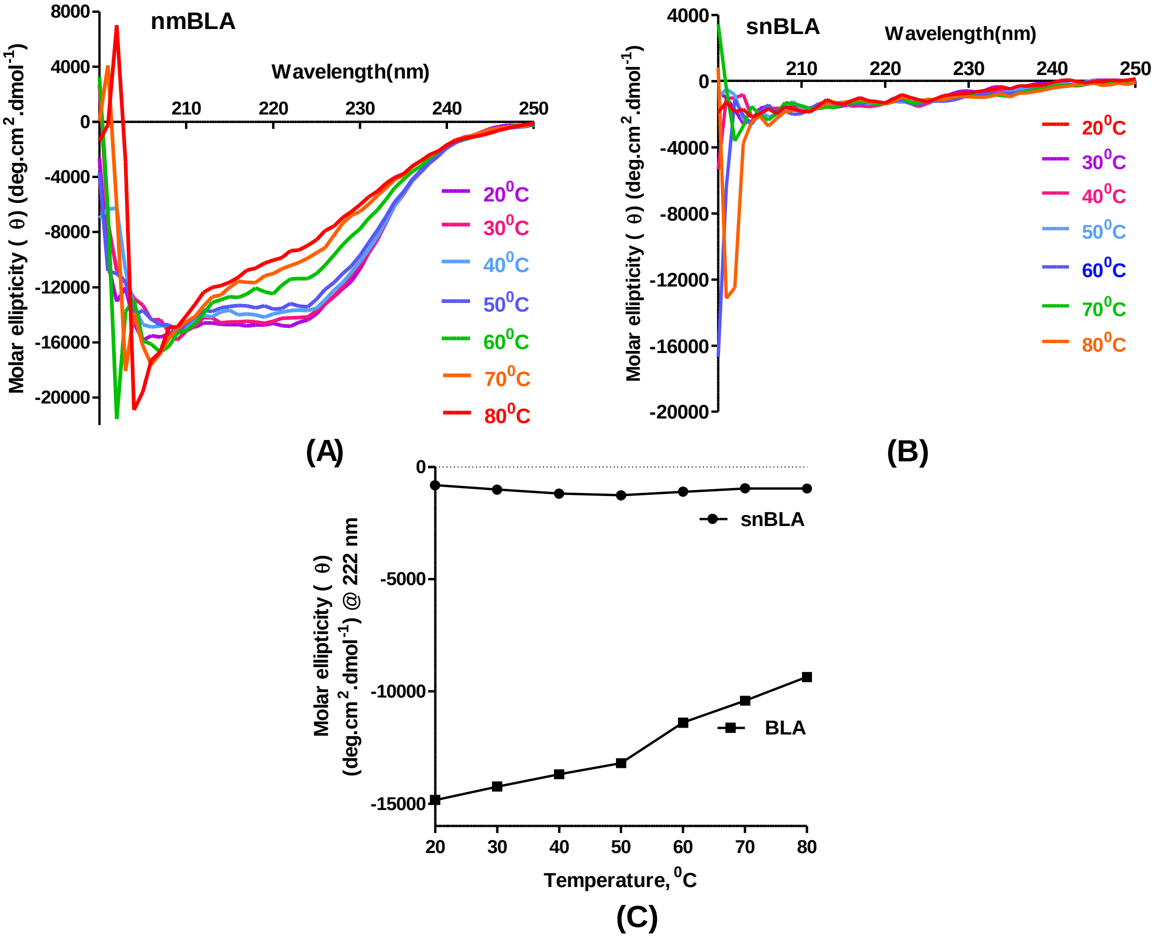

(A)

(B)

(C)

Figure 4.8 Thermal stability analysis of (A) native bovine α-lactalbumin (nmBLA), (B) self-assembled nanostructured bovine α-lactalbumin (snBLA) by CD spectroscopy. (C) Comparison of the change in molar ellipticity of nmBLA and snBLA at 222nm (α-helix). All data were expressed as the mean of three readouts generated from the instrument.

In order to assess the thermal stability of both snLYZ and snBLA, we also measured the Trp fluorescence at varying temperature conditions. We found that the drop in Trp fluorescence for snLYZ (Fig.4.9A, B and C)and snBLA(Fig.4.10A, B and C)were comparatively less compared to their native states.

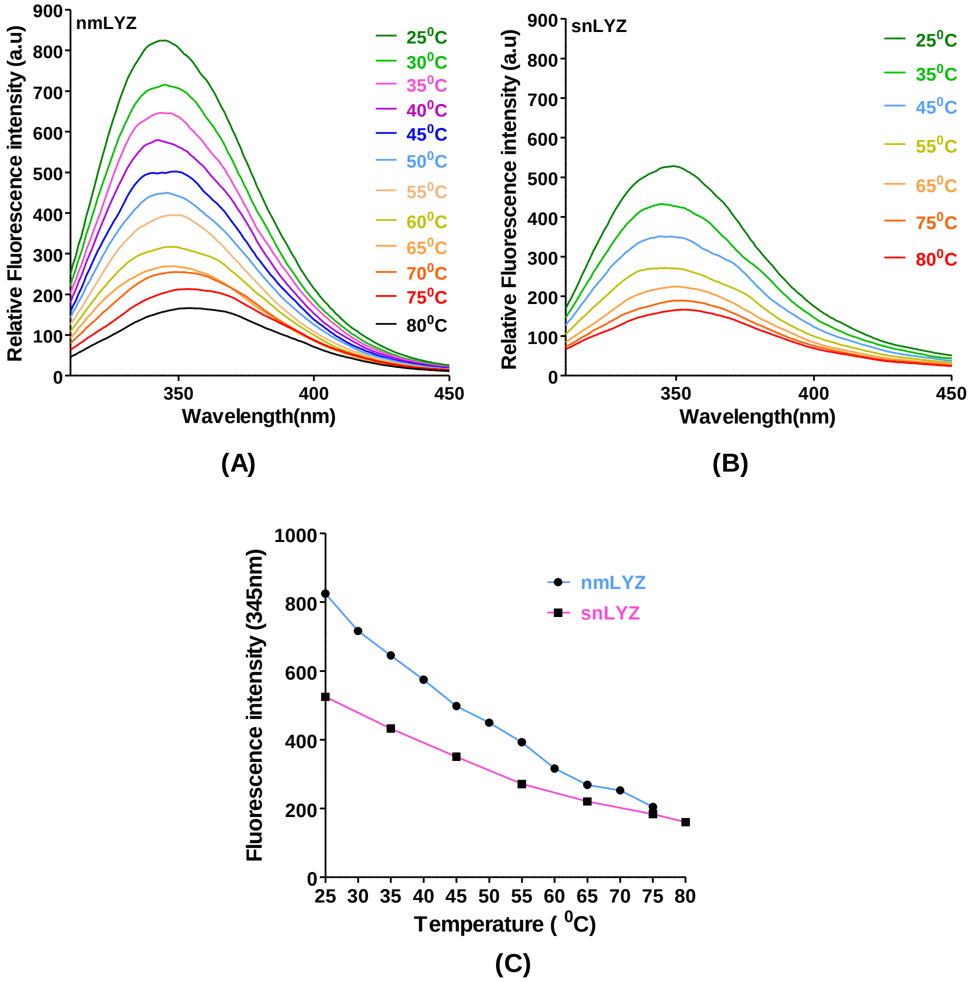

(A)

(B)

(C)

Figure 4.9 Thermal stability analysis of (A) native lysozyme (nmLYZ), (B) self-assembled nanostructured lysozyme (snLYZ) by Tryptophan (Trp) fluorescence spectroscopy. (C) Comparison of the change in Trp fluorescence of nmLYZ and snLYZ. All data were expressed as the mean of three readouts generated from the instrument.

The increased drop in fluorescence of the native proteins due to increase in temperature suggests that the Trp residues present on the surface moved from the surface of the protein to the core of the protein structure or the Trp residues moved to region surrounded by hydrophobic residues.

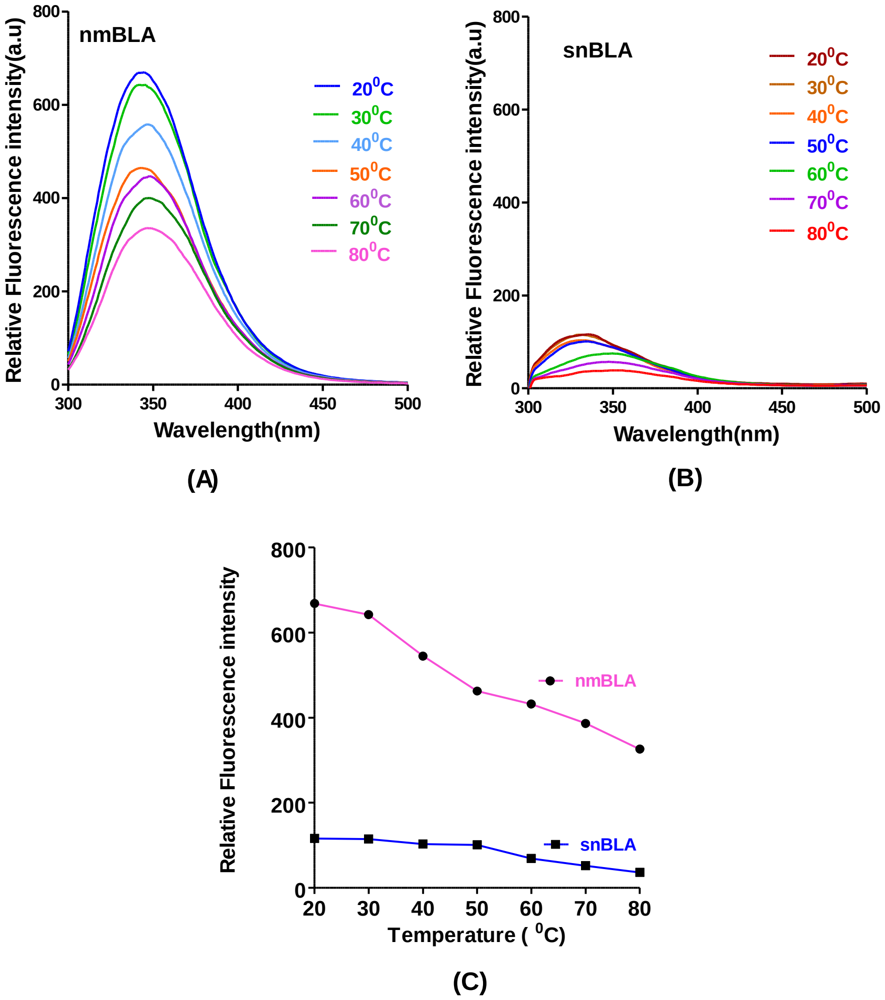

(A)

(B)

(C)

Figure 4.10 Thermal stability analysis of (A) native bovine α-lactalbumin (nmBLA), (B) self-assembled nanostructured bovine α-lactalbumin (snBLA) by Tryptophan (Trp) fluorescence spectroscopy. (C) Comparison of the change in Trp fluorescence of nmBLA and snBLA. All data were expressed as the mean of three readouts generated from the instrument.

Since, the Trp residues directly contribute to the Trp fluorescence, any decrease in the number of Trp residues on the surface of the of the protein would cause a reduction in the overall fluorescence intensity. Such a change in Trp fluorescence is also an indicative of structural change and the environment around the Trp residues present on the surface of the protein.

ANS is a surface hydrophobicity marker for proteins and usually used for the indirect measurement of the surface hydrophobicity on the surface of the protein. The increase in protein-bound ANS fluorescence is an indicator of an increase in surface hydrophobicity of the protein. The protein bound ANS fluorescence for nmLYZ showed that with an increase in temperature the surface hydrophobicity of native protein increased indicating an increase in surface hydrophobicity (see Fig 4.11A and C).

snLYZ demonstrated no change in ANS fluorescence intensity till 60^0C, however a slight increase in ANS fluorescence intensity indicating a slight increase in surface hydrophobicity was observed at 70 and 80^0C (see Fig 4.11 B and C).

The results indicate that with the increase in temperature structural changes occurred on the surface, of the native protein. Such a change on the surface of the protein may be due to the weakening of the hydrogen bonds present in the protein. The increase in surface hydrophobicity is also a protective mechanism that protects the protein against thermal stress (Gromiha et al., 2013).

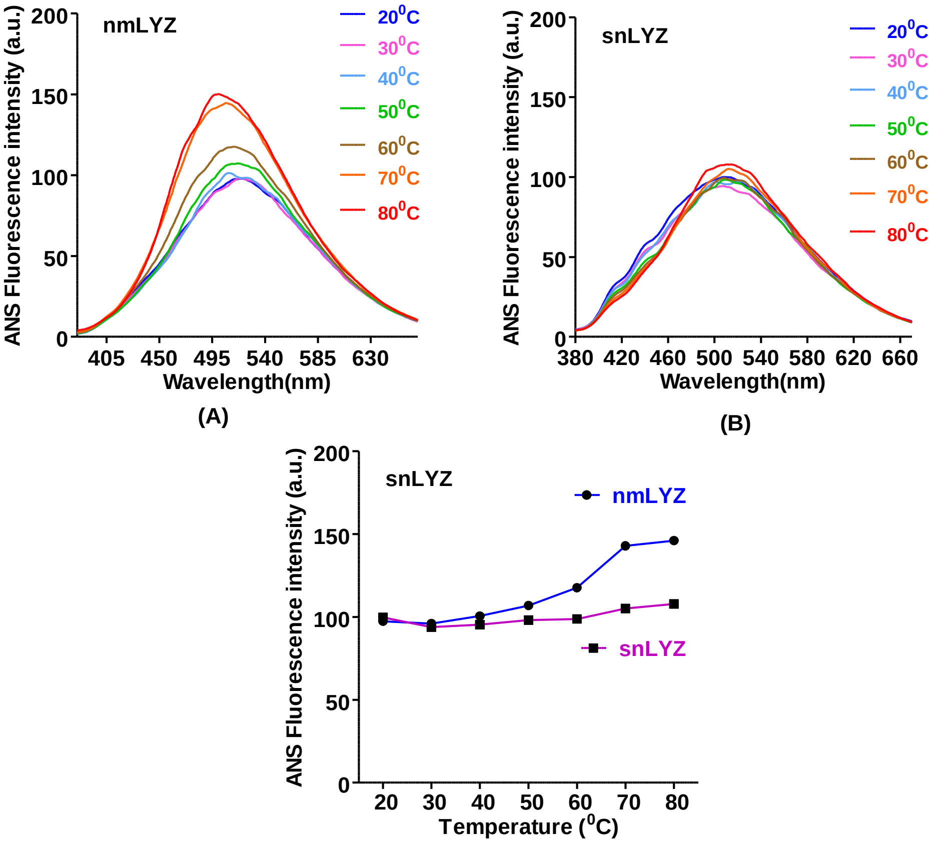

(A)

(B)

(C)

Figure 4.11 Thermal stability analysis of (A) native Lysozyme (nmLYZ), (B) self-assembled nanostructured lysozyme (snLYZ) by ANS fluorescence spectroscopy and (C) Comparison of the change in ANS fluorescence of nmLYZ and snLYZ. All data were expressed as the mean of three readouts generated from the instrument.

The protein bound ANS fluorescence for nmBLA and snBLA also showed that with increase in temperature the surface hydrophobicity of native protein decreased indicating instability whereas the surface hydrophobicity of snBLA increased slightly indicating more stability (Fig.4.12 A, B and C).

Since, ANS binds with the hydrophobic residues present on the surface of the protein, the increase in the intensity of the ANS bound fluorescence is an indirect measure of the surface hydrophobicity of the protein.

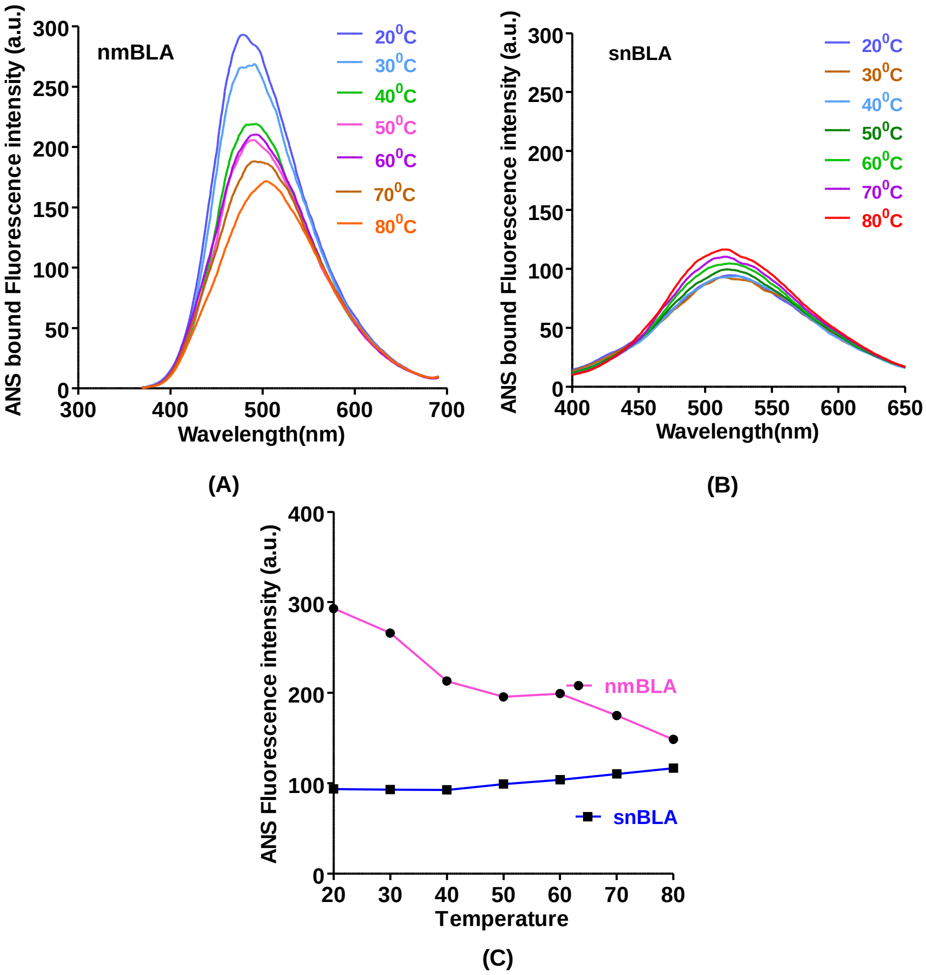

(A) (B)

(C)

Figure 4.12 Thermal stability analysis of (A) native bovine α-lactalbumin (nmBLA), (B) self-assembled nanostructured bovine α-lactalbumin (snBLA) by ANS fluorescence spectroscopy. (C) Comparison of the change in ANS fluorescence of nmBLA and snBLA. All data were expressed as the mean of three readouts generated from the instrument.

The reason for such a change on the surface of the protein may be due to the weakening of the hydrogen bonds present in the protein. Moreover, the increase in surface hydrophobicity is also a protective mechanism that protects the protein against thermal stress.

4.2.2.2 Stability of snLYZ and snBLA against varying pH

snLYZ and snBLAwereincubated in buffers at various pH ranging from pH 3-8 for nmLYZ and pH 5-10 for snBLA respectively. The CD spectra were recorded along with the Trp fluorescence and ANS fluorescence for snLYZ and snBLA.

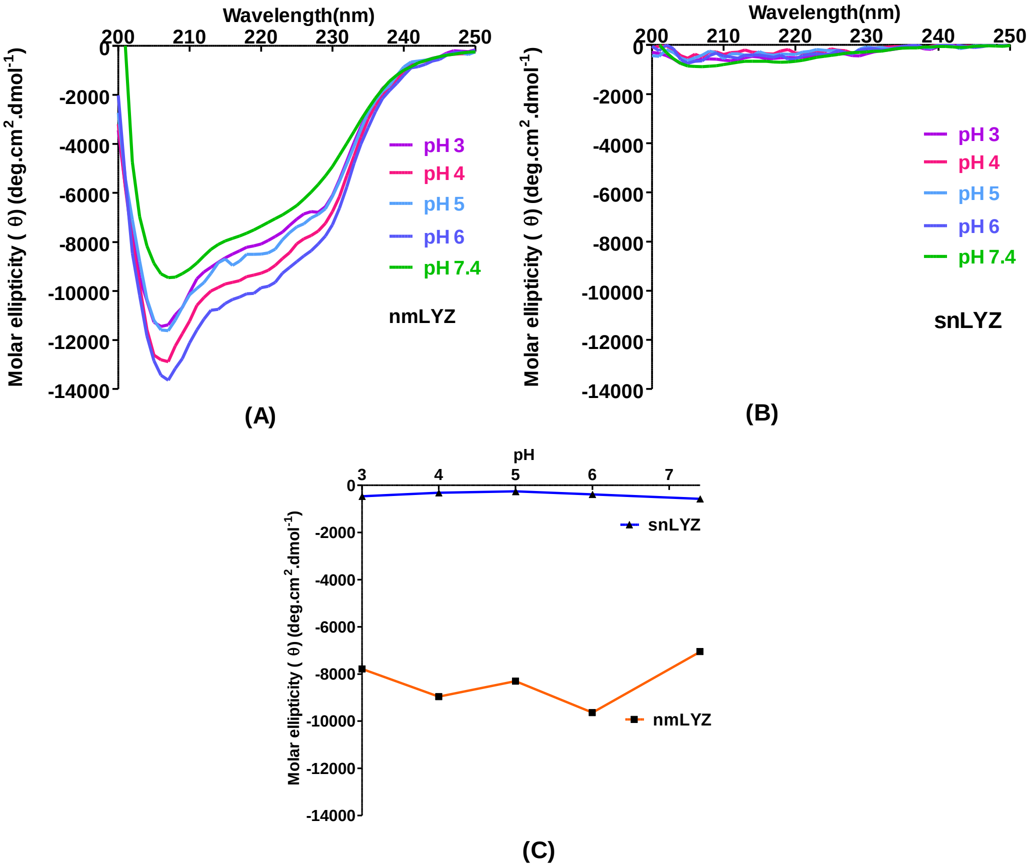

(A) (B)

(C)

Figure 4.13 pH stability analysis of (A) native lysozyme (nmLYZ), (B) self-assembled nanostructured lysozyme (snLYZ) by Circular dichroism (CD) spectroscopy. (C) Comparison of the change in the structure of nmBLA and snBLA by measuring the CD signal at 222 nm. All data were expressed as the mean of three readouts generated from the instrument.

The results show that the CD signal of snLYZ was fairly constant compared to nmLYZ where the CD signal was found to change rapidly (see Fig.4.13A, B and C).The CD results of snBLA show that the signal was relatively constant compared to nmBLA where the CD signal was found to change rapidly (see Fig.4.14A, B and C). The reason for such instability in nmLYZ and nmBLA may be due to the alteration in the electrostatic interactions between charged aminoacids present in the protein. Such interactions lead to the denaturation of nmLYZ and nmBLA.

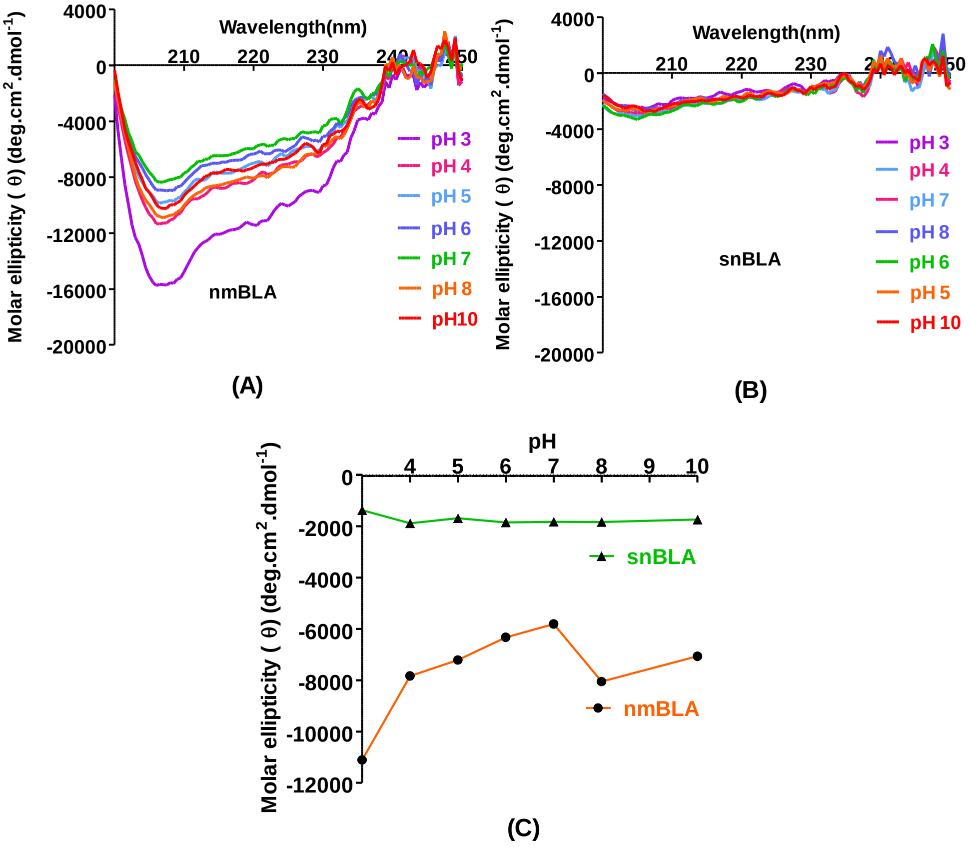

Figure 4.14 pH stability analysis of (A) native bovine α-lactalbumin (nmBLA), (B) self-assembled nanostructured bovine α-lactalbumin (snBLA) by CD spectroscopy.

(C) Comparison of the change in the structure of protein nanostructures by CD spectroscopy @ 222 nm. All data were expressed as the mean of three readouts generated from the instrument.

However, the CD signal remained constant for snLYZ and snBLA with varying pH because of no change in the ionization state of the charged amino acids, that cause spectral differences (Kwaambwa and Maikokera, 2008).

We also measured the Trp fluorescence of snLYZ and snBLA under varying pH conditions from pH 3 to 7.4.

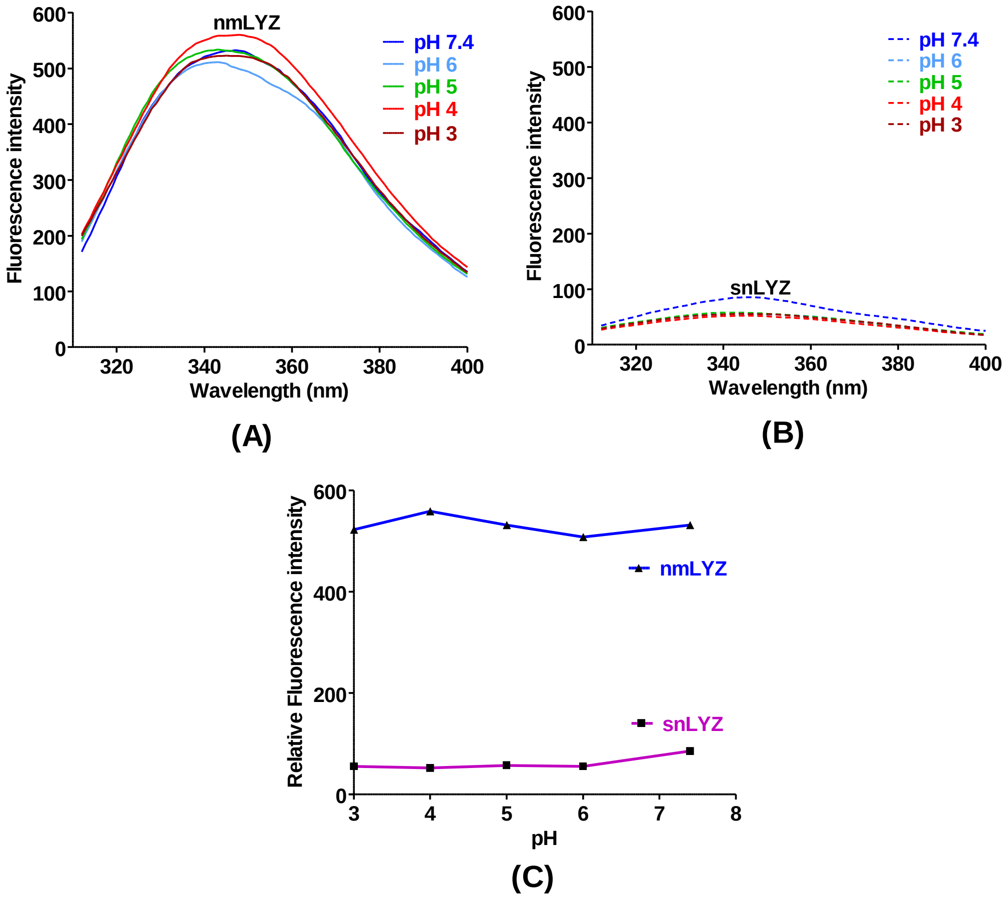

(A)

(B)

(C)

Figure 4.15 pH stability analysis of (A) native lysozyme (nmLYZ), (B) self-assembled nanostructured lysozyme (snLYZ) by Trp fluorescence spectroscopy. (C)

Comparison of the change in protein bound Trp fluorescence of nmBLA and snBLA. All data were expressed as the mean of three readouts generated from the instrument.

The Trp fluorescence of nmLYZ showed variation with an increase in pH whereas the Trp fluorescence from snLYZ remained fairly constant. The results indicated that snLYZ resisted the pH induced structural change whereas nmLYZ underwent frequent structural changes as evidenced from the variation in Trp fluorescence intensity (Fig.4.15A, B andC).

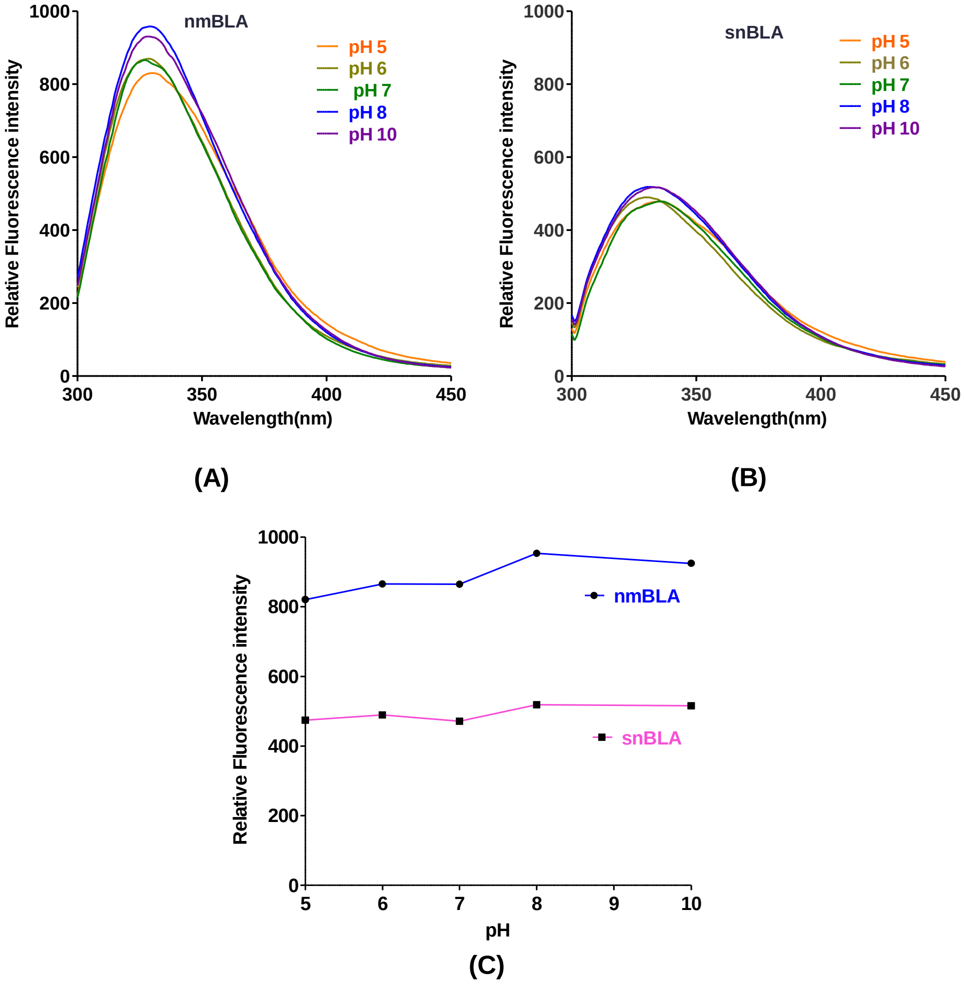

Figure 4.16 pH stability analysis of (A) native bovine α-lactalbumin (nmBLA), (B) self-assembled nanostructured bovine α-lactalbumin (snBLA) by Trp fluorescence

spectroscopy. (C) Comparison of the change in protein bound Trp fluorescence of nmBLA and snBLA. All data were expressed as the mean of three readouts generated from the instrument.

Similarly, snBLA was found to be more stable compared to the nmBLA when exposed to varying pH environments as evidenced from the Trp fluorescence intensity (Fig.4.16 A, B and C).The Trp fluorescence intensity of nmBLA showed the variable intensity with increase in pH,however, the Trp fluorescence intensity of snBLA had subtle variations but was observedrelatively constant (Fig. 4.16 C).

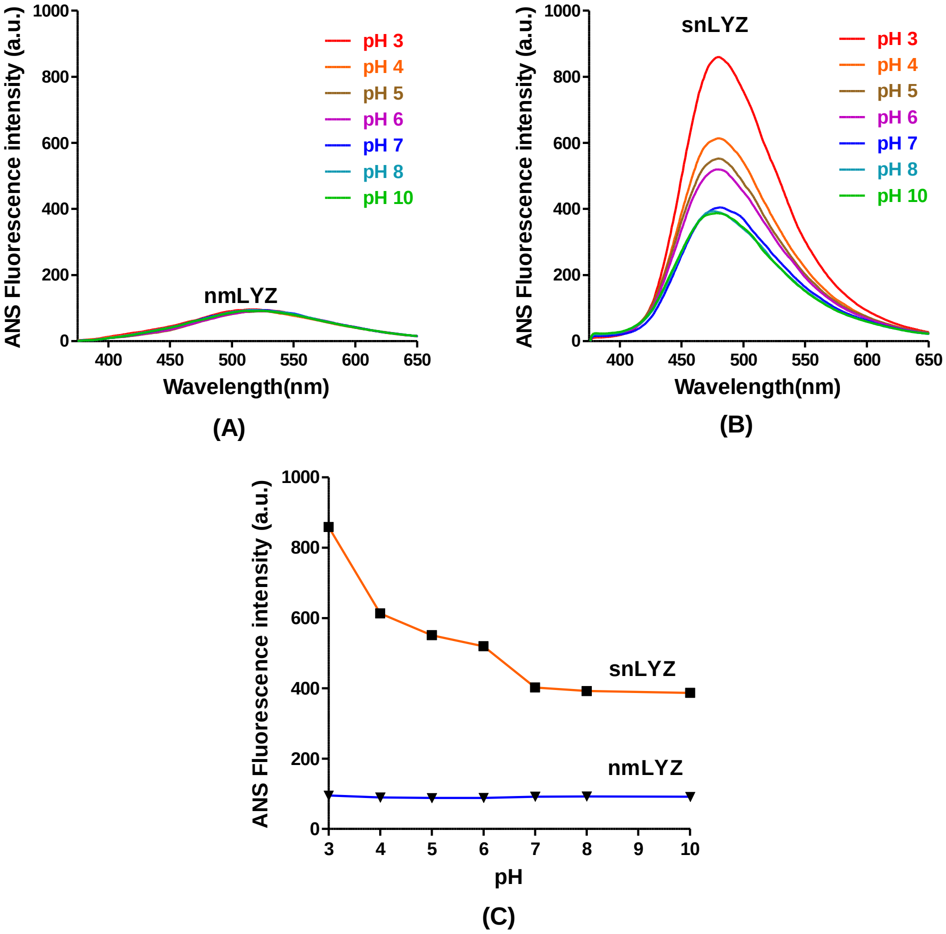

(A)

(B)

(C)

Figure 4.17 pH stability analysis of (A) native lysozyme (nmLYZ), (B) self-assembled nanostructured lysozyme (snLYZ) by ANS fluorescence spectroscopy. (C)

Comparison of the change in protein bound ANS fluorescence of nmLYZ and snLYZ. All data were expressed as the mean of three readouts generated from the instrument.

Such a change in nmBLA was due to the change in the ionization state of the charged amino acids, which cause spectral differences, (Kwaambwa and Maikokera, 2008). We also observed the protein bound ANS fluorescence of snLYZ and snBLA with an increase in the environment pH. So that we can obtain the information about the surface characteristics of the protein nanostructures.

The protein bound ANS fluorescence of snLYZ decreased rapidly with increase in pH whereas the ANS fluorescence of nmLYZ remained fairly constant.

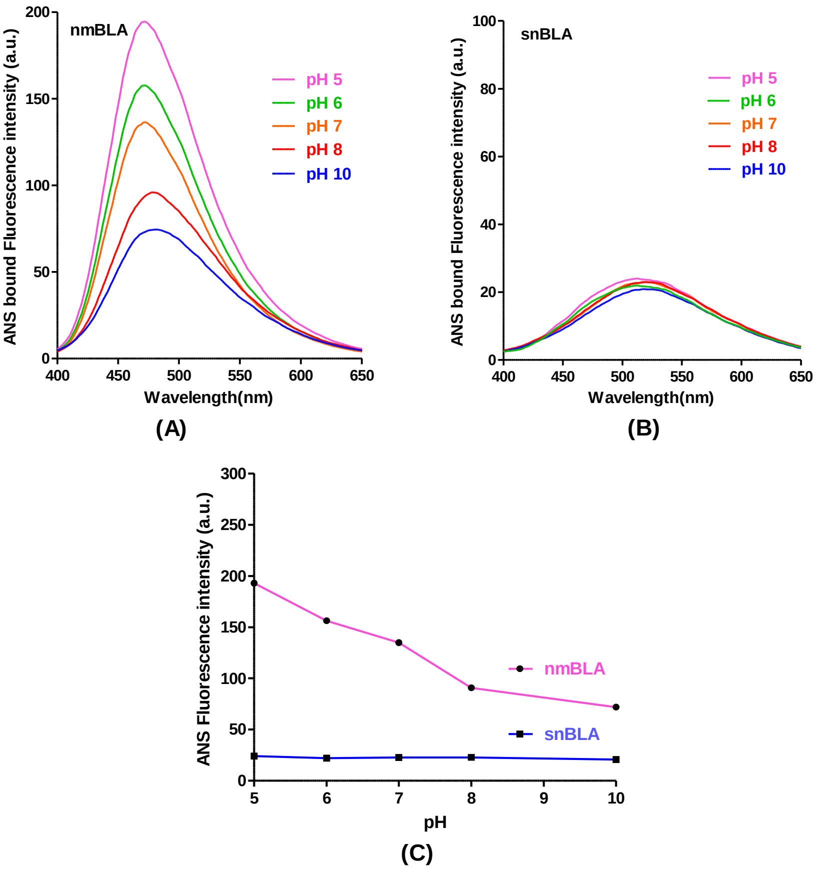

(A) (B)

(C)

Figure 4.18 pH stability analysis of (A) native bovine α-lactalbumin (nmBLA), (B) self-assembled nanostructured bovine α-lactalbumin (snBLA) by ANS fluorescence spectroscopy. (C) Comparison of the change in protein bound ANS fluorescence of nmBLA and snBLA. All data were expressed as the mean of three readouts generated from the instrument.

These results indicated that nmLYZ resisted the pH induced change in surface hydrophobicity whereas snLYZ underwent rapid decrease in surface hydrophobicity as evidenced from the drop in ANS fluorescence intensity with increase in pH (Fig.4.17 A, B and C).

The results obtained for snBLA were quite different from the results of snLYZ. The protein bound ANS fluorescence for snBLA and native BLA clearly show that the surface hydrophobicity of native BLA decreased rapidly with increase in pH (see Fig. 4.18 A,B and C) indicating instability,whereas snBLA showed no change in its snBLA bound ANS fluorescence intensity indicating incresed stability.

The results clearly indicate that the surface hydrophobic character of snLYZ decreases rapidly and for snBLA remains intact with increase in pH.

Proteinase K (PK) assay was performed to observe the stability of the protein nanostructures in the presence of PK. Proteinase K solution is stable over a broad range of pH (4.0-12.5) with an optimum pH of 8.0 (Burrell, 1993). Proteinase K is a nonspecific serine protease that preferentially digests proteins after hydrophobic amino acids (Brar et al., 2013). For globular proteins, the hydrophobic residues reside inside the core of the structure while the polar residues reside on the surface of the protein. Upon unfolding under stress, the proteins go into non-native state with substantial hydrophobic residues exposed to the solvents which make Proteinsae K easy to digest the protein. PK normally digests non-native proteins very fast but not the native one, however the high amount of PK can also attack native structure as well.

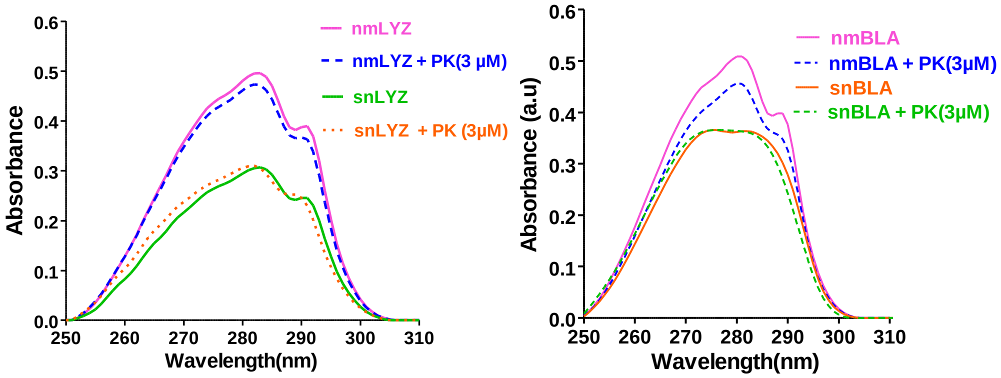

(A) (B)

Figure 4.19 UV-Vis spectroscopic measurement of nmBLA and snBLA before and after treatment with 3 μM Proteinase K (PK). The protein nanostructures resist Proteinase K related stress. All data were expressed as the mean of three readouts generated from the instrument.

In this case, nmLYZ and BLA were native but snLYZ and snBLA was partially denatured as well as partly unfolded but self-assembled by crosslinking with 0.1% GTD. After PK digestion, spectroscopic measurement of snLYZ and snBLA showed almost no change in the peak of spectra indicating increased stability against PK digestion compared to nmLYZ (Fig. 4.19A and B). Necessary baseline correction was done in order to compare the plots.

The above result also indicates a possibility that both in snLYZ and snBLA, the digestion sites were perhaps not well accessible to PK due to the self-assembly process of nmLYZ and nmBLA. Moreover, such stability both against pH and PK might be due to higher contents of β-sheet (37.7%) in snLYZ (see Table 1) than nmLYZ. All of the above results collectively led to the conclusion that snLYZ might be considered to be structurally, functionally and biologically stable, which satisfies one of essential requirements for a drug.

The activity assay of LYZ was performed to observe the lysozyme activity of snLYZ. The lytic activity of LYZ in snLYZ with varying pH, was presented in the Fig.4.20 which revealed a very minimal change in the lytic activity of snLYZ in a range of pH from 5.0 to 9.0. The loss in the LYZ activity of snLYZ may be due to the structural change that occurred ofLYZ molecule in snLYZ compared to nmLYZ.

However, some basal lysozyme activity was still present in snLYZ which did not change significantly with anthe increase in pH. In contrary the nmLYZ demonstrated maximum activity at pH 5, followed by a rapid decrease in its activity till pH 9.

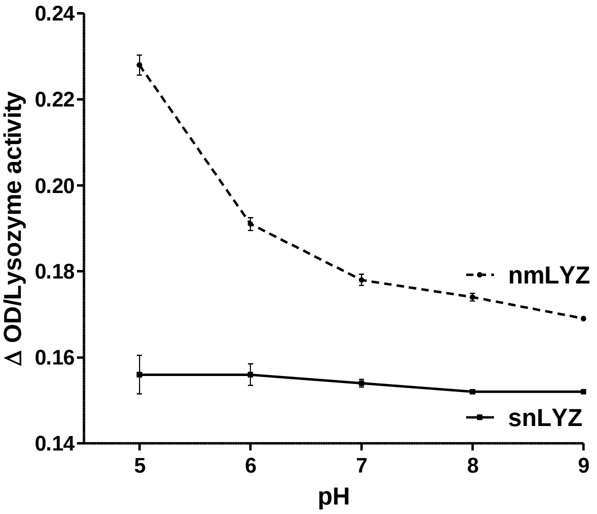

Figure 4.20 Plot of the biological activity of LYZ in nmLYZ and snLYZ at various pH (5-9) by *Micrococcus lysodekticus* assay. The protein nanostructure snLYZ retains its activity. All data are expressed as Mean ± S.E.M, n = 3.

However, nmLYZ showed a drastic drop in activity towards higher pH starting from pH 5.0, with a maximum drop at pH 9.0.

The thermal stability of a protein is also positively correlated with its higher surface hydrophobic character. Hence, measuring the surface hydrophobicity of snLYZ and snBLA can throw light on the stabilizing effect. ANS is an anionic, aliphatic fluorescence dye that spontaneously interacts with non-polar surface residues of a protein and exhibit strong fluorescence.

Hence, measuring the ANS bound fluorescence will provide information about the surface hydrophobicity of snLYZ and snBLA.

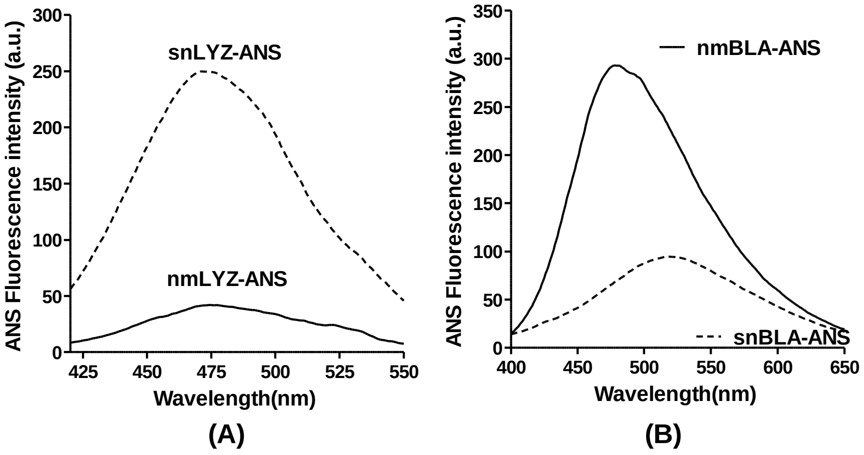

Figure 4.21 Surface hydrophobicity assessment of protein nanostructures using ANS Fluorescence spectra. (A) snLYZ and (B) snBLA. Surface hydrophobicity of snLYZ was found to increase whereas snBLA was found decreased. All data are expressedas a mean of three readouts generated from the instrument.

From our results (Fig.4.21 A), it was clear that our prepared snLYZ demonstrated higher hydrophobic surface (as reflected by a higher amount of snLYZ bound ANS fluorescence) than nmLYZ-bound fluorescence. Hence, we concluded that more non-polar residues were relocated on the surface of snLYZ that also support our previous data obtained from Trp fluorescence spectroscopy (Fig. 4.5 B).

However, snBLA demonstrated decreased surface hydrophobicity (see Fig.4.21 B) as evidenced from the decrease in the snBLA bound ANS fluorescence intensity.The results of the Trp (see Fig. 4.5B) and ANS bound fluorescence emission (see Fig.4.21B) clearly indicates that the self assembly related structural change resulted in the movement of the Trp as well as the hydrophobic residues towards the core of the protein structure.

4.2.2.3 Thioflavin T (ThT) assay

Thioflavin T assay was used for the detection of amyloids in various protein nanoassemblies. ThT upon binding with the amyloid fibrils causes a peak-shift from 450 to 490 nm. ThT (20µM) bound protein fluorescence was recorded to monitor the presence of amyloid fibrils in snLYZ and snBLA. However, since snLYZ and snBLAare protein nanoassemblies, there could be a chance that such cytotoxicity might be due to the toxicity associated with the amyloid formation in cells.

However, in CD results, we have observed that snLYZ contains 37.7% β-sheet that is considered to be quite high compared to nmLYZ. Juarez et al recently demonstrated in HSA (human serum albumin) protein that progressive increase of β-sheet content up to 26% was required for fibrillar amyloid formation (Juarez et al., 2009). Therefore, there was a necessity to monitor the formation of fibril structure like amyloid formation both in snLYZ and snBLA.

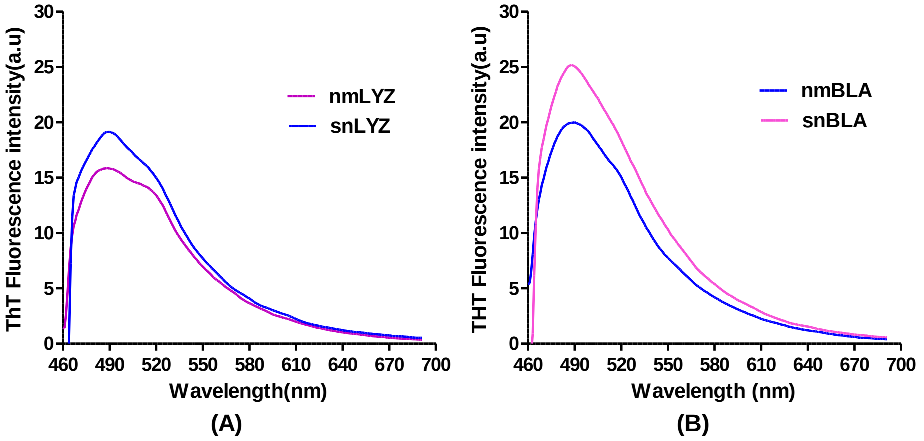

Figure 4.22 Thioflavin T assay for the assessment of the presence of amyloid in the protein nanostructures (A) snLYZ and (B) snBLA. The presence of amyloid produces a very intense peak at 490 nm. All data are expressed as a mean of three readouts generated from the instrument.

Here we observed that both in snLYZ and snBLA a very intense peak at 490 nm was not observed clearly indicating the absence of any amyloid content (see Fig.4.22).

Hence, we concluded that the cellular toxicity of snLYZ was produced by other mechanisms such as ROS generation (snLYZ) with no contribution from amyloid toxicity.

However, in our study, we observed that while the surface hydrophobicity of snLYZ was increased substantially, for snBLA, it was reduced significantly Increase in surface hydrophobicity of nano-assemblies can also facilitate the loading of hydrophobic drugs on the surface of protein nano-assemblies and functionalized nanoparticles having hydrophobic character.

Chapter 5

Protein Nanoassembly mediated cytotoxicity, mechanisms and targeting of cancer cells.

5.1 Materials and Methods

5.1.1 Materials

N-acetylcysteine (NAC), Glutaraldehyde (GTD) (25%), Tamoxifen citrate (TAM), N-hydroxysuccinimide (NHS), Bicinchoninic assay kit, Oleic acid and Whatman filter paper were purchased from Sigma-Aldrich, India. Lysozyme, Bovine α-lactalbumin, Folic acid (FA), MTT assay kit, Ethanol, DMEM, Fetal bovine serum (FBS), antibiotics, DAPI, acridine orange, Fluorescein diacetate, Nitrocellulose membrane from HiMedia India Pvt. Ltd. Milli-Q water was used in all the experiments. T-25 flasks, 96 well plates and all other plasticwares were purchased from Tarsons Pvt. Ltd.

Both primary and secondary antibodies of Hsp 90, Caspase 3 and β-actin were obtained from Abcam. 3T3 (murine fibroblast cell line), HaCaT (human keratinocyte cell line), A549 (human lung adenocarcinoma epithelial cell line) MDAMB-231 and MCF-7 (Breast cancer cell line) cells were procured from NCCS, Pune, India.

Caspase 3 inhibitor (218750) and Triton-X was purchased from Calbiochem, India. Human blood (B +ve) was freshly obtained from the donor before the experiments. All the glasswares used in the study were purchased from Borosil, India. All other reagents were of analytical grade.

5.1.2 Methods

5.1.2.1 Preparation and Characterization of BAMLET (Bovine α-lactalbumin made lethal to tumor cells)

BAMLET was prepared using a protocol described by Kamijima et al. (Kamijima et al., 2008). A mixture of protein and fatty acid (1:120 molar equivalents) was dissolved in 5 ml of PBS (pH 7.4) and incubated at 50 °C. After incubation for 10 min, the mixture was cooled down to room temperature and excess oleic acid was carefully removed by centrifugation. BAMLET. The characterization of BAMLET was carried out using CD spectroscopy as per the protocol mentioned in Chapter 4 "Materials and Methods Section".

5.1.2.2 Cell viability assay

The cytotoxicity study of snLYZ was evaluated in MCF-7 Breast cancer cells and snBLA was examined in four different cell lines; Breast cancer (MCF-7 and MDAMB-231), cervical cancer (HeLa) and lung carcinoma cells (A549) using MTT [3-(4, 5-Dimethylthiazol – 2 - yl) - 2, 5 - Diphenyltetrazolium Bromide] assay at various concentrations (16.66 - 333.33 µg/ml).

Normal cells such as HaCaT (Human keratinocyte cell line) and 3T3 (murine fibroblast cells) were used as a control and treated with similar concentrations of snBLA and snLYZ. All the cells were cultured in DMEM (Dulbecco's Minimum Essential Medium) containing 10% fetal bovine serum and 0.1 mg/ml penicillin and streptomycin.

Cells were cultured in T-25 flasks and were incubated at 37^0C in a humidified CO_2 incubator. All the cells were cultured till 80% confluence and the cells were trypsinized followed by seeding at a density of $1x10^4$ cells/ml. The cells were seeded in a 96 well plate containing 300 µl of DMEM in each well, and the cells were allowed to proliferate for 24 h. snBLA and snLYZwere administered to the cells, and the end point effect was monitored by MTT assay at the end of next 24 h. MTT (10 µl of 5 mg/ml stock) was added 6 h before the end point. In the end, media was removed, and 100 µl of DMSO was added to dissolve the formazan formed and the absorbance was measured at 595 nm. The absorbance values were recorded, and percentage cell viability was calculated from the absorbance values and the result was plotted.

5.1.2.3 Folate conjugation for targeting cancer cells

The presence of folic acid receptor (FR) in cancer cells can be exploited for targeting snLYZ/snBLA against cancer cells (Gaspar et al., 2015; Lu et al., 2014). MCF-7 and MDAMB-231 are cell lines that express Folic acid (FA) receptors on its surface. We prepared activated folic acid (FAa) preparing N-hydroxysuccinimide ester of folate i.e. NHS folate was already reported (Leamon and Low, 1991).

Hence, we conjugated snLYZ and snBLA with FAa using 0.1% glutaraldehyde as a cross-linker leading to the formation of snLYZ/snBLA-folic acid conjugate (snLYZ/snBLA-FAa). For the preparation of snLYZ/snBLA-FA conjugate, the protocol reported by Li et al. was followed (Li et al., 2011).

To evaluate the uptake effect of snLYZ/snBLA in cells that do not express FR, we used A549 cells as control. Various concentrations (13.33-333.33 µg/ml) of snBLA-FAa conjugate were administered to both MDAMB-231 cells and A549 cells, and 0-200µg/ml of snLYZ-FAa was administered to MCF-7 cells and A549 cells. MTT assay was performed as per the protocol mentioned in section 5.1.1.

5.1.2.4 Cellular Uptake of snBLA/snLYZ in MCF-7 cells

We performed the fluorescence imaging of MCF-7 cancer cells using fluorescence and confocal laser scanning microscope. Fluorescent dyes such as DAPI was used to stain the nucleus, and acridine orange was used to observe the cellular uptake of snBLA. snLYZ/snBLA - acridine orange conjugate were prepared by crosslinking the protein nanostructures with acridine orange using 0.1% glutaraldehyde. The cells were exposed to snLYZ/snBLA - acridine orange conjugate for 12 h. At the end of 12 h, we observed the presence of snLYZ/snBLA particles exhibiting orange fluorescence inside the cytoplasm of MCF-7 Breast cancer cells.

5.1.2.5 Reactive oxygen species (ROS) mediated cell death

To ascertain ROS generation for snBLA-mediated cancer cell death, we applied 333.33 µg/ml of snBLA in both MCF-7 and MDAMB-231 cells and kept a corresponding group pre-treated with 2 mM N-acetylcysteine (NAC), a ROS inhibitor. Similarly, for ROS generation from snLYZ we treated MCF-7 cells with 60-200µg/ml of the same in the presence and absence of NAC. MTT assay was performed as per the protocol mentioned in section 5.1.1

5.1.2.6 Role of Caspase 3 mediated apoptotic cell death

To find the role of apoptosis in cancer cell death mediated by snBLA, cell viability assay of MDAMB-231 cells was performed in the presence of 100 µg/ml gallic acid (GA) and Caspase-3 inhibitor. GA induces apoptosis in various cells mediated by caspase-3. We also evaluated the Caspase-3 expression to support our cell viability results. Further, we also performed the same experiment with BAMLET for comparison. We treated MDAMB-231 cancer cells with native BLA, snBLA and BAMLET for 12 h.

After treatment, cells were collected and lysed in lysis buffer in the presence of protease inhibitor cocktail. The supernatant was obtained after centrifugation at 12,500 g for 10 min at 4°C. The concentration of protein in the supernatants was measured by the bicinchoninic acid (BCA) assay. Then equal amounts of protein (60 μg) were separated by 10% sodium dodecyl sulfate polyacrylamide gel electrophoresis (SDS-PAGE) and transferred to the nitrocellulose membrane (Millipore, Billerica, MA). The blots were incubated with respective primary antibodies overnight at 4°C followed by incubation with the secondary antibody for 4 h at 37°C. Chemiluminescent detection was performed by the chemiluminescent documentation system (MF-Chemibis 2.0; DNR Bioimaging, Israel).

5.1.2.7 Hemocompatibility assay

To perform the haemocompatibility assay, 5 ml of B^{+ve} human blood was collected by an expert Medical practitioner in heparinized centrifuge tubes. The contents were gently resuspended and centrifuged at 1000 g for 10 min. The supernatant was removed and the erythrocyte collected at the bottom was washed three times by gentle suspension with 10 times the volume of pyrogen-free saline (0.9% NaCl).

The erythrocyte pellet was gently resuspended in normal saline and diluted to 0.8% (v/v). The solution was placed in a sterile centrifuge tube, and various test samples were administered to evaluate their hemolytic potential. Triton-X (1%) was used as a positive control and erythrocyte suspension treated with none was used as a negative control. The absorbance of the hemoglobin released was measured at 405 nm. The percentage hemolysiswas calculated at 1h, and the graph was plotted between percent hemolysis and time (h).

5.2 Results and Discussion

5.2.1 Preparation and Characterization of BAMLET

BAMLET was prepared as per the protocol mentioned in the “Materials and Methods section”. BAMLET is a formulation comprising of bovine α-lactalbumin and oleic acid. The synthesized BAMLET was characterized by CD spectroscopy and the spectra was similar to earlier reported results by Kamijima et al. (Kamijima et al., 2008) (see supplementary figure S8).

5.2.2 Cytotoxicity study of snLYZ and snBLA

The cytotoxicity assay of snLYZ and snBLA was performed in human breast cancer cells MCF-7 and MDAMB-231 cells. Results showed that the administration of nmLYZ and nmBLA caused very little effect on cancer cell killing compared to control (administered with none) till a dose of 200 and 333.33µg/ml respectively (Fig. 5.1A and B). However, snLYZ and snBLA demonstrated a dose-dependent cell killing with more than 90 % and 80.86 % cell death at 200 µg/ml and 333.33 µg/ml respectively after 24 h administration in MCF-7 cells (Fig. 5.1A and B).

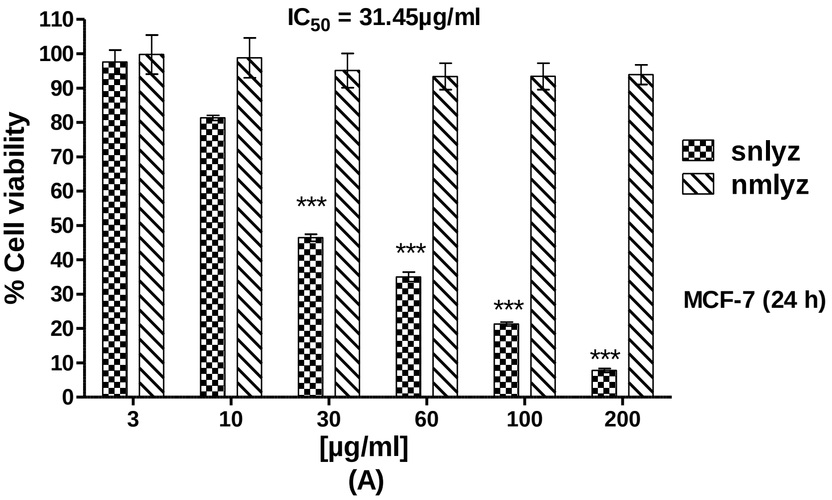

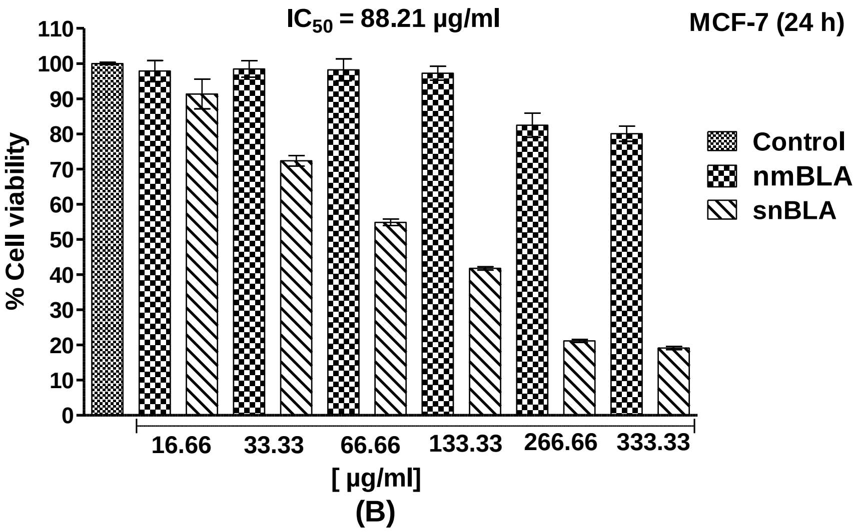

Figure 5.1 Dose-dependent cytotoxic effect of (A) snLYZ and (B) snBLA on the MCF-7 cell viability at the end of 24 h. Statistically significant vs control group, *** $p < 0.001$ by One way ANOVA and post Tukey test. All data are expressed as Mean ± S.E.M, n = 3.

The IC_{50} values for snLYZ and snBLA were calculated to be 31.45 and 88.21µg/ml respectively at 24 h post administration. Similarly, snLYZ and snBLA demonstrated a dose-dependent cell killing with more than 95.34 % and 95.04 % cell death at 100 µg/ml and 333.33 µg/ml respectively at 48 h post administration (Fig.5.2 A and B).

snLYZ demonstrated strong anti-proliferative activity among both the protein nanoassembly with the maximum cytotoxicity observed at 100 µg/ml compared to 333.33µg/ml for snBLA. The IC_{50} values for snLYZ and snBLA were 12.90 and 51.65 µg/ml respectively at 48 h post administration. Administration of various lower doses of snBLA ranging from 16.66 to 133.33 µg/ml did not exhibit any toxicity to MCF-7 cells (see Fig.5.2B).

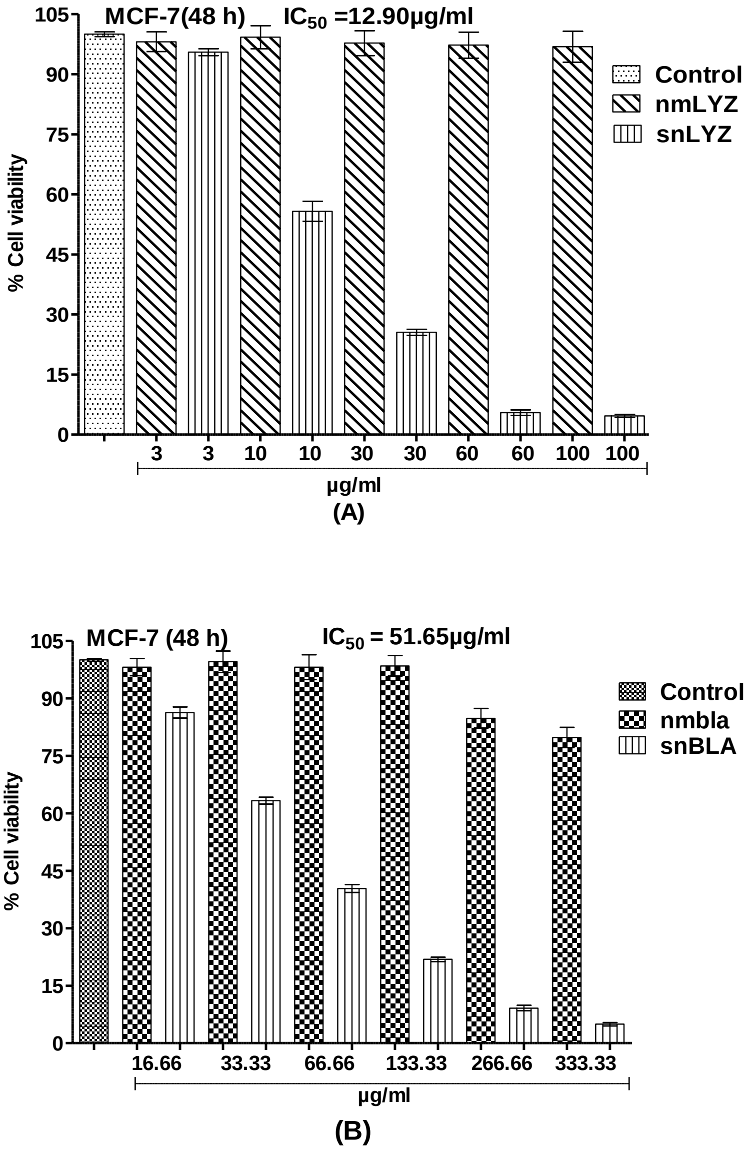

Figure 5.2 Dose-dependent cytotoxic effect of (A) snLYZ and (B) snBLA on the MCF-7 cell viability at the end of 48 h. Statistically significant vs control group, *** $p < 0.001$ by One way ANOVA and post Tukey test. All data are expressed as Mean ± S.E.M, n = 3.

We wanted to validate our results of snLYZ and snBLA in other breast cancer cell line such as MDAMB-231. Hence, we performed the cytotoxicity study of snLYZ and snBLA in MDAMB-231 cells.

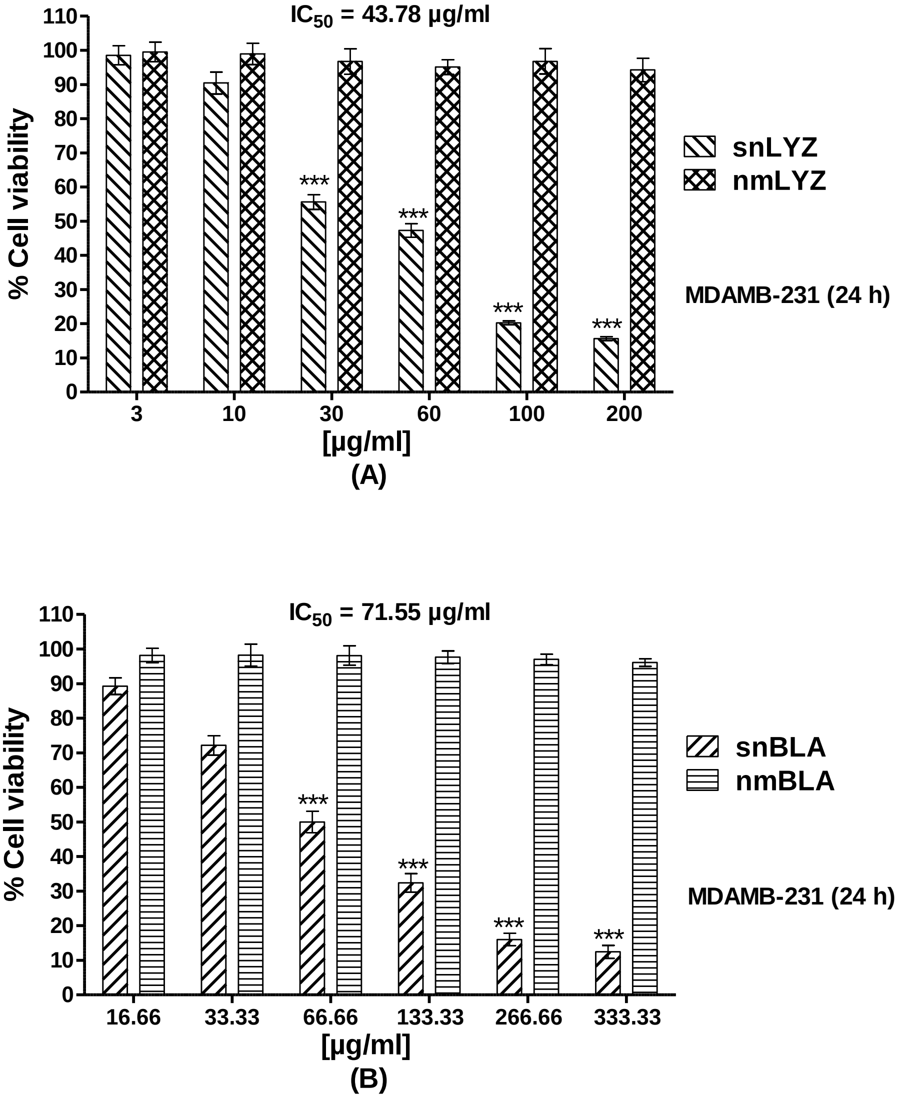

Figure 5.3 Dose-dependent cytotoxic effect of (A) snLYZ and (B) snBLA on the MDAMB-231 cell viability at the end of 24 h. Statistically significant vs control group, *** $p < 0.001$ by One way ANOVA and post Tukey test. All data are expressed as Mean ± S.E.M, n = 3.

From the Fig.5.3A and B we observed that snLYZ and snBLA demonstrated a dose-dependent cell killing with more than 84.35 % and 87.56 % cell death at 200 µg/ml and 333.33 µg/ml respectively at 24 h post administration. snLYZ demonstrated very similar levels of anti-proliferative activity at a much lower dose of 200µg/ml maximum compared 333.33µg/ml for snBLA. The IC_{50} values for snLYZ and snBLA were 43.78 and 71.55 µg/ml respectively at 24 h post administration.

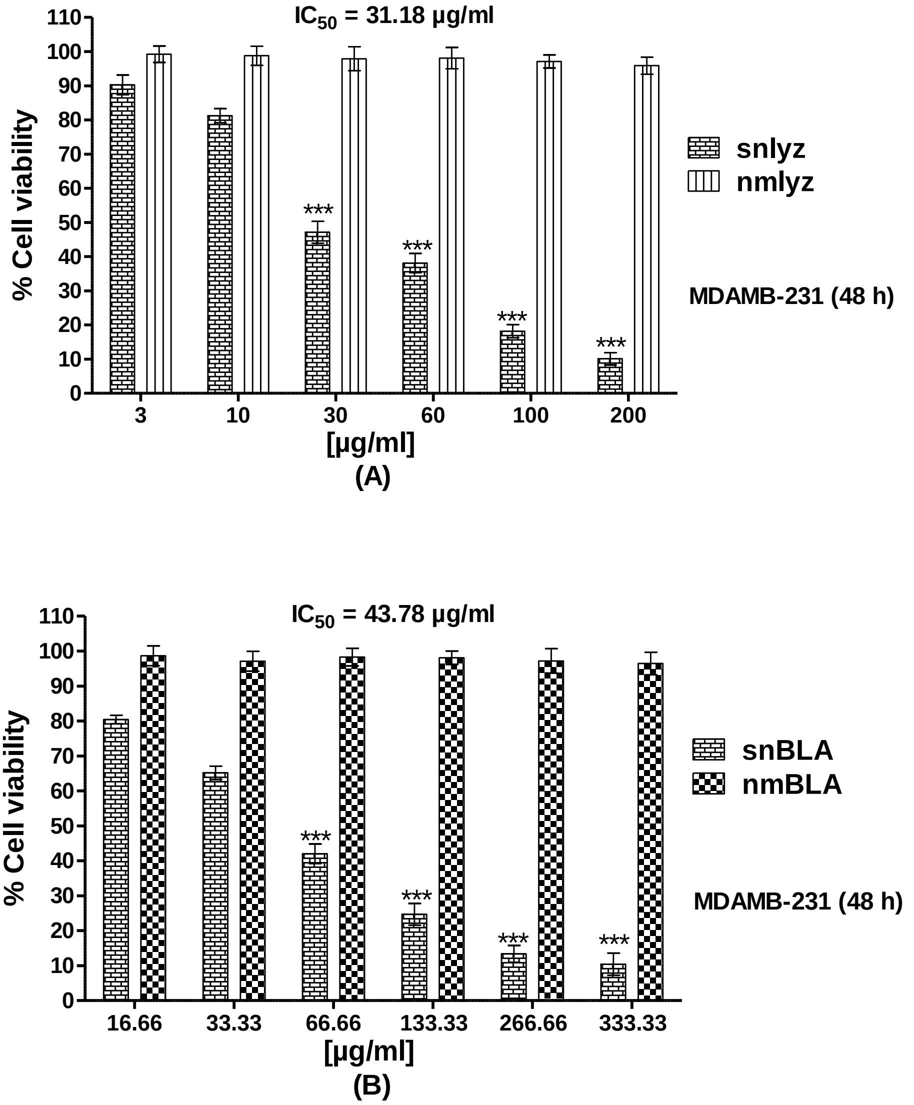

Figure 5.4 Dose-dependent cytotoxic effect of (A) snLYZ and (B) snBLA on the MDAMB-231 cell viability at the end of 48 h. Statistically significant vs control group, *** $p < 0.001$ by One way ANOVA and post Tukey test. All data are expressed as Mean ± S.E.M, n = 3.

We also observed the cytotoxic effect of snLYZ and snBLA at 48 h post administration in MDAMB-231 cells. The results showed that both the protein nanoassemblies demonstrated exactly similar levels of cytotoxicity at 48 h post administration in MDAMB-231 cells (Fig.5.4A and B).

The IC_{50} values for snLYZ and snBLA were 31.18 and 43.78 µg/ml respectively at 48 h post administration. Interestingly, the IC_{50} values of both snLYZ and snBLA were very less in MCF-7 cells compared to MDAMB-231 cells, which clearly indicates that snLYZ and snBLA are more potent in MCF-7 cells compared to MDAMB-231 cells, although both snLYZ and snBLA are toxic against MCF-7 and MDAMB-231 cells. Tamoxifen (TAM), a chemotherapeutic agent is commonly used in breast cancer, was also used here as a positive control for comparison.

From the above cell viability assays of snLYZ and snBLA in MCF-7 cells, we made a comparison between their IC_{50} values (see Fig.5.5). snLYZ demonstrated lower IC_{50} values compared to snBLA, indicating higher cytotoxic potential than snBLA at 24 and 48h.

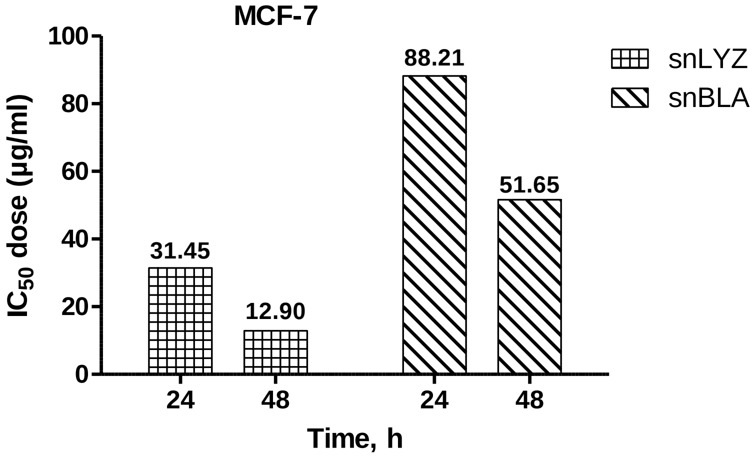

Figure 5.5 Comparison of the IC_{50} values of snLYZ and snBLA on MCF-7 cells at the end of 24 and 48 h.

To test whether the cytotoxicity of the protein nanoassembly was specific to cancer cells, we performed cytotoxicity study against mouse fibroblast cells 3T3 (see Fig. 5.6A and B) and human keratinocyte cells HaCaT cells (see Fig.5.7A and B).

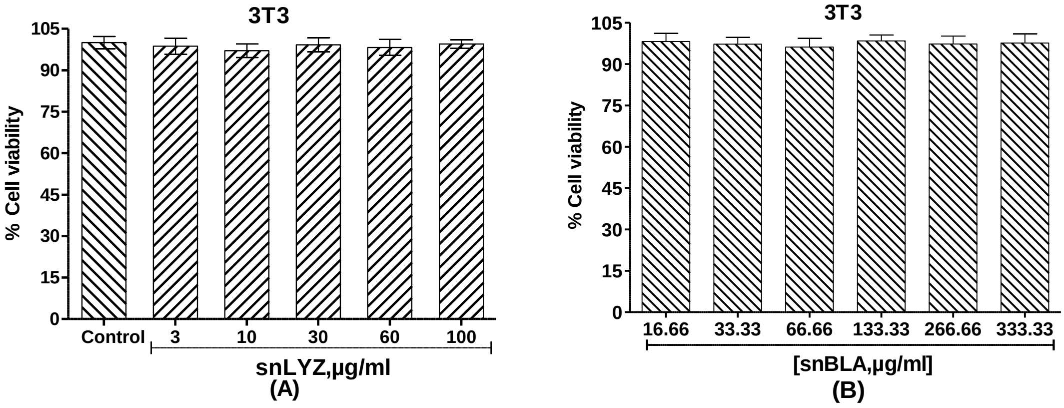

Figure 5.6 Cell viability assay of protein nanoassembly in 3T3 (mouse fibroblast cells) cells (A) snLYZ and (B) snBLA. snLYZ and snBLA did not have any cytotoxic effect in normal cells. All data are expressed as Mean ± S.E.M, n = 3.

All the doses of snLYZ and snBLA administered to 3T3 and HaCaT cells showed no signs of toxicity. This clearly indicates that snLYZ and snBLA have high cytocompatibility with normal cells.

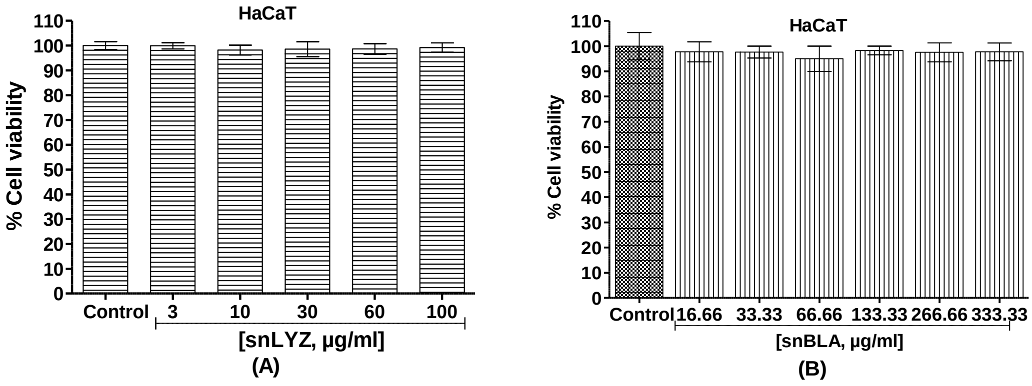

Figure 5.7 Cell viability assay of protein nanoassembly in HaCaT (human keratinocyte) cells (A) snLYZ and (B) snBLA. snLYZ and snBLA did not have any cytotoxic effect in normal cells. All data are expressed as Mean ± S.E.M, n = 3.

Indeed, due to their proteinaceous composition both snLYZ and snBLA were least expected to induce any toxic effects in normal cells such as HaCaT and 3T3.

The cytotoxicity of TAM was evaluated in MCF-7 cells at different concentration (Fig.5.8). The IC_{50} of TAM was found to be 6.66 µg/ml.

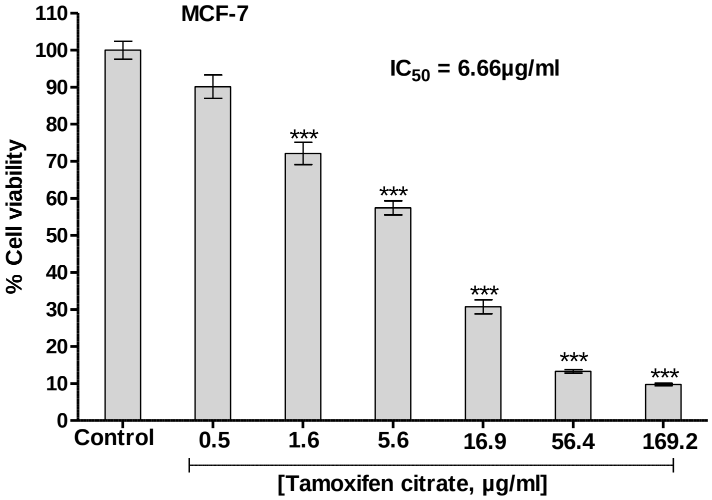

Figure 5.8 Dose-dependent cytotoxic effect of Tamoxifen citrate on the MCF-7 cell viability at the end of 24 h. Statistically significant vs control group, *** $p < 0.001$ by One way ANOVA and post Tukey test. All data are expressed as Mean ± S.E.M, n = 3.

A comparison of the IC_{50} values of snLYZ, snBLA and TAM were presented in Table 5.1.

Table 5.1 Comparison of IC_{50} values of snLYZ, snBLA and TAM in MCF-7 cells.

Agent	**IC_{50} (µg/ml) at 24 h**	**IC_{50} (µg/ml) at 48 h**
TAM	6.66	
snLYZ	31.45	12.90
snBLA	88.21	51.65

IC_{50} values indicates the dose at which 50% of the cells are killed and is a measure of potency of the substance administered compared to other known drugs. Hence, using IC_{50} values we can easily make a comparison of potency between the protein nanoassembly and TAM. We clearly observed that among the two protein nanoassembly snLYZ showed a better IC_{50} value compared to snBLA at both 24 and 48 h. This indicates that snLYZ at much lower doses inflicted the same amount of cytotoxicity compared to snBLA. Hence, among the two protein nanoassembly snLYZ was proved to be more potent compared to snBLA. In order to observe whether the cytotoxicity caused by snLYZ and snBLA is specific to their specific structure, we had prepared a self assembly of bovine serum albumin (snBSA) (see the supplementary figure S12) using the same protocol and observed its effect on the cell viability of 3T3 and MCF-7 cells (see the supplementary figure S13). We observed from supplementary figure S13 that no toxicity was demonstrated by snBSA. The IC_{50} value of TAM was found to be the best among all with an IC_{50} value of 6.66 µg/ml at 24 h post administration. Such low IC_{50} values indicate that Tamoxifen is more potent than both snLYZ and snBLA. However, the side effect of TAM has been a great concern and we would study the same in further section.

5.2.3 Folate conjugation for targeting cancer cells

In order to increase the specificity of snLYZ for cancer cells expressing folate receptors (FR), we prepared conjugate of snLYZ with activated folic acid (NHS-FAa) and observed its cytotoxic effect in MCF-7cells.

We observed an dose-dependent increase in cytotoxicity of snLYZ after conjugation with activated folic acid. The snLYZ-FAa conjugate showed dose-dependent increase in cytotoxicity compared to snLYZ alone at 24 (see Fig. 5.9) and 48 h post administration (see Fig.5.10). snLYZ-FAa inflicted 93.67 % cell death in MCF-7 cells compared to 78.28 % cell death induced by snLYZ alone at a dose of 100 µg/ml.

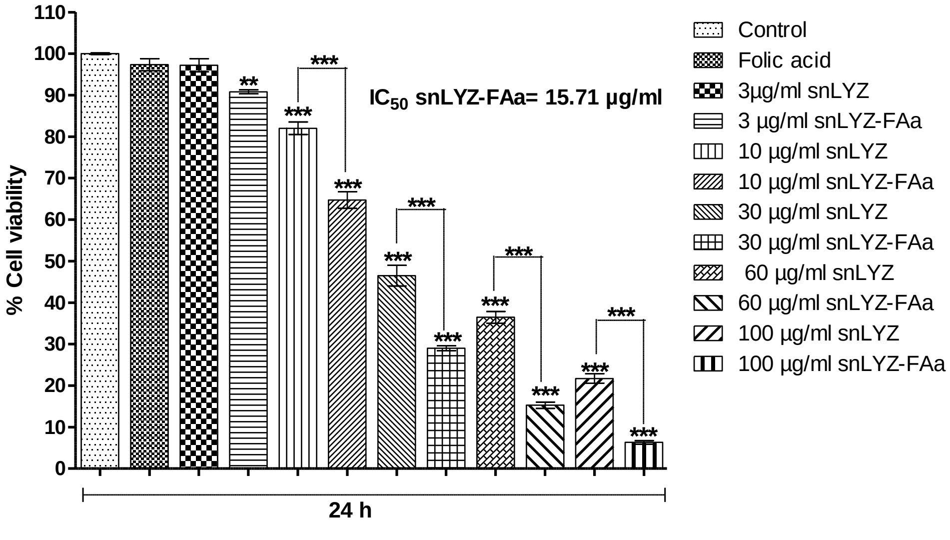

Figure 5.9 Cell viability assay of snLYZ-FAa in MCF-7 cells at 24 h post administration. Folic acid conjugation enhances cytotoxicity in MCF-7 cells.

Statistically significant vs control group, *** $p < 0.001$ by One way ANOVA and post Tukey test. All data are expressed as Mean ± S.E.M, n = 3.

The result clearly indicates that conjugationof snLYZ with FAa improved the cytotoxicity of snLYZ significantly.

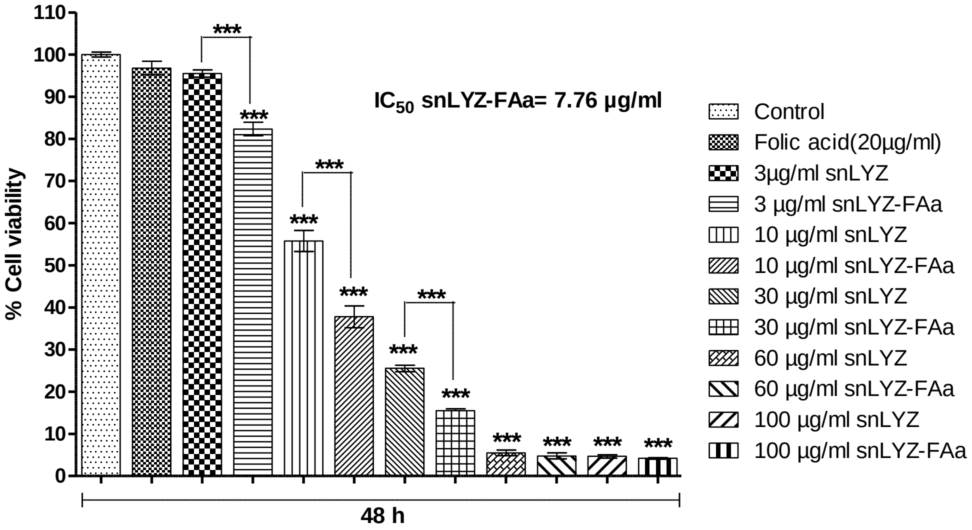

Figure 5.10 Cell viability assay of snLYZ-FAa in MCF-7 cells at 48 h post administration. Folic acid conjugation enhances cytotoxicity in MCF-7 cells. Statistically significant vs control group, *** $p < 0.001$ by One way ANOVA and post Tukey test. All data are expressed as Mean ± S.E.M, n = 3.

The result was also confirmed from the IC_{50} values obtained for snLYZ-FAa at 24 and 48 h respectively. The IC_{50} value of 15.71 and 7.76 µg/ml for snLYZ-FAa at 24 and 48 h was found to be less than that of snLYZ (see Table 5.1) at similar time points.

This clearly indicates that snLYZ-FAa is more potent than snLYZ alone indicating that the association of folic acid increased the cytotoxicity probably through the folate receptors (FR) present on the surface of MCF-7 cancer cells. The increased uptake resulted in the increase in cytotoxicity of snLYZ-FA against MCF-7 cells. We anticipated that the increase in cytotoxicity might be due the presence of FR receptors present on the MCF-7 cell surface. The receptors facilitated the internalization of snLYZ-FAa by receptor-mediated endocytosis.

In order to observe the effect of snLYZ-FAa on cells that do not express folic acid receptors, we performed cell viability studies in A549 cells. When we administered snLYZ-FAa in A549 cells and observed its effect at the end of 24 h we found reduced cytotoxicity of snLYZ-FAa in A549 cells (see Fig.5.11) compared to MCF-7 cells (see Figure 5.2.A). The result clearly indicates that folic acid expressing cancer cells are more susceptible to the cytotoxicity of snLYZ-FAa, compared to cancer cells that do not express folate receptors.

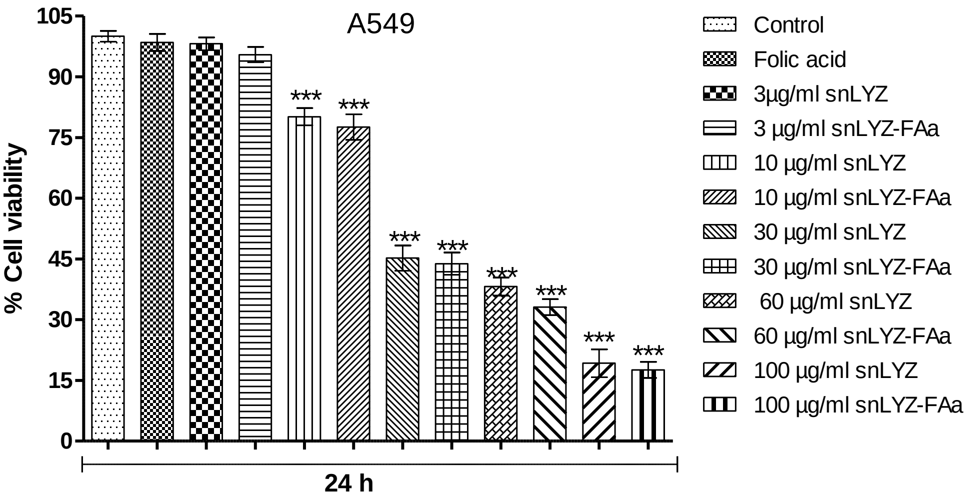

Figure 5.11 Cell viability assay of snLYZ and snLYZ-FAa in A549 cells measured by MTT assay. Folic acid conjugation did not affect the cytotoxicity in A549 cells. Statistically significant vs control group, *** $p < 0.001$ by One way ANOVA and post Tukey test. All data are expressed as Mean ± S.E.M, n =3.

In a similar way we also conjugated snBLA with activated folic acid and observed its effect on FR + ve MDAMB-231 cells.

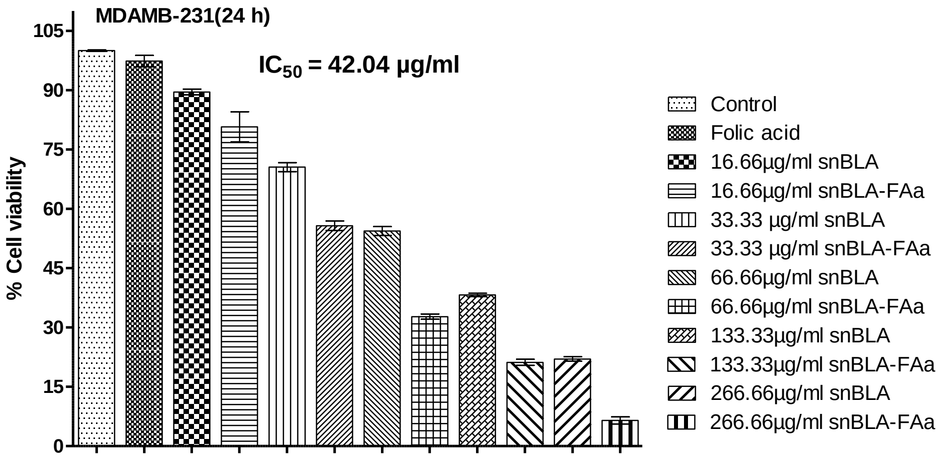

Figure 5.12 Cell viability assay of snBLA-FAa in MDAMB-231 cells at 24 h post administration. Folic acid conjugation enhances cytotoxicity in MDAMB-231cells. Statistically significant vs control group, *** $p < 0.001$ by One way ANOVA and post Tukey test. All data are expressed as Mean ± S.E.M, n = 3.

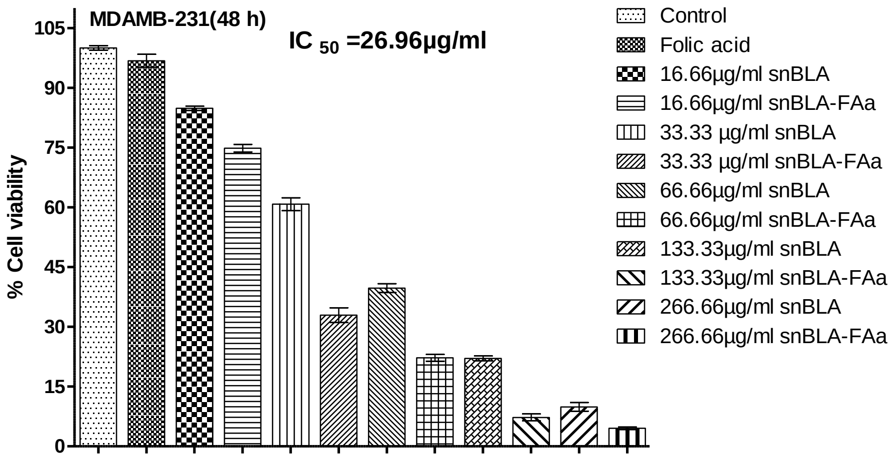

Figure 5.13 Cell viability assay of snBLA-FAa in MDAMB-231 cells at 48 h post administration. Statistically significant vs control group, *** $p < 0.001$ by One way ANOVA and post Tukey test. All data are expressed as Mean ± S.E.M, n = 3.

We observed an increase in cytotoxicity of snBLA upon conjugation with folic acid. The snBLA-FAa conjugate showed increased cytotoxicity at 24 (see Fig.5.12) and 48h (see Fig.5.13) post administration in MDAMB-231 cells compared to snBLA alone (Fig. 5.2 B).

This clearly indicated that the conjugation of folic acid with snBLA improved the cytotoxicity of snBLA significantly. The result was also confirmed from the fact that the IC_{50} values of snBLA-FAa were lower than snBLA alone at 24 and 48 h, respectively. The IC_{50} value of snBLA-FAa at 24 and 48 h were 42.04 and 26.96 µg/ml respectively, which was lower than that of snBLA at similar time points (see Table 5.1). In order to increase the specificity of snBLA for cancer cells expressing folate receptors (FR), we prepared conjugate of snBLA and activated folic acid (FAa) and observed its ytotoxic effect in MDAMB-231 (FR + ve) and A549 (FR - ve) cells.

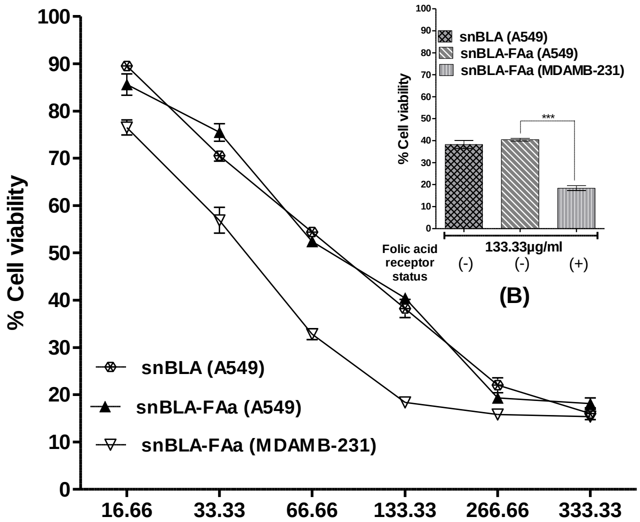

Figure 5.14 Cell viability assay of FAa-conjugated snBLA (A) MDAMB-231 cells and A549 cells. (B) Inset shows the percentage of cell viability of A549 and MDAMB-231 cells treated with snBLA and snBLA-FAa at a dose of 133.33 µg/ml.

Folic acid conjugation enhances cytotoxicity in MDAMB-231cells. Statistically significant vs. control group, ***p< 0.001 by One way ANOVA and post Tukey test. All data are expressed as Mean ± S.E.M, n = 3.

We observed an increase in anti-proliferative activity by snBLA-FAa in MDAMB-231 cells (see Fig.5.10 and 5.11) than snBLA alone (Fig.5.2B), however, such increase in conjugate cytotoxicity was not observed in A549 cells (see Fig.5.14), inset shows the effect of snBLA, snBLA-FAa at a dose of 133.33 µg/ml in A549 and MDAMB-231 cells. This fact is due to the expression of folate receptors on the membrane surface of MDA-MB-231 cells that facilitated the entry of snBLA-FAa inside cells.

Since, A549 cells do not express FR, hence, the entry of snBLA inside the cytoplasm follows the normal route of entry into cells, i.e., Caveoli mediated, phagocytosis, etc.

Therefore, it was established that FA conjugation increased the efficiency of cellular uptake in FR +ve cancer cells. Thus such strategies can be used for selective targeting of cancer cells.

The comparison of the IC50 values clearly shows that snBLA-FAa is more potent than snBLA alone. The result also indicates that the conjugation of folic acid resulted in an increase in the cellular uptake of snBLA resulting in increased cytotoxicity.

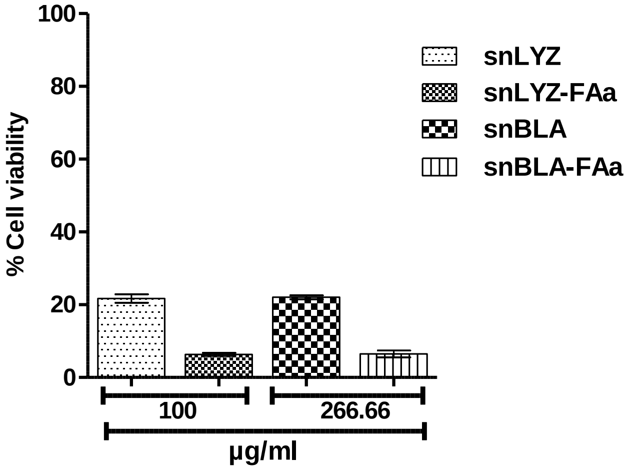

Figure 5.15 Comparison of cytotoxic effect of snLYZ, snLYZ-FAa in MCF-7 cells and snBLA, snBLA-FAa in MDAMB-231 cells by MTT cell viability assay at 24 h post administration. All data are expressed as Mean ± S.E.M, n = 3.

In order to support our conclusions we made a comparison of the doses of the protein nanostructures snLYZ and snBLA along with their folic acid conjugates producing maximum toxicity in MCF-7 and MDAMB-231 cells. We observed an increase in toxicity of snLYZ/snBLA-FAa compared to snLYZ/snBLA alone (Fig. 5.15).

5.2.4 Cellular uptake of snLYZ/snBLA in MCF-7 cells

We also anticipated that cellular uptake could be a major reason behind cell death.

To ascertain the cellular uptake of snLYZ, we performed fluorescence imaging of cancer cells using fluorescent dyes such as DAPI, Fluorescein diacetate, and acridine orange. Cells stained with DAPI clearly showed blue fluorescence for the nucleus in live cells and Fluorescein diacetate exhibited green fluorescence for the cytoskeletal component of cells. Fig 5.16 shows the uptake of snLYZ in MCF-7 cells.

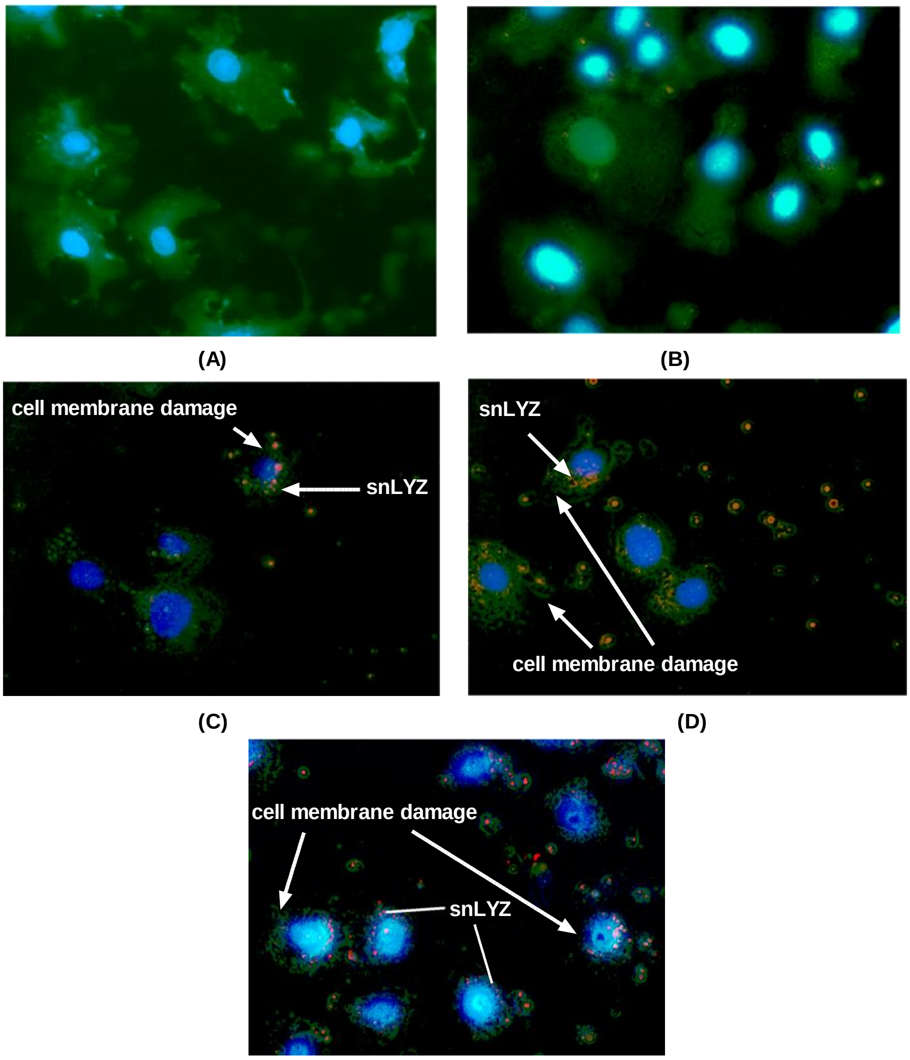

(A) (B)

(C) (D)

(E)

Figure 5.16 Fluorescent images of MCF-7 cancer cells showing internalization of acridine orange tagged snLYZ. (A) Control, administered with none; (B) Cell images after administration of acridine orange tagged snLYZ uptake for 1 h; (C) Acridine orange tagged snLYZ uptake at 3 h; (D) Acridine orange tagged snLYZ uptake at 6 h; (E) Acridine Orange tagged snLYZ uptake at 12 h.

Cancer cells at 0th h were presented in Fig.5.16 (A), which showed the intact nucleus (blue fluorescence) with uniform cytoskeletal components and intact boundary of cells. Fig.5.16 (B-E) clearly showed that with an increase in time (1-12 h), more amount of snLYZ was internalized in cancer cells resulting in the formation of cytoplasmic granules causing damage to the cell membrane.

Babudieri-Callerio earlier reported that native LYZ (0.1 to 5 mg/ml) upon administration in human tumorigenic cell lines resulted in the formation of many azurophilic granules in the cytoplasm (diameter ~1 µm). The result was anticipated as one of the reason behind LYZ-based cell death. Here, a similar kind of granular formation was also observed (Fig.5.16 B, C, D, and E). Subsequently, the same group reported that the generation of the granular structure within the cytoplasm was due to the interaction of LYZ with the endoplasmic reticulum membrane.

The interaction occurred through an enzymatic mechanism involving homogenization of its fibrillar structure. In this study, we observed similar interaction, which resulted in overwhelming ROS production and triggered profound cell death.

Moreover, the appearance of the damaged cytoplasmic membrane with intact and slightly swollen nucleus (Fig. 5.16 E), is indicative of cellular necrosis. Interestingly, the granular formation within the cytosol seemed to initiate the cytosolic damage. Accordingly, after entering into cells, snLYZ caused cytosolic damage and increased permeability of the cellular membrane.

In a similar way we also examined the cellular uptake process of snBLA in MCF-7 cells.

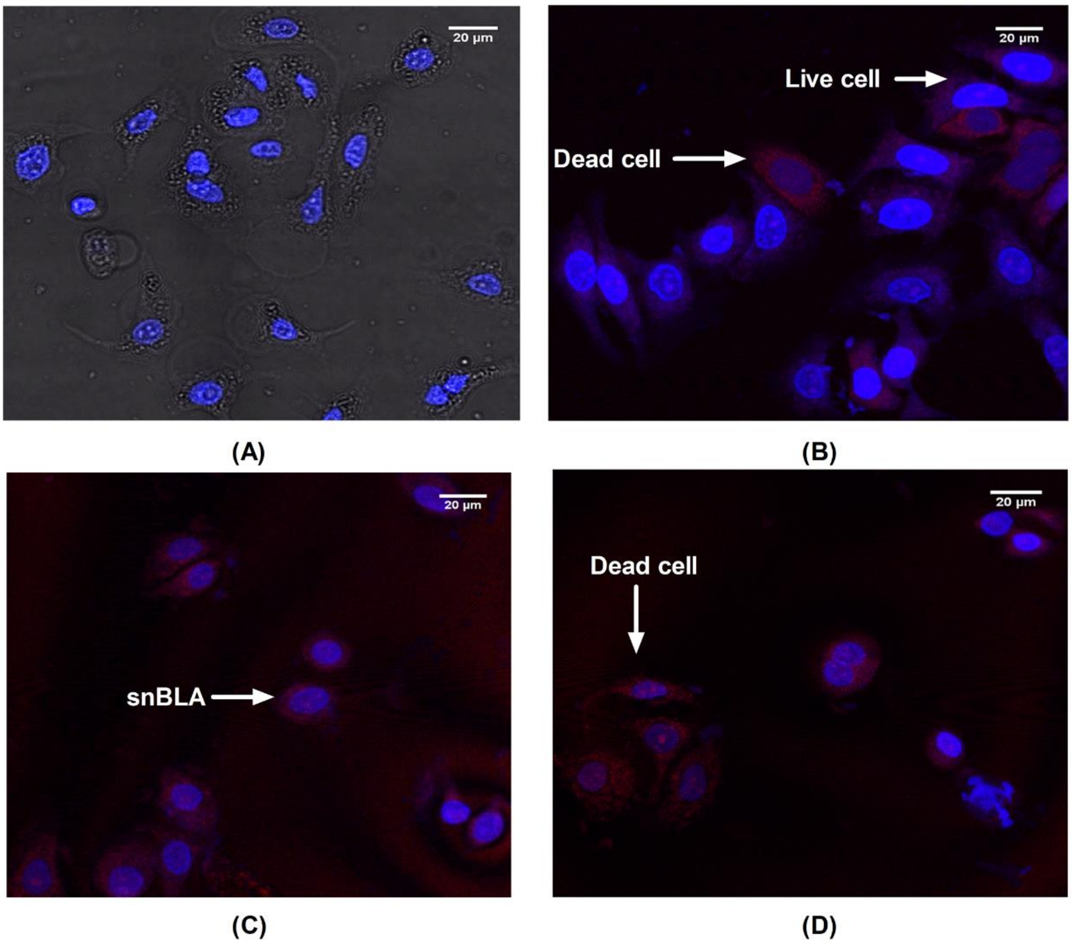

(A) (B)

(C) (D)

Figure 5.17 Fluorescence microscopic image of MCF-7 cells at (A) 0, (B) 3, (C) 6 and (D) 12 h post administration of snBLA conjugated with acridine orange. The orange fluorescence emitted by the particles inside the cytoplasm are due to the internalised snBLA. The internalization of snBLA was observed within 3 h of administration.

Cells stained with DAPI clearly exhibited blue fluorescence for the nucleus in live cells (see Fig.5.17 A) and snBLA tagged with acridine orange exhibited orange fluorescence (see Fig.5.17 C, D and E). At the end of 12 h post-administration of snBLA conjugated acridine orange, we observed the appearance of snBLA particles exhibiting orange fluorescence inside the cytoplasm of MCF-7 Breast cancer cells (see Fig.5.17 D), indicative of cellular uptake of snBLA in MCF-7 cells.

Hence, we anticipated that cellular internalization was probably one of the crucial reason of generating toxicity in cells and subsequent cancer cell death for both snLYZ and snBLA. For snBLA also, the cytoplasm was found disintegrated with intact nuclei, which was also an indicative of necrotic like cell death. Hence, for both snLYZ and snBLA the cell death mechanism observed to be similar.

5.2.5 Reactive oxygen species (ROS) mediated cell death

In order to understand the cell death mechanism mediated by snLYZ, we administered N-acetyl-L-cysteine (NAC) in cell culture medium to examine the possibility of cell death caused by reactive oxygen species (ROS). NAC is an antioxidant/free-radical scavenger or reducing agent that protects cells against ROS-mediated death. In our investigation, NAC (2 mM) was used to inhibit ROS-based effect. If NAC was administered in the cell medium, ROS generation would be inhibited and cell killing induced by ROS would be prevented.

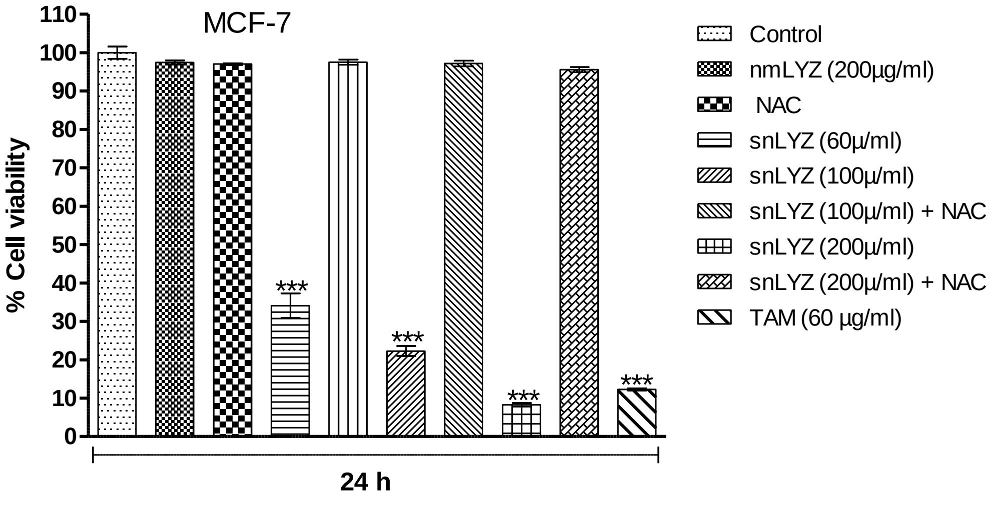

Figure 5.18 Cell viability assay of snLYZ in the presence and absence of NAC at 24 h post administration in MCF-7 cells. Statistically significant vs control group, *** p

<0.001 by One way ANOVA and post Tukey test. All data are expressed as Mean ± S.E.M, n = 3.

From Fig. 5.18, it was found that snLYZ at a concentration of 60, 100 and 200 µg/ml shows 34.09, 22.27 and 8.27 % cell viability respectively.However, administration of NAC (2 mM) caused almost no cell death, clearly indicating a complete ROS-mediated cancer cell death mechanism by snLYZ.

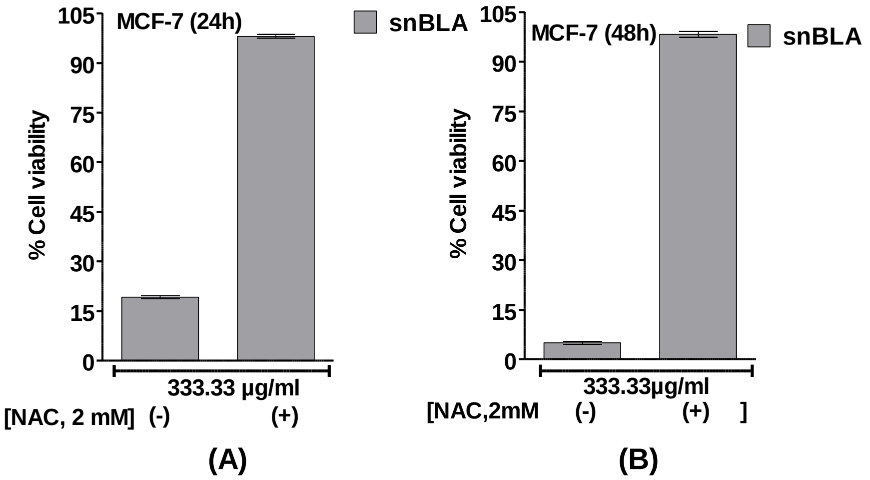

Figure 5.19 Cell viability assay of snBLA in the presence and absence of NAC at 24 h post administration in MCF-7 cells. The presence of NAC reversed the cytotoxicity indicating a ROS based mechanism. Statistically significant vs control group, *** $p < 0.001$ by One way ANOVA and post Tukey test. All data are expressed as Mean ± S.E.M, n = 3.

Similarly for by snBLA, we pre-treated the cell culture medium with N-acetyl-L-cysteine (NAC) followed by addition of 333.33 µg/ml to examine the possibility of cell death caused by reactive oxygen species (ROS).

We observed that the addition of NAC completely reversed the cell killing effect of snBLA at 333 µg/ml (see Fig. 5.19). Moreover, the effect of NAC was also found to be more pronounced at the end of 48 h (see Fig. 5.19). The result clearly indicates that the cell killing effect of snBLA in MCF-7 cells was mediated through ROS.

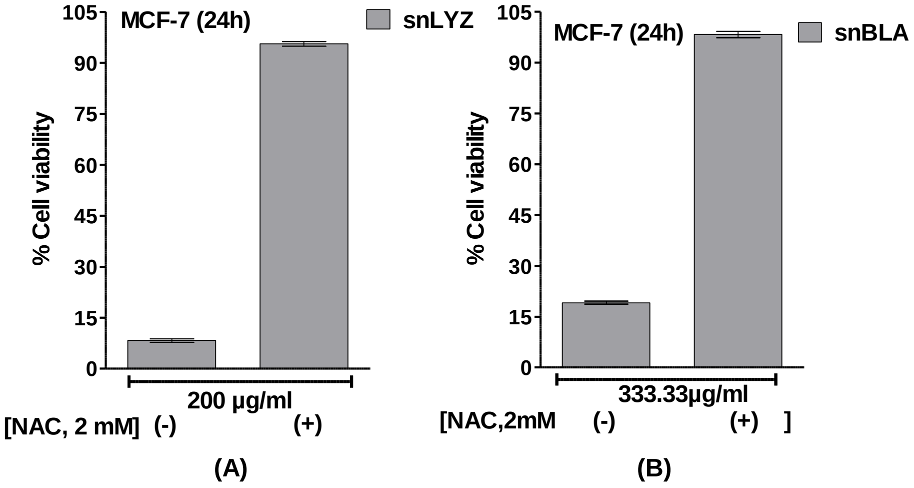

Figure 5.20 Comparison of cell viability in MCF-7 cells at doses of snLYZ and snBLA inducing maximum cytotoxic effects in the presence and absence of NAC at 24 h post administration. All data are expressed as Mean ± S.E.M, n = 3.

It was well established that both snLYZ and snBLA caused cell death through ROS generation. Based on the above results we have made a comparison of cytotoxicity of both snLYZ and snBLA at their doses inflicting maximum toxicity. We found that snLYZ at a dose of 200 µg/ml inflicted maximum toxic effect (91.72 %) compared to snBLA (80.85 %) at a much higher dose of 333.33 µg/ml at the end of 24 h post administration (Fig.5.20 A and B).

In both the cases we observed that pre-treating the cells with NAC (2mM) prior to administration of snLYZ and snBLA resulted in the complete inhibition of cytotoxicity. This clearly indicates that ROS has a very dominant role in the cell killings induced by snLYZ and snBLA. Moreover, comparatively lower amount of snLYZ is required to achieve higher level of toxicity compared to snBLA.

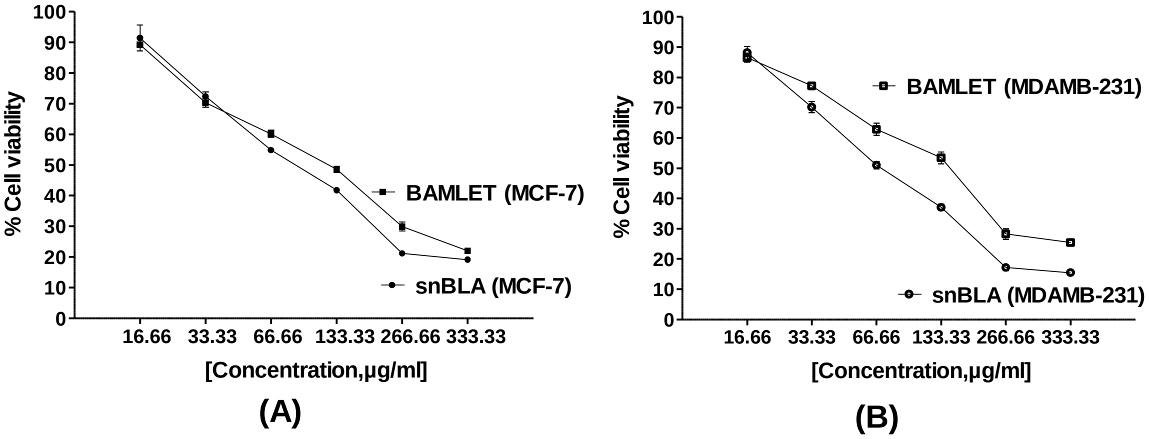

Figure 5.21 Comparison of cell viability in MCF-7 and MDAMB-231 cells at 24 h post administration of snBLA and BAMLET in a dose range of 16.66 - 333.33 µg/ml. snBLA was found to have a better cytotoxic profile than BAMLET. All data are expressed as Mean ± S.E.M, n = 3.

HeLa cells are the cells derived from one of the most aggressive forms of cancer called cervical cancer and cytotoxicity study against this particular cell line will help us realize the true potential of snBLA compared to BAMLET. BAMLET was never an effective treatment option for treating HeLa cells. Hence, evaluating the cytotoxic effect of snBLA on HeLa cells will be a challenge. The cytotoxicity study of our prepared snBLA was examined in four different cell lines such as MCF-7 and MDAMB-231 (Breast cancer), HeLa (cervical cancer) and A549 (lung carcinoma) using a range of concentrations (16.66 to 333.33 µg/ml).

In snBLA (Fig.5.21 A, and B), Fig.5.22A and B results clearly showed strong cytotoxicity of snBLA against all the cell lines. We also performed the same assay with BAMLET using same concentration of BLA (in BAMLET) to compare its cellular toxicity with that obtained by snBLA. The IC_{50} value of BAMLET in MCF-7 was found to be 105.8 µg/ml. While snBLA shows more than 80% cell death in all cell lines after 24 h of administration, BAMLET exhibits comparable toxicity in MCF-7 cell line (Fig. 5.21 A), however, in MDAMB-231 (Fig. 5.21 B) and A549 cell lines (see Fig. 5.22 B) it demonstrated lower anti-proliferative activity than snBLA.

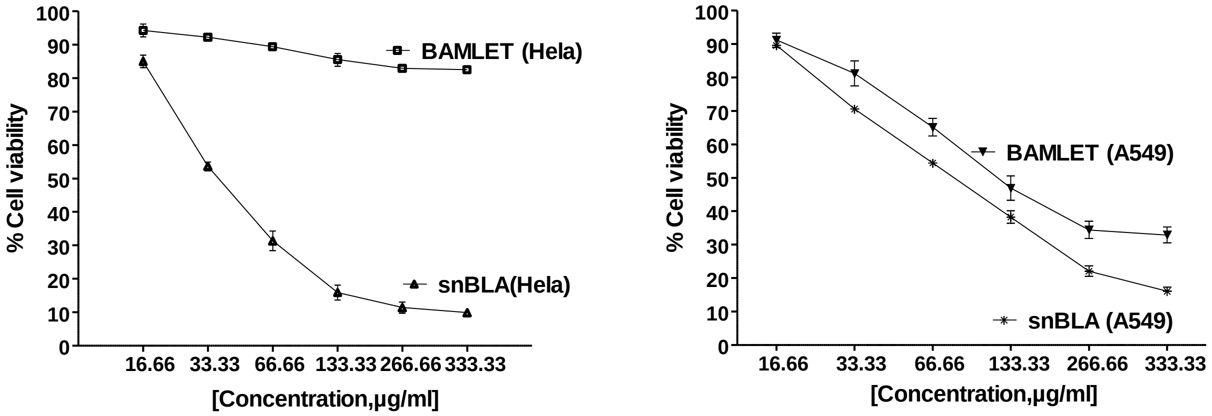

(A) (B)

Figure 5.22 Comparison of cell viability of snBLA and BAMLET in (A) HeLa and (B) A549 cells at 24 h post administration. snBLA was found to have a better cytotoxic profile than BAMLET. All data are expressed as Mean ± S.E.M, n = 3.

It was also observed that BAMLET showed little anti-proliferative activity in HeLa cells (17.46 % cell death) (see Fig.5.22 A), and in comparison snBLA demonstrated 90% cell death. Similarly, BAMLET demonstrated lower anti-proliferative activity in A549 cells (67.12 % cell death) (see Fig.5.22 B), compared to snBLA which demonstrated 83.98 % cell death. A cancer therapeutic agent should be highly selective and toxic towards cancer cells with various levels of invasiveness. HeLa cells are highly invasive than MDAMB-231, A549 and MCF-7 and hence, here we conclude that snBLA has a higher anti-proliferative potential in cancer cells compared to BAMLET.

We also examined snBLA and BAMLET in normal cell lines such as HaCaT (human keratinocyte cells) and 3T3 (murine fibroblast cells). snBLA showed less toxicity compared to BAMLET at similar concentrations (see Fig.5.23 A and B).

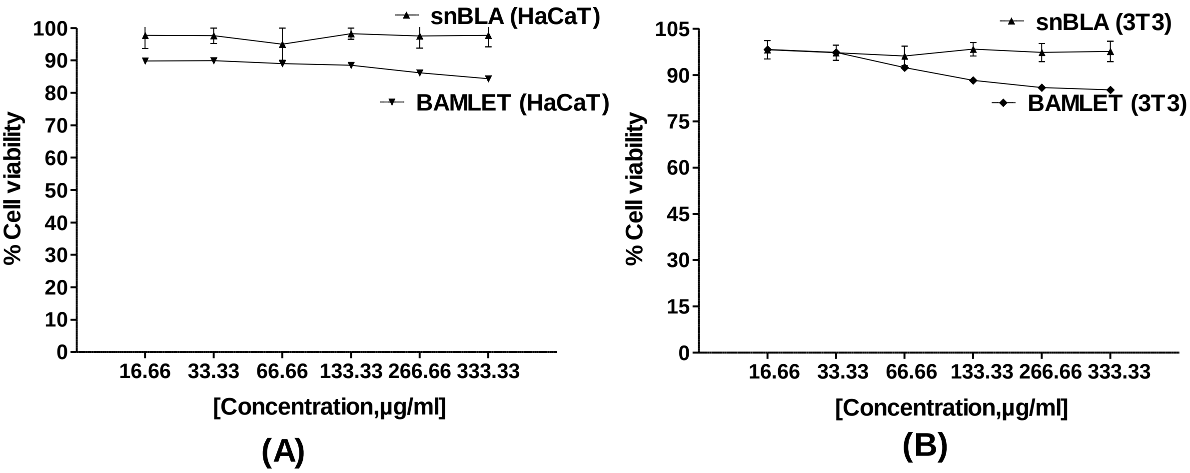

Figure 5.23 Comparison of cell viability of snBLA and BAMLET in (A) HaCaT and (B) 3T3 cells at 24 h post administration. snBLA was found to have a better cytotoxic profile than BAMLET. All data are expressed as Mean ± S.E.M, n = 3.

In order to understand whether ROS was involved in the process of cancer cell death, we administered NAC in MCF-7 and MDAMB-231 culture medium and observed the effect of snBLA both in the presence and absence of NAC (see Fig.5.24).

We observed that the administration of NAC completely inhibited the ROS-based cell death induced by snBLA in MCF-7 cells (Fig.5.22 A and B) and in MDAMB-231 cells (Fig.5.25 A and B). Since NAC is a ROS inhibitor, we concluded that snBLA generates sufficient ROS in cancer cells which subsequently triggers rapid cell death of MCF-7 cells.

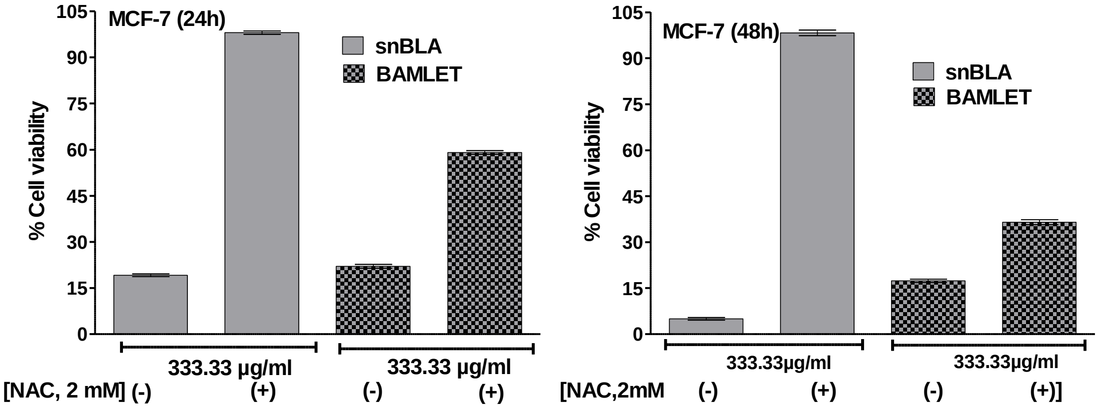

(A) (B)

Figure 5.24 Comparison of cytotoxic effects of snBLA and BAMLET due to ROS generation in MCF-7 cells at 24 h post administration. The presence of NAC reversed the cytotoxicity indicating a ROS based mechanism in snBLA, however, the presence of NAC partially reversed the cytotoxicity indicating a partial contribution of a ROS based mechanism. All data are expressed as Mean ± S.E.M, n = 3.

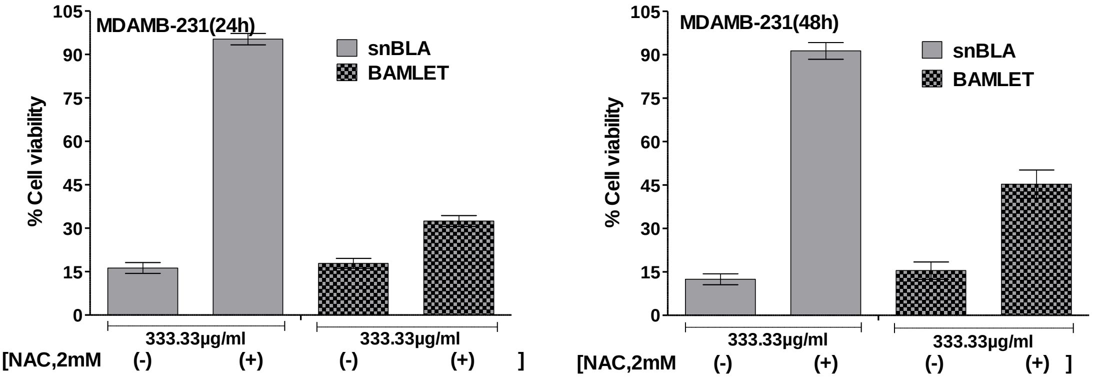

(A) (B)

Figure 5.25 Comparison of cytotoxic effects of snBLA and BAMLET due to ROS generation in MDAMB-231 cells at 24 h post administration. The presence of NAC reversed the cytotoxicity indicating a ROS based mechanism in snBLA, however, the presence of NAC partially reversed the cytotoxicity indicating a partial contribution of a ROS based mechanism. All data are expressed as Mean ± S.E.M, n = 3.

We also performed the same experiment with BAMLET and we observed a partial regain of cell viability in MCF-7 cells (Fig.5.24 A and B) and MDAMB-231 cells (Fig.5.25 A and B).Therefore, the results indicated that BAMLET mediates cancer cell death through some other mechanism besides ROS-based mechanism.

Multiple reports ae available related to cell death induced by BAMLET, however, they all were prepared using various methods. The BAMLET which we prepared here (Kamijima et al., 2008) were already reported to cause apoptosis-mediated cell death. However, lysosomal-mediated cell death induced by BAMLET was also observed when prepared using other methods (Knyazeva et al., 2008; Spolaore et al., 2010; Svensson et al., 2000). Therefore, our result also validates the point that BAMLET have multiple mechanism of cell death. However, snBLA which has higher potential of cancer cell death than BAMLET, triggers only ROS pathway to generate ample ROS that surpassed the cellular resistance to combat ROS-based stress.

We have observed from our earlier experiments such as the snBLA uptake study (see Fig. 5.17) and found a ROS mediated cancer cell death mechanism (see Fig.5.24 A and B) and (see Fig.5.25 A and B).

However, from the uptake study, we found that the cell and nucleus size was increased after the treatment of snBLA which is in contrary to the normal apoptosis process where cell volume shrinkage is observed. The above morphological changes are associated with cell necrosis rather than apoptosis. Hence, the role of Caspase-3 that is associated with apoptosis required further investigation.

5.2.6 Role of Caspase-3 mediated apoptotic cell death

We performed independent cell viability assay in the presence of caspase-3 inhibitor (potent, cell-permeable, and irreversible; $C_{21}H_{31}$ Cl N_4O_{11}, molecular weight of 551.0) that prevents caspase-3 mediated apoptosis and gallic acid (GA) which induces caspase-3 mediated apoptosis in MDAMB-231 cells to confirm whether the cytotoxicity was due to apoptosis or any other mechanism.

GA was used as a positive control, since it causes apoptosis in a caspase-3 mediated mechanism of action. We have also used the caspase-3 inhibitor to rule out the contribution of apoptosis through a caspase-3 mediated process. Various combinations of treatment both in the presence of gallic acid and caspase-3 inhibitors were administered along with snBLA in MDAMB-231 cells (see Fig.5.26).

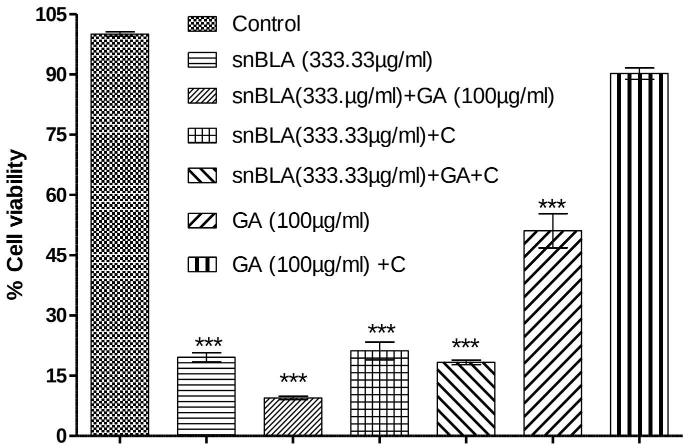

Figure 5.26 MTT assay of snBLA in MDAMB-231 cells both treated in the presence and absence Caspase-3 inhibitor, Gallic acid (GA), C (Caspase inhibitor) at the end of 24h. Statistically significant vs control group, ***p< 0.001 by One way ANOVA and post Tukey test. All data are expressed as Mean ± S.E.M, n = 3.

From the results (Fig. 5.26), we see that snBLA (80.43 % cytotoxicity) in combination with GA (90.54 % cytotoxicity) increased the cytotoxicity in MDAMB-

231 cells. However, snBLA in the presence of caspase-3 inhibitor (78.83%) produced similar levels of toxicity as that of snBLA alone. We observed that the cell death induced by snBLA was Caspase-3 independent which clearly ruled out the possibility of cell death due to apoptosis.

We also examined Caspase 3 expression by Western Blotting at the end of 12 h post incubation to ascertain our results obtained from Fig.5.27. We found that the basal expression level of Caspase 3 hardly changed compared to control, however, the caspase-3 level slightly increased for BAMLET. Caspase 3 has direct correlation with apoptosis (Saladi et al., 2013).

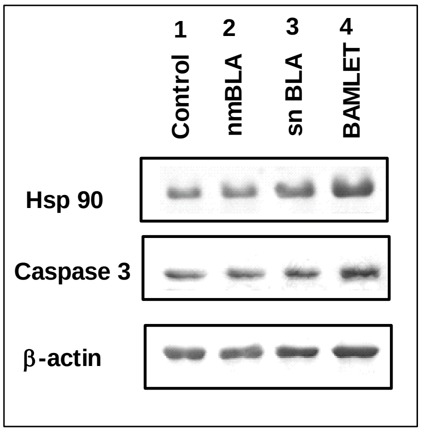

Figure 5.27 Western blot analysis of Caspase 3 and Hsp90 expression in MDAMB-231 cells treated with snBLA and BAMLET. The expression of Hsp 90, Caspase 3 is observed in the samples labelled vertically, Lane 1 (control), Lane 2 (nmBLA), Lane 3 (snBLA) and Lane 4 (BAMLET). β- actin is used as a loading control.

Since, cell death induced by BAMLET is mainly through apoptosis, we found a higher expression level of Caspase-3 in BAMLET (see Fig. 5.27). As, the expression level of Caspase-3, did not increase after the treatment of snBLA and remains same as that of the basal state, cell death mediated by apoptosis is totally ruled out and cell necrosis remains the only mechanism of cell death. Moreover, the Hsp90 expression level was slightly increased after the treatment of snBLA, however the expression of Hsp-90 was more pronounced with BAMLET treatment (see Fig. 5.27). Hsp90 expression positively correlates with the measure of the stress. Hence, the result clearly indicates that the increased expression of Hsp90 after treatment of snBLA was due to the generation of excessive stress due to ROS formation in MDAMB-231cells.

5.2.7 Hemolysis assay:

It was essential to know the hemocompatibility nature of snLYZ and snBLA, and hence, hemolytic analysis was performed using Triton-X (1%) as positive control and saline water (0.9% NaCl) as a negative control.

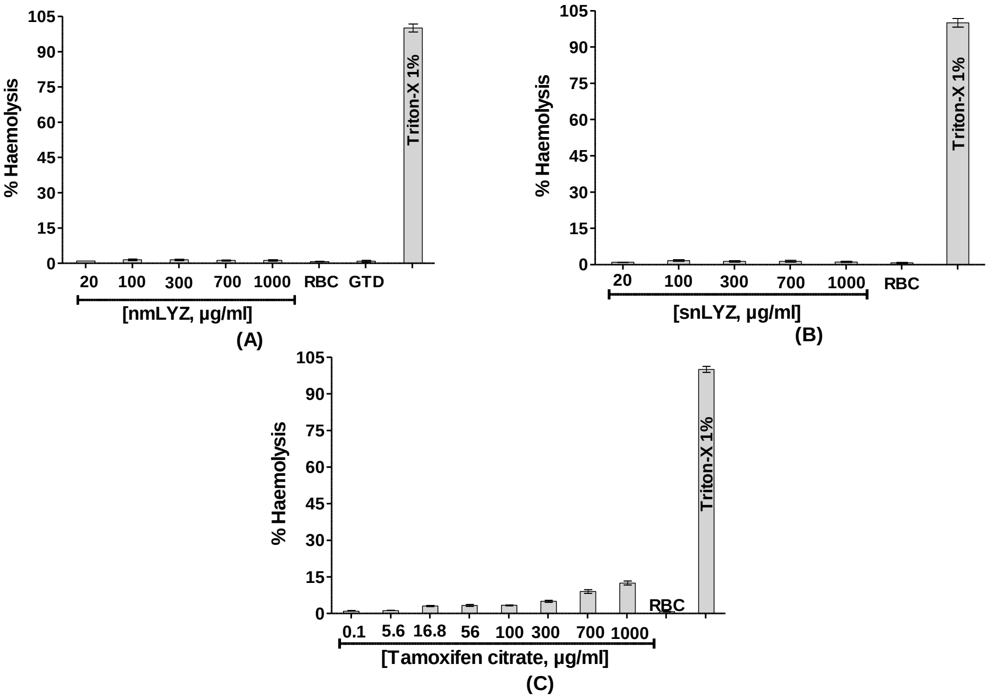

Figure 5.28 Hemolysis assay results of various samples. (A) nmLYZ and 0.1% GTD, (B) snLYZ, (C) Tamoxifen. Appropriate (-ve) control RBC and (+ve) control TritonX was used. All data are expressed as Mean ± S.E.M, n = 3.

We clearly observed that nmBLA and snBLA did not produce hemolysis till a concentration as high as 333.33 µg/ml (see Fig.5.29 A and B). However, BAMLET a protein based formulation shows high hemotoxicity from 16.66 µg/ml onwards (see Fig.5.29 C).

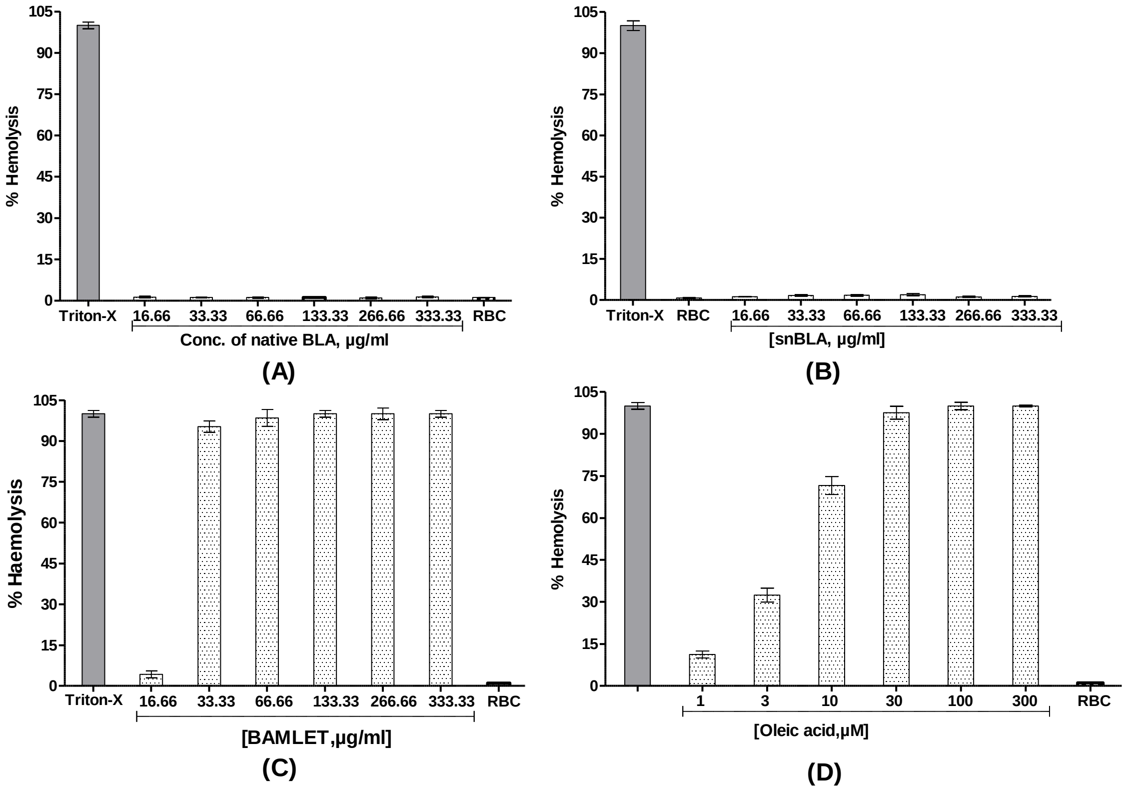

Figure 5.29 Hemolysis assay results of the samples. (A) nmBLA, (B) snBLA, (C) BAMLET and (D) Oleic acid. Appropriate (-ve) control RBC and (+ve) control Triton X was used. All data are expressed as Mean ± S.E.M, n = 3.

It is interesting to note that snBLA also contains the same protein component bovine α-lactalbumin, and it does not produce haemolysis as that of BAMLET. Oleic acid (OA) may be the major contributor towards haemolysis from BAMLET as OA induces haemolysis from concentrations as low as 1µM (see Fig.5.29D). Hence, snBLA is a better performer than BAMLET from all aspects such as cytotoxicity against cancer cells, cytocompatibility and hemocompatibility.

Our objective was to assess the possibility of using snLYZ and snBLA as a potential Breast cancer therapeutic agent for human use and in order to examine that it was essential to study its hemocompatible property. Both snLYZ and snBLA did not show hemolytic activity till a concentration as high as 1000 and 333.33µg/ml. However, TAM showed signs of haemolysis beyond the concentration of 16.8 µg/ml. Triton X (1%) was used as positive control showing 100% haemolysis.

It was clear from the results that snLYZ showed negligible hemolytic potential compared to TAM. The reason behind the hemocompatible nature of snLYZ was due to its proteinaceous composition. The mean size of the protein nanoassembly is 300 nm with spherical shape which would facilitate the smooth flow in blood and provides least resistance against flow. Moreover, the zeta potential values are +40 mV (snBLA) and -39.1 mV (snLYZ), respectively which also clearly indicate that they are highly stable in the solution without forming aggregation. All the mentioned properties facilitate smooth and prolonged circulation in blood. Moreover, we also demonstrated that folate conjugated snLYZ and snBLA can be used as targeted therapy in cancer which would trigger the tumor accumulation of protein nanoassemblies.

Based on our results obtained in Fig. 5.30, we proposed a model of how our developed snLYZ/snBLA might have killed cancer cells efficiently.

In normal cells, the cellular internalization takes place by phagocytosis, caveolar/clarithrin mediated endocytosis, micropinocytosis, and pinocytosis mechanisms followed by formation of early endosomes, late endosomes and lysosomes. snLYZ/snBLA is released in to the cytoplasam but the basal levels of antioxidant enzymes such as SOD (Superoxide dismutase) and GST (Glutathione S-transferase) prevent its interaction with the fibrillar cell membrane of the endoplasmic reticulum, hence, no toxicity and cell death.

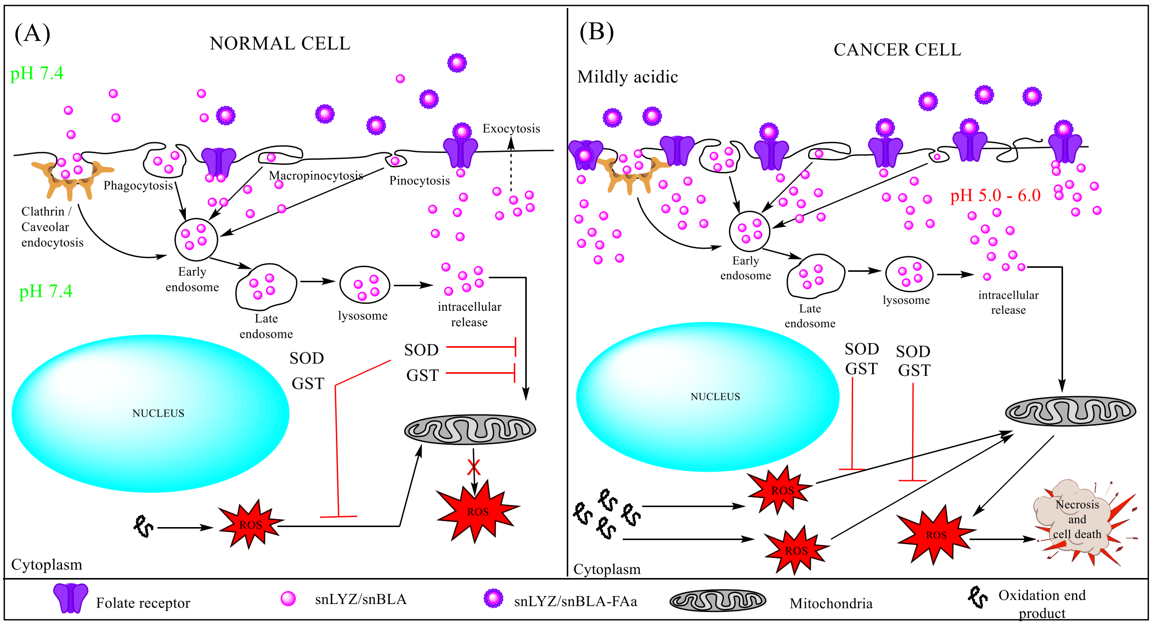

Figure 5.30 Proposed model of how nanoassembly proteins (snLYZ and snBLA) and snLYZ/snBLA-FAa and cause cell death in cancer cell. (A) In normal cells, (B) In cancer cells.

This was also evident from our haemolysis assays where normal RBC's tolerated high concentration of snLYZ till 1mg/ml and snBLA till 333.33µg/ml without hemolysis. In cancer cells, the extracellular and intracellular environment is slightly acidic (McCarty and Whitaker, 2010) with intracellular being more acidic in nature due to accumulation of various oxidation end products (Bareford and Swaan, 2007; Madhusudhan et al., 2014; Ulbrich and Subr, 2004). Hence, the cancer cells are already in a highly stressed state due to higher intracellular ROS generation from oxidation end products.

The mechanism of entry of snLYZ/snBLA into the cancer cells is the same as that of normal cells. However, during intracellular release of snLYZ/snBLA the basal levels of SOD and GST are already exhausted. Since no more SOD and GST is available for protecting the cancer cell from further ROS generation, snLYZ/snBLA probably interacts with fibrillar cell membrane of the endoplasmic reticulum and causes formation of granular cytoplasm and increased permeability of the cell membrane and cell death**.**

Although protein nanoassembly caused insignificant level of haemolysis to normal human erythrocytes or normal cells like HaCaT, it caused a rapid ROS dependent cancer cell death. The result suggests that snLYZ/snBLA prevents the cancer cell-specific mechanism of counteracting additional ROS generation, perhaps through extra antioxidant production. Liu et. al., earlier demonstrated that LYZ ameliorated oxidative stress in normal cells. LYZ by binding to agents such as advanced glycation end products (AGE) generated ROS using its unique 18 amino acid domain (Liu et al., 2006).

It is plausible that in snLYZ, such domain function was diminished due to conformational changes, which further reverted to a partially unfolded state that suppressed the extra antioxidant generation mechanism in cancer cells.

Chapter 6

In-vitro drug loading, release studies and evaluation of their cytotoxicity

6.1 Materials and Methods

6.1.1 Materials

N-acetylcysteine (NAC), Glutaraldehyde (GTD) (25%), Tamoxifen citrate (TAM), Bovine α-lactalbumin were purchased from Sigma-Aldrich, India. Lysozyme, *Micrococcus lysodekticus*, MTT assay kit, Ethanol, DMEM, Fetal bovine serum (FBS), antibiotics, HiMedia India Pvt. Ltd. Milli-Q water was used in all the experiments. T-25 flasks, 96 well plates and all other plasticwares were purchased from Tarsons Pvt. Ltd.MCF-7 (Breast cancer cell line) cells were procured from NCCS, Pune, India. All the glasswares used in the study were purchased from Borosil, India. All other reagents were of analytical grade.

6.1.2 Methods

6.1.2.1 Preparation of self-assembled protein and Tamoxifen conjugate

For the preparation of snLYZ/snBLA-TAM conjugate, 2.0 mg/ml of the protein nanoassembly solution was taken and a varying amount of TAM was added. The solution containing the protein nanoassembly and TAM was stirred for 5 min at 500rpm. Glutaraldehyde was added to the solution for cross-linking to achieve a final crosslinker concentration of 0.1%. In order to facilitate the proper crosslinking between the protein nanoassembly and TAM, the solution was kept under stirring at 500 rpm for 8 h.

At the end of 8 h the solution was centrifuged at 25,000 g for 5 min and the supernatant was taken for the estimation of the concentration of TAM. The amount of the drug present in the supernatant was estimated by measuring the absorbance of the solution at 235 nm. The concentration of TAM was extrapolated from the absorbance values of TAM (Abs. vs. Concentration) standard curve.

The amount of 'drug loaded' was calculated from the following formula.

$$\text{Amount of drug loaded} = \text{Amount of drug added for loading} - \text{Amount of drug present in the supernatant} \quad ....(6.1)$$

6.1.2.2 Drug loading study

Various amounts of TAM (0.5 - 6.6 mg) were added for loading on the protein nanoassembly snLYZ and snBLA by the above method. The amount of drug loaded was estimated from the Eqn. (6.1), mentioned in the above section. Based on the amount of drug loaded, we can calculate the drug loading efficiency by using Eqn. (6.2), mentioned below.

$$\text{Drug loading efficiency (\%)} = \frac{(\text{Amount of drug used for loading} - \text{Amount of free drug in solution})}{\text{Amount of drug carrier used in formulation}} \text{ X } 100.......(6.2)$$

6.1.2.3 pH-responsive drug release studies

In order to observe the drug release from the snLYZ/snBLA-TAM conjugate, we performed both the cumulative and non-cumulative release of TAM from the formulation at various ph. For performing cumulative drug release study, the snLYZ/snBLA-TAM conjugate (2.0 mg/ml) was kept in a dialysis bag and kept in a beaker containing buffer of pH 3.0, 4.0, 5.0, 6.0 and 7.4, respectively. The dialysis bag containing the snLYZ/snBLA-TAM conjugate was clipped with the wall of the beaker and dipped inside the buffer solution. The contents of the beaker were kept for stirring at 60 rpm. Samples of the buffer were collectedfrom the beaker at 1, 2, 3, 6 and 12 h to calculate the amount of drug release from the snLYZ/snBLA-TAM conjugate kept in the dialysis bag. The concentration of the drug in the supernatant was calculated from the standard curve of TAM (Abs. vs. Conc.).

Non-cumulative drug release was performed at various time points such as 1, 2, 3, 6, 12, 24 and 30 h. Here, other procedures kept same as mentioned above for cumulative drug release study except an equivalent volume of buffer was replaced for the volume of sample taken from the beaker for estimation of TAM content as well as to maintain a concentration gradient of drug between ‘loaded state’ and in ‘solution state’ for maximum drug release.

Here, we wanted to define the state of snLYZ/snBLA-TAM conjugate after the maximum amount of TAM released from snLYZ/snBLA-TAM conjugate at pH 6.0 (till a point where no more drug release was observed) as the ‘reconstituted state’ of snLYZ/snBLA-TAM conjugate.

6.1.2.4 Preparation of reconstituted protein nanoassembly

The reconstituted snLYZ/snBLA-TAM conjugate was prepared by performing the non-cumulative drug release from the snLYZ/snBLA-TAM conjugate in an acidic environment, i.e., at pH of 6.0. The amount of drug from snLYZ/snBLA-TAM conjugate was allowed to release at pH 6.0 for 30 h (till no further drug release was observed). The solution containing the snLYZ/snBLA-TAM conjugate was centrifuged at 20,000 g for 10 min. The supernatant solution containing the drug was removed and the pellet was resuspended in 1 ml of Milli-Q water and termed as 'reconstituted snLYZ/snBLA'.

6.1.2.5 Characterization of 'reconstituted snLYZ'

The solution of snLYZ-TAM conjugate was subjected to in-vitro drug release at pH 6.0. After the drug release process was completed, supernatant containing the drug was removed and pellet was resuspended with fresh buffer. The process was repeated at different time points (1, 2, 3, 6, 12 and 24 h) till no further release of the drug was observed. The 'reconstituted snLYZ/snBLA' was characterized using both tryptophan (Trp) as well as ANS fluorescence spectroscopy. Fluorescence emission spectra were recorded in the range of 300 to 400 nm for fluorescence measurement. The excitation and emission slit widths were set at 5 and 10 nm, respectively.

6.1.2.6 Activity assay of nmLYZ and snLYZ

Cells of *Micrococcus lysodekticus* (9 mg) were suspended in 30 ml of 100 mM sodium phosphate buffer pH 7.4, shortly before the assay. Each of the microplate wells contained 50µl sample and 200 µl of micrococcus cell suspension. The plate was gently shaken for 1.0 min in a microplate reader (iMark, Bio-Rad) followed by measurement of absorbance at 450 nm and continued for 10 min at 1 min interval.

Lysozyme activity (Ng et al., 2013) was measured by measuring the change in O.D (absorbance) over a period of 10 min and is represented by the following formula.

$$\text{Lys activity (Change in O.D)} = \text{O.D}_{\text{initial}} - \text{O.D}_{(10\ \text{min})} \text{-----------------------------------} (6.3)$$

6.1.2.7 Cell viability assay of various formulations of snLYZ/snBLA-TAM conjugates containing different ratios of snLYZ/snBLA:TAM and their reconstituted forms

The cytotoxicity of snLYZ/snBLA-TAM conjugate was assessed in breast cancer cell line MCF-7 using MTT assay. MCF-7 cells were cultured in DMEM (Dulbecco's Minimum Essential Medium) and supplemented with 10% foetal bovine serum, 2 mM glutamine and 0.1 mg/ml penicillin and streptomycin. Cells were cultured in T-25 flasks and were maintained at 37^0C in humidified, 5% CO_2 atmosphere in a CO_2 incubator. The MCF-7 cells were cultured till 80% confluence was achieved. The cells were trypsinised and seeded at a density of $1x10^4$ cells/ml. The cells were seeded in a 96 well plate with 100 µl of DMEM in each well and were allowed to proliferate for 24 h. Various test samples were administered to the MCF-7 cells and the end point effect was monitored by MTT assay at the end of next 24 h and 48 h. MTT (10 µl of 5 mg/ml stock) was added 6 h before the end point. At the end point, media was removed and 100 µl of DMSO was added to dissolve the formazan formed and the absorbance was measured at 595 nm. The absorbance values were recorded and percentage cell viability of MCF-7 cells was calculated from the absorbance values and the result was plotted.

6.1.2.8 Evaluation of the mechanism of toxicityof snLYZ/snBLA and snLYZ/snBLA-TAM conjugates

To examine the generation and effect of reactive oxygen species (ROS) in MCF-7 cell death, we applied N-acetyl-cysteine (NAC), a well-known ROS inhibitor (Mayer and Noble, 1994) in cell culture medium. NAC was added to a final concentration of 2 mM in MCF-7 culture and cells were allowed to proliferate as described above. After 24 and 48 h post-administration of snLYZ/snBLA and snLYZ/snBLA-TAM in MCF-7 cells, MTT assay was performed and the results compared with the samples without NAC.

6.1.2.9 Hemolysis assay of snLYZ/snBLA and snLYZ/snBLA-TAM conjugates

To perform, the hemocompatibility assay, an expert technician under the supervision of an invited physician collected 5 ml of B $^{+ve}$ human blood. Blood was collected in a centrifuge tube containing 2 mg of disodium EDTA (anti-coagulant). The content was gently resuspended and centrifuged at 1000 g for 10 min. The supernatant was removed and the RBC collected at the bottom of the centrifuge tube was washed three times by gentle resuspension with 10 times the volume of pyrogen free saline (0.9% NaCl), and followed by centrifugation at 1000 g for 10 min at room temperature.

The RBC pellet was gently resuspended in pyrogen free saline and was diluted to 0.8% (v/v). The resuspended RBC solution (3 ml) was placed in sterile glass vials and various test samples were added to evaluate their hemolytic potential.

Triton X (1%) was used as a positive control for monitoring maximum hemolysis and RBC suspension treated with sodium phosphate buffer, pH 7.4 was used as a negative control. The percentage hemolysis was calculated at 1 h and the graph was plotted between percent hemolysis and time (h).

6.2 Results and Discussion

6.2.1 Preparation of snLYZ/snBLA-TAM conjugates

The snLYZ/snBLA-TAM conjugates were prepared by the method mentioned in section 6.1.The drug loaded snLYZ-TAM was characterized using AFM imaging (see supplementary Fig S10).

6.2.2 Drug loading efficiency

Many scientists have recently reported that protein nanoparticles can be used as drug carriers (Avachat et al., 2014; Gradishar et al., 2005). Although, we have demonstrated here the selective cytotoxic nature of snLYZ and snBLA for cancer cells, we also wanted to observe the drug-loading and release potential of snLYZ and snBLA. TAM loading onto the snLYZ and snBLA was examined by loading of various amount of drug onto the fixed amount of snLYZ and snBLA concentration (2.0 mg/ml) using 0.1% GTD as cross linker.

It was observed that saturation level of drug loading was achieved at 2.58 mg of TAM amount onto 2 mg of snLYZ (beyond which no further loading was observed) (see Table 6.1 and Fig 6.1), indicates more than 100% drug loading w/w.

Such exceptionally high loading must be due to the cross linking of TAM and surface characteristics of snLYZ molecules. The drug (Tamoxifen) loading capacity (payload) of snBLA and snLYZ was calculated using Eqn. no. 6.1 and the pH-responsive drug release profile was studied at pH 6.0. Since, pH 6.0 is close to physiological pH environment of cancer cells, the in-vivo drug release study was performed at pH 6.0 to simulate the condition

Table 6.1 In vitro drug loading of Tamoxifen (TAM) on snLYZ and its release at pH 5.0 and 6.0. The duration of drug loading was 8 h.

Amount of drug added (µg)	Amount of snLYZ (µg)	Amount of drug loaded (µg)	Drug Loading efficiency (%)	Amount of drug (µg) release at pH 5.0	Amount of drug (µg)release at pH 6.0
6660	2000	2578.49	128.92	1317.6	902.5
2500		2498.22	124.91	1276.6	874.4
2000		1998.11	99.91	1021	699.3
1500		1497.79	74.89	765.4	524.2
1000		998.11	49.91	510	349.3
500		498.43	24.92	254.7	174.5

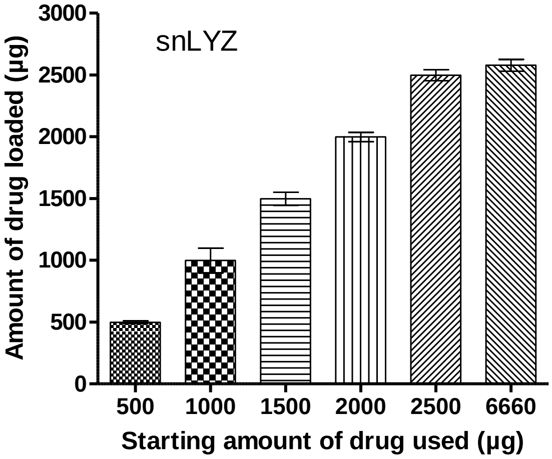

Figure 6.1 Estimation of the maximum loading capacity of the protein nanoassembly, snLYZ. All data are expressed as Mean ± S.E.M, n = 3.

An amount of 2 mg of snBLA was used for crosslinking with 4 mg of TAM. After 8 h of loading of TAM by crosslinking, we observed almost 3.926 mg of drug was successfully loaded onto it, which was almost double the weight of snBLA and higher than snLYZ. Further, various amount of TAM was loaded onto snBLA and the loading efficiency was estimated using the Eqn.6.2 (mentioned in “Materials and Methods” section). The drug loading data was presented Table 6.2.

From our study we found that snBLA exhibited higher drug loading efficiency than snLYZ. The amount of loading of drug onto protein nanoassembly depends on the 3-D structure of individual protein unit in the nanoassembly as well as their surface character.

Table 6.2 In vitro drug loading of Tamoxifen (TAM) on snBLA and its release at pH 6.0. The duration of drug loading was 8 h.

Amount of drug added (μg)	**Amount of snBLA (μg)**	**Amount of drug loaded (μg)**	**Loading efficiency (%)**	**Amount of drug (μg)release at pH 6.0**
6000	2000	3931	93.1	2507.98
4000		3926	192.6	2465.52
2000		2000	100	716
250		250	12.5	91.27
100		100	5	36.5

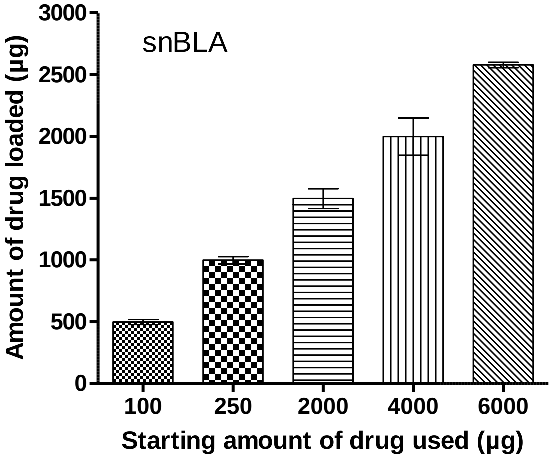

Figure 6.2 Estimation of the maximum loading capacity of the protein nanoassembly, snLYZ. All data are expressed as Mean ± S.E.M, n = 3.

6.2.3 In vitro pH-dependent release

Since cancer cells achieves an acidic pH intracellularly and extracellularly, a pH-dependent drug release study was essential to evaluate the conditional drug-release potential of snLYZ/snBLA-TAM conjugate. Although, the pH-dependent in vitro drug release study was performed till 12 h, the time-dependent drug release profile at all the pH used in the study showed that drug release process attained a steady state after 6 h (Fig. 6.3) of release.

For the drug release study, snLYZ-TAM was used in the ratio of 1:1 w/w. This formulation was used for drug release study under varying pH conditions. The result clearly revealed that with lowering the pH value, increased the amount of drug released and it was found to be 3.5 %, 48.9 %, 65.45%, 79.47% and 91.29% at pH 7.4, 6.0, 5.0, 4.0 and 3.0 respectively (see Fig. 6.3) which indicates pH responsive drug release potential of snLYZ-TAM conjugate. Such pH sensitive release helps in targeted drug delivery in cancer due to the acidic environment of cancer cells.

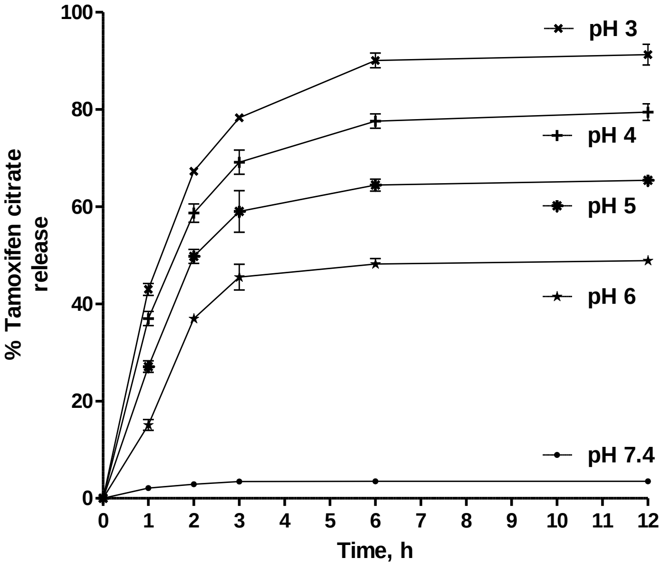

Figure 6.3 Percentage release of TAM from snLYZ-TAM conjugate at various pH with time till 12 h. A pH dependent increase in drug release was observed in snLYZ-TAM conjugate. All data are expressed as Mean ± S.E.M, n = 3.

This may be due to the fact that the crosslinkages of glutaraldehyde (GTD) between the protein nanoassembly and the drug were weak at acidic pH. Usually crosslinkages due to GTD are highly stable in an alkaline pH but become unstable at acidic pH. Hence, the pH dependent drug release was triggered due to the weakening of the glutaraldehyde crosslinkages.

The non-cumulative drug release for both snLYZ-TAM and snBLA-TAM conjugates were performed at pH 6.0. In order to observe the maximum amount of drug release at an environment closely similar to the cancer cells, non-cumulative release of TAM from snLYZ-TAM conjugate was performed at pH 6.0. We observed that 64.82 % of the loaded drug was released at pH 6.0, till 24 h, beyond which, no further release of the drug was observed (see Fig. 6.4).

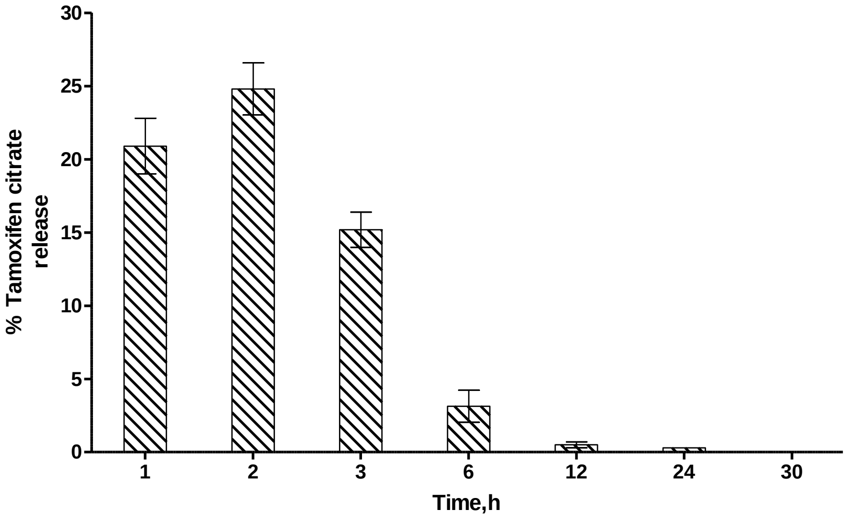

Figure 6.4 Percentage non-cumulative release of TAM from snLYZ-TAM conjugate at pH 6.0 with time till 30 h. No further release of drug was observed beyond 24 h indicating the maximum possible release of the drug. All data are expressed as Mean ± S.E.M, n = 3.

This result clearly showed that 35.18 % of the drug was still present in snLYZ-TAM conjugate. This may be due to the fact that still a few crosslinkages between the protein nanoassembly and the drug existed, which were intact at pH 6.0.

The pH-dependent in vitro drug release study for snBLA-TAM was also performed till 12 h. However, the time-dependent drug release profile at pH (3-7.4) showed that drug release process attained a steady state at 6 h (Fig. 6.5). The cumulative drug release observed at pH 3, 4, 5, 6 and 7.4 were 84.09, 68.7, 60.18, 44.52 and 1.4 % respectively (see Fig. 6.5).

Here, we also observed a similar trend of drug release pattern for snBLA-TAM where increased amount of drug was released with lowering of pH. The results showed that with the decrease in pH, the amount of drug release was increased from snBLA-TAM.

The same reason was attributed here for snLYZ-TAM also holds true here i.e., due to the weakening of the GTD crosslinkages.

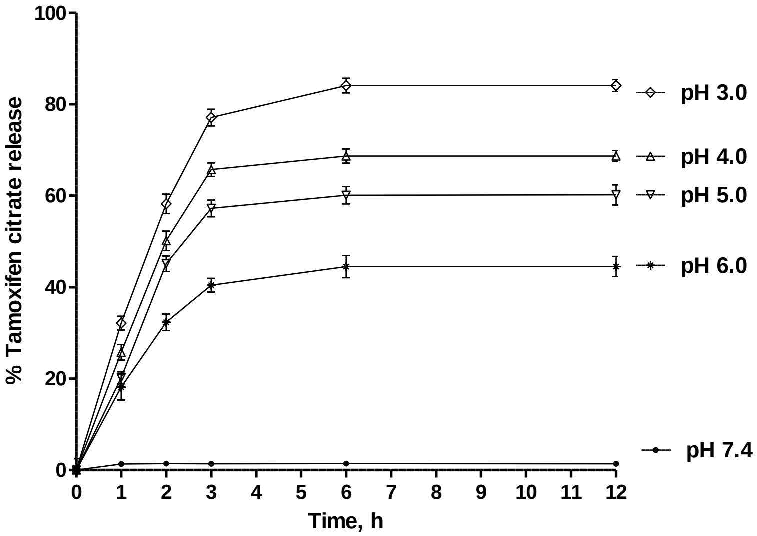

Figure 6.5 Percentage cumulative release of TAM from snBLA-TAM conjugate at various pH (3-7.4) with time till 12 h. A pH dependent increase in drug release was observed in snLYZ-TAM conjugate. All data are expressed as Mean ± S.E.M, n = 3.

Non-cumulative release of various formulations of snBLA-TAM conjugates (1:1, 4:1 and 10:1 w/w) was performed at pH 6.0 till 30 h in order to observe the maximum amount of possible drug release. The results showed that 63.81, 59.75 and 55.19 % of the drug was released from snBLA-TAM formulation of 1:1, 4:1 and 10:1 w/w respectively (see Fig. 6.6). We also observed that with the increase in the amount of protein nanoassembly in the formulation from 1:1 to 10:1, gradually the amount of drug release was decreased at pH 6.0. The reason may be due to the increased number of cross-linkages of GTD formed between snBLA and TAM. Since, the cross-linking between snBLA and TAM was increased, limited number of cross-linkages exposed to pH 6.0 was broken and hence, lower amount of TAM was released.

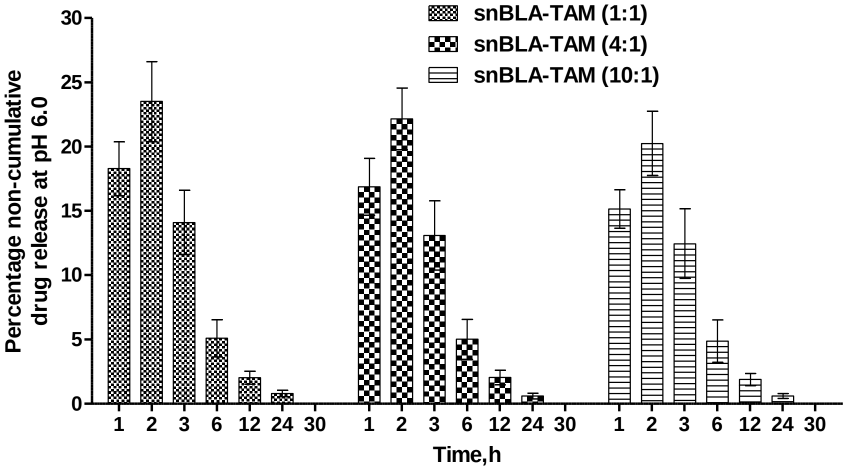

Figure 6.6 Percentage non-cumulative release of TAM from snBLA-TAM conjugate at pH 6.0 with time till 30 h. No further release of drug was observed beyond 24 h indicating the maximum possible release of the drug. All data are expressed as Mean ± S.E.M, n = 3.

Since the protein structure is inherently very sensitive to pH change, here, although sufficient crosslinkages were responsible to form a stable protein-drug conjugate, the crosslinkages in snLYZ molecule perhaps could not provide sufficient resistance against the change in pH from 7.4 to 6.0. Such a change, must have induced the breakage of crosslinkages followed by a little conformational distortion of snLYZ that initiated the drug release process. However, it was not possible to break the crosslinkages, which were formed deeper inside the structure, which remained bound with the snLYZ molecules, and hence only ~65% of the total drug was released at pH 6.0.

The protein nanoassembly is stable at pH 3.0. In the present case, our protein self-assembly changes its structure at low pH (not as drastic as its native state) in tumor environment such that it releases drug molecules instantly but not completely. Such partial release of drug brings permanent change of protein structure (we called it 'reconstituted snBLA/snLYZ) and the nano-assembly which hitherto did not act as anticancer agent, would turn lethal to cancer cells. Such dual anticancer therapeutic mechanism is unique in our study instead merely a 'pH-dependant drug release-based anticancer therapy' however upon prolonged circulation and in the presence of intracellular proteases the protein nanoassembly will eventually degrade leading to the complete release of the drug

6.2.4 Activity assay of LYZ in reconstituted snLYZ-TAM

As observed in the Chapter No.4, LYZ activity was assessed at pH 5.0. Here we wanted to know the LYZ activity of various samples like snLYZ-TAM (1:1) and 'reconstituted snLYZ'. The result could provide the activity of catalytic sites of LYZ in various samples. Accordingly we performed activity assay at pH 5.0.

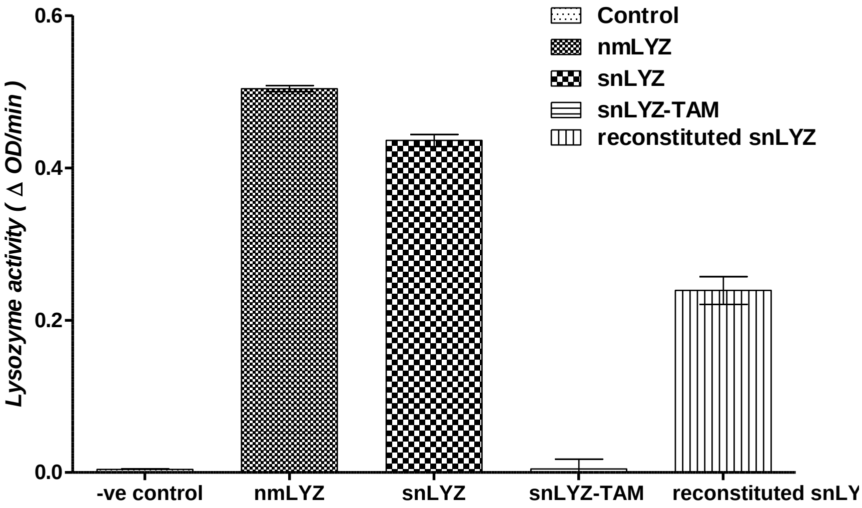

Figure 6.7 LYZ activity of various states of LYZ in snLYZ measured by *Micrococcus lysodekticus* assay. Both snLYZ and 'reconstituted snLYZ' retain partial LYZ activity. All data are expressed as Mean ± S.E.M, n = 3.

It was found that the snLYZ-TAM conjugate regained fair amount of lytic activity after releasing ~65% of total loaded drug at pH 5.0(we can call it reconstituted snLYZ)(see Fig. 6.7). The reactivation efficiency was above 50%.

The result indicates that the active sites of LYZ was exposed to the solution due to the release of more than ~65% TAM, which were possibly earlier covered by the TAM molecules. Here, the post drug release state of snLYZ-TAM conjugate was referred as ‘reconstituted snLYZ’.

The tryptophan (Trp) fluorescence study of ‘reconstituted snLYZ’ revealed that the microenvironment around the Trp residues was not changed substantially as the fluorescence spectra showed close resemblance with snLYZ-TAM fluorescence spectra (Fig.6.8).

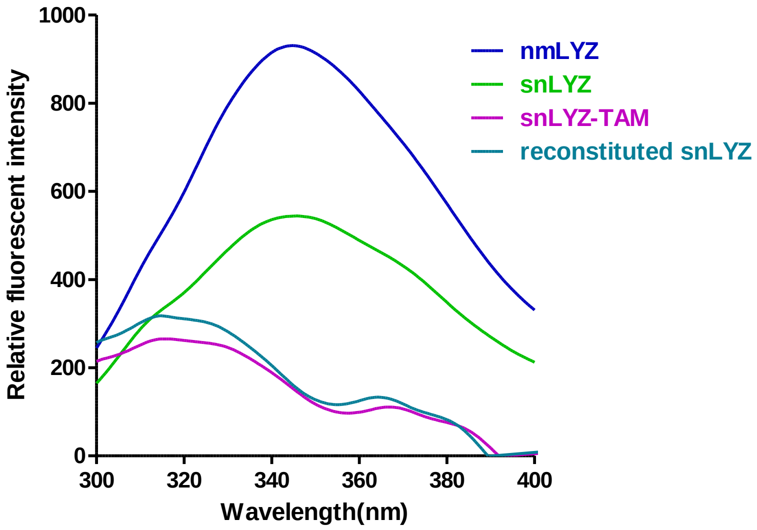

Figure 6.8 Tryptophan fluorescence spectra of nmLYZ, snLYZ, snLYZ-TAM and ‘reconstituted snLYZ’ recorded between 300–400 nm. The drop in fluorescence intensity of snLYZ, snLYZ-TAM and ‘reconstituted snLYZ’ indicates probable translocation of Trp residues to the surface of the protein structure or to a more

hydrophobic region. All data were expressed as the mean of three readouts generated from the instrument.

However, the small increase in the Trp fluorescence intensity of ‘reconstituted snLYZ’ may be due to the release of the drug which caused a structural change of LYZ molecules exposing some of the Trp residues to the outer surface of the protein nanoassembly. The ‘reconstituted snLYZ’ still contain ~35% of initial loaded drug which, would probably release only after the degradation of snLYZ.

The Trp fluorescence intensity of snLYZ was quenched substantially compared to that of nmLYZ. This may be due to the structural change in the snLYZ where Trp residues might have translocated to a more polar region.

When, ANS-bound fluorescence measurement of ‘reconstituted snLYZ’ was recorded, the spectra clearly demonstrated a higher hydrophobicity (because higher ANS fluorescence intensity indicates higher surface hydrophobicity) than snLYZ-TAM conjugate, which indicates a state where more non-polar residues of snLYZ were relocated on the surface (Fig.6.9) during drug release process.

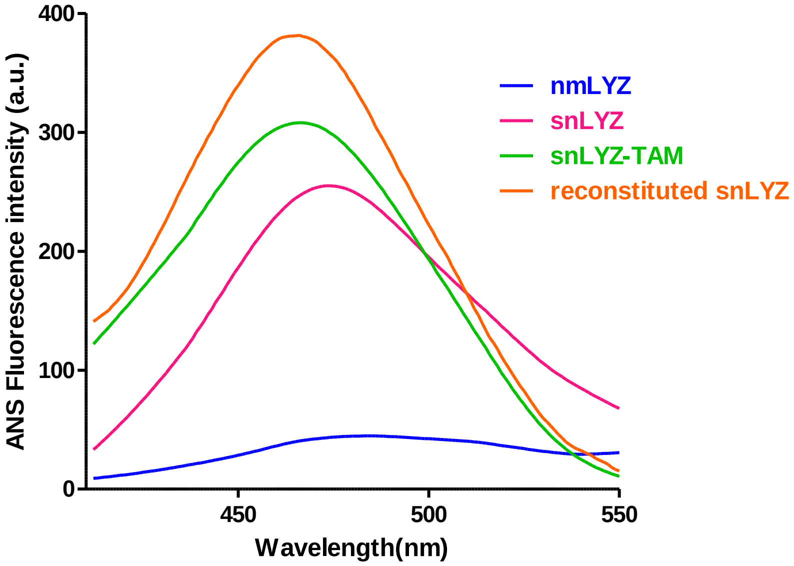

Figure 6.9 Protein bound ANS fluorescence spectra of nmLYZ, snLYZ, snLYZ-TAM and 'reconstituted snLYZ'. The surface hydrophobicity of samples increased in the following order, snLYZ < snLYZ-TAM < 'reconstituted snLYZ'. Some of the Trp residues on the surface of the 'reconstituted snLYZ' got exposed to ANS after the drug release from snLYZ, hence an increase in fluorescence intensity. All data were expressed as the mean of three readouts generated from the instrument.

We also performed the similar experiment on snBLA-TAM. Fig 6.10 showed the Trp fluorescence spectra of snBLA-TAM and 'reconstituted snBLA'. We observed an increase in fluorescence intensity of 'reconstituted snBLA' compared to snBLA-TAM. Such result may be due to the release of the drug, TAM from the snBLA-TAM conjugate, resulting in a structural change of the 'reconstituted snLYZ'. The resulting structural change induced the movement of Trp residues to a more non polar region or to the core of the protein nanostructure thereby increasing the intensity of 'reconstituted snLYZ'.

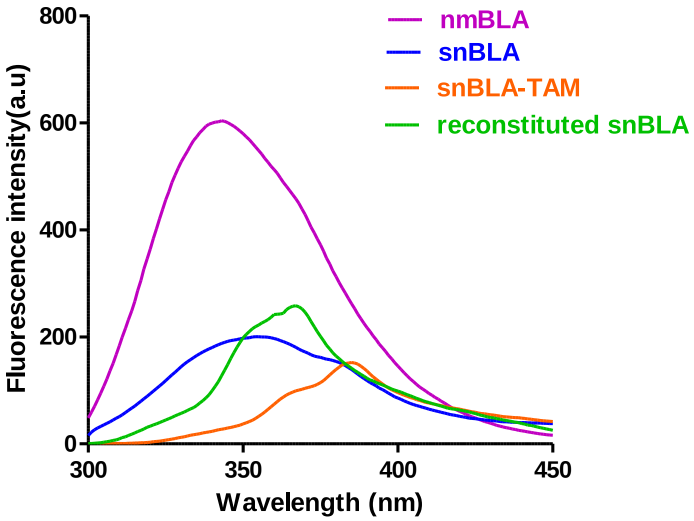

Figure 6.10 Tryptophan fluorescence spectra of nmBLA, snBLA, snBLA-TAM and reconstituted snLYZ. The drop in intensity of snLYZ, snLYZ-TAM and reconstituted snLYZ indicates translocation of Trp residues to a more hydrophobic region. All data were expressed as the mean of three readouts generated from the instrument.

Further, the small amount of peak change observed in ‘reconstituted snBLA’ (Fig.6.10) might be due to structural change of snBLA induced by the drug release process.

Further we wanted to observe the surface hydrophobicity character of snBLA-TAM and its ‘reconstituted state’ and accordingly, ANS bound fluorescence spectra was recorded. The snBLA-TAM bound ANS fluorescence intensity was found to reduce marginally compared to ‘reconstituted snBLA’ (Fig.6.11). This may be due to the slight change that occurred in ‘reconstituted snBLA’ following drug release which resulted in the translocation of the hydrophobic residues on to the surface of snBLA.

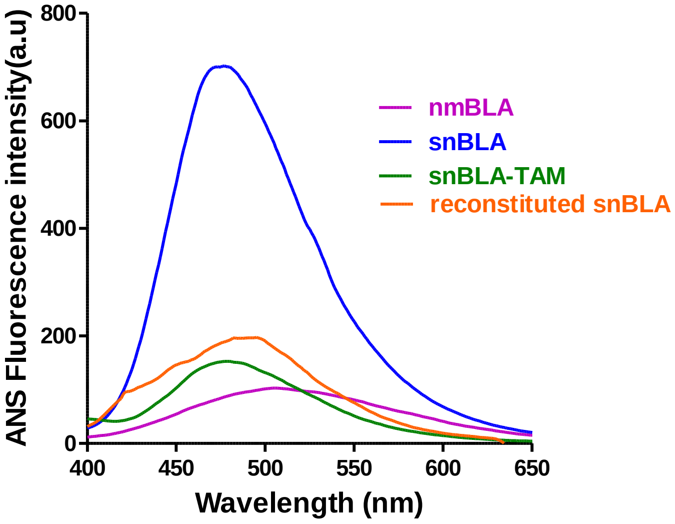

Figure 6.11 ANS fluorescence spectra of nmBLA, snBLA, snBLA-TAM and reconstituted snBLA. The surface hydrophobicity increased in the following order, nmBLA < snBLA-TAM < ‘reconstituted snBLA’< snBLA. All data were expressed as the mean of three readouts generated from the instrument.

6.2.5 Cytotoxicity study of snLYZ-TAM

It was essential to know the cytotoxic potential of drug-loaded snLYZ and post drug release state of snLYZ-TAM conjugate (referred as ‘reconstituted snLYZ’). It was understood that drug molecules were loaded through crosslinking with snLYZ, however, the release of TAM (~65% release) at low pH like 6.0 left a specific conformational state of snLYZ. Here, we examined the cytotoxic potential of ‘reconstituted snLYZ’ in MCF-7 cells. In cells, reconstituted snLYZ might either be degraded or be reused as free snLYZ. However, here we realized that its anticancer potential must be investigated.

Therefore, in this section, the cytotoxicity potential of various samples like snLYZ, snLYZ-TAM and ‘reconstituted snLYZ’ was assessed in MCF-7 breast cancer cells and compared. In this experiment, the amount of snLYZ-TAM (used 4:1 ratio w/w) conjugate was used in an increasing manner, from 60 to 200 µg/ml in the conjugate.

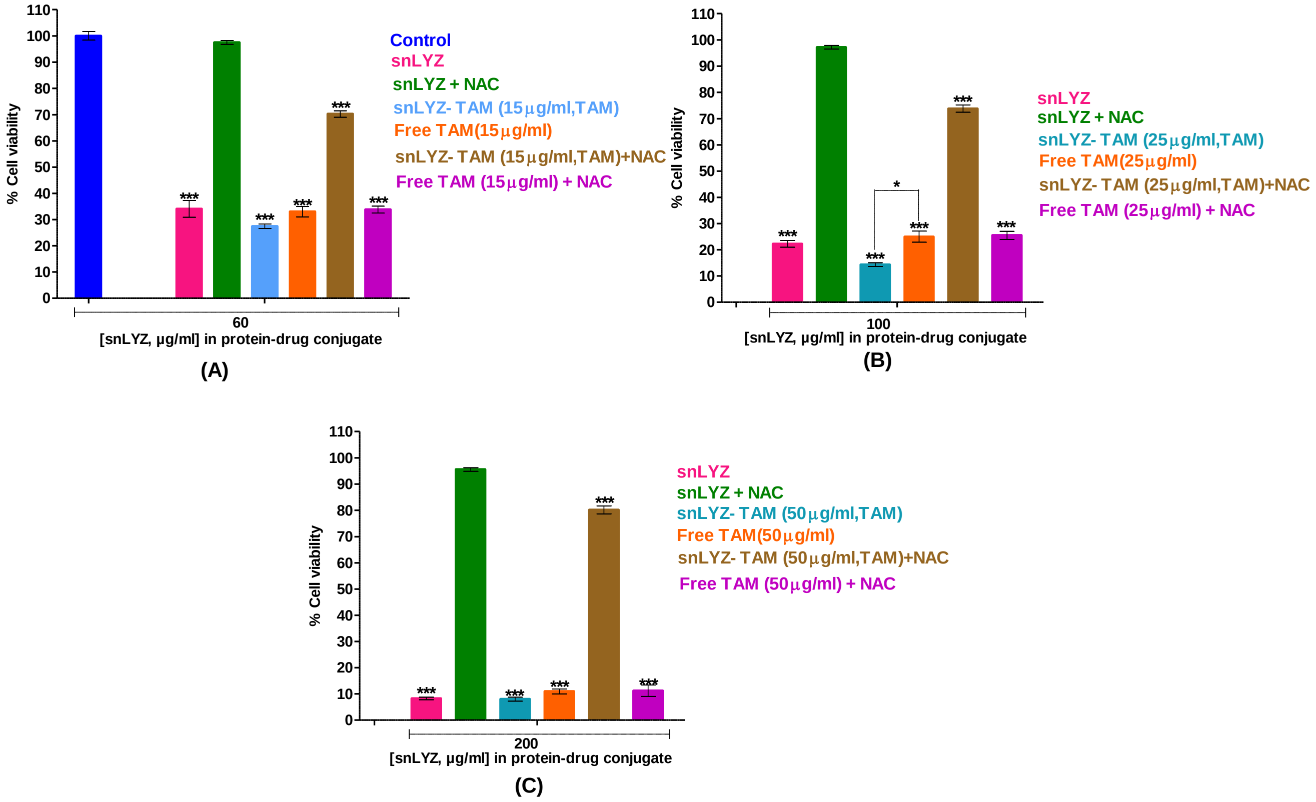

(A)

(B)

(C)

Figure 6.12 Cell viability assay of free TAM, nmLYZ, snLYZ and snLYZ-TAM conjugates in MCF-7 cells. Three different snLYZ concentration (A) 60, (B) 100 and (C) 200 µg/ml along with TAM (15, 25, 50 µg/ml) were used with protein: TAM and maintained at 4:1 ratio. The increased amount of TAM in the conjugate increased the cytotoxicity in MCF-7 cancer cells. Statistically significant vs control group, ***p< 0.001,*p<0.05 by One way ANOVA and post Tukey test. All data are expressed as Mean ± S.E.M, n = 3.

Fig. 6.12 A clearly demonstrated that at lower concentration of snLYZ (60 µg/ml) in snLYZ-TAM, the conjugate produced a better cell killing effect (72.55%) than the free snLYZ (64.91%). With the increase of snLYZ amount in conjugate (from 60 to 100 µg/ml), the snLYZ-TAM demonstrated better cytotoxicity (85.64%) compared to free snLYZ (75%) (see Fig.6.12 B). However, at snLYZ concentration of 200 µg/ml (Fig. 6.12 C) in conjugate (where 50µg/ml TAM was used), the cell killing effect from both free snLYZ (91.73%) and snLYZ-TAM (91.99%) conjugate was found almost equal.

NAC was incorporated in the media in order to validate the ROS mediated cell death. The presence of NAC reduced the cytotoxicity of all the formulations of snLYZ-TAM conjugate leading to the conclusion that the cytotoxicity of snLYZ-TAM was predominantly ROS based (Fig. 6.12).

Further, we also assessed the cytotoxicity of reconstituted snLYZ in MCF-7 cells and compared with other formulations of snLYZ-TAM (see Fig. 6.13).

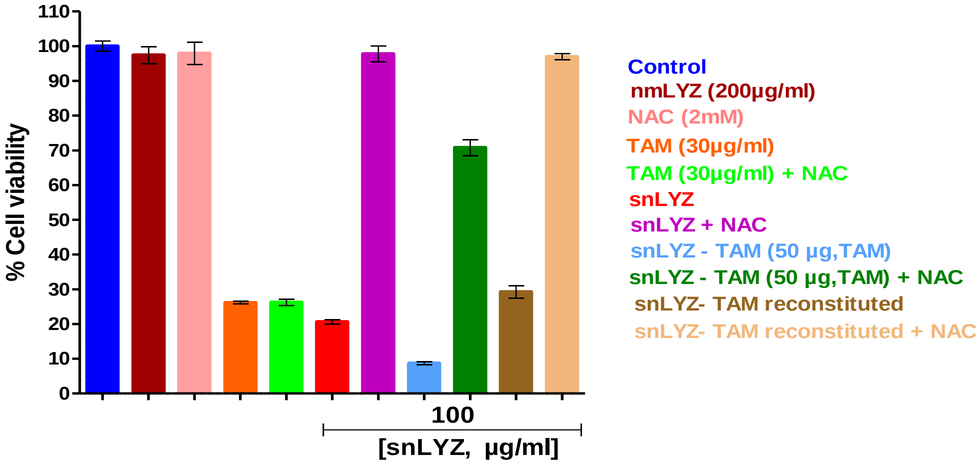

Figure 6.13 Effect of reconstituted samples of snLYZ on the cell viability of MCF-7 cells and comparison of their cytotoxic effect with other formulations. The presence of NAC reversed the cytotoxicity of snLYZ in cancer cells, however, in case of

snLYZ-TAM it was however, in case of snLYZ-TAM it was observed to be partially reversed. All the data are expressed as Mean ± S.E.M, n = 3.

From Fig.6.4 the non-cumulative drug release at pH 6 was found to be 64.82%. The post-drug release state of snLYZ-TAM is referred to as ‘reconstituted snLYZ’. We applied snLYZ-TAM conjugate where 100 µg/ml of snLYZ and 50 µg/ml of TAM (2:1, protein: drug) conjugated, to MCF-7 cells. The reason of using 2:1 ratio was to see the effect of higher TAM on cell killing in the formulation and to see the effect of reconstituted snLYZ. Since, the non-cumulative drug release is around 60 % at pH 6.0, we calculated a release of 60% from 50 µg of loaded TAM i.e. 30µg. Hence, 30 µg/ml of TAM was kept as control (see Fig.6.13).

We observed that snLYZ-TAM conjugate demonstrated better cytotoxicity (91.29%) compared to snLYZ (79.39%) alone (Fig. 6.13). In the presence of NAC the cytotoxicity was reduced to only 29.22%.This fact clearly indicated that snLYZ had a major contribution (~62%) in the toxicity generated by snLYZ-TAM as TAM did not mediate ROS generation, while snLYZ solely generated ROS. However, since complete inhibition of cytotoxicity was not observed, a smaller (29%) contribution of TAM in the cytotoxicity produced by snLYZ-TAM cannot be ruled out.

The results further showed that the ‘reconstituted snLYZ’ demonstrated comparable level of cytotoxic effect (29.22%) as like free TAM (26.16%), however with completely ROS-based mechanism as reflected from Fig 6.13. It is interesting to note that ‘reconstituted snLYZ’ produces similar levels of cytotoxicity with less amount of residual drug (10.5 µg/ml, ~ 35% drug retained) compared to free TAM (30 µg/ml). The reason was the crosslinked TAM molecules which were unreleased in the reconstituted snLYZ and hence, could not show the cytotoxic effect.

The fact indicated, residual TAM molecules in 'reconstituted snLYZ' had little contribution in cell killing compared to snLYZ in snLYZ-TAM and hence, the majority of the cytotoxic effect was due to the sole contribution of snLYZ.

6.2.6 snBLA-TAM based design of various formulations

We have already demonstrated increased cytotoxicity of snBLA nanoassembly in breast cancer cells. snBLA has already shown excellent drug release properties at acidic pH, however, TAM has potential toxicity problems at high doses. Therefore, we designed various low dose formulations of snBLA:TAM (1:1, 4:1 and 10:1 w/w ratio) for finding possible synergistic effect against breast cancer cells. The objective was to prepare a formulation with least hemolytic activity and enhanced cytotoxicity in cancer cells.

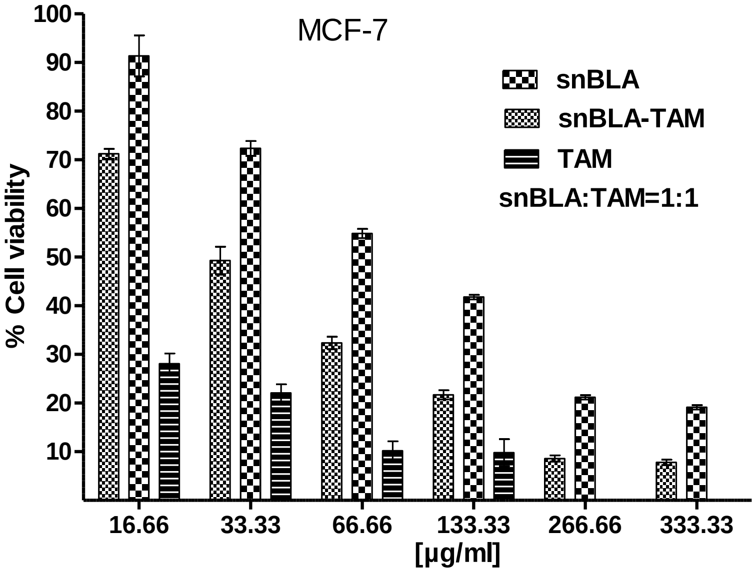

Figure 6.14 MTT based cell viability assay of snBLA, snBLA-TAM and TAM in MCF-7 cells at 24 h post administration. The ratio of snBLA: TAM used is 1:1 (w/w). The loading of the drug TAM in snLYZ increased the cytotoxicity at all doses. All data are expressed as Mean ± S.E.M, n = 3.

When we examined the cytotoxicity of snBLA-TAM (1:1) in MCF-7 cells, we observed increased toxicity at all doses of snBLA-TAM (1:1) compared to drug free snBLA (see Fig.6.14). This improved cytotoxic profile which may be due to the incorporation of low doses of TAM in the formulation snBLA-TAM (1:1) that probably acted in a synergistic manner along with snBLA.

Further, since the drug TAM was released at an acidic pH, snBLA-TAM (1:1) might have released the fair amount of drug in the acidic environment of the cancer cells. TAM was released in the acidic environment of cancer cells which contributed to the toxicity. This process was followed by the toxic effect produced by snBLA in cancer cells. Contribution of both TAM and snBLA mediated cytotoxicity may be the reason behind the overall increase in the toxicity.

In order to observe the change of cytotoxic effect by varying the drug loading in snBLA, we prepared three different formulation of ‘snBLA-TAM’ containing various ratios of protein to drug ratio such as 1:1, 4:1 and 10:1. We found that all formulations of snBLA-TAM (1:1, 4:1 and 10:1) exhibited higher cytotoxicity than snBLA alone (see Fig. 6.15).

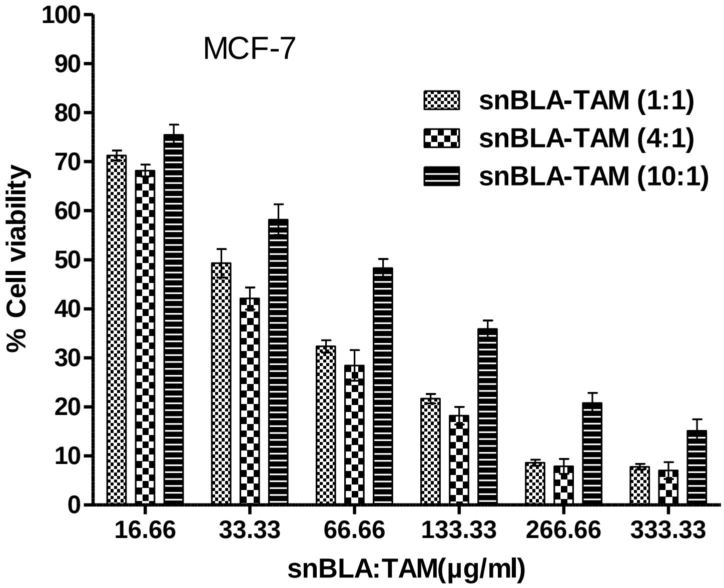

Figure 6.15 MTT based cell viability assay of various formulations of snBLA-TAM in MCF-7 cells at 24 h post administration. snBLA-TAM formulations having snBLA: TAM ratios of 1:1, 4:1 and 10:1 were administered in MCF-7 cells. snBLA-TAM (4:1) maximum cytotoxic effect. All data are expressed as Mean ± S.E.M, n = 3.

Moreover, we observed highest cell killing potential induced by snBLA-TAM (4:1) that demonstrated more than 90 % cancer cell death of MCF-7 cells at 24 h at a snBLA concentration of 333.33 µg/ml (see Fig.6.15).

The increase in cell killing activity must have generated from the drug, TAM in the formulation. The cell killing activity of snBLA-TAM (4:1) formulation showed higher toxicity than the formulation of snBLA-TAM (1:1). To understand the reason, we examined the cytotoxicity of the post-drug release state (reconstituted state) of each formulation.

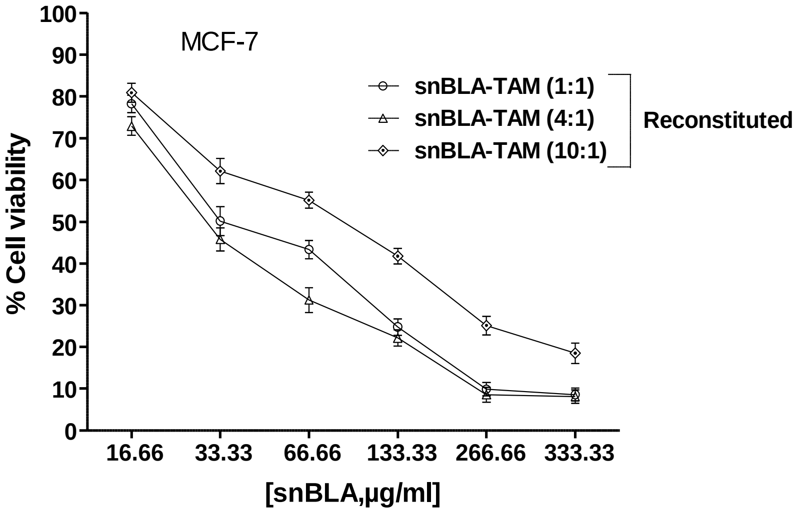

Figure 6.16 MTT based cell viability assay of various reconstituted forms of snBLA-TAM in MCF-7 breast cancer cells. The various ratios of the snBLA: TAM used were 1:1, 4:1 and 10:1 (w/w). The reconstituted snBLA-TAM (4:1) demonstrated maximum cytotoxic effect. All data are expressed as Mean ± S.E.M, n = 3.

From Fig 6.16 we observed that the ‘reconstituted snBLA’ having the snBLA:TAM ratio of 4:1 exhibited highest cytotoxicity in MCF-7 cells, followed by 1:1 and 10:1. The result clearly showed that the same amount of snBLA used with three different amount of TAM, the ‘reconstituted snBLA’ formulation and with optimal amount of snBLA in the ‘reconstituted snBLA’ (4:1) could generate highest cytotoxicity in MCF-7 breast cancer cells. Since, both protein assembly as well as chemotherapeutic drug were used in the formulation and both pre and post-drug release state was examined for evaluating the cytotoxicity in cancer cells, further assessment on the cell death mechanism should be performed.

6.2.7 Mechanism of cytotoxicity of reconstituted snBLA

We found that the ‘reconstituted snBLA’ (4:1) (Fig 6.16) demonstrated highest cytotoxic effect in MCF-7 cancer cells (more than 90% cell death). To understand the mechanism of cell death by various formulations of snBLA-TAM and their reconstituted state, we performed cell viability assay in the presence of NAC (Fig 6.17A and B). NAC is a ROS inhibitor and its administration would inhibit cell death due to ROS effect.

We observed that with the increase of loaded TAM amount, the ROS contribution towards cell death was reduced, indicated TAM contribution that was not mediated by ROS. Since, TAM was present on the surface of snBLA, the contribution of ROS generated by snBLA will be minimal in snBLA-TAM compared to snBLA alone where the surface is exposed to generate ROS in cancer cells.

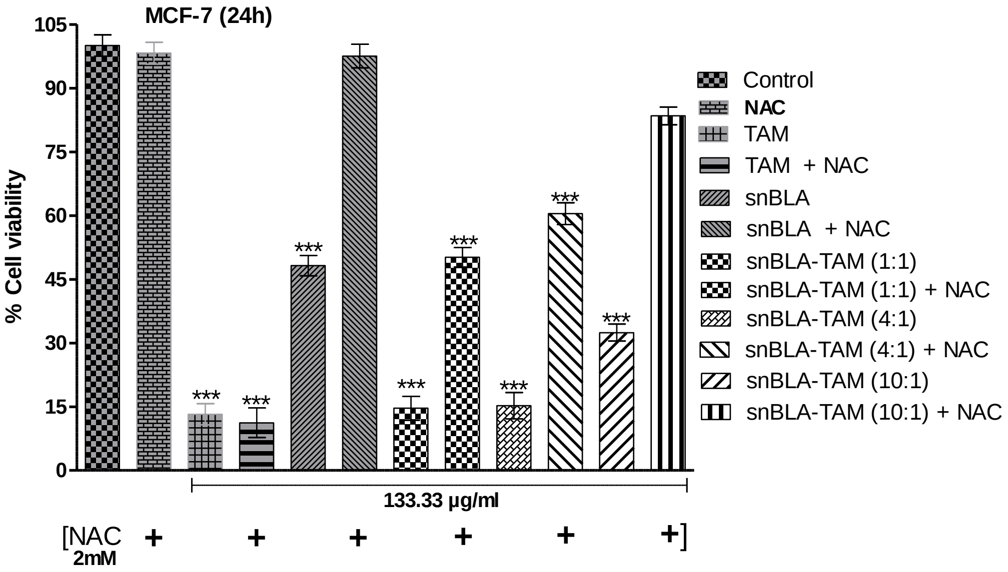

(A)

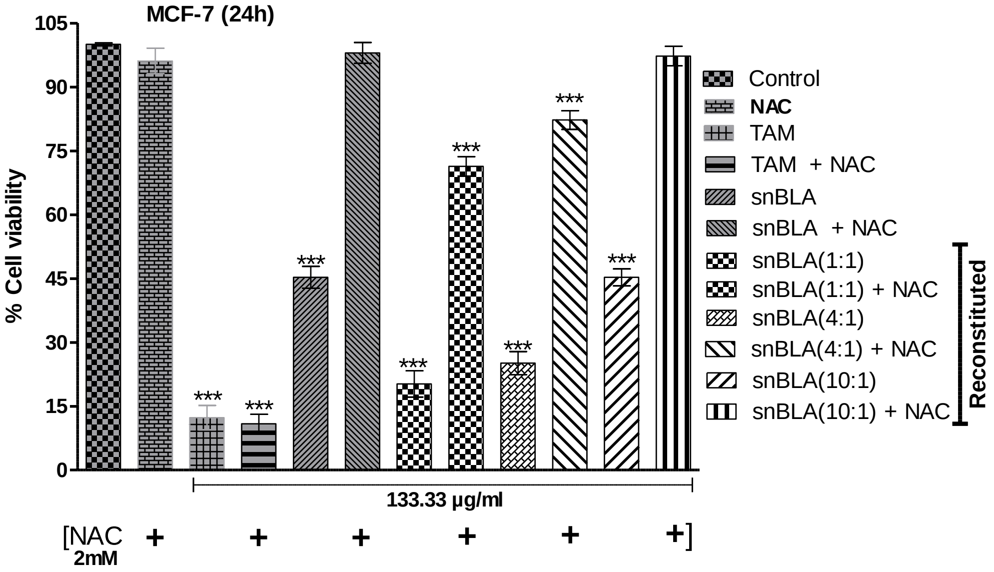

(B)

Figure 6.17 MTT assay based assessment of ROS mediated cell killing induced by various formulations of snBLA. (A) snBLA:TAM (1:1, 4:1 and 10:1). (B) Reconstituted snBLA (1:1, 4:1 and 10:1). The reconstituted snBLA demonstrated to snBLA alone. Statistically significant vs control group, ***p< 0.001 by One way ANOVA and post Tukey test. All data are expressed as Mean ± S.E.M, n = 3.

However, in ‘reconstituted snBLA’ where 40% TAM was still retained but cannot be released, ROS-based death was found predominant (Fig. 6.15B), indicated the death caused by snBLA (reconstituted). Thus, we proved that snBLA-TAM (4:1) was the best formulation among all. Further we also wanted to evaluate its hemocompatibility in human erythrocytes. When we examined the effect of reconstituted snBLA in human erythrocytes, the reconstituted formulations did not show any hemolytic activity (see Supplementary Fig.S9), which proved its hemocompatibility.

Such fact collectively confirmed a unique multifaceted character of snBLA which exhibited lethal activity against cancer, however turns inactive in snBLA-TAM conjugate (as evidenced from Fig. 6.17A), and regains its cytotoxic activity in cancer cells in its reconstituted state (Fig. 6.17B). Therefore, such nanomaterials can be used both as therapeutic agent as well as drug delivery system simultaneously which can exhibit a highly efficient protein based therapeutic strategy in breast cancer.

Chapter 7

Preparation and Characterization of GOns and BLA functionalized GOns

7.1 Materials and Methods

7.1.1 Materials

Citric acid, bovine α-lactalbumin, glutaraldehyde (GTD, 25%), N-acetyl-L-cysteine (NAC) and fluorescein diacetate were purchased from Sigma-Aldrich, India. MTT [3-(4,5-Dimethylthiazol-2-yl)-2,5-Diphenyltetrazolium Bromide] assay kit, DMEM, fetal bovine serum, (FBS), DAPI, acridine orange,1-anilino napthalene-8-sulfonic acid (ANS), ethanol, sodium cacodylate, sodium hydroxide, ethanol, hydrochloric acid and sodium phosphate buffer were purchased from HiMedia India Pvt. Ltd. We used HPLC grade water in all the experiments. All other reagents were of analytical grade. All glassware used in the present study was purchased from Borosil, India.

7.1.2 Methods

7.1.2.1 Preparation of graphene oxide nanosheets (GOns) by pyrolysis of citric acid

GOns was prepared directly by the pyrolysis of citric acid (CA) as described by Dong et al. (Dong et al., 2012), however with a little modification. Briefly, 2g CA was added into a 5ml test tube and heated at 200 ^{0}C using a microwave oven. About 5 min later, the CA attained a pale yellow liquid state and then to orange in 30 min. After 2 h, a black solid mass was formed. The black solid mass was dissolved in 50 ml of 10 mg/ml NaOH solution kept under constant sonication. The pH of the solution was adjusted to 7.4 by the addition of HCl (1M). The solution was sonicated for 10 min before use.

7.1.2.2 Preparation of BLA functionalized GOns (FGOns)

FGOns was prepared with slight modification of the protocol described by Arroyo-Maya et al (Arroyo-Maya et al., 2012). A volume of two ml of 2 mg/ml aqueous solution of BLA was stirred at 500 rpm using a magnetic stirrer at room temperature for 10 min followed by addition of 8 ml ethanol (desolvating agent) gradually at the rate of 0.5 ml/min. After desolvation, GOns was immediately added at equivalent concentrations of protein followed by the addition of glutaraldehyde to a final concentration of 0.1% and stirred continuously (500 rpm) at room temperature for 8 h. The prepared nanoconjugate was purified by 3 cycles of centrifugation at 20,000 g for 30 min. Finally, the pellet was resuspended in 2 ml of deionized water. Field Emission Scanning Electron Microscope (FESEM) was used to determine the shape and morphology of the prepared FGOns.

7.1.2.3 Preparation of acridine orange conjugated GOns and FGOns for observing the cellular uptake in cancer cells.

The samples of GOns and FGOns are stirred in a solution containing acridine orange (20 µg/ml) respectively. Glutaraldehyde (GTD) was added to a final concentration of 0.1% in both the solutions. Both the solutions were stirred for 4 h for the complete cross-linking process. At the end the samples were centrifuged at 20,000g for 20 min. The pellet was washed with Milli Q water. The centrifugation process was repeated four times for removing the residual GTD. The pellet containing GOns-acridine orange and FGOns-acridine orange were resuspended in Milli-Q water for further use.

7.1.2.3.4 Characterization of GOns and FGOns

UV-Visible spectroscopic measurement was taken using10µg/ml of GOns solution in the wavelength range of 200-800nm. Using the excitation maxima from the UV-Visible spectroscopy, fluorescence emission spectra were obtained using the same concentration of GOns in the range of 240-500 nm. The excitation and emission slit width were used at 10nm. The photoluminescence spectra of GOns were analyzed by exciting GOns from 300-500 nm keeping the slit width for excitation and emission at 10 nm.

7.1.2.3.4.1 Electron Microscope analysis

High-resolution microscopic images of various samples were captured using Field emission scanning electron microscope (FESEM, NOVA NANO SEM 450). A volume of 10 µl of GOns and FGOns (1 mg/ml) was spread on a glass slide and dried in a desiccator. The glass slides with GOns and FGOns were fixed on a carbon-coated tape attached to the aluminium stub, after drying. The aluminium stub was placed in a gold sputtering unit for 30 s. The samples were subsequently placed in the FESEM (NOVA NANO SEM 450) sample chamber, and images were captured at a voltage of 5 kV.

7.1.2.3.4.2 Atomic Force Microscopy

AFM imaging was carried out using a Bioscope Catalyst AFM (Bruker Corporation, Billerica, MA). GOns (10 µl of 1 mg/ml stock) was placed on a fresh mica sheet and dried under continuous flow of N_2 gas. The mica sheets were gently washed with Milli-Q water. The mica sheets were dried in a desiccator overnight. The standard tapping mode was used for capturing the images of different samples. The nominal spring constant of the cantilever used was 20-80 N/m, and a scan rate of 0.5 Hz with 512 samples per line was used for imaging the samples.

7.1.2.3.4.3 X-ray diffraction (XRD) and Raman spectra analysis

XRD of GOns was analyzed by Rigaku made X-ray diffractometer with monochromatic CuKα, radiation (λ=1.5406 Å). Data were collected from 5° to 40° at a scan rate of 0.1° min-1. Raman spectra of GOns was recorded by a micro Raman setup equipped with an air cooled Ar^+ laser (model 177-G1205, Spectra Physics, USA) at λ=532 nm laser power (1.7 mW), 50 x objective lens, 0.9 NA, as the excitation light source, a single monochromator (TRIAX 550, JY, France), and a CCD detector. Experiments were performed at 25ºC.

7.1.2.3.4.4 DLS particle size and zeta-potential analysis

The average particle size analysis and ζ-potential measurement of the aqueous suspensions of GOns and FGOns were performed in a Malvern Zetasizer Nano-ZS dynamic light scattering (DLS) analyzer. GOns (10 µl of 1 mg/ml stock) and FGOns were taken separately, each was diluted with 1990µl of deionized water, and applied to DLS for size analysis.

7.1.2.3.4.5 Fourier Transform Infra-red (IR) spectroscopy

The spectra were recorded using the ALPHA-FT-IR (BRUKER) spectrometer equipped with ATR accessory. A sample volume of 100 µl of native BLA, GOns and FGOns were used for analysis. The samples were analyzed at pH 7.0 in ATR mode. The spectral range was used between 4000 $cm^{-1}$and 500 cm^{-1} with a resolution of 2 cm^{-1} and 25 scans per spectrum.

7.1.2.3.4.6 Circular Dichroism (CD) and fluorescence measurement

CD spectra of FGOns (GOns:BLA is 1:1 w/w %) was measured using a JASCO, Model J-1500 polarimeter with BLA as control. The solution was incubated for 1 h in 20 mM sodium cacodylate buffer, pH 7.4. All the measurements were carried out at room temperature (25ºC) under a constant flow of N_2. Each spectrum depicted the average of three accumulations recorded between wavelengths of 200 and 250 nm, with a 0.2 nm resolution, a bandwidth of 1.0 nm, a scan speed of 100 nm/min and a cuvette of path length of 0.1 cm.

The buffer contribution was subtracted from each measurement. The CD spectrum was reported in mdeg (obtained from the instrument). The percentage of secondary structural components (α-helix, β-sheet and random coil) were calculated using the software provided along with the instrument.

For fluorescence spectroscopy measurement, 20 mM sodium phosphate buffer at pH 7.4 was used. The change in the fluorescence spectra of BLA samples was measured after 1h of incubation using a Perkin-Elmer LS-55 Luminescence Spectrometer at 25°C. Excitation wavelength was kept at 290 nm. The tryptophan (Trp) fluorescence spectrum of BLA was recorded in the range of 300 to 400 nm. The excitation and emission slit widths were set at 5 and 10 nm, respectively. Background corrections were made with buffer without protein in all cases.

To examine the surface hydrophobic character of FGOns, we measured protein-bound fluorescence of ANS. ANS is an anionic fluorescence dye that readily interacts with the hydrophobic residues of proteins and exhibits increased fluorescence. Hence, a higher amount of ANS bound fluorescence is a measure of the increase in surface hydrophobicity of the protein. Before measurement, the samples were incubated with ANS for 1 h. The samples were excited at 350 nm, and the ANS fluorescence was measured in the range of 400 to 700 nm. The excitation and emission slit width were kept at 10 nm.

7.5 Results and Discussion

7.5.1 Synthesis of GOns and functionalized GOns (FGOns)

GOns was prepared by controlled pyrolysis of citric acid. The different stages of GOns production were shown in Fig. 7.1A. FGOns was prepared by crosslinking of BLA with GOns using 0.1% glutaraldehyde (GTD). The different stages involving the preparation of GOns and FGOns are shown in Fig. 7.1B.

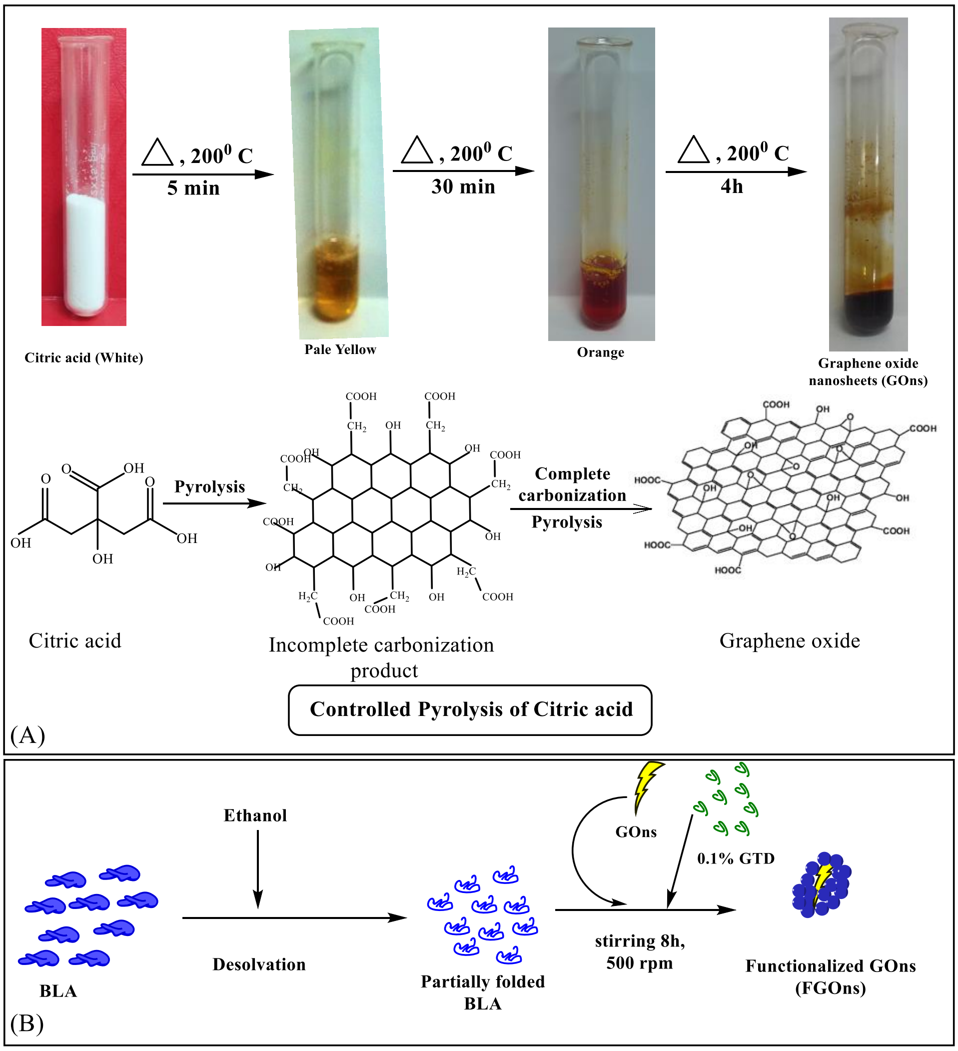

Figure 7.1 Different steps in the preparation of (A) graphene oxide nanosheets (GOns) using controlled pyrolysis of citric acid. (B) GOns functionalization method.

7.5.2 Preparation of Acridine orange conjugated GOns and FGOns for observing the cellular uptake in cancer cells.

The acridine orange conjugated GOns and FGOns were prepared as per the protocol mentioned in the "Materials and Methods section". Acridine orange will add orange fluorescence to the GOns/FGOns-acridine orange conjugates and the fluorescence can be visually observed very easily using the fluorescent microscope and confocal microscope.

7.5.3 UV absorbance, photoluminescence and fluorescence spectroscopy

The UV-Vis spectroscopic measurement clearly revealed (Fig. 7.2A) a broad peak at 230 nm that corresponds to the π- π^* plasmon peak. The optical absorption of GOns is mainly dominated by the π- π^* plasmon peak near 230 nm (Eda et al., 2010). A characteristic shoulder peak, which is usually present in the GOns spectra, was not identified in our results (see Fig.7.2A).

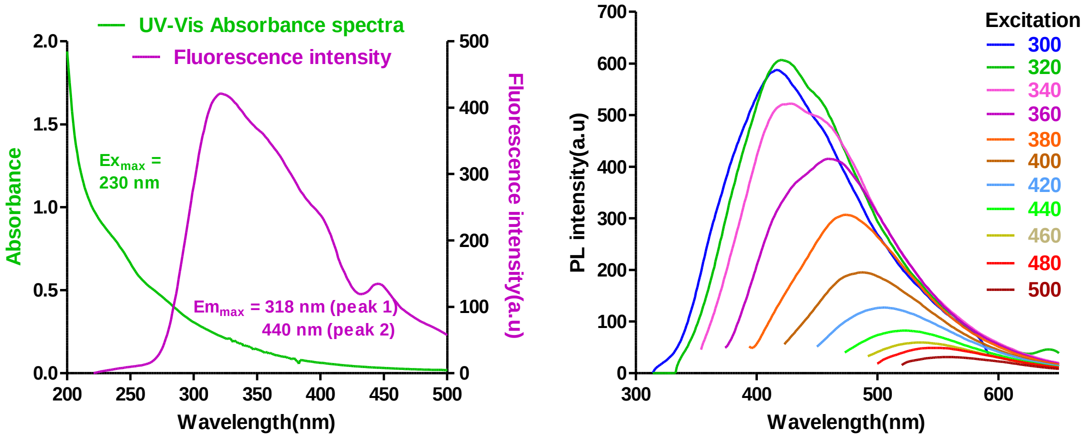

(A) (B)

Figure 7.2 Characterization of GOns based on UV-Vis and fluorescence spectroscopy (A) UV-Vis absorption and fluorescence spectra of GOns synthesized using controlled pyrolysis of citric acid. Both excitation and emission slit widths for fluorescence spectroscopy measurement was used as 10 nm each. (B) The photoluminescence spectra of GOns at various excitation wavelengths. All data are expressed as mean of three readouts generated from the instrument.

This broadening of the peak at 230 nm and unidentifiable shoulder peak at 310 nm was mainly due to the formation of multi-layered GOns (Lai et al., 2012). The peak of GOns is normally sharp and prominent at 230 nm for single layered GOns, however, in our case, the GOns is 5 layer thick (Fig.7.3B) and hence a broad peak is obtained. The fluorescence spectrum was also obtained by exciting GOns at 230 nm. The fluorescence emission spectra shows the presence of two peaks at 318 and 440 nm (see Fig.7.2A) that are the characteristic fluorescence emission peaks of GOns (Kozawa et al., 2013). The peaks observed close to 318 nm and 440 nm are not sharp and due to the formation of multilayered (05 layers) GOns (see Fig7.3B). Fig. 7.2 B shows the characteristic photo-luminescence spectra of GOns at various excitation wavelengths.

7.5.4 AFM, FESEM imaging, XRD, Raman scattering DLS size distribution and zeta-potential measurement

AFM results shown in Fig.7.3A revealed that the width of GOns was in the range of 100-200 nm with an average height of 5.0 nm (Fig.7.3B) that is equivalent to almost a stack of five layers of single-layered GOns (Lai et al., 2012). The inset showed the height and 3D morphology of GOns.

The AFM image shows the irregular shape of GOns with sharp edges. The fact was also supported by the FESEM images where we can easily see the sharp edges of GOns (see Fig.7.4A).

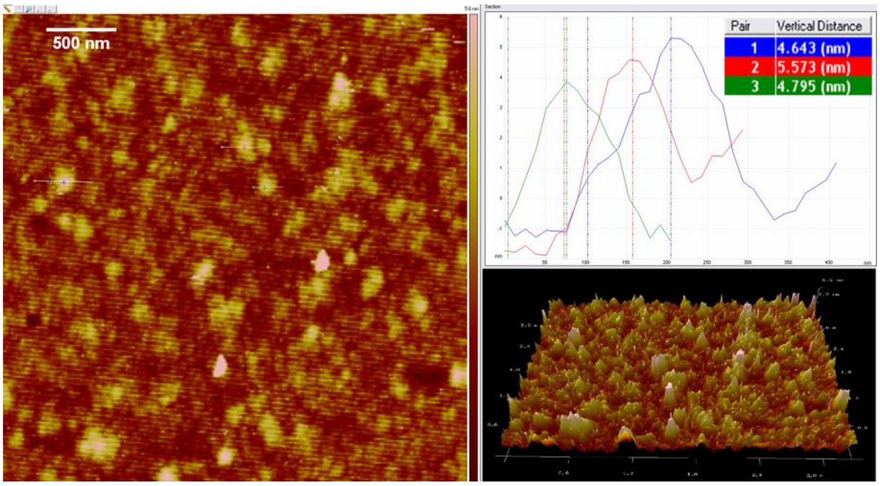

(A) (B)

Figure 7.3 Characterization of GO nanosheet (GOns) by AFM imaging. (A) AFM image of GOns. (B) 3D surface morphology of GO nanosheets.

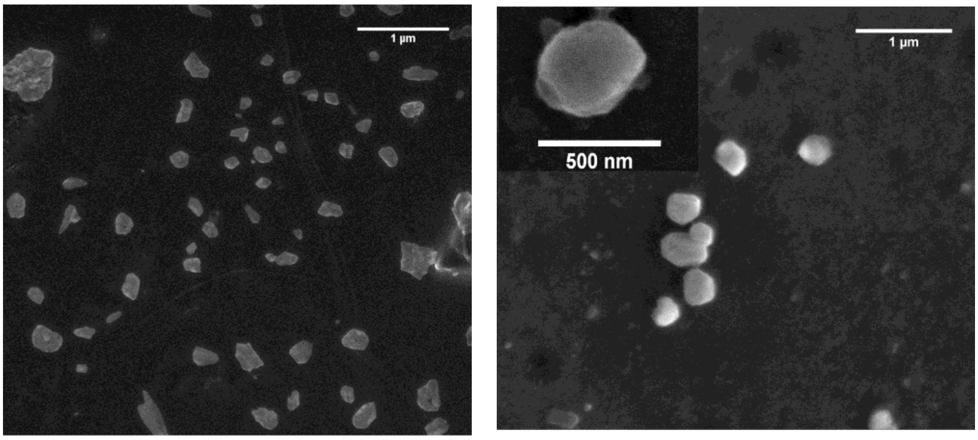

(A) (B)

Figure 7.4 Characterization of GO nanosheet (GOns) by FESEM imaging. (A) FESEM image of GO sheet. (B) FESEM images of functionalized GOns (FGOns) inset shows the magnified image of FGOns.

The FESEM images of GOns (Fig.7.4 A) and FGOns (Fig.7.4 B) also confirmed the nanosheet formation with sharp edges of GOns and smooth edges of FGOns.

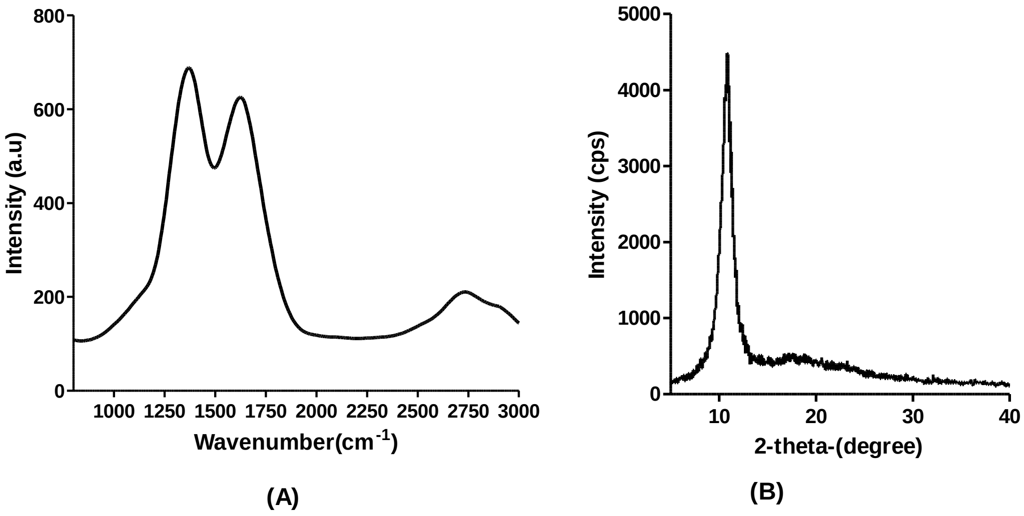

Figure 7.5 Characterization of GO nanosheet (GOns) by (A) Raman spectra of GOns; the G peak at 1580 cm^{-1} and the D peak at 1350 cm^{-1}. (B) XRD analysis of GOns; the sharp diffraction peak for GOns was observed at 2θ = 10.80^0.

Fig.7.5 A shows the typical Raman spectra of GOns. We observed that the G peak was at 1580 cm^{-1} and the D peak at 1350 cm^{-1}. The Fig.7.5 B shows the XRD spectra in which the sharp diffraction peak for GOns was observed at 2θ =10.80°. XRD analysis is an important tool for the identification of different states of GOns. While 2θ ~10° is assigned for the oxidized state of GOns, 2θ ~ 23° is assigned for reduced GOns.

The hydrodynamic size distribution of GOns showed the average particle size of 150 nm in a size range of 122-190 nm (see Fig.7.6 A). However, functionalized GOns (FGOns) showed an average size of 300 nm in a range of 141-458 nm (see Fig.7.6 B).

The size distribution closely matched with results obtained from FESEM and AFM images. In order to understand the stability of GOns and FGOns we measured the zeta potential of both in solution. The zeta potential value of both GOns and FGOns were estimated to be -31.2 mV and -39.6 mV, which indicated their stability in suspension.

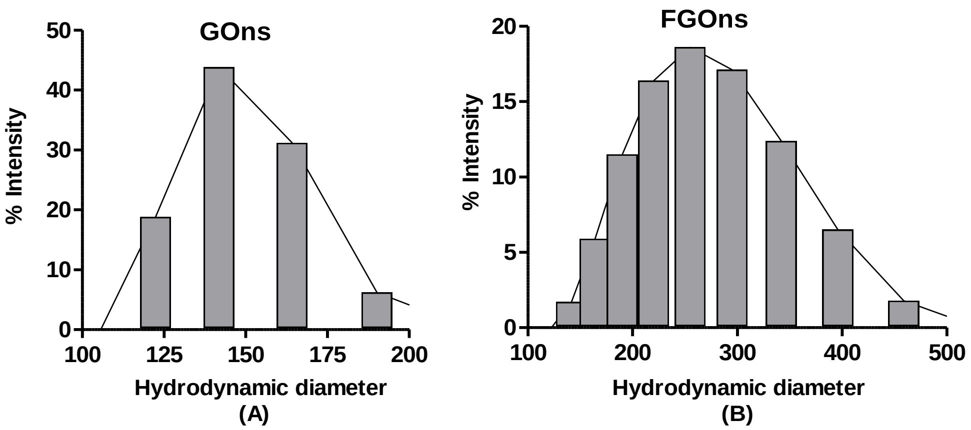

Figure 7.6 Distribution of hydrodynamic diameter analysed by DLS particle size analyser of (A) GOns (122-190 nm), (B) FGOns (141-458 nm).

FESEM images of FGOns clearly showed the formation of smooth edges of GOns (Fig. 7.4 A and B) using BLA coating. It has been already reported that the sharp edges of GOns caused the damage of bacterial membrane (Akhavan and Ghaderi, 2010; Hu et al., 2010). FESEM images of synthesized GOns also showed sharp edges that can damage human cells including erythrocytes using a similar kind of mechanism.

7.5.5 FTIR analysis of GOns and FGOns

FTIR spectra of native BLA, GOns and FGOns were shown in Fig.7.7. The presence of various functional groups containing oxygen were confirmed for GOns at 3477 cm^{-1} (OH stretching vibrations), at 1722 cm^{-1} (stretching vibrations from C=O, carbonyl/carboxy), at 1203 cm^{-1} (stretching vibrations from C-O, epoxy) and at 1042 cm^{-1} (C-O stretching vibration, alkoxy) (Xu et al., 2008). In addition to these peaks, C-O stretching vibration (1388 cm^{-1}, carboxy) was also observed.

Native BLA (Fig. 7.7) showed the presence of characteristic peaks of Amide I and Amide II that typically exist in proteins. These peaks arise from the amide bonds that act as a link between the amino acids.

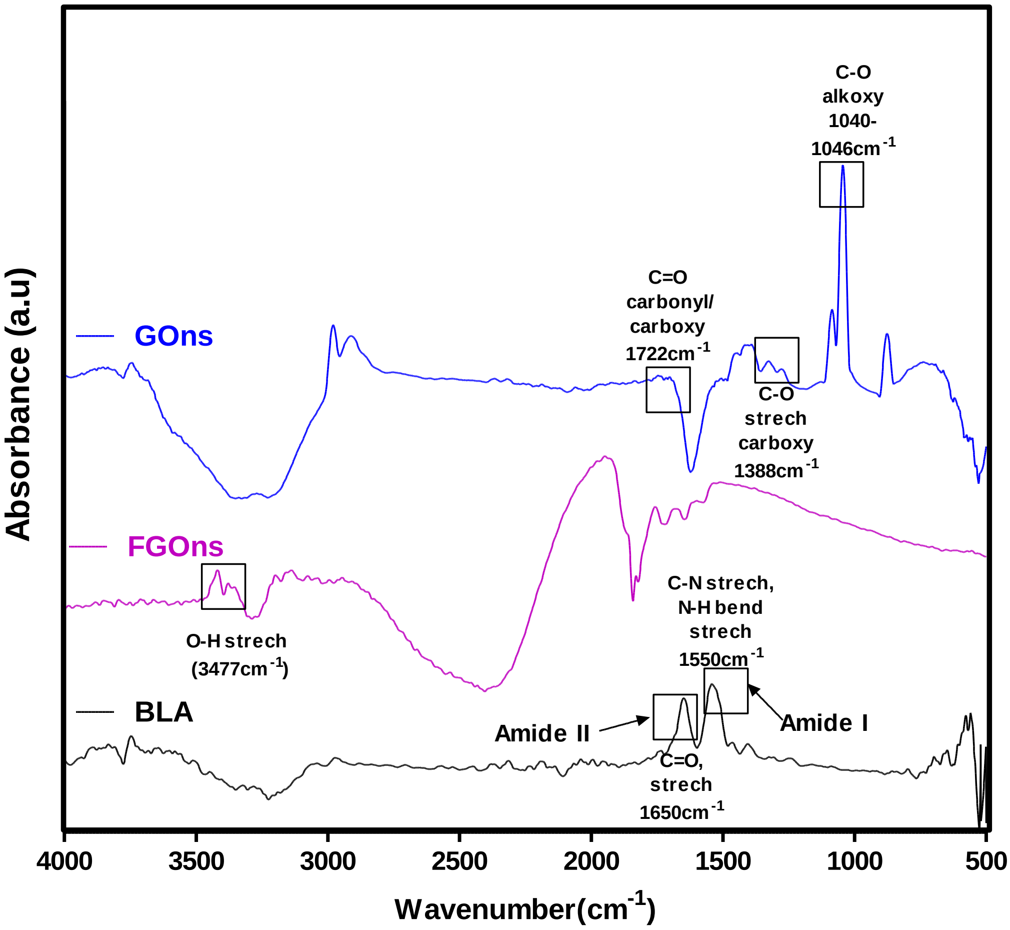

Figure 7.7 FTIR analysis based characterization of GOns, BLA and FGOns (BLA cross-linked GOns). The characteristics peaks for GOns, BLA and FGOns are observed.

The Amide I signal produced due to mainly stretching vibrations of the C=O bond and C-N bond while Amide II band arose due to the bending vibrations of the N-H bond and fewer contributions coming from C-N and C-C stretching vibrations. O-H stretching vibration was also observed at 3464 cm^{-1}. FGOns sample upon analysis, revealed the loss of characteristic peaks of Amide I and Amide II along with the loss of O-H stretching vibration (Fig.7.7). Comparing GOs and FGOns we observe that upon functionalization peaks for C-O (alkoxy, 1040-1046cm^{-1}) and C-O stretch (carboxy, 1388cm^{-1}) in GOns were missing in GOns possibly due to coating of BLA. Moreover, the loss of Amide I and Amide II peaks in FGOns may be due to the crosslinking with glutaraldehyde.

Other peaks that were retained for GO were at 1046 cm^{-1} (C-O stretching vibration, alkoxy), at 1388 cm^{-1}(carboxy) C-O stretching vibration and at 1722 cm^{-1} (stretching vibrations from C=O, carbonyl/carboxy). The information also confirmed the presence of both BLA and FGOns.

7.5.6 Circular dichroism (CD) and Trp fluorescence spectroscopy of BLA in FGOns

BLA is a small monomeric protein of 14 kDa molecular mass containing four Trp residues and four disulfide bonds (Engel et al., 2002). Therefore, BLA is a suitable candidate to study the conformational change using both CD, as well as fluorescence spectroscopy.

Moreover, four disulfide bonds can provide stability to the structure, which also favours its use to functionalize GOns in biomedical applications. The CD spectra measured at far UV region i.e. 200 to 250 nm clearly showed the secondary structural change of BLA in FGOns (see Fig. 7.8).

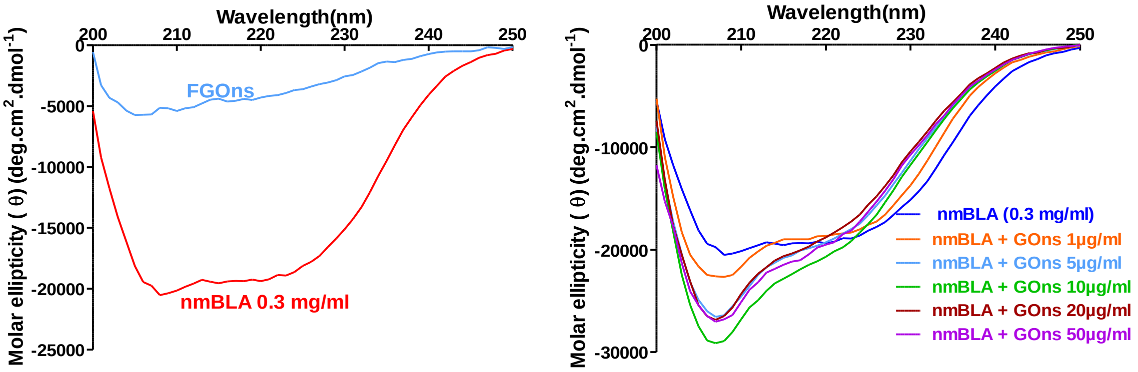

(A) **(B)**

Figure 7.8 Circular Dichroism based spectroscopy of (A) FGOns and (B) interaction of native BLA with GOns. Significant change in secondary structure was observed in FGOns and nmBLA treated with GOns. All data were expressed as the mean of three readouts generated from the instrument.

The α-helix and β-sheet contents were also estimated using the software provided along with the instrument and shown in Table 7.1.

Table 7.1 The change of BLA secondary structural components in FGOns samples measured by CD spectroscopy.

BLA (0.3mg/ml)	**α-helix (%)**	**β-sheet (%)**
BLA	26.5	10.3
BLA in FGOns (BLA: GOns, 1:1, w/w %)	14.4	35.9

Substantial reduction of overall CD signal was observed associated with the gross increase in % of β-sheet (from 10.3 to 35.9%) and decrease in % of α-helix contents of BLA in FGOns (see Table 7.1).

Table 7.2 The change of BLA secondary structural components during interaction with GOns measured by CD spectroscopy.

BLA (0.3 mg/ml)	**α helix (%)**	**β -sheet (%)**
BLA	26.5	10.3
BLA + GOns(1 µg/ml)	20	36
BLA + GOns(5 µg/ml)	13.6	51.1
BLA + GOns(10 µg/ml)	12.8	50.2
BLA + GOns(20 µg/ml)	12.4	51.7
BLA + GOns(50 µg/ml)	11.3	49.9

The increase in β-sheet probably provided higher stability as obtained from zeta potential measurement. To understand the specific conformational change that took place in BLA due to crosslinking with GOns, we also monitored the physical interaction between free BLA and GOns (without GTD) using CD spectroscopy (see Fig. 7.8 B). The experiment revealed the increase in % of β-sheet and decrease in % of α-helix contents (Table 7.2). However, overall CD signal was found higher than free BLA with β-sheet content as high as ~52% at 20 µg/ml of GOns concentration (see Table 7.2). Therefore, CD results concluded that crosslinking of BLA with GOns caused havoc overall structural change of BLA, which was different from the structural change induced to BLA during its physical interaction with GOns.

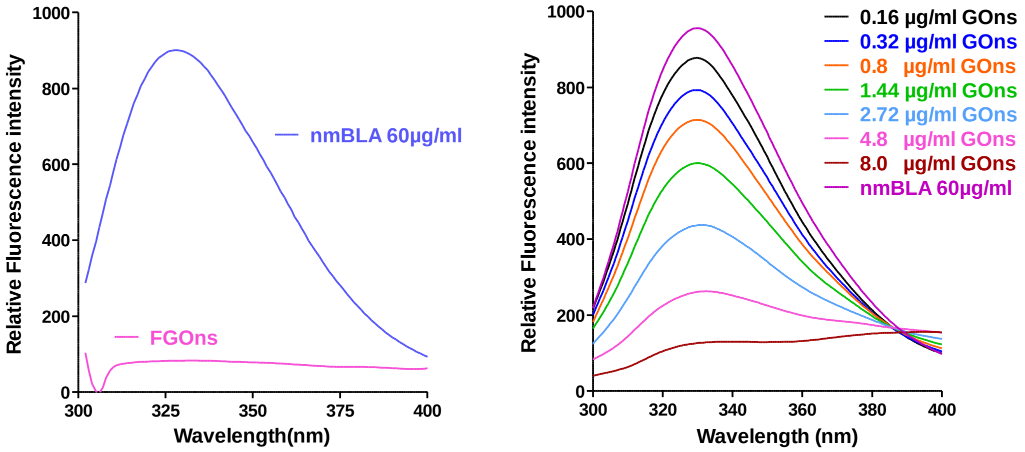

(A) (B)

Figure 7.9 Tryptophan fluorescence measurement of (A) FGOns, and (B) The solution of native BLA with increasing concentrations of GOns. The drop in fluorescence intensity was due to translocation of Trp residues to a more hydrophobic region. All data were expressed as the mean of three readouts generated from the instrument.

The drop in BLA fluorescence in FGOns (Fig.7.9A) and during interaction with increasing of GOns concentration compared to nmBLA also revealed their conformational change (see Fig.7.9 B) around the Trp residues.

Such a decrease in the Trp fluorescence may be attributed to the translocation of the Trp residues on the surface of the protein to an environment having more polar residues which quenches the fluorescence. As the Trp fluorescence is directly contributed from the Trp residues present on the surface of the protein any increase in the number of Trp residues present on the surface of the protein may result in the quenching of the Trp fluorescence intensity.

However, in Fig.7.9 B, no peak shift of the spectra was observed, indicating BLA fluorescence was quenched by GOns. In fact, it has already been reported that GOns is a universal quencher, and it interacts with proteins through static as well as dynamic quenching (Li et al., 2012).

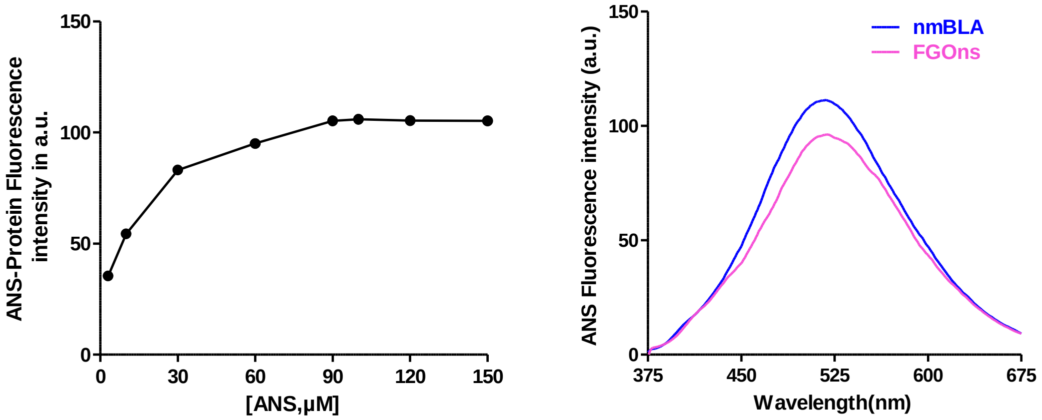

(A)

(B)

Figure 7.10 (A) Optimization of ANS concentration for fluorescence spectra of native BLA, and FGOns, and (B) Protein bound ANS fluorescence spectra of native BLA and FGOns. Small drop in surface hydrophobicity was observed in case of FGOns. All data were expressed as the mean of three readouts generated from the instrument.

To understand the surface hydrophobic character of FGOns, extrinsic fluorescence using 1-anilino napthalene-8-sulfonic acid (ANS) was also performed. The optimized concentration of ANS was determined to be 90 µM (see Fig. 7.10A) which exhibited maximum fluorescence. Fig. 7.10B clearly showed that protein-bound ANS fluorescence intensity was reduced for FGOns compared to free BLA,which revealed that the surface hydrophobicity of FGOns was slightly less than the same amount of free BLA. This information also proved that the BLA functionalization of GOns conferred FGOns with increased water dispersibility. Therefore, collectively it can be concluded that crosslinking of BLA with GOns during the preparation of FGOns induced gross overall structural change of the protein.

Chapter 8

Preparation and Characterization of ZnO nanoparticles and their functionalization with BLA

8.1 Materials and Methods

8.1.1 Materials

Bovine α lactalbumin (BLA), Glutaraldehyde (GTD, 25%) and Zinc nitrate hexahydrate were purchased from Sigma-Aldrich, India. Ethanol, Sodium cacodylate, sodium hydroxide and sodium phosphate buffer were purchased from HiMedia India Pvt. Ltd. We used Milli-Q water in all the experiments. All other reagents were of analytical grade. All glassware used in the present study was purchased from Borosil, India.

8.1.2 Methods

8.1.2.1 Preparation of ZnO (ZnONP):

ZnONP was synthesized from zinc nitrate hexahydrate by wet chemical method with slight modifications (Nair et al., 2009). Zinc Nitrate hexahydrate (10mM) was sonicated in water to obtain a clear solution. NaOH (20mM) was added dropwise to the zinc nitrate solution with continuous stirring for 4-5 h. The precipitate formed was centrifuged at 10000 g for 10 min, washed three to four times, and collected after drying at 80^0C. The ZnONP was diluted to the desired concentration and sonicated for 15 min at 100Hz before use. Although many expensive ZnONP are commercially available, however the detailed synthesis protocol are not available which is one of the major limitations of using the commercially available forms of ZnONP. Moreover, ZnONP upon prolonged storage in powdered form suffers from caking effect which results in the cake formation in the containers. Hence, we synthesized ZnONP using low-cost chemical synthesis method with slight modifications

8.1.2.2 Preparation of Bovine α-lactalbumin conjugated ZnO nanoparticles i.e., Functionalized Zinc oxide nanoparticles (FZnONP):

For the preparation of FZnONP, 4 mg of BLA was dissolved, in 2ml of deionised water. The solution was stirred for 5min at 500 rpm followed by addition of ethanol (8ml) dropwise with constant stirring. Immediately 4 mg of ZnONP was added followed by addition of glutaraldehyde (final concentration 0.1%).

The contents were constantly stirred for 8 h at 500rpm. The solution was subjected to five cycles of centrifugation at 25000g for 30 min. The pellet formed was redispersed in 1ml of deionised water and stored at 4^0C for further use.

8.1.2.3 Characterization of ZnONP and FZnONP by FESEM analysis

High-resolution microscopic images of ZnONP and FZnONP, were captured using Field emission scanning electron microscope (NOVA NANO SEM 450). A volume of 10µl of ZnONP and FZnONP (1 mg/ml) was spread on a glass slide and dried in a desiccator. After drying, the glass slides with ZnONP and FZnONP were fixed on a carbon-coated tape attached to the aluminium stub. The aluminium stub was placed in a gold sputtering unit for 30 sec. The samples were placed in the instrument sample chamber, and images were captured at a voltage of 5 kV.

8.1.2.3.1 DLS particle size analysis and zeta-potential analysis

The average particle size analysis and ζ-potential measurement of the aqueous suspensions of ZnONP and FZnONP were performed in a Malvern Zetasizer Nano-ZS dynamic light scattering (DLS) analyzer. Ten microlitres of ZnONP and FZnONP was added with 1990µl of deionized water, and analysed for size analysis.

8.1.2.3.2 FTIR analysis

The FTIR spectra were recorded using the ALPHA-FT-IR (BRUKER) spectrometer equipped with ATR accessory. Samples of 100 µl of BLA (native), BLANP and FZnONP were analyzed at pH 7.0 in ATR mode. The spectral range was used between 4000 $cm^{-1}$and 500 cm^{-1} with a resolution of 2 cm^{-1} and 25 scans per spectrum.

8.1.2.3.3 Circular Dichroism (CD), Tryptophan fluorescence (Trp) and ANS fluorescence measurement

CD spectra of FZnONP, was recorded using a JASCO J-1500 CD spectrometer. To monitor the secondary structural changes of BLA, BLANP and FZnONP, we used 20 mM sodium cacodylate buffer, pH 7.4 for the CD signal measurement under a constant flow of N_2 gas. All the measurements were carried out at room temperature (25ºC). Each spectrum represented the average of three readouts recorded between wavelengths of 200-250 nm, with a resolution of 0.2 nm, a bandwidth of 1.0 nm, a scan speed of 100 nm/min and a standard sensitivity using a cuvette of path length of 0.1 cm.

The buffer contribution was deductedfor each measurement. The CD spectrum was reported in mdeg (obtained from the instrument). The percentage contents of the different secondary structural components (α-helix, β-sheet and random coil) were calculated using the software provided along with the instruments.

We performed the fluorescence spectroscopy analysis to observe the conformational change of BLA, in FZnONP. For fluorescence spectroscopy measurement, 20 mM sodium phosphate buffer at pH 7.4 was used. The change in the fluorescence spectra was measured with a Fluorescence spectrometer at 25°C keeping the excitation wavelength at 290 nm.

The Trp fluorescence emission spectrum of BLA was recorded in the range of 300 to 500 nm. The excitation and emission slit widths were set at 10 nm. The samples were analyzed in quartz cuvettes (1cm x 1cm). Background corrections were made with buffer without protein in all cases.

8.1.2.4 Stability analysis under varying conditions of temperature and pH:

The stability analysis of FZnONP was performed using CD, Trp and ANS fluorescence spectroscopy with varying temperature and pH. While CD signal is an indicative of secondary structure contents, fluorescence spectroscopy provides conformation change around Trp and surface hydrophobicity.

The thermal stability analysis of FZnONP across a temperature range of 20-80 ^{0}C was performed in a CD spectrometer. The thermal stress may cause the change in the conformation of the protein layer over ZnONP in FZnONP. Both Trp and ANS fluorescence of FZnONP was measured in a temperature range of 20-80 ^{0}C. Rest of the procedure for performing the CD, Trp and ANS fluorescence spectroscopy was as mentioned in section 8.5.3.

Hence, to study secondary structural change in the protein layer over ZnONP due to increased thermal stress, CD and fluorescence spectroscopy was performed. To assess the pH dependent stability of FZnONP the CD spectrum was also recorded by varying the pH of the buffer in the pH range of 3-10. The Trp fluorescence was measured in a pH range of 3.0 to 10 for FZnONP. Rest of the procedure for performing the CD, Trp and ANS fluorescence spectroscopy remains same as mentioned in section 8.5.3.

8.2 RESULTS AND DISCUSSION:

8.2.1 Preparation and Characterization of ZnO nanoparticles (ZnONP) and FZnONP:

The FESEM images of the synthesized ZnONP showed a particle size in the range of 100- 250 nm (see Fig.8.1A). The AFM image of ZnONP also showed the particle size in the range of 100-200 nm(see Fig.8.2).FZnONP prepared by the crosslinking of BLA with ZnONP (100-250nm) and the size was found to be 500 nm (see Fig.8.1B).

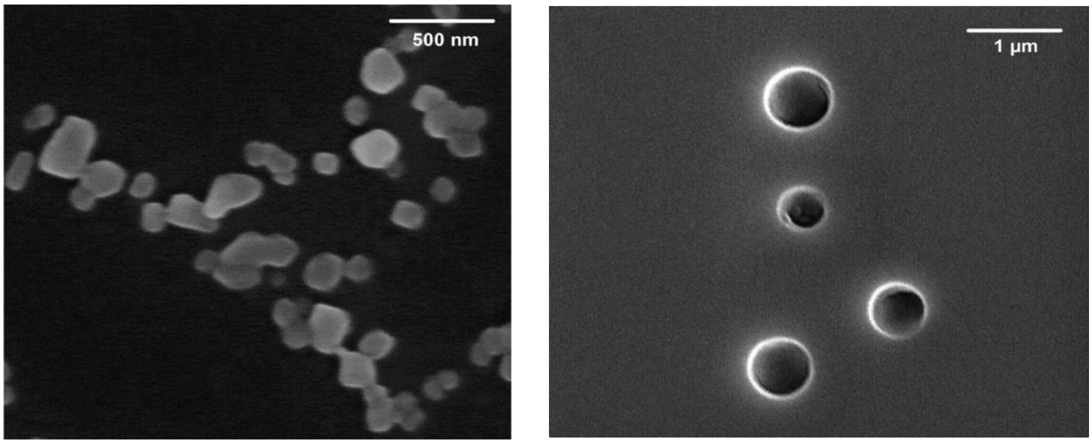

(A) (B)

Figure 8.1 Characterization of size and shape using FESEM images of (A) ZnONP, (B) FZnONP conjugates

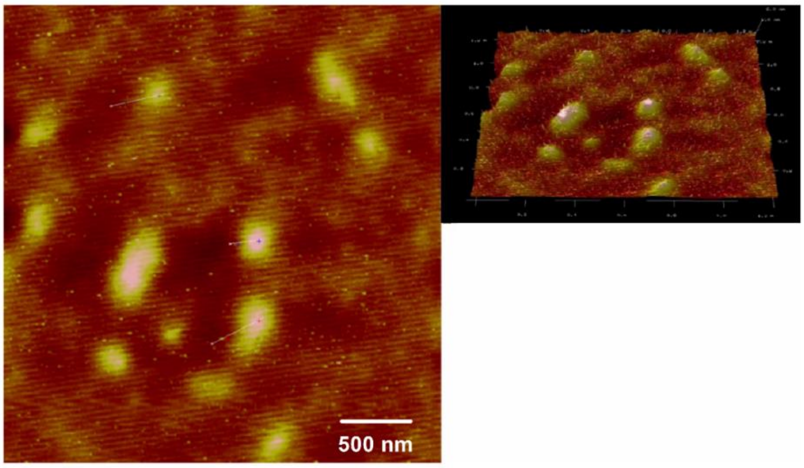

Figure 8.2AFM image of ZnONP, inset shows the 3D morphology of ZnONP.

8.2.2 DLS particle size and Zeta potential analysis

The DLS particle size analysis of ZnONP and FZnONP as shown in Fig.8.3 (A) and (B) showed the average hydrodynamic size as 295 and 460 nm respectively. The DLS results also supports the FESEM- based size distribution. To understand the stability zeta potential was also measured. The zeta potential value of ZnO and FZnONP was estimated to be -48 and -25mV respectively.

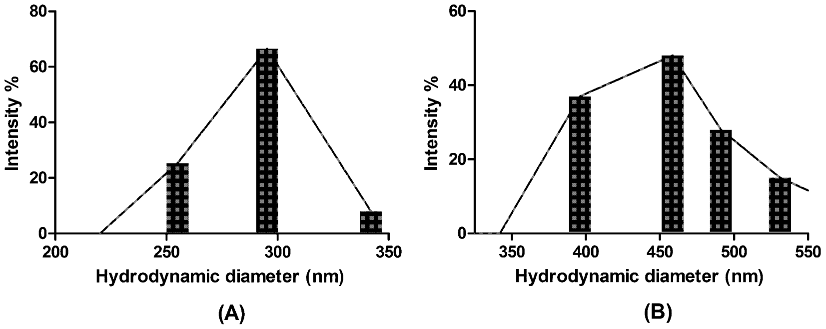

Figure 8.3 DLS particle size analysis of various samples in suspension (A) ZnONP and (B) FZnONP.

8.2.3 FTIR analysis:

Fig 8.4 shows the FTIR spectrum of native BLA, FZnONP and ZnONP showed the characteristic peaks of Amide I and Amide II that normally exist in proteins.

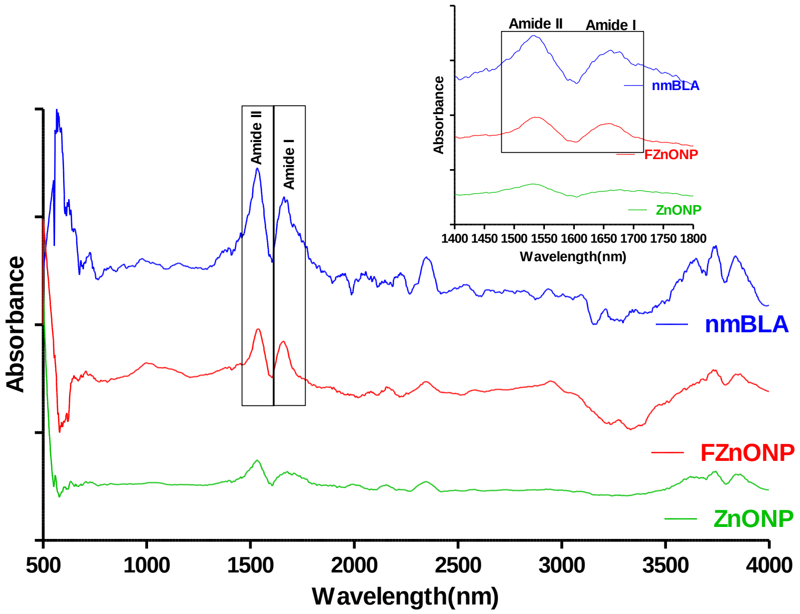

Figure 8.4 FTIR spectrum of Native BLA, FZnONP and ZnONP. Inset shows the spectra between 1400 – 1800 cm^{-1} highlighting the Amide I and Amide II peaks.

These peaks are due to the amide bonds that act as a link between the amino acids. The Amide I signal develops due to the stretching vibrations of the C=O bond and C-N bond while Amide II bondgenerates due to the bending vibrations of the N—H bond and minimal contributions to the peak also come from C-N and C-C stretching vibrations. The presence of prominent Amide-I and Amide-II peaks in the FZnONP sample confirmed the presence of cross-linked protein.

8.2.4 Circular Dichroism (CD), Trp fluorescence and ANS fluorescence measurement:

CD spectra of both nmBLA (0.2 mg/ml) and FZnONP were recorded based on the protocol mentioned in the ‘Materials and Methods’ section. The CD spectral analysis provides information about the secondary structural contents of the protein.

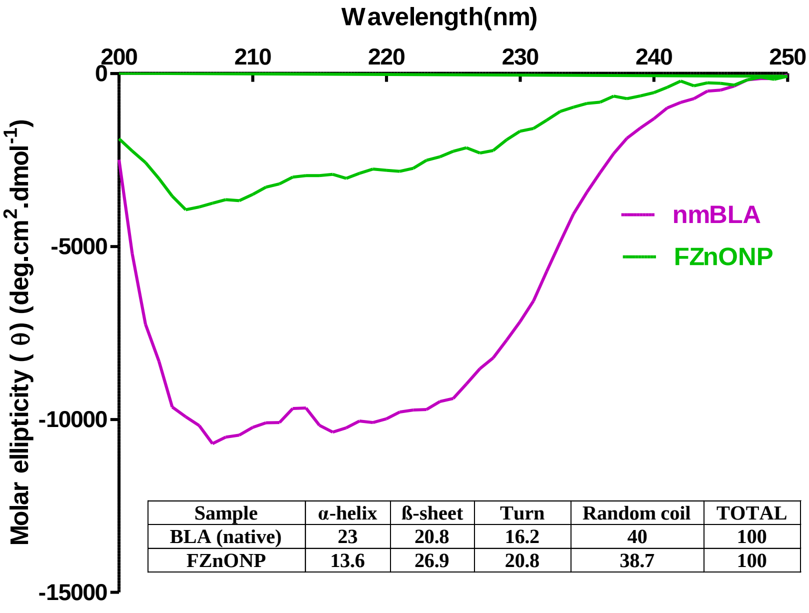

Sample	α-helix	ß-sheet	Turn	Random coil	TOTAL
BLA (native)	23	20.8	16.2	40	100
FZnONP	13.6	26.9	20.8	38.7	100

Figure 8.5 Characterization of nmBLA and FZnONP with respect to its conformational state analyzed by the CD spectra of nmBLA and FZnONP. Significant change in the secondary structure was observed for FZnONP. All data were expressed as the mean of three readouts generated from the instrument.

The percentage of secondary structural components such as α-helix, ß-sheet of the protein and its various conjugated states was estimated by the software provided along with the instrument. From (Fig.8.5) it was found that FZnONP contains reduced amount of α-helix and an increased amount ofβ-sheet and turns(see Fig.8.5).The increase of ß- sheet here has a lot of importance. It indicates higher stability in the FZnONP.

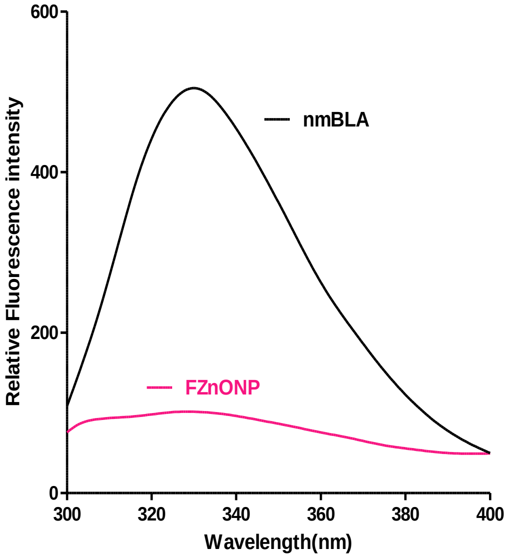

Figure 8.6 Trp fluorescence spectra of BLA and FZnONP. The drop in fluorescence intensity of FZnONP was due to translocation of Trp residues from the surface of the protein to the core of the protein or to a more hydrophobic region. All data were expressed as the mean of three readouts generated from the instrument.

Such, a change in the secondary structural components is bound to induce a change in Trp fluorescence intensity. The Trp fluorescence measurement of nmBLA and FZnONP was shown in Fig.8.6, which clearly showed a huge drop in the fluorescence intensity of BLA in FZnONP indicating that the Trp residues were moved to the surface of the protein and in proximity of solvent molecules. Alternatively, they might have moved to some location of higher polar groups and hence fluorescence was quenched. Moreover, it might be possible that the presence of ZnONP could have quenched the fluorescence of Trp residues of BLA in FZnONP.

Based on the results of the Trp fluorescence measurements of native BLA and FZnONP, we performed ANS fluorescence measurements to observe the suface hydrophobic character of FZnONP.

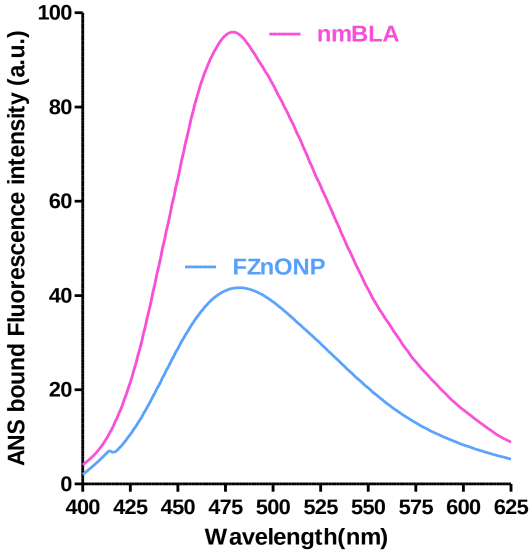

Figure 8.7 ANS fluorescence spectra of nmBLA and FZnONP. The surface hydrophobicity of FZnONP was reduced compared to nmBLA indicated a structural change at the surface. All data were expressed as the mean of three readouts generated from the instrument.

The ANS fluorescence measurements also demonstrated a drop in fluorescence intensity of ANS in FZnONP compared to native BLA as shown in Fig.8.7.The result clearly indicates a drop in surface hydrophobiciity compared to native BLA. This result also supported our claim that the specfic structural change occured in the surface coated BLA which has resulted in the drop in surface hydrophobicity. It also supports our previous hypothesis that Trp residues in FZnONP moved to a location of highly hydrophobic in character.

8.2.5 Stability Analysis due to varying temperature and pH

8.2.5.1 Thermal Stability

The CD signal remained stable for FZnONPcompared to nmBLA in a temperature range of 20-80 ^{0}C indicating increased stability for FZnONP compared to their native forms where we observed a clear variation in the CD signal indicating instability (Fig. 8.8 A, B and C).

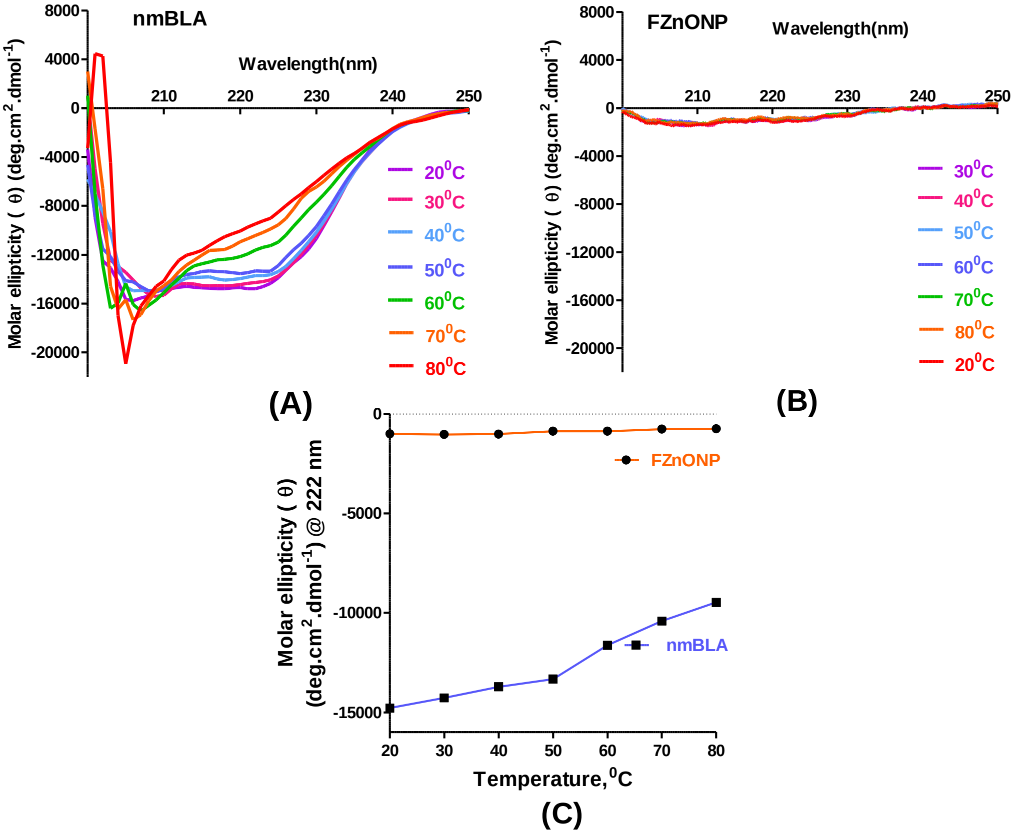

Figure 8.8 Thermal stability analysis by CD spectroscopy of (A) native bovine α-lactalbumin (nmBLA), (B) Functionalized Zinc oxide nanoparticle (FZnONP) and (C)

Comparison of the change in molar ellipticity of nmBLA and FZnONP at 222nm (α-helix). All data were expressed as the mean of three readouts generated from the instrument.

However, beyond a certain level of thermal stress the protein suddenly deviates from the natural CD signal as observed in nmBLA (see Fig.8.8 A and C).The overall change in the CD signal at 222 nm is shown in Fig. 8.8C. We have choosen the CD signal at 222 nm for comparison between nmBLA and FZnONP since, it represents the signal from the α- helix region . Moreover, the region around the α- helix shows visible change in signal intensity which can be extrapolated to obtain a line graph between Temperature and CD signal.

In order to assess the thermal stability of snBLA and FZnONP we also measured the Trp fluorescence at varying temperature conditions. We found a drop in Trp fluorescence for nmBLA and FZnONP (Fig.8.9 A, B and C).

The increased drop in fluorescence of the nmBLA and FZnONP due to increase in temperature suggests that the Trp residues present on the surface moved from the surface of the protein to the core of the protein structure or the Trp residues moved to region surrounded by hydrophobic residues.

Since, the Trp residues directly contribute to the Trp fluorescence, any decrease in the number of Trp residues on the surface of the of the protein would cause a decrease in the overall fluorescence intensity. Such a change in Trp fluorescence is also an indicative of structural change and the environment around the Trp residues present on the surface of the protein.

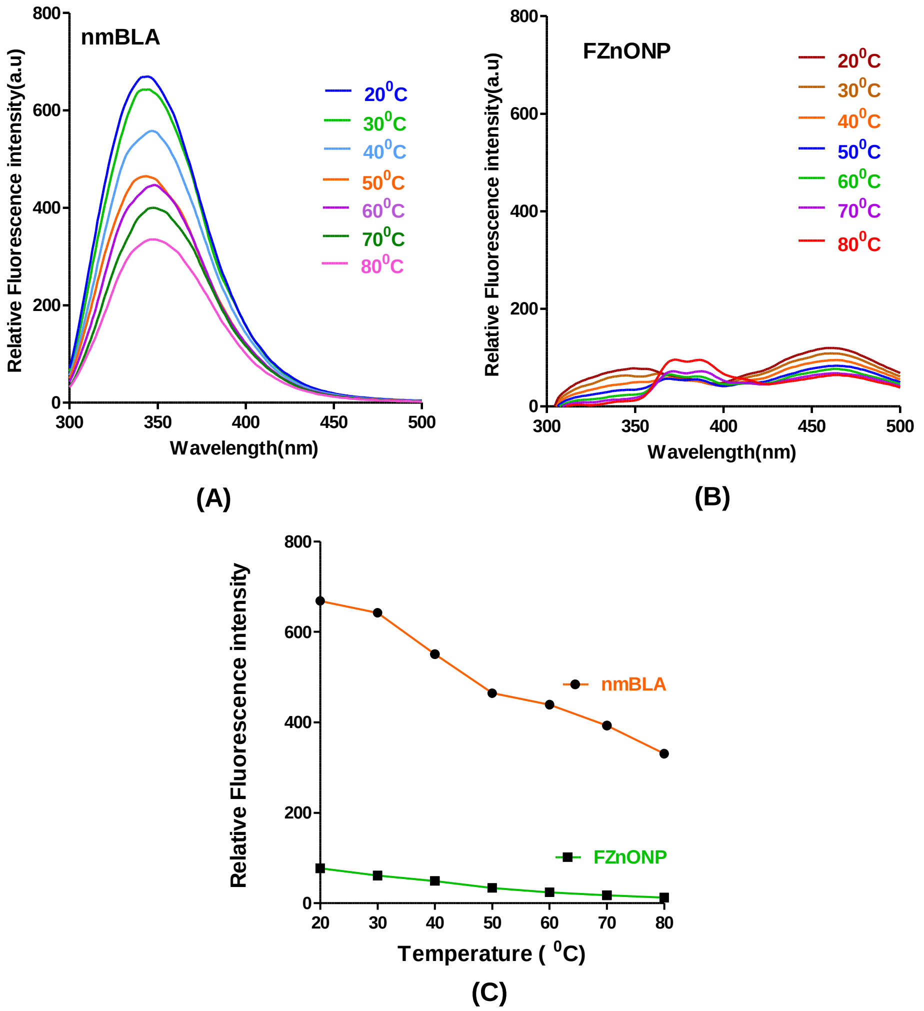

Figure 8.9 Thermal stability analysis by measurement of Trp fluorescence spectroscopy of (A) native bovine α-lactalbumin (nmBLA), (B) Functionalized Zinc oxide nanoparticle (FZnONP) and (C) Comparison of the change in Trp fluorescence of nmBLA and FZnONP. All data were expressed as the mean of three readouts generated from the instrument.

ANS is a surface hydrophocity marker for proteins and usually used for the indirect measurement of the surface hydrophobicity on the surface of the protein. The increase in protein bound ANS fluorescence is an indicator of increase in surface hydrophobicity of the protein.

The protein bound ANS fluorescence for nmBLA showed that with increase in temperature the surface hydrophobicity of native protein deccreased indicating deccreased in surface hydrophobicity (see Fig 8.10 A and C).

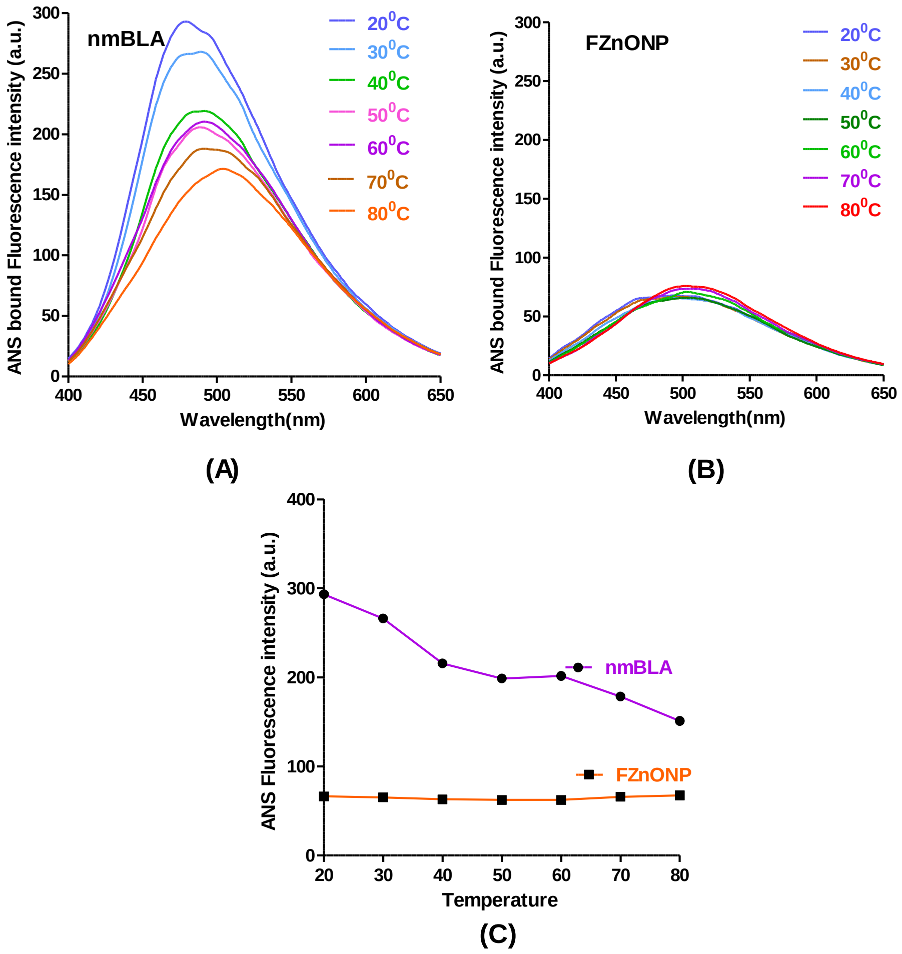

(A) (B)

(C)

Figure 8.10 Thermal stability analysis by measurement of ANS fluorescence spectroscopy of (A) native bovine α-lactalbumin (nmBLA), (B) Functionalized Zinc oxide nanoparticle (FZnONP) and (C) Comparison of the change in Trp fluorescence of nmBLA and FZnONP. All data were expressed as the mean of three readouts generated from the instrument.

The results indicate that with the increase in temperature structural changes occured on the surface, of the native protein. Such a change on the surface of the protein may be due to the weakening of the hydrogen bonds present in the protein. The increase in surface hydrophobicity is also a protective mechanism that protects the protein against thermal stress (Gromiha et al., 2013).

However, a decrease in the surface hydrophobicity with increase in temperature is an indication of decrease in stability as observed in nmBLA(see Fig.8.10 A and C). FZnONP demonstrated a stable ANS fluorescence intensity till 80^0C (see Fig 8.10 B and C) indicating that there was no change in the surface hydrophobicity and remained stable.

8.2.5.2 Stability against varying pH

The CD signal remained stable for FZnONP compared to nmBLA (Fig. 8.11 A, B and C) in a pH range of 3-10. This indicates increased stability for FZnONP compared to the nmBLA where we observed a clear variation in the CD signal indicating instability.

The native proteins change their structure in response to pH stress so that they can maintain their stability, however beyond a certain level of pH related stress the protein looses its native conformational state (see Fig.8.11 A and C).

The overall change in the CD signal at 222 nm is shown in Fig. 8.11C. We have chosen the CD signal at 222 nm for comparison between nmBLA and FZnONP since, it represents the signal from the α- helix region . Moreover, the region around the α helix shows visible change in signal intensity which can be extrapolated to obtain a line graph between pH and CD signal.

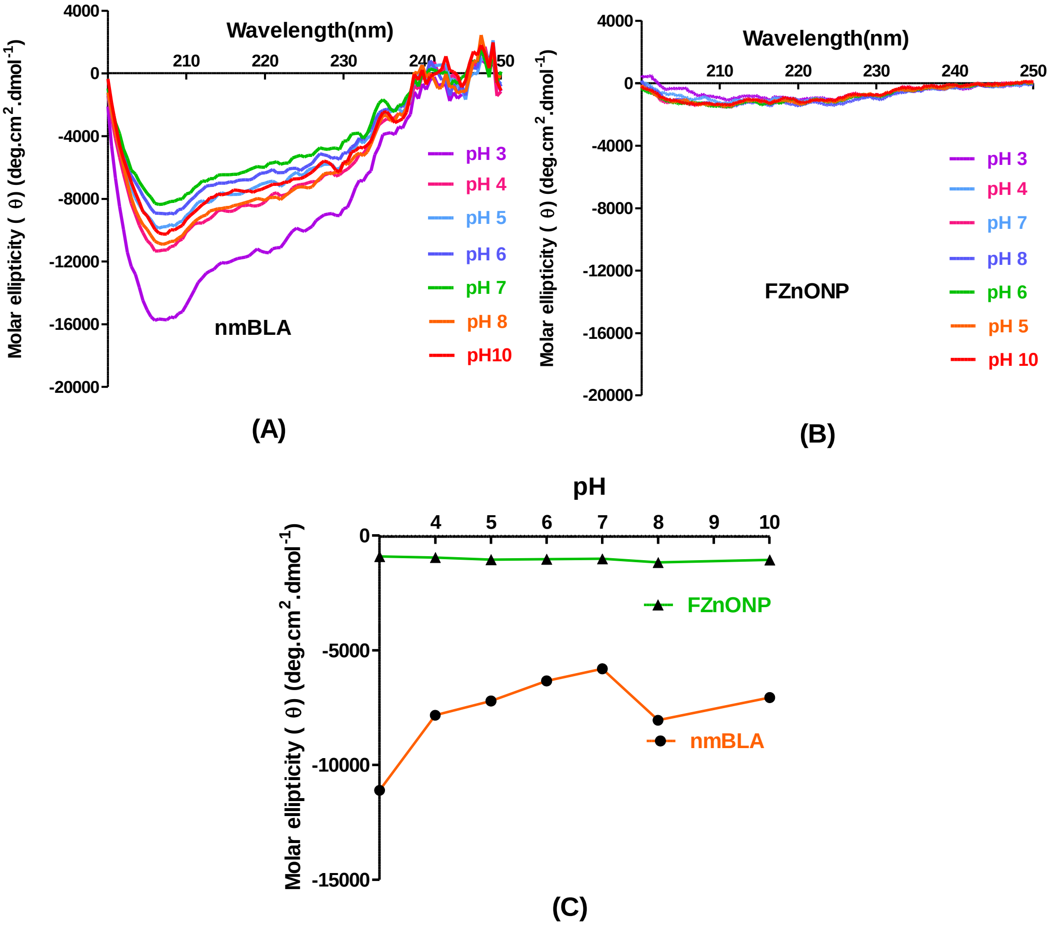

(A)

(B)

(C)

Figure 8.11 pH stability analysis by CD spectroscopy of (A) native bovine α-lactalbumin (nmBLA), (B) Functionalized Zinc oxide nanoparticle (FZnONP) and (C) Comparison of the change in molar ellipticity of nmBLA and FZnONP at 222nm (α-helix). All data were expressed as the mean of three readouts generated from the instrument.

The Trp fluorescence intensity of nmBLA showed variable intensity with increase in pH, however, the Trp fluorescence intensity of FZnONP had subtle variations but was observed fairly constant (Fig. 8.12 A, B and C). Such changes in nmBLA was due change in the ionization state of the charged amino acids, which caused the spectral differences, (Kwaambwa and Maikokera, 2008).

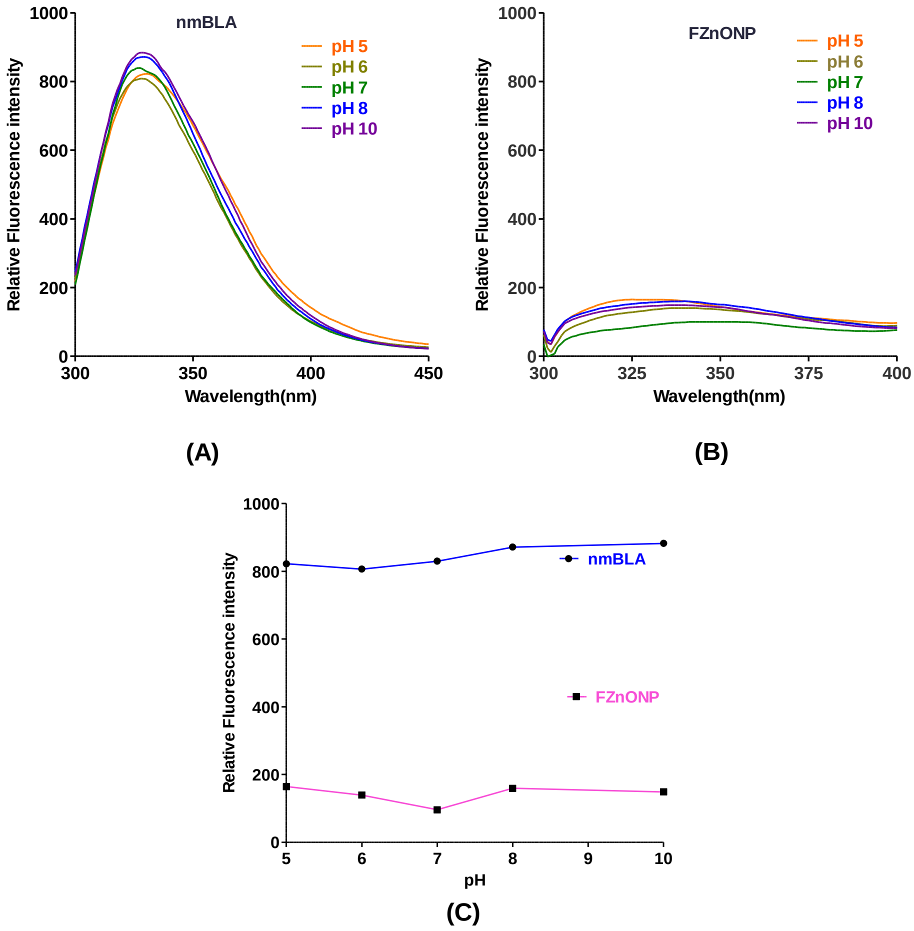

(A) (B)

(C)

Figure 8.12 pH stability analysis by measurement of Trp fluorescence spectroscopy of (A) native bovine α-lactalbumin (nmBLA), (B) Functionalized Zinc oxide nanoparticle (FZnONP) and (C) Comparison of the change in Trp fluorescence of nmBLA and FZnONP. All data were expressed as the mean of three readouts generated from the instrument.

The protein bound ANS fluorescence for native BLA clearly show that the surface hydrophobicity of native BLA decreased rapidly with increase in pH (see Fig. 8.13 A, B and C) indicating instability, whereas FZnONP showed no change in its FZnONP bound ANS fluorescence intensity indicating increased stability.

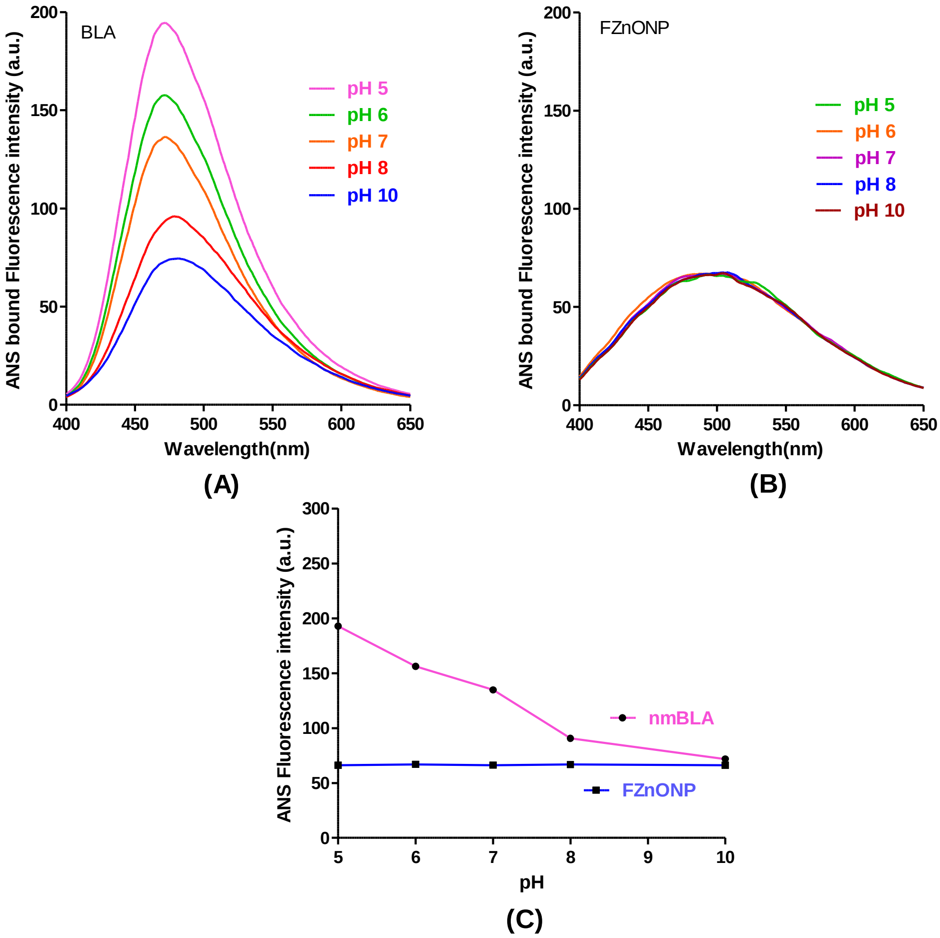

Figure 8.13 pH stability analysis by measurement of ANS fluorescence spectroscopy of (A) native bovine α-lactalbumin (nmBLA), (B) Functionalized Zinc oxide nanoparticle (FZnONP) and (C) Comparison of the change in Trp fluorescence of nmBLA and FZnONP. All data were expressed as the mean of three readouts generated from the instrument.

The results clearly indicate that the surface hydrophobic character of nmBLA decreases rapidly and for FZnONP remains intact with an increase in pH. The protein bound ANS fluorescence for FZnONP and nmBLA clearly show that the surface hydrophobicity of nmBLA decreased rapidly with increase in pH (see Fig. 8.13 A, B and C) indicating instability, whereas FZnONP showed no change in its FZnONP bound ANS fluorescence intensity indicating increased stability. The results clearly indicate that the surface hydrophobic character of nmBLA decreases rapidly and for FZnONP remains intact with an increase in pH.

Chapter 9

Biocompatibility and Cell Viability Assays of Graphene oxide nanosheets (GOns) and Zinc oxide nanoparticle (ZnONP)

9.1 Materials and Methods

9.1.1 Materials

Triton-X and Sodium Chloride were purchased from Sigma-Aldrich, India. MTT assay kit, Ethanol, DMEM, Fetal bovine serum (FBS), antibiotics, disodium EDTA ,DAPI, Fluorescein diacetate, HiMedia India Pvt. Ltd. Milli-Q water was used in all the experiments. T-25 flasks, 96 well plates and all other plasticwares were purchased from Tarsons Pvt. Ltd. MCF-7, MDAMB-231 (Breast cancer cell line), HaCaT, 3T3 cells were procured from NCCS, Pune, India. All the glasswares used in the study were purchased from Borosil, India. All other reagents were of analytical grade.

9.1.2 Methods

9.1.2.1 Hemolysis assay

A volume of 5ml of B +ve human blood was collected by an expert medical practitioner.Blood was collected in a centrifuge tube containing 2 mg of disodium EDTA (anti-coagulant). The contents were gently resuspended and centrifuged at 1000 g for 10 min. The supernatant was removed and the erythrocyte collected at the bottom was washed three times by gentle resuspension with 10 times the volume of pyrogen-free saline (0.9% NaCl). The solution was further centrifuged at 1000 g for 10 min at room temperature.

The erythrocyte pellet was gently resuspended in normal saline and was diluted to 0.8% (v/v). The suspended erythrocyte solution (3 ml) was placed in sterile glass vials, and various test samples were administered to evaluate their hemolytic potential. Triton-X (1%) was used as a positive control and erythrocyte suspension treated with none were used as a negative control.

The absorbance of the hemoglobin released was measured at 405 nm. The percentage hemolysis was calculated from the absorbance values with respect to Triton X-1% (Positive control) at 1 h. FESEM and phase-contrast microscopic images of human erythrocytes treated with GOns and FGOns were also captured for analysis. For ZnONP and FZnONP, FESEM images were also analyzed for observing the extent of erythrocyte damage or percentage hemolysis.

9.1.2.2 Cellular uptake of GOns and FGOns

Both GOns and FGOns-acridine orange conjugates were administered to the MCF-7 cells and the cellular uptake of GOns and FGOns was observed at the end of 12 h post administration. At the end of 12 h DAPI (blue fluorescence) and fluorescein diacetate (green fluorescence for the cytoskeletal component) was added to the sample cells to visualize the cells. The samples were analysed using fluorescence and confocal microscopy.

9.1.2.3 Cytotoxicity study

The cytotoxicity of GOns and FGOnswere assessed against two human Breast cancer cell lines (MCF-7 and MDAMB-231) and two normal cell lines, HaCaT (human keratinocyte cell line) and 3T3 (murine fibroblast cells) using MTT assay.For

ZnONP and FZnONP the cytotoxicity as well as cytocompatibility assay was performed in MDAMB-231 cells and HaCaT cells.All the cells were cultured in DMEM (Dulbecco's Minimum Essential Medium) containing 10% foetal bovine serum. Cells were grown in T-25 flasks that were incubated at 37^0C in a humidified 5% CO_2 incubator. The cells were grown to 80% confluence, trypsinized followed by seeding at a density of $1x10^4$ cells/ml.

The cells were seeded in a 96 well plate containing 100 µl of DMEM in each well and allowed to proliferate for 24 h. GOns, FGOns, ZnONP and FZnONPwere administered to the cells and cytotoxicity was evaluated by MTT assay at the end of next 24 h. MTT (10 µl of 5 mg/ml stock) was added 6 h before the end point.

In the end, media was removed, and 100 µl of DMSO was added to dissolve the formazan formed and the absorbance was measured at 595 nm. The absorbance values were recorded, and percentage cell viability of the cells was calculated from the absorbance values and the result was plotted. Reactive oxygen species (ROS) inhibitor, N-acetylcysteine (NAC) with 2mM final concentration was also administered to confirm ROS-based cell death.

9.2 Results and Discussion

9.2.1 Hemolysis assay for GOns, FGOns, ZnONP and FZnONP

We performed the hemolysis assay of GOns as well as FGOns for evaluating their effect on human erythrocytes. We used human erythrocytes with normal saline as the negative control and 1% Triton-X as a positive control. Fig. 9.1A and B showed the hemolytic propensity of GOns and FGOns.

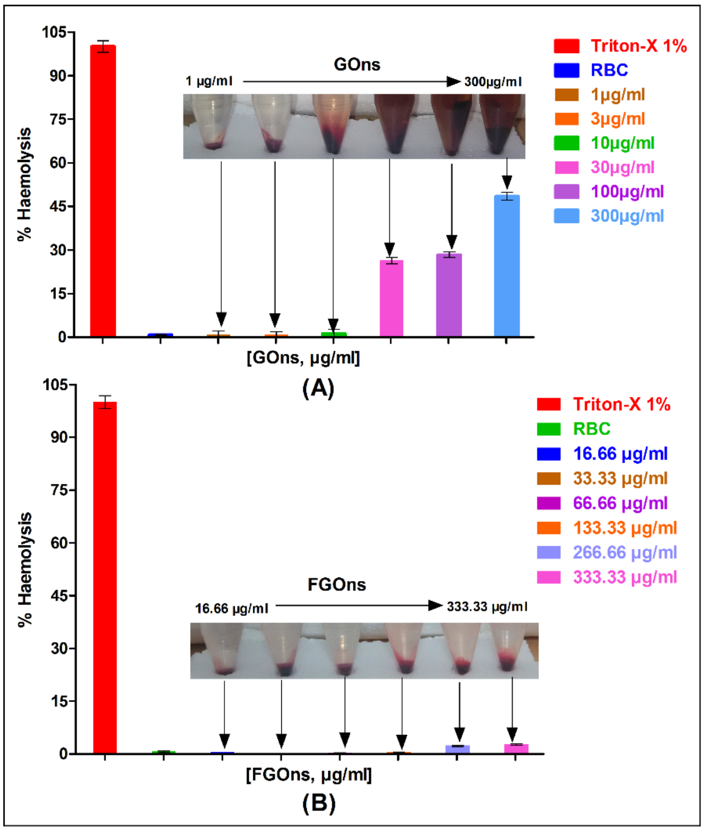

Figure 9.1 Hemolysis assay of (A) GOns and (B) FGOns. FGOns demonstrates excellent hemocompatibility compared to GOns. All data were expressed as Mean ± S.E.M, n = 3.

The results clearly revealed a high hemolytic activity of GOns beyond 10 µg/ml concentration (Fig. 9.1A) while FGOns exhibited negligible hemolytic potential (Fig. 9.1 B) at the same concentration and less than 5% hemolysis was observed at 333 µg/ml of GOns concentration in FGOns.

Moreover, noticeable damage of erythrocytes was observed in FESEM images of GOns treated erythrocytes sample (see Fig. 9.2 B) while FGOns treated sample (see Fig.9.2 C-F) showed intact erythrocytes. The image of normal erythrocyte was shown in Fig. 9.2 A as control.

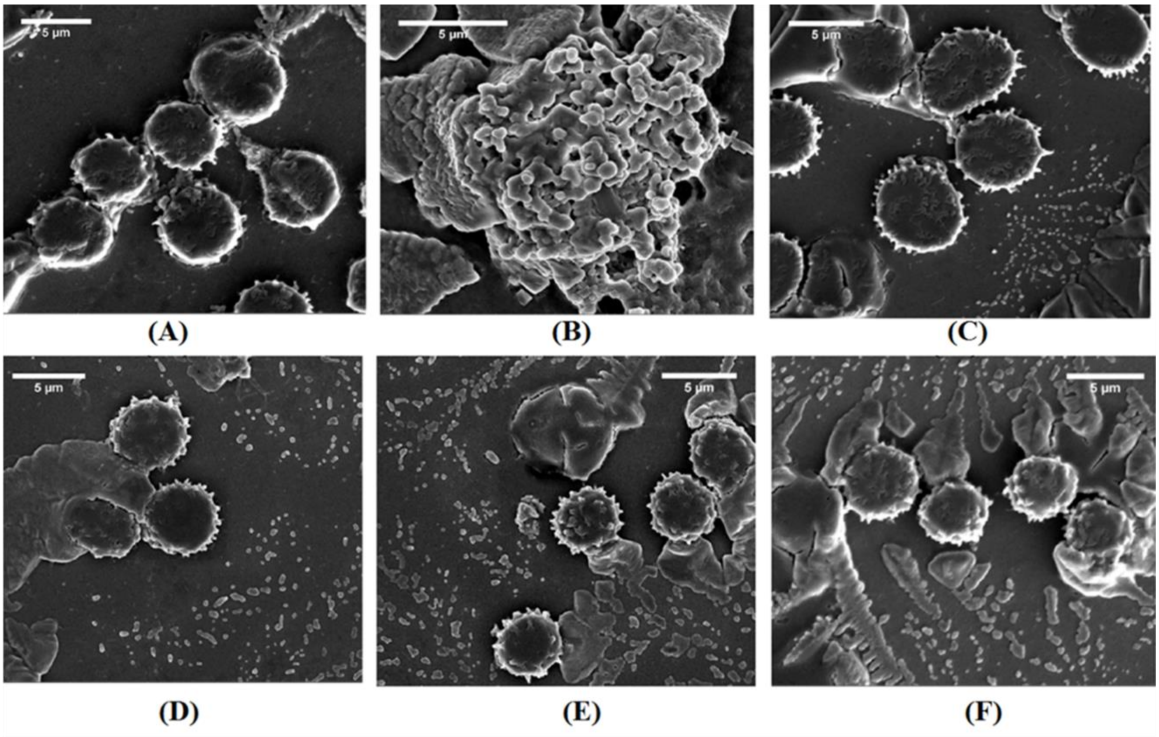

Figure 9.2 FESEM images of erythrocytes treated with various samples. (A) Control; erythrocytes administered with none. Administered with (B) 15µg/ml of GOns (C) administered with 15µg/ml of FGOns (GOns and BLA was 1:1 w/w). (D) 66 µg/ml FGOns, (E) 133 µg/ml FGOns and (F) 333 µg/ml FGOns. FGOns demonstrates excellent hemocompatibility compared to GOns.

When erythrocytes were treated with 15 µg/ml of GOns at different periods such as 15, 30 and 60 min, the microscopic images (Fig.9.3) showed the initiation of erythrocyte damage after 15 min of GOns administration. Cell shrinkage was also found associated with the initiation of erythrocyte damage followed by the gradual disintegration of cells.

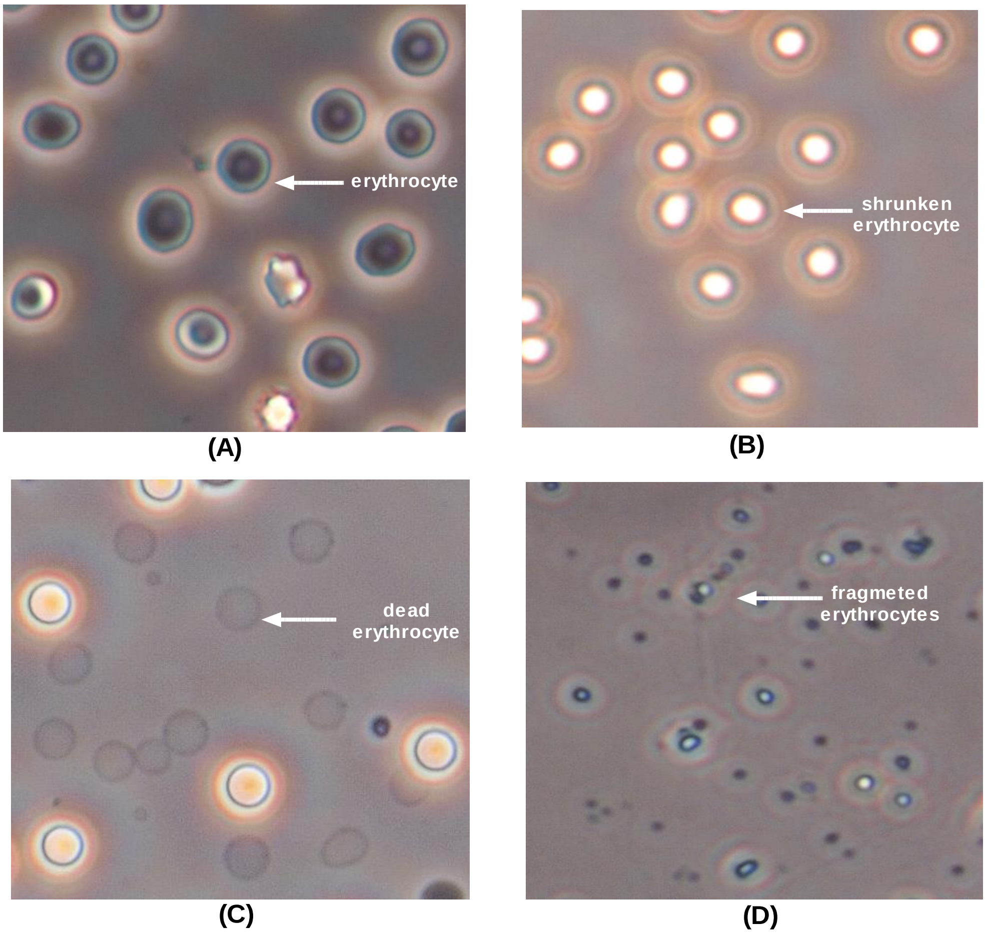

(A) (B) (C) (D)

Figure 9.3 Microscope images of human erythrocytes exposed to GOns (15 µg/ml) at different time points. (A) Control at 0 min, (B) 15min, (C) 30 min and (D) 60 min. Magnification is (800X). GOns induces visible damage to human erythrocytes.

Here, we demonstrated the GOns-mediated hemolysis of erythrocytes. Although numerous reports demonstrated the evidence of GOns-based hemolysis, no specific reason was clearly mentioned or explained behind hemotoxicity. However, ROS-based damage of erythrocytes may be one of the causes. Moreover, studies of GO-based treatment on few bacteria also reported the cell death due to sharp edges of GOns (Akhavan and Ghaderi, 2010)**.** Our experimental results clearly demonstrated that the protein-coated GOns (FGOns) prevented the hemolysis of human erythrocytes.

Based on our results, we proposed a model how GOns and its functionalized form caused damage to human erythrocytes (Fig 9.4).

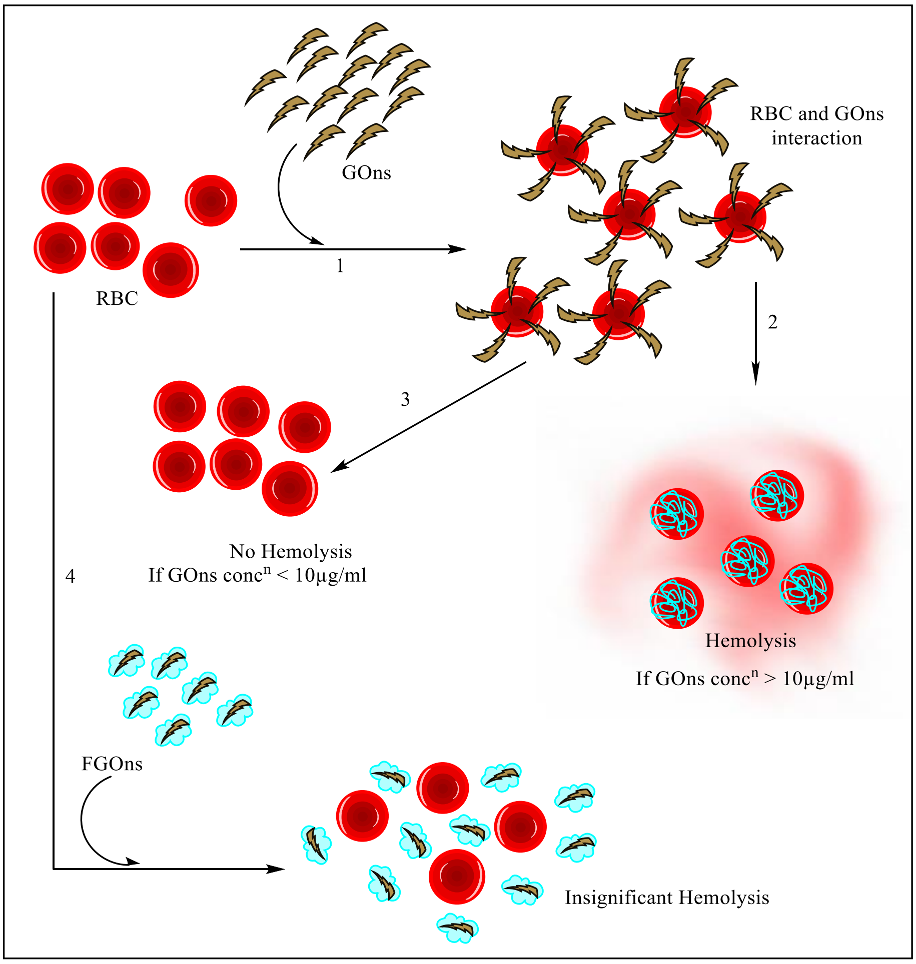

Figure 9.4 Schematic representation of the interaction of GOns and FGOns with human erythrocytes: Step (1) GOns come in contact with erythrocytes. Step (2) GOns attach on the surface of erythrocytes and cause haemolysis if the concentration of GOns is greater than 30 µg/ml. Step (3) GOns attach on the surface of erythrocytes and do not cause haemolysis if the concentration of GOns is less than 30µg/ml. Step (4) FGOns nanosheets do not interact with RBC's hence, insignificant haemolysis.

We also performed the hemolysis assay for ZnONP and FZnONP for assessing the hemocompatibility in human erythrocytes.

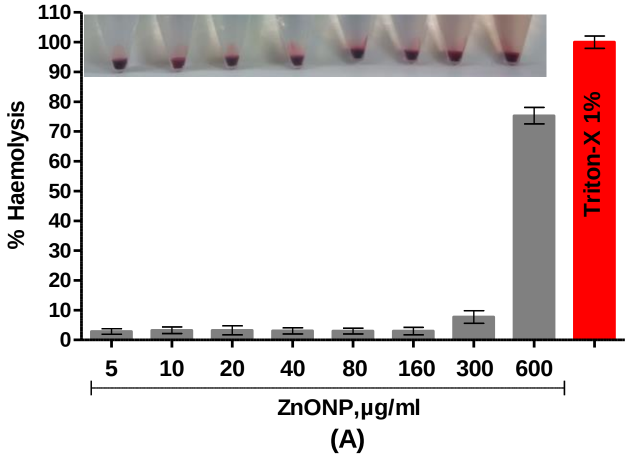

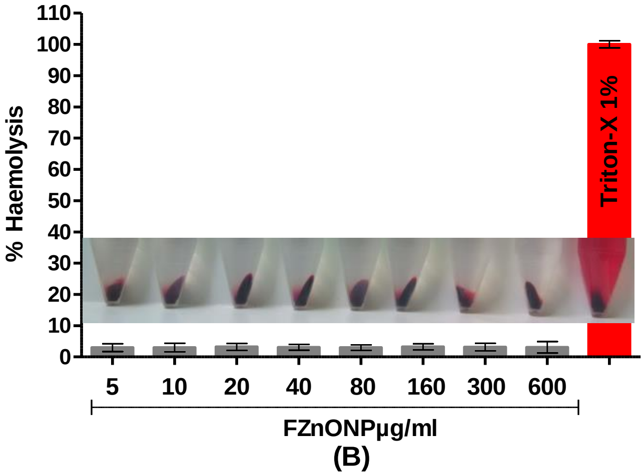

Figure 9.5 Hemolysis assay of (A) ZnONP, (B) FZnONP. FZnONP shows enhanced hemocompatibility compared to ZnONP alone. All data were expressed as Mean ± S.E.M, n = 3.

The results of the hemolysis assay for ZnONP and FZnONP (see Fig.9.5 A and B) clearly revealed that ZnONP at concentrations of 300 µg/ml and 600 µg/ml, caused 7.7 % and 75.3 % haemolysis of human erythrocytes respectively. However, the BLA-

ZnONP exhibited no hemolysis till 600 µg/ml. The results clearly established the hemocompatibility of ZnONP till 160 µg/ml and BLA-ZnONP till 600 µg/ml.

9.2.2 Cellular Uptake of GOns and FGOns

To observe the cellular uptake of GO samples, we performed the fluorescence imaging of MCF-7 cancer cells. Fluorescent dyes such as DAPI (blue fluorescence for the nucleus), fluorescein diacetate (green fluorescence for the cytoskeletal component) and acridine orange (FGOns) were used for fluorescence imaging. At the end of 12 h post-administration of FGOns-conjugated acridine orange, we observed the appearance of FGOns particles exhibiting orange fluorescence inside the cytoplasm of MCF-7 breast cancer cells (see Fig. 9.6A–E).

When the image of the same sample was analyzed by confocal laser scanning microscopy it showed the cytoplasm containing granular particles exhibit orange fluorescence (see Fig. 9.6H and I). Therefore, the results confirm the cellular internalization of FGOns in MCF-7 cancer cells.

When we performed the experiments with GOns, we observed fluorescence image exhibiting orange fluorescence inside the cytoplasm (see Fig. 9.6G). However, such cells were found damaged (Fig. 9.6F) and the amount of fluorescence from the cells was quite low compared to FGOns in MCF-7 cells. Thus, we hypothesized that GOns perhaps was not uptaken by the intact cells, however, it first damaged the cell membrane due to its surface geometry (sharp edges) using strong shear forces that subsequently induced intracellular ROS generation via mitochondria and cause cell death.

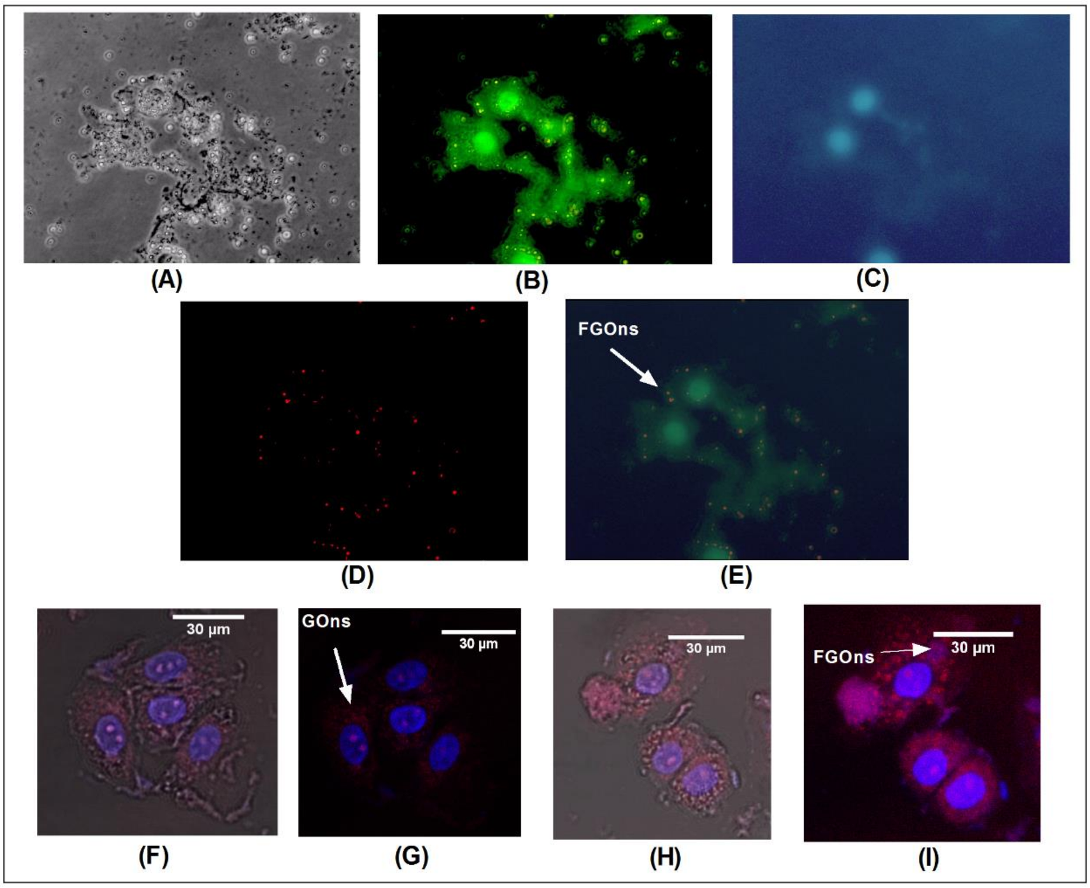

Figure 9.6 Imaging of MCF-7 cells at 12 h post administration of FGOns. (A) Phase contrast image (B) Cells stained with fluorescein di-acetate (green fluorescence) highlighting cytoplasmic boundary (C) Cells stained with DAPI (blue fluorescence) highlighting the intact nucleus (D) Acridine orange cross-linked FGOns (E) Merged images of A–D. Confocal microscopy images of cellular uptake (12h post administration) of GOns and FGOns cross-linked with acridine orange (F) Merged Phase contrast image showing the degraded cytoplasmic regions treated with GOns.(G)The image highlighting the cellular uptake of GOns (H) merged phase contrast image showing a comparatively intact cytoplasmic boundary of the MCF-7 cells treated with FGOns.(I) The image shows the cellular uptake of FGOns.

Earlier in the hemolysis section, we also demonstrated a similar kind of mechanism of action for GOns damaged erythrocytes (Fig. 9.2B) and such mechanism also supports our current hypothesis of cellular damages of induced by GOns in cancer cells. The overall results also revealed that the cellular internalization of any molecule is not only size dependent, but also shape and surface geometry dependent.

The cellular uptake study also revealed that the cellular damage induced by GOns was faster than FGOns. However, as we observed the mechanism of action by which both GOns and FGOns generated their toxicity in cancer cells were different. It also signifies the fact that the preparation of a stable protein functionalized GOns (FGOns) assist the successful uptake of FGOns by cancer cells towards ROS generation that consequently cause cell death.

9.2.3 Cytotoxicity study of GOns, FGOns, ZnONP and FZnONP

We already observed the high hemolytic potential of GOns, however excellent hemocompatibility was noticed for FGOns. Such a fact can allow us to use a high concentration of GOns in FGOns in various biomedical applications. Hence, we performed their cytotoxicity study on human Breast cancer cell lines MCF-7 and MDAMB-231.

We found that GOns induced more than 85 % cytotoxicity to the cells within 24 h, however, the toxicity was reduced to 21% in the presence of NAC (2 mM) a ROS inhibitor (see Fig.9.7 A and C).

Therefore, this ~64 % reduction in toxicity was due to the ROS-mediated cell death, which also proves that rest 21% cytotoxic effect is due to some other mechanism, which we assumed to be the shear stress-mediated membrane damage induced to cancer cells by sharp edges of GOns.

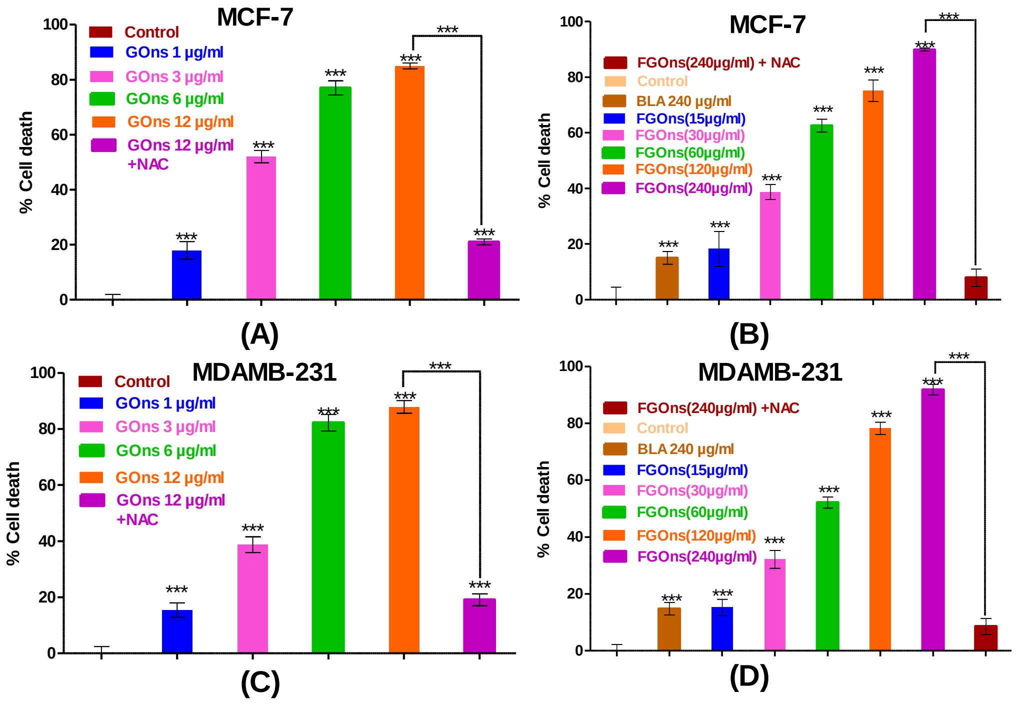

Figure 9.7 Relative cytotoxicity of GOns and FGOns in various cancer. (A) and (B) MCF-7 cells; (C) and (D) MDAMB-231 cells. The cell cytotoxicity was presented as the percentage of mean value. Statistically significant vs. control group, *** $p < 0.001$ by One way ANOVA and post Tukey test. All the data were expressed as Mean ± S.E.M, n = 3.

When FGOns was administered to cancer cells, it showed a maximum cytotoxicity of ~90% which decreased to 8% due to the presence of 2mM NAC (see Fig.9.7B and D). This reduction in cytotoxicity of 82% was solely due to the ROS inhibitor NAC.

Similar results were also found in the caseof MDAMB-231 cells treated with GOns. It showed a maximum cytotoxicity of 88% at 12 µg/ml. However, in the presence of NAC, the cytotoxicity was reduced to 19%, revealed a ROS-based death (see Fig.9.7A). Rest 19% cell death perhaps occurred due to shear stress that induced membrane damage mediated by the sharp edges of GOns. Similar result was also observed in MDAMB-231 cells (Fig.9.7C).

The effect of GOns and FGOns in normal human cells like HaCaT (human keratinocyte cells) and murine fibroblast cells 3T3 was also assessed. The MTT assay of GOns revealed dose-dependent increase of cytotoxicity with more than 50% and 45% cell killing at a GOns concentration of 30 µg/ml in HaCaT and 3T3 cells, respectively. The administration of NAC in cell culture medium resulted in the inhibition of HaCaT and 3T3 cell death significantly (Fig. 9.8A and C) indicating a ROS-mediated cytotoxicity induced by GOns.

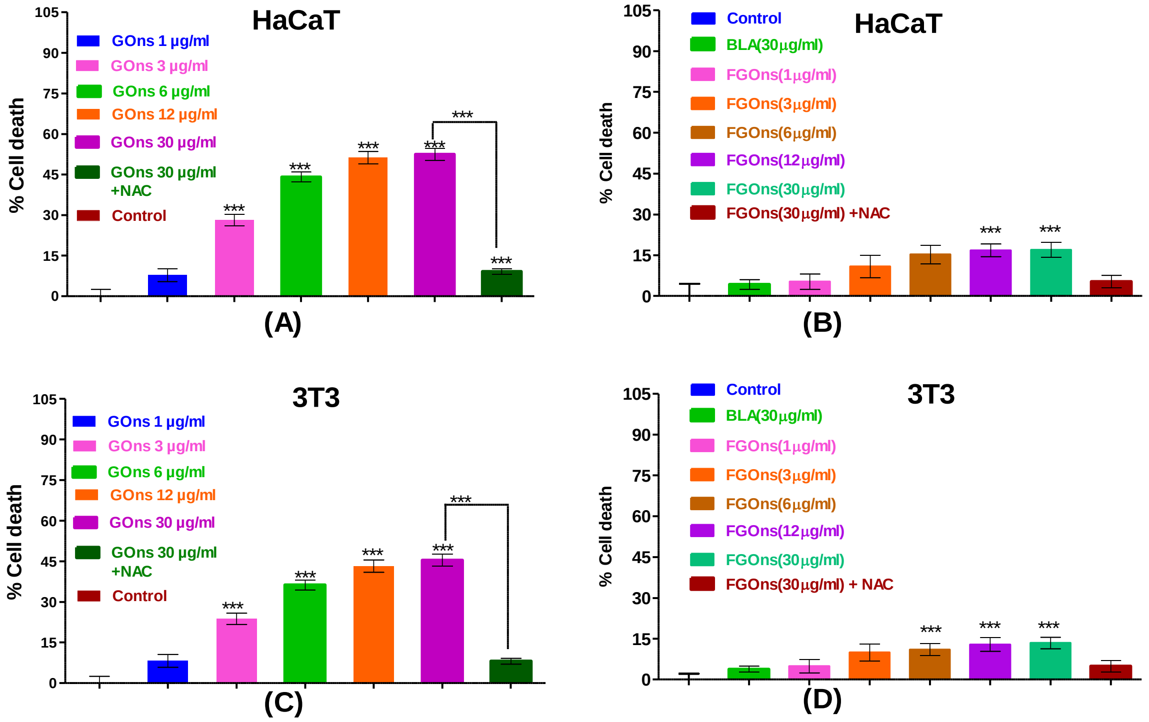

Figure 9.8 Relative cytotoxicity of GOns and FGOns in various cancer and normal cells. (A) and (B) HaCaT cells (C) and (D) 3T3 cells. The cell cytotoxicity was presented as the percentage of mean value. Statistically significant vs. control group, *** $p < 0.001$ by One way ANOVA and post Tukey test. All the data were expressed as Mean ± S.E.M, n = 3.

However, after the addition of NAC, low cell death in HaCaT and 3T3 cells was observed, which revealed the existence of a second mechanism of cell death and we anticipated that to be the shear force induced by sharp edges of GOns.

In our second set of experiments, we evaluated the cytotoxicity of FGOns in normal cells like HaCaT and 3T3 cells (see Fig. 9.8 B and D). FGOns demonstrated a maximum cytotoxicity of 17 % and 13.4% at a concentration of 30 µg/ml in HaCaT and 3T3 cells respectively, which is almost 35.4 % and 31.99 % less cytotoxic compared to GOns at a similar dose. Although, 30µg/ml FGOns (GOns/BLA is 1:1 w/w %) contains an equal amount of GOns and BLA, the cytotoxicity induced by FGOns reduced significantly. Such a decrease in cytotoxicity was perhaps due to the surface coating of GOns using BLA molecules.

Therefore, we assumed that the surface character of GOns and its sharp edges were probably responsible for causing such toxicity to HaCaT and 3T3 cells that were significantly suppressed when GOns was functionalized by BLA.

In both the cases of MCF-7 and MDAMB-231 cells, the surface of GOns was coated with protein, hence, the only source of ROS generation was due to the specific folded state of BLA. The specific conformational variant of BLA in FGOns perhaps generated sufficient ROS for killing the cancerous cells.

This may be due to the fact that the cancerous cells were already in a stressed state utilizing all the superoxide dismutase (SOD) and glutathione-s-transferase (GST) for protecting the cell. The cancerous cells were not able to withstand the extra burden of ROS generated due to the specific folding variant of BLA in FGOns.

From the cytotoxicity study, we concluded that ROS generation was the reason behind the cytotoxicity of GOns against normal cells and cancer cells apart from the cell death resulting from the sharp edges of GOns.

We also examined the anti-proliferative activity of ZnONP in both MDAMB-231 and MCF-7 cancer cell lines. ZnONP clearly demonstrated dose-dependent cytotoxicity in MDAMB-231 and MCF-7 breast cancer cells with 83 and 87.7% cytotoxicity at a dose of 100 µg/ml. In the presence of NAC, MDAMB-231 and MCF-7 breast cancer cells demonstrated 38.61 and 21.22% cytotoxicity at 100 µg/ml respectively.

The presence of NAC could reverse the cytotoxicity by 61.39and 78.78% respectively (Fig.9.9A). The result clearly indicates that the cytotoxicity induced by ZnONP in MDAMB-231 and MCF-7 cells is mediated primarily through ROS generation.

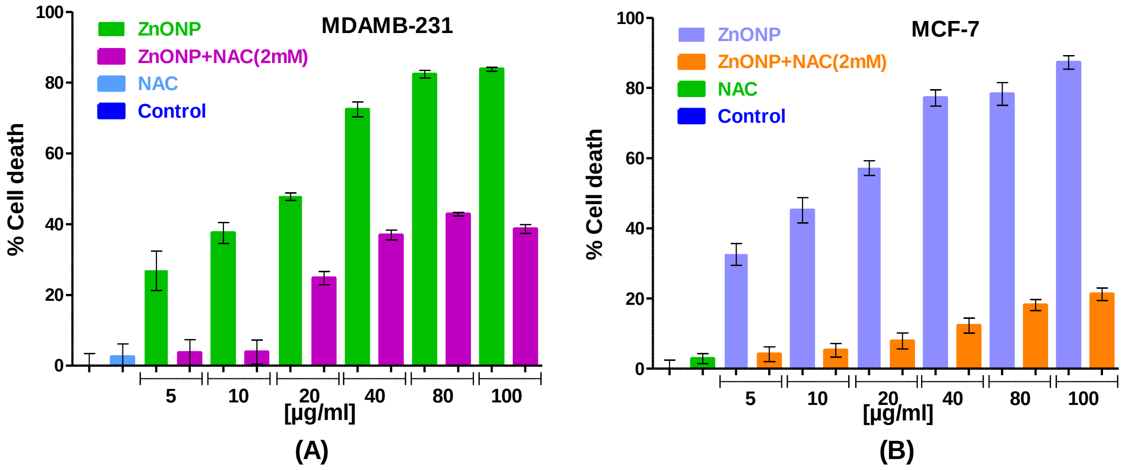

Figure 9.9 MTT assay of ZnONP in breast cancer cells, both in the presence and absence of NAC, (A) MDAMB-231 cells and (B) MCF-7 cells. ZnONP shows a dose dependent increase in cytotoxicity and acts by a ROS dependent mechanism. All the data were expressed as Mean ± S.E.M, n = 3.

FZnONP clearly demonstrated dose-dependent cytotoxicity in MDAMB-231 and MCF-7 breast cancer cells with 89.74 and 97.24 % cytotoxicity at 100 µg/ml. However, in the presence of NAC, MDAMB-231 and MCF-7 breast cancer cells demonstrated 37.27 and 12.75% cytotoxicity at 100 μg/ml respectively (Fig.9.10A and B).

The result indicates that FZnONP generates cytotoxicity in MDAMB-231 and MCF-7 cells mainly through ROS due to the fact that the amount of ROS generated by FZnONP was nullified by the presence of NAC by 62.73 (partially) and 87.25% (primarily) respectively (Fig.9.10A and B).

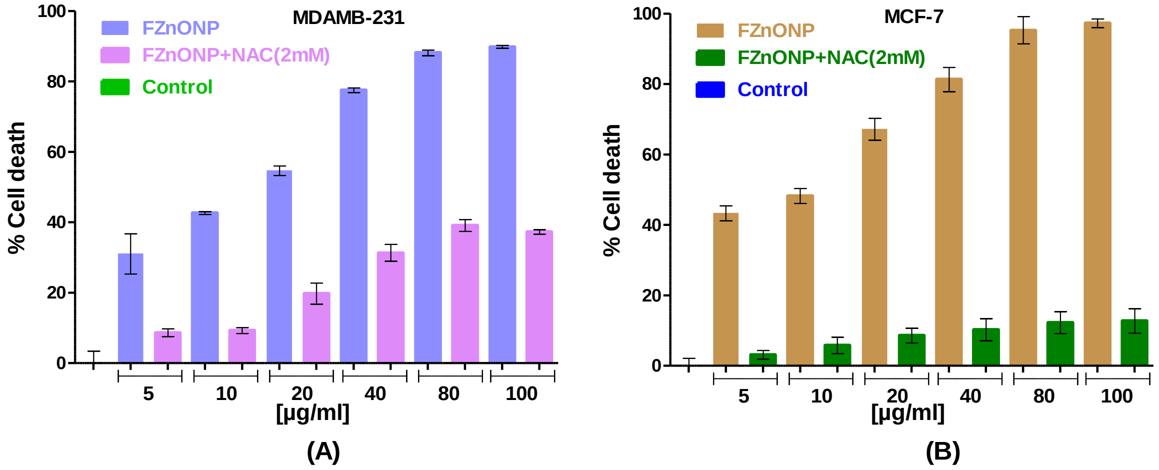

Figure 9.10 MTT assay of FZnONP in breast cancer cells, both in the presence and absence of NAC, (A) MDAMB-231 cells and (B) MCF-7 cells. ZnONP shows a dose dependent increase in cytotoxicity and acts by a ROS dependent mechanism. All the data were expressed as Mean ± S.E.M, n = 3.

We also evaluated the effect of ZnONP and FZnONP in normal cells such as HaCaT in order observe the cytocompatibility of ZnONP and FZnONP. ZnONP showed a dose dependent cytotoxicity in HaCaT cells, however, in the presence of NAC the cytotoxic effect was reduced significantly (see Fig.9.11). The cytotoxicity of ZnONP in HaCaT cells was due to ROS generation since; the treatment of NAC (ROS inhibitor) reduced the cytotoxicity significantly (see Fig.9.11). The administration of

ZnONP in HaCaT cells generated sufficient ROS which was responsible for the HaCaT cell death.

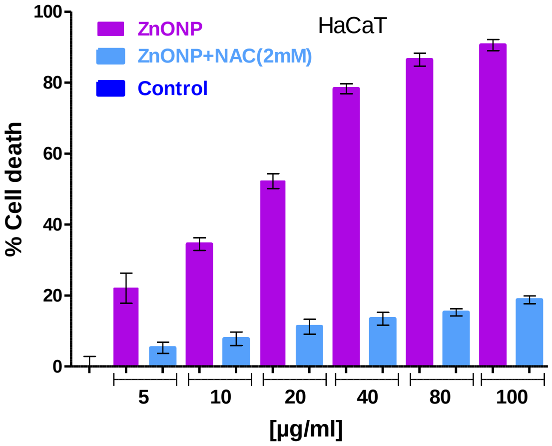

Figure 9.11 MTT assay of ZnONP in HaCaT cells, both in the presence and absence of NAC. ZnONP shows a dose dependent increase in cytotoxicity and acts by a ROS dependent mechanism. All the data were expressed as Mean ± S.E.M, n = 3.

The treatment of HaCaT cells with FZnONP did not result in any cytotoxicity till a dose of 100 µg/ml both in the presence and absence of NAC (see Fig.9.12).

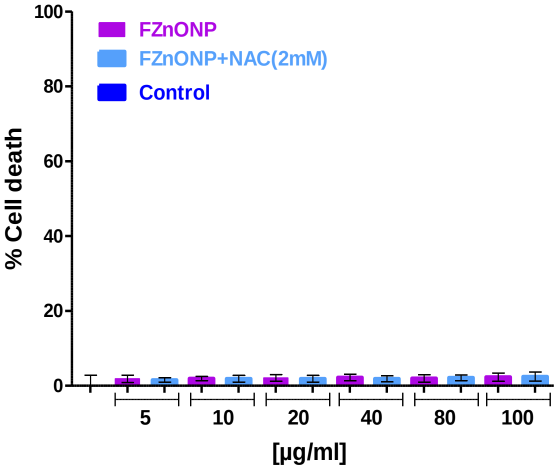

Figure 9.12 MTT assay of FZnONP in HaCaT cells, both in the presence and absence of NAC. FZnONP did not show any cytotoxicity in HaCaT cells. All the data were expressed as Mean ± S.E.M, n = 3.

The result clearly indicates that the layer of BLA over ZnONP reduced the cytotoxicity of ZnONP in HaCaT cells.

The cancer cells are already in a stressed state and the ROS inhibitory mechanism is already overloaded. Hence, the specific structural state of the BLA coat was responsible for the toxicity generated in MDAMB231 cells. The additional ROS generated by the BLA coat over ZnONP proved fatal for the MDAMB231 cells as the internal ROS inhibitory mechanism failed to with stand the additional ROS load.

Chapter 10

Conclusion

Overall, in our present study we have developed small protein based therapeutic strategies for the therapy of breast cancer, where self-assembled structure of two small globular proteins demonstrated strong cytotoxicity in two human breast cancer cells, without causing any toxicity in normal cells. Moreover, both protein nanoassemblies demonstrated to act as excellent drug delivery system in cancer. Furthermore, they proved to be a far better therapeutic option than Zinc oxide nanoparticles (ZnONP) or Graphene oxide nanosheet (GOns) based therapeutic approach.

Based on the whole experimental study, the following are the specific conclusions are derived:

1. The self-assembled nanostructured hen egg white lysozyme (snLYZ) and bovine α-lactalbumin (snBLA) were synthesized using a simple desolvation technique through chemical crosslinking using 0.1% glutaraldehyde for 8 h. Both the nanoassembly were of 300 nm average size with spherical shape and were highly stable in a wide range of pH, temperature and proteinase K environment. Moreover, we concluded that substantial change in conformation change as well as surface hydrophobicity of the proteins took place in the proteins in their nanoassembly state compared to their respective native state.

2. Both the protein nanoassembly caused rapid cell death in breast cancer cells MCF-7 and MDAMB-231 through cellular uptake and reactive oxygen species

(ROS) generation however, were found highly biocompatible as reflected from their excellent hemocompatibility as well as their cytocompatibility in normal human and murine cell lines.

3. Both the protein nanoassemblies (snLYZ and snBLA) were rapidly taken up in breast cancer cells resulted in cellular size and nucleus followed by cytoplasmic degradation resulting in cellular death. Cellular necrosis was the mechanism behind such morphological changes in breast cancer cells.

4. Both snLYZ and snBLA demonstrated increased cytotoxicity when conjugated with folic acid (FA) compared to their unconjugated forms. The folic acid conjugation was found to be an interesting approach as it enhances the uptake of snLYZ-FA and snBLA-FA in cancer cells expressing folate receptors (FR). Thus, we can easily target cancer cells that express folate receptors and induce higher levels of cytotoxicity.

5. The protein nanoassembly of snBLA was compared with an anti-cancer agent, a lipid-conjugated protein popularly known as BAMLET (Bovine α-lactalbumin made lethal to tumor cells). However, our synthesized snBLA demonstrated increased toxicity and proved to be a clear winner compared to BAMLET in four different cell lines such as MDAMB-231 and MCF-7 (Breast cancer), HeLa (Cervical Cancer) and A549 (Lung cancer). While BAMLET followed the apoptotic pathway involving Caspase-3, snBLA induced necrosis in cancer cells and did not cause Caspase-3 mediated apoptosis as evidenced from Caspase-3 expression.

6. Both the nanoassembly demonstrated high Tamoxifen loading (124%) through chemical crosslinking process and release of drug efficiently in a pH-responsive manner. Furthermore the drug release process was completely regulated by conformational change of the protein in nanoassembly.

7. Although drug-loaded, both the protein nanoassembly showed predominantly only drug-mediated anti-proliferative activity, the post-drug release state of nanoassembly, however, demonstrated the complete recovery of its inherent anti-proliferative activity due to conformational reconstitution.

8. Multilayer Graphene oxide nanosheet (GOns) with a size in the range of 100-200 nm and an average height of 5.0 nm and ZnO nanoparticles (ZnONP) with the size in the range of 100- 250 nm were synthesized. Both GOns and ZnONP caused strong cytotoxicity in breast cancer cells and exhibited fair level of toxicity against normal cells such as HaCaT and 3T3. However, BLA-functionalized GOns (FGOns) and ZnONP (FZnONP) exhibited enhanced cytotoxicity against MCF-7 and MDAMB-231 cells, compared to their non-functionalized form (GOns and ZnONP) in a ROS dependent manner, with negligible cytotoxicity against normal cells under the same condition.

9. Both GOns and FGOns were internalised by the cancer cells. FGOns was found to internalize more efficiently than GOns that entered the cells by damaging the cell membrane through its sharp edges. The cytoplasmic damage due to internalization was clearly visible in both the cases.

10. GOns exhibited hemotoxicity beyond a concentration of 10µg/ml whereas the functionalized GOns (FGOns) was observed to be hemocompatible till 333.33µg/ml. However, ZnONP was found hemolytic beyond the concentration of 160 µg/ml, however when functionalized with BLA no hemolysis was observed till 600 µg/ml. Such enhanced compatibility was due to the protein functionalized form of GOns and ZnONP.

11. ZnONP was found equally toxic in breast cancer cells (MDAMB-231 and MCF-7) as well as normal cells (HaCaT). When functionalized with bovine α-lactalbumin (FZnONP), induced specific toxicity in breast cancer cells without affecting the normal cells. The toxicity of FZnONP was found to be mediated through ROS generation by the protein layer over ZnONP.

On the whole the present study clearly established that the self-assembled nanostructured lysozyme (snLYZ) and bovine α-lactalbumin (snBLA) proved to be better therapeutic agents in breast cancer cells with excellent biocompatibility.

Chapter 11

Future Work

The following studies are hereby proposed as future work.

1. Detailed in-vivo studies in various animal models followed by histopathological studies for observing biodistribution. Such study will help to validate our in-vitro findings.
2. In-vitro experiments may be performed in cell lines from different types of cancers to observe the applicability of our protein nanoassembly in other cancers other than breast cancers.
3. Detailed study may be performed on the use of protein nanoassembly with various promising anti-cancer drugs.
4. Exploration of protein nanoassembly may be performed in other areas such as biomaterials, tissue engineering and regenerative medicine etc.

Appendix: Supplementary figures

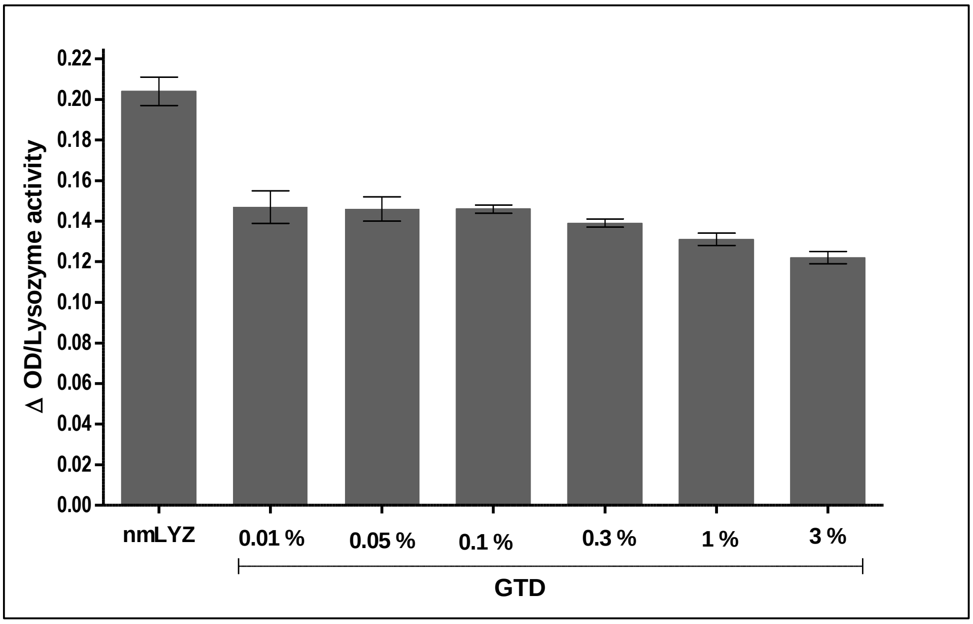

Figure S1. Optimization of glutaraldehyde concentration used in the preparation of nanostructured LYZ. Lytic activity of LYZ in snLYZ prepared with various concentrations of GTD. All data are expressed as Mean ± S.E.M, n = 3.

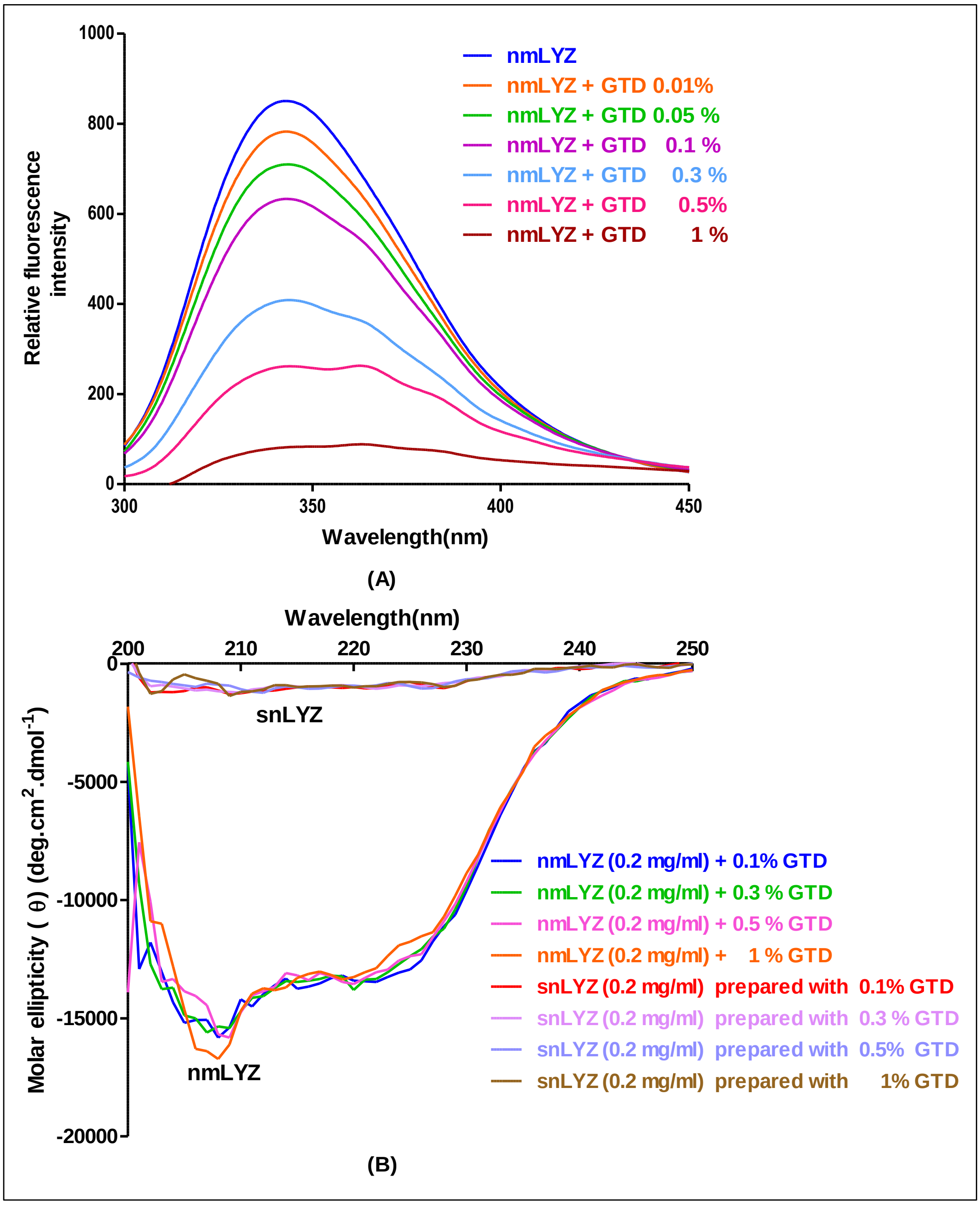

Figure S2. (A)Trp fluorescence spectra of 2 μM of nmLYZ with increasing concentration of GTD. nmLYZ solution was incubated with varying concentration of GTD for 1hr followed by fluorescence spectra measurement. (B) CD spectra of nmLYZ treated with increasing concentration of GTD and snLYZ prepared using increasing concentration of GTD. All data are expressed as mean of three readouts generated from the instrument.

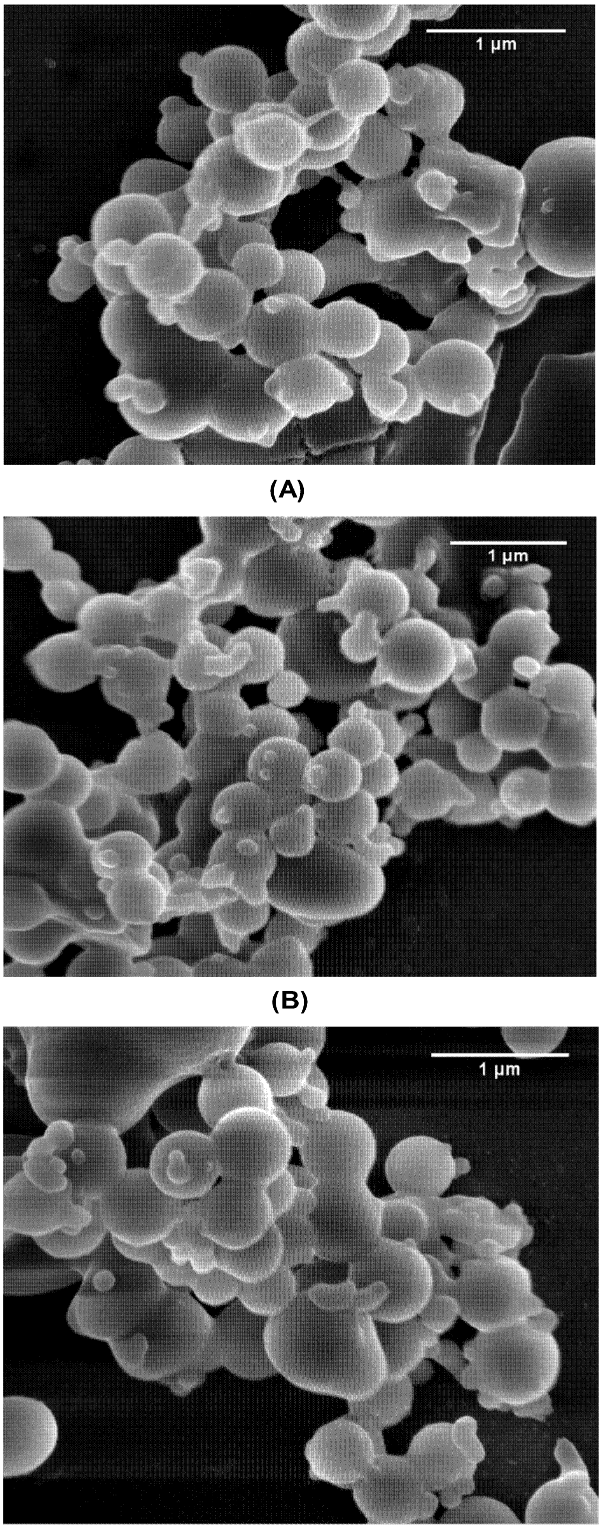

Figure S3 FESEM images of snLYZ prepared using various concentrations of the cross-linker Glutaraldehyde(GTD) **(A)** snLYZ prepared using 0.3% GTD. **(B)** snLYZ prepared using 1 % GTD. **(C)** snLYZ prepared using 3 % GTD.

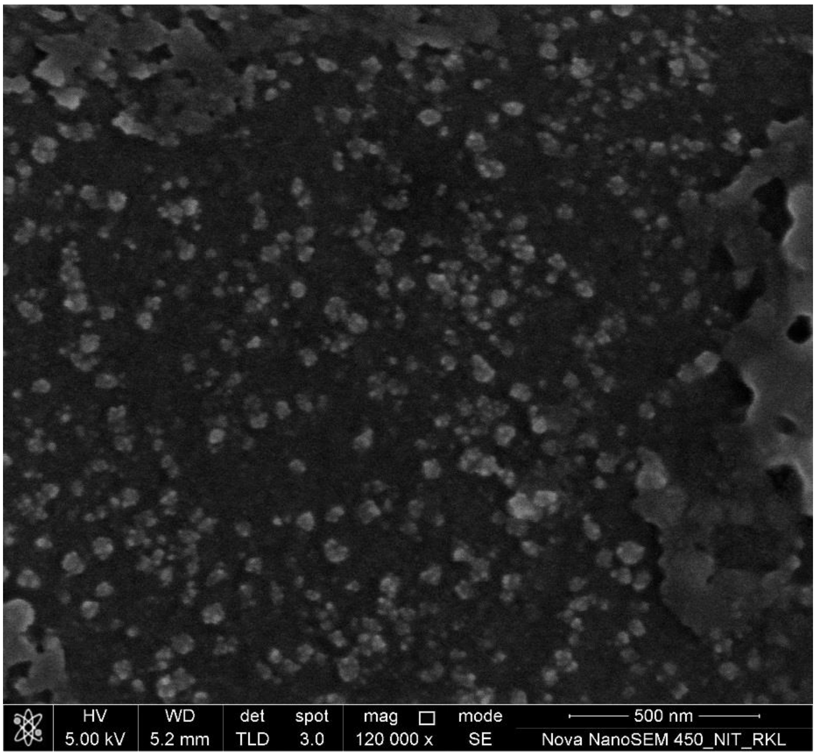
HV
5.00 kV
WD
5.2 mm
det
TLD
spot
3.0
mag □
120 000 x
mode
SE
500 nm
Nova NanoSEM 450_NIT_RKL

(A)

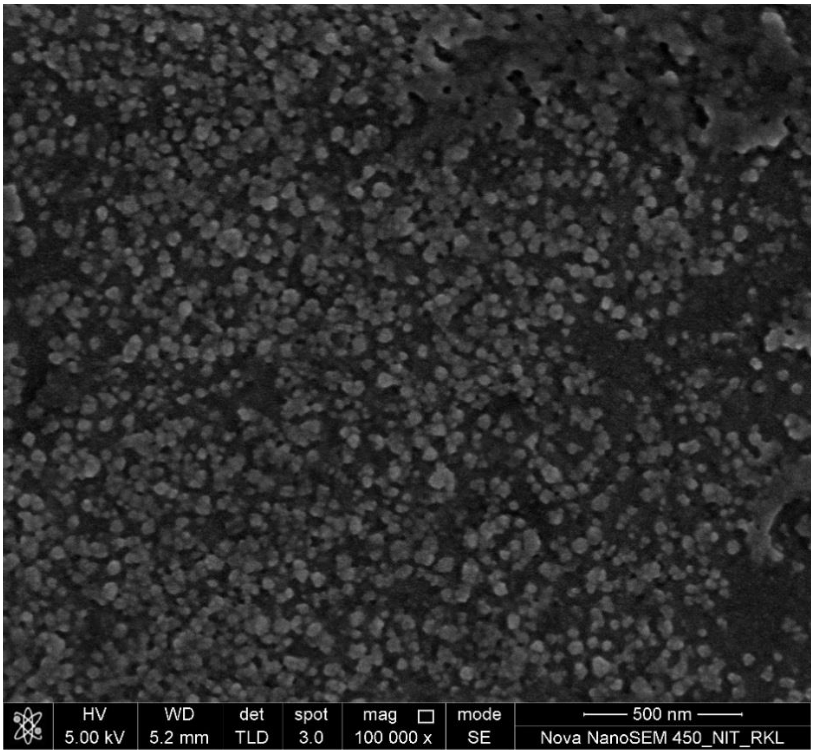
HV
5.00 kV
WD
5.2 mm
det
TLD
spot
3.0
mag □
100 000 x
mode
SE
500 nm
Nova NanoSEM 450_NIT_RKL

(B)

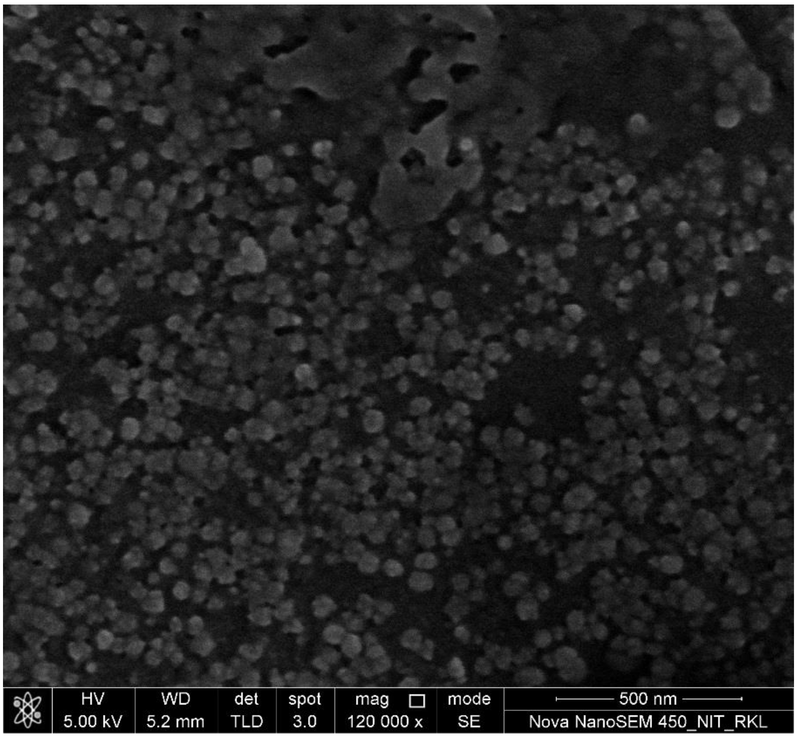
HV
5.00 kV
WD
5.2 mm
det
TLD
spot
3.0
mag ☐
120 000 x
mode
SE
500 nm
Nova NanoSEM 450_NIT_RKL

(C)

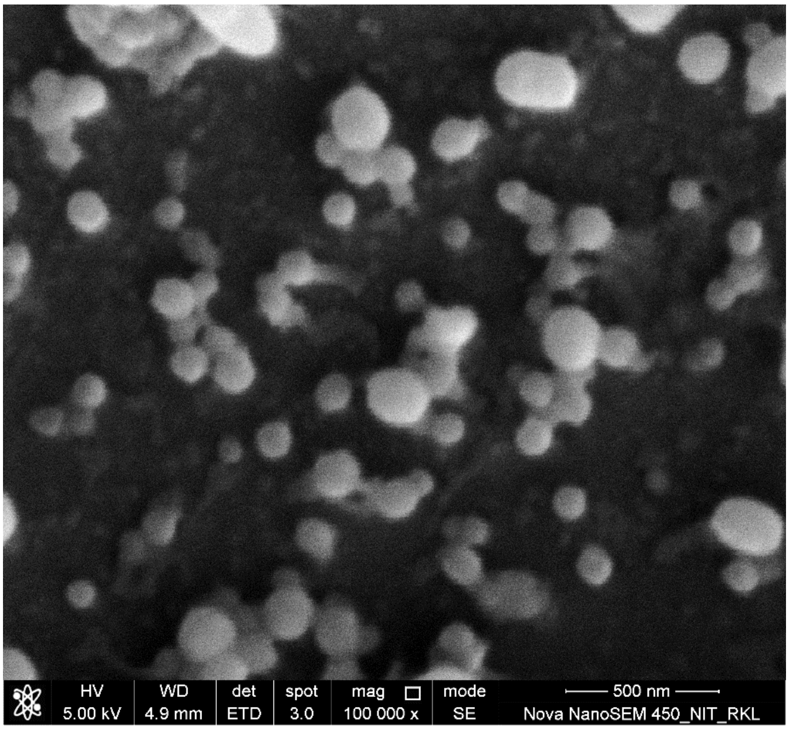
HV
5.00 kV
WD
4.9 mm
det
ETD
spot
3.0
mag ☐
100 000 x
mode
SE
500 nm
Nova NanoSEM 450_NIT_RKL

(D)

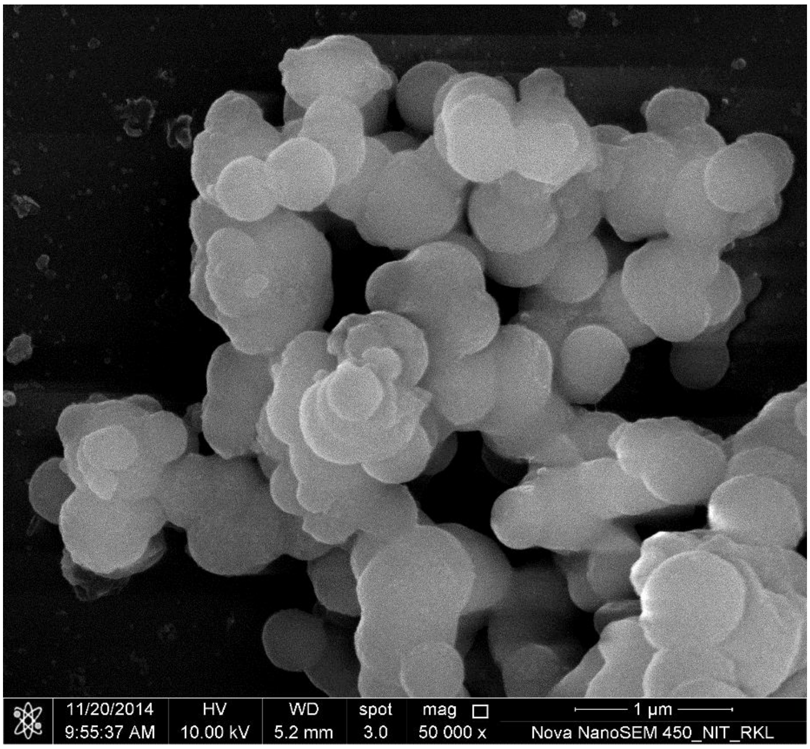

(E)

Figure S4 Optimization of the amount of starting protein material for preparation of protein nanoparticles. (A) BLA 1mg (B) BLA 3mg (C) BLA 5mg (D) BLA 10mg (E) BLA 20mg.

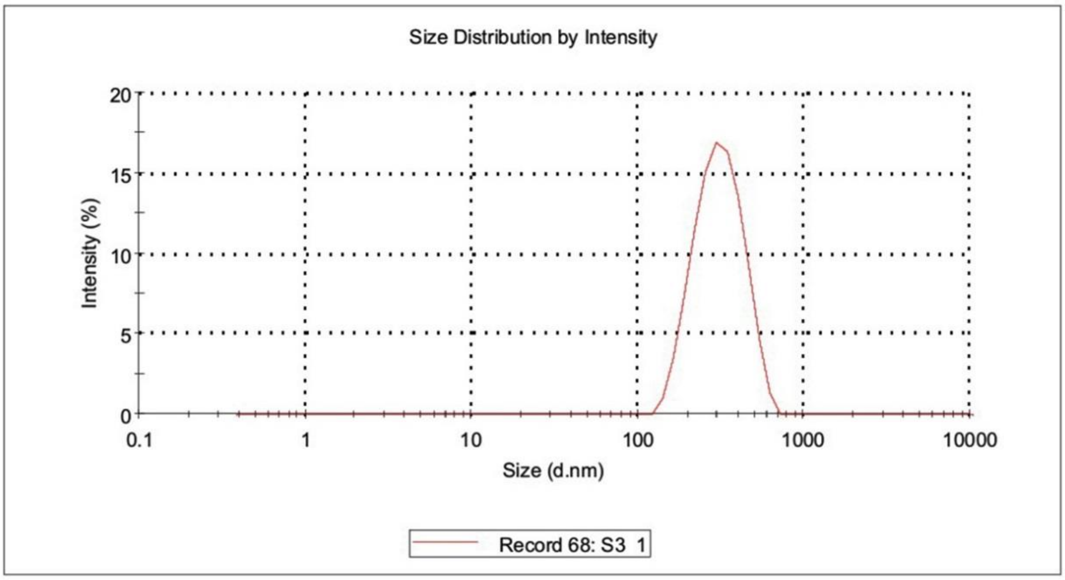

(A)

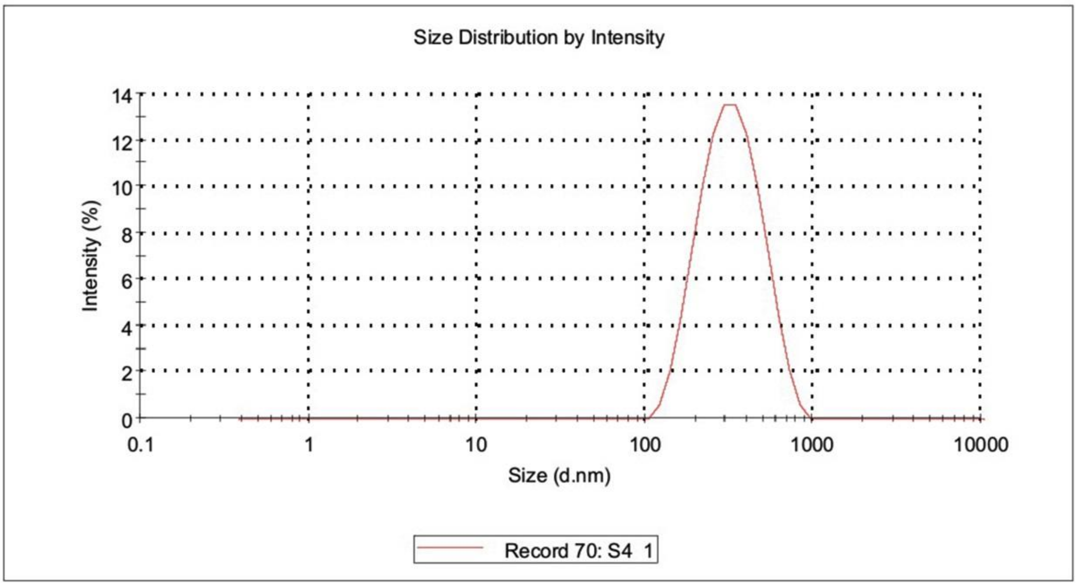
Size Distribution by Intensity
Intensity (%)
14
12
10
8
6
4
2
0
0.1
1
10
100
1000
10000
Size (d.nm)
Record 70: S4 1

(B)

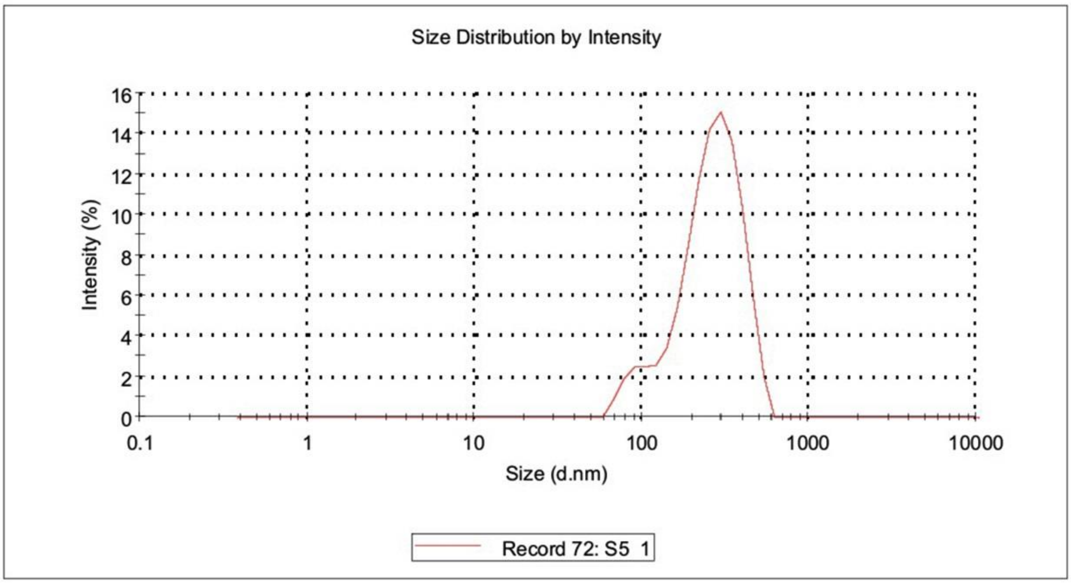
Size Distribution by Intensity
Intensity (%)
16
14
12
10
8
6
4
2
0
0.1
1
10
100
1000
10000
Size (d.nm)
Record 72: S5 1

(C)

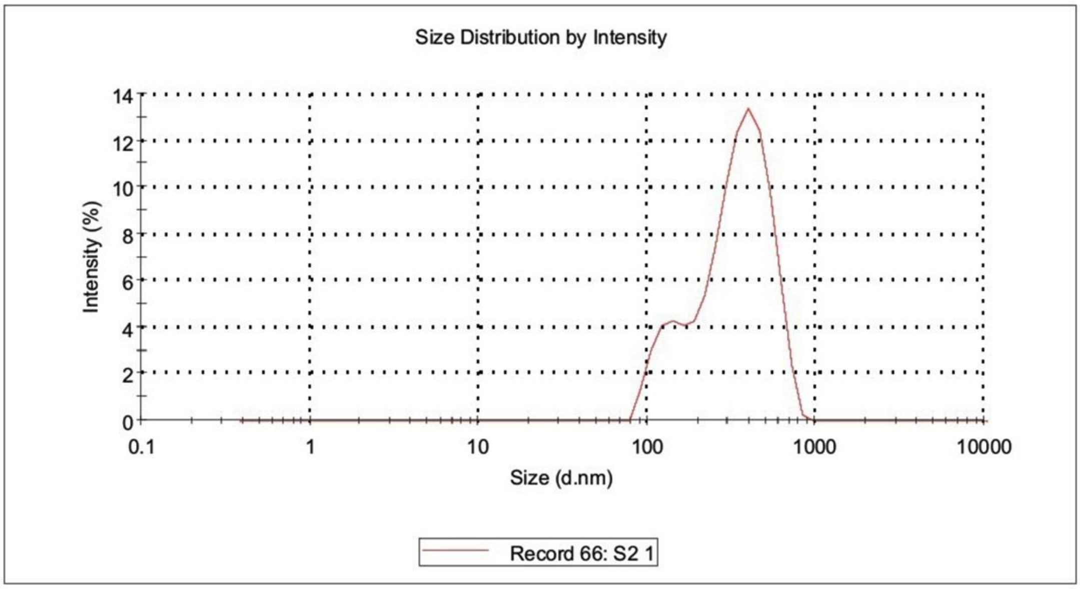

(D)

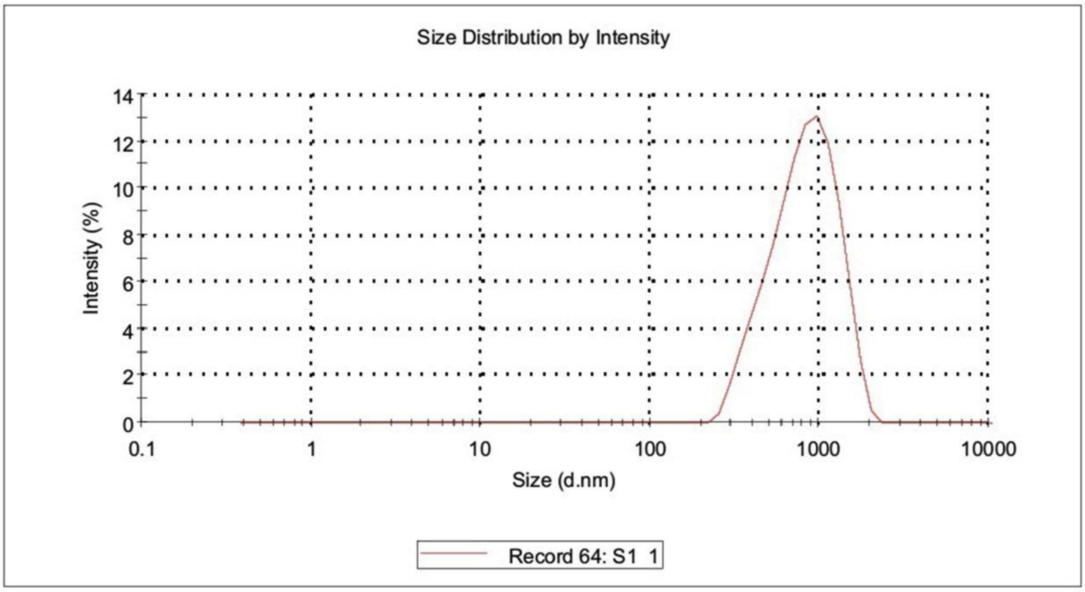

(E)

Figure S5 Optimization of the amount of glutaraldehyde concentration for the preparation of protein nanoparticles using dynamic particle size analysis. (A) 0.1% glutaraldehyde (B) 0.3 % glutaraldehyde (C) 1 % glutaraldehyde (D) 3 % glutaraldehyde (E) 8% glutaraldehyde.

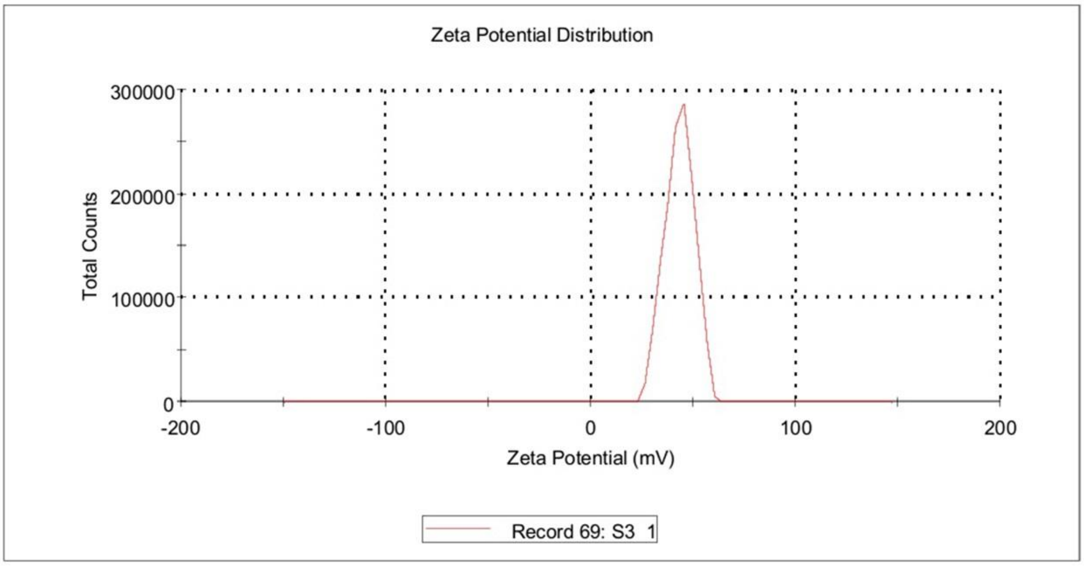
Zeta Potential Distribution
Total Counts
300000
200000
100000
0
-200
-100
0
100
200
Zeta Potential (mV)
Record 69: S3 1

(A)

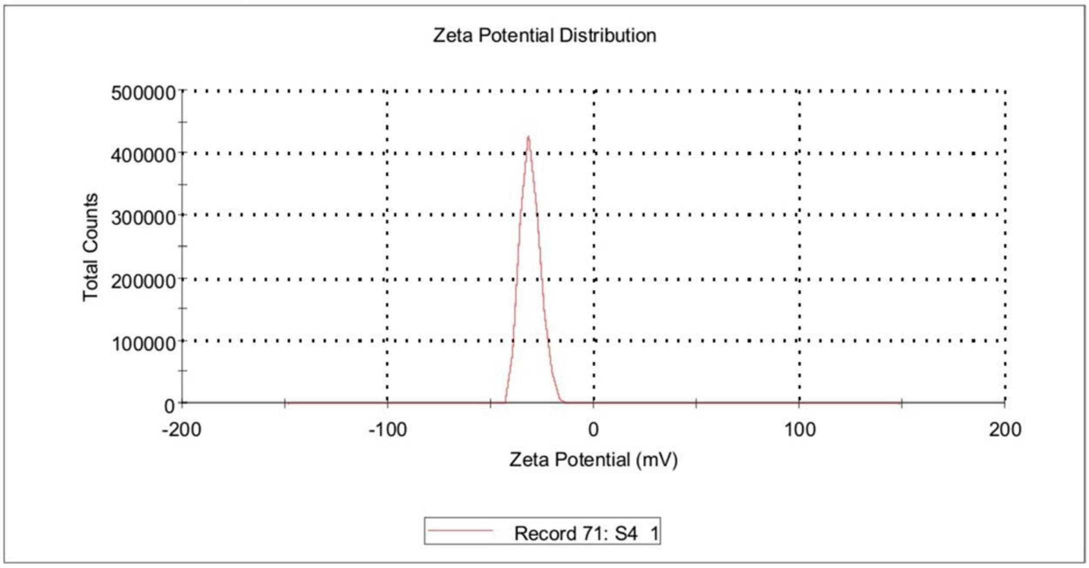
Zeta Potential Distribution
Total Counts
500000
400000
300000
200000
100000
0
-200
-100
0
100
200
Zeta Potential (mV)
Record 71: S4 1

(B)

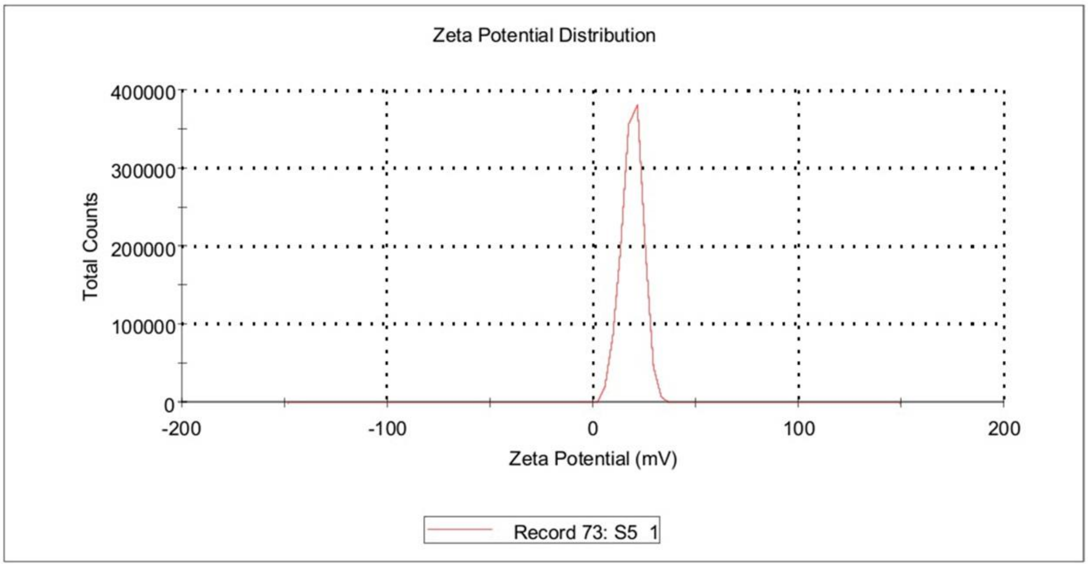
Zeta Potential Distribution
Total Counts
400000
300000
200000
100000
0
-200
-100
0
100
200
Zeta Potential (mV)
Record 73: S5 1

(C)

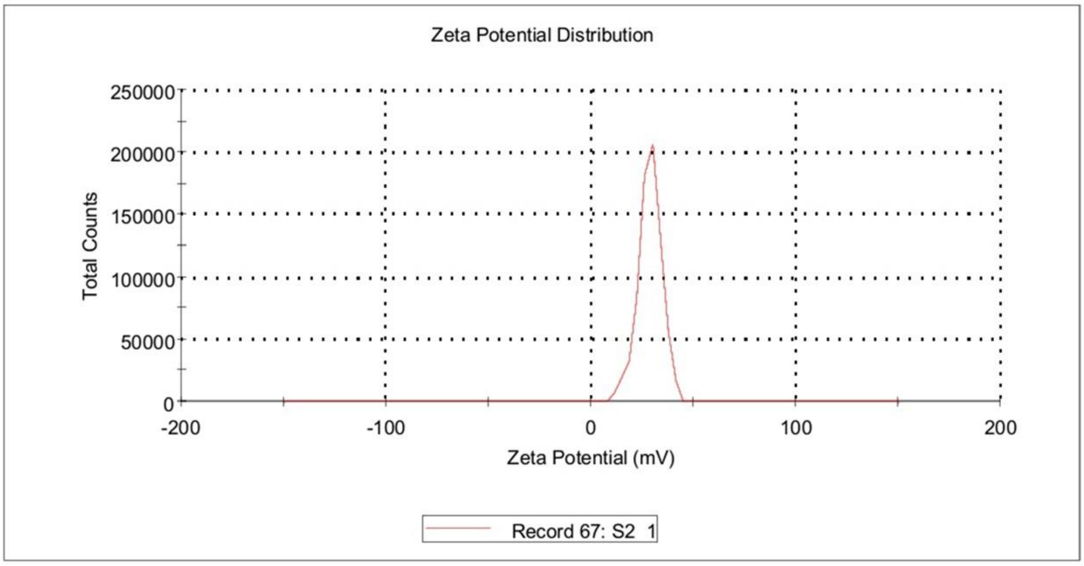
Zeta Potential Distribution
Total Counts
250000
200000
150000
100000
50000
0
-200
-100
0
100
200
Zeta Potential (mV)
Record 67: S2 1

(D)

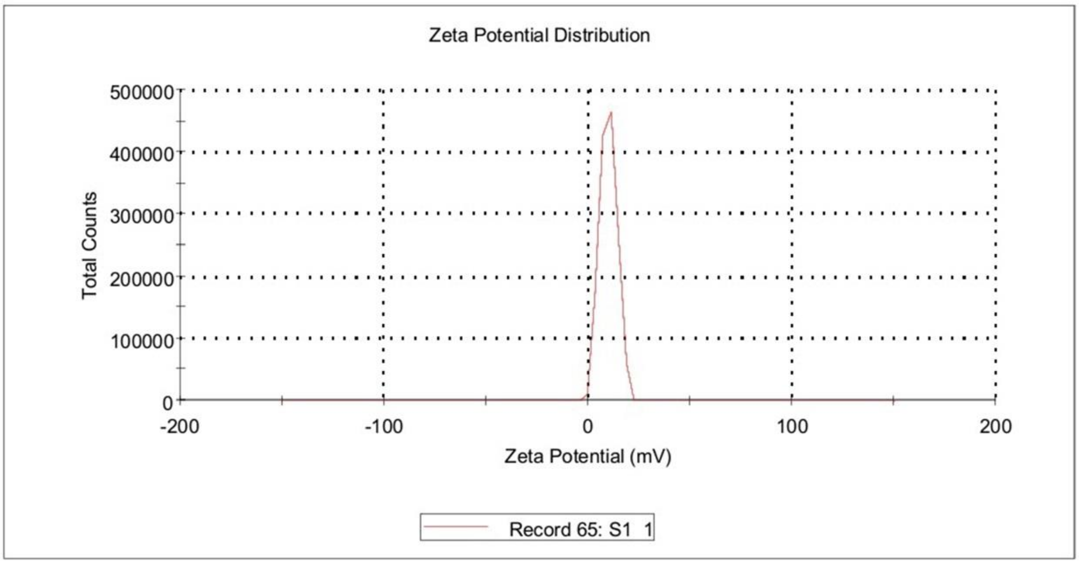

(E)

Figure.S6. Optimization of the amount of glutaraldehyde concentration for the preparation of protein nanoparticles using dynamic particle size analysis. Zeta potential of protein nanoparticles prepared using (A) 0.1 % glutaraldehyde (B) 0.3 % glutaraldehyde (C) 1 % glutaraldehyde (D) 3 % glutaraldehyde (E) 8% glutaraldehyde.

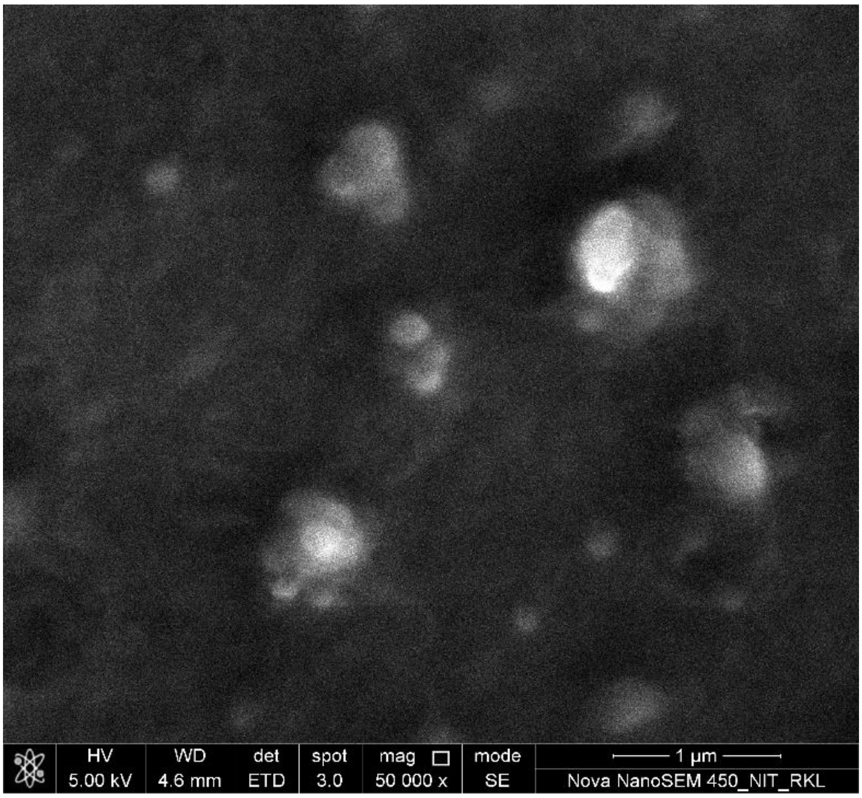
HV
5.00 kV
WD
4.6 mm
det
ETD
spot
3.0
mag
50 000 x
mode
SE
1 μm
Nova NanoSEM 450_NIT_RKL

(A)

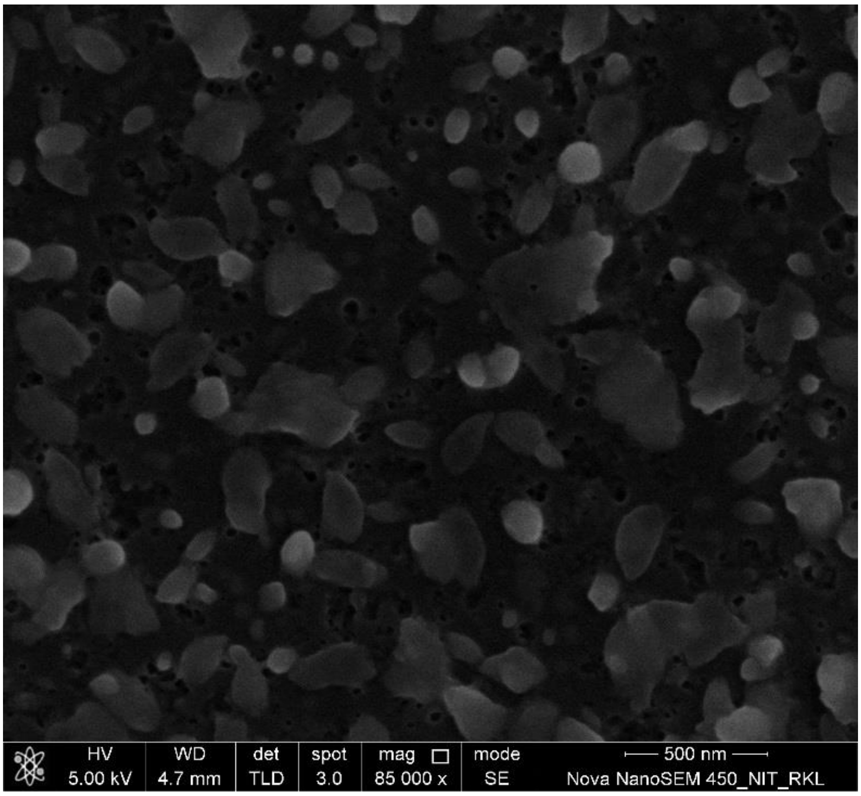
HV
5.00 kV
WD
4.7 mm
det
TLD
spot
3.0
mag
85 000 x
mode
SE
500 nm
Nova NanoSEM 450_NIT_RKL

(B)

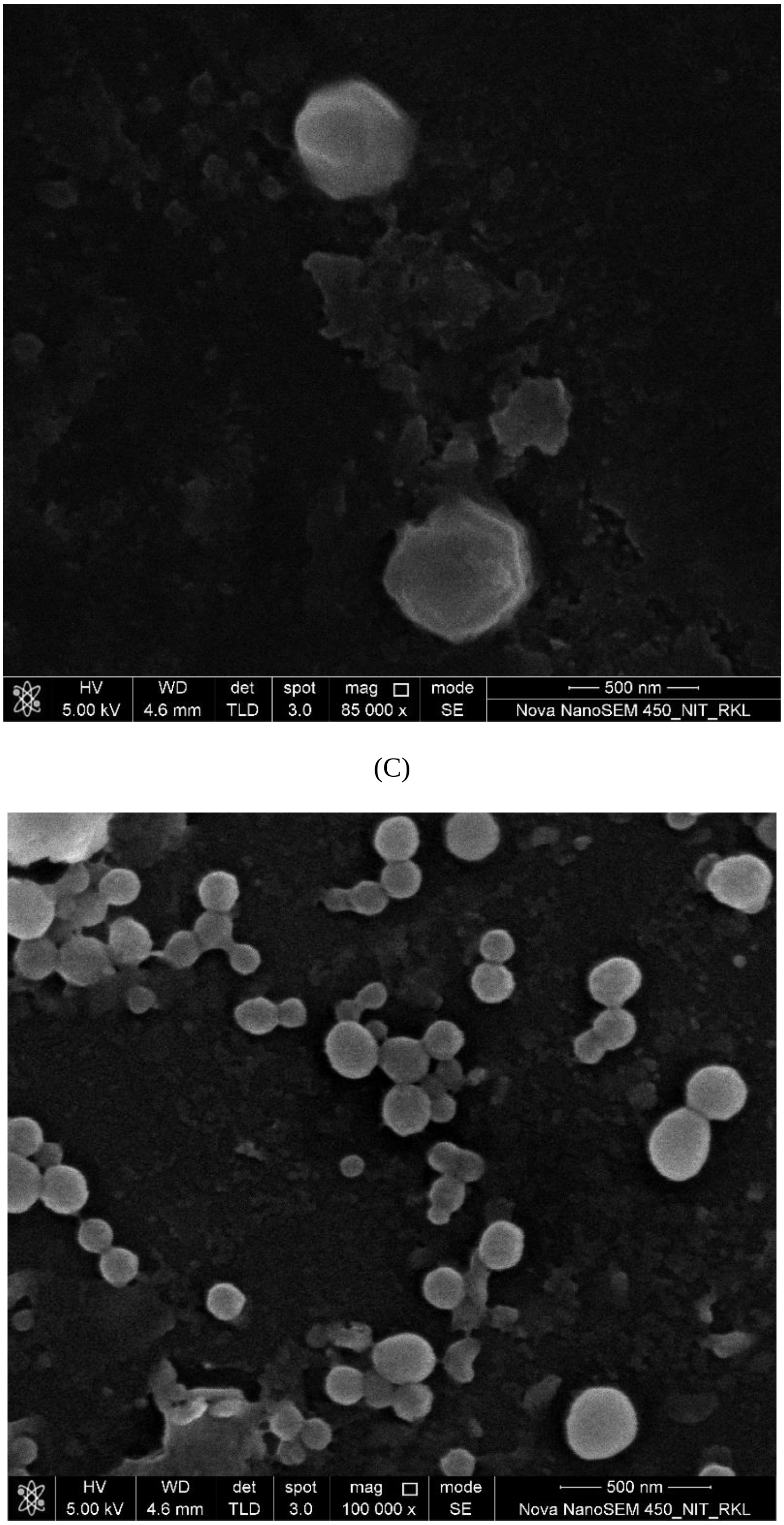

(C)

(D)

Figure S7 Optimization of the duration of glutaraldehyde crosslinking process for the preparation of protein nanoparticles (A) 1h (B) 3h (C) 5h (D) 8h.

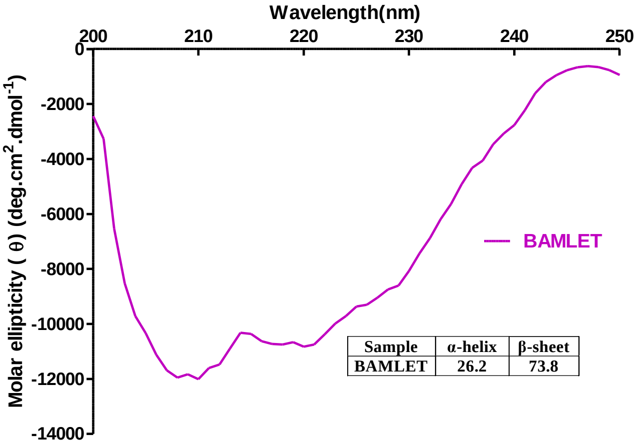

Sample	α-helix	β-sheet
BAMLET	26.2	73.8

Figure S8 Characterization of prepared BAMLET by CD spectroscopy

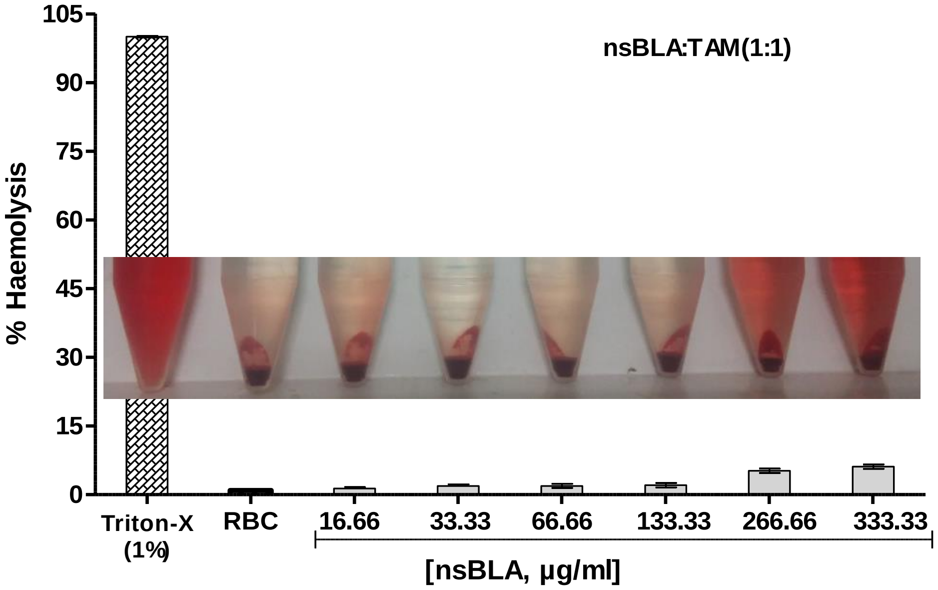

(A)

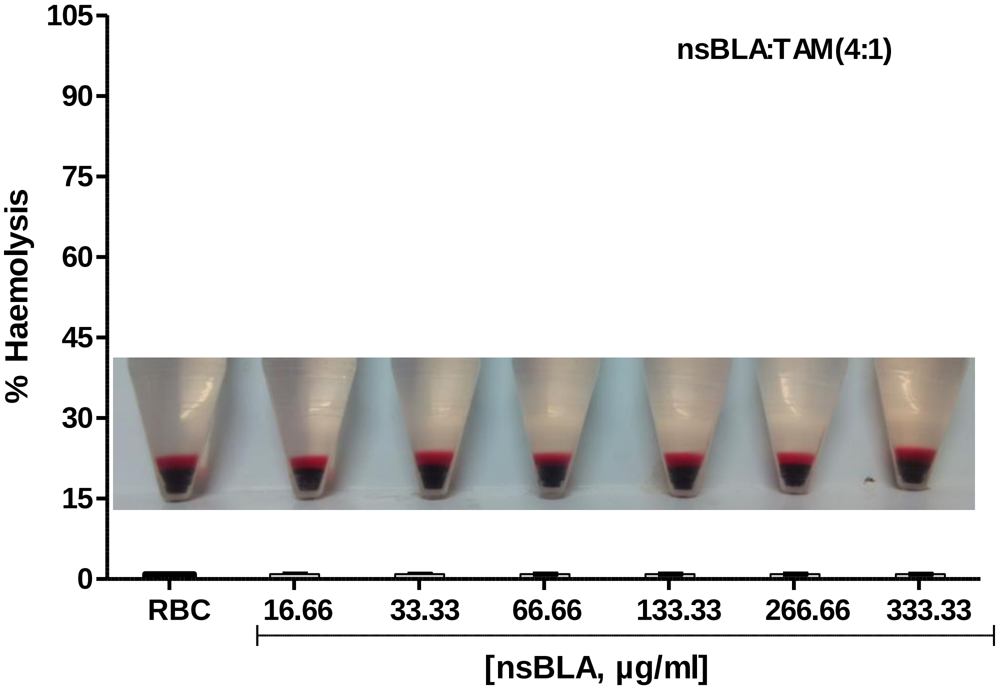
nsBLA:TAM(4:1)
% Haemolysis
105
90
75
60
45
30
15
0
RBC
16.66
33.33
66.66
133.33
266.66
333.33
[nsBLA, µg/ml]

(B)

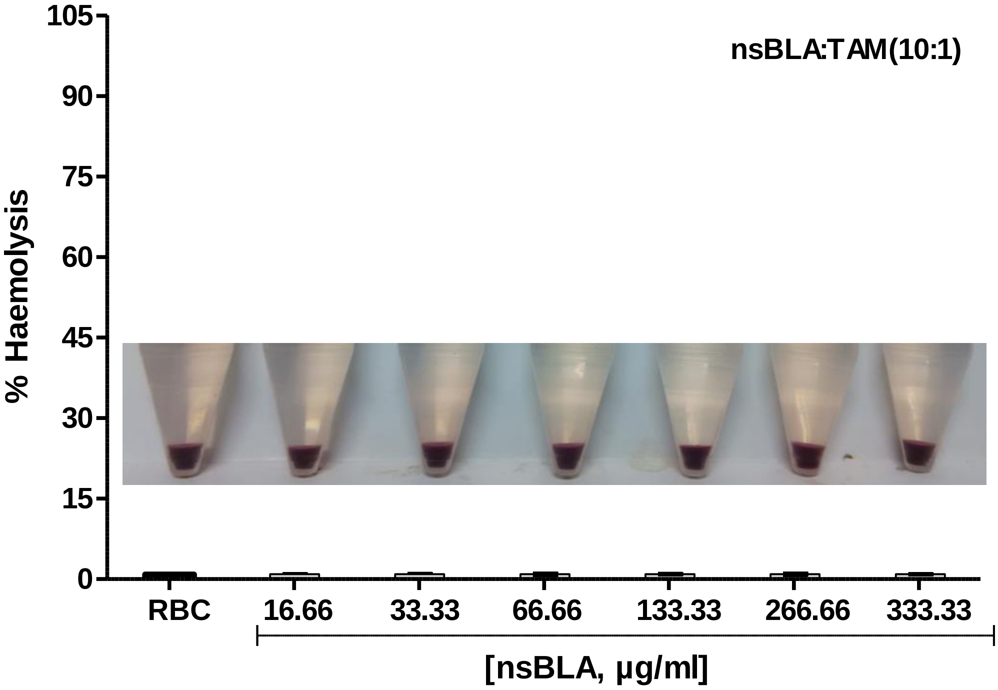
nsBLA:TAM(10:1)
% Haemolysis
105
90
75
60
45
30
15
0
RBC
16.66
33.33
66.66
133.33
266.66
333.33
[nsBLA, µg/ml]

(C)

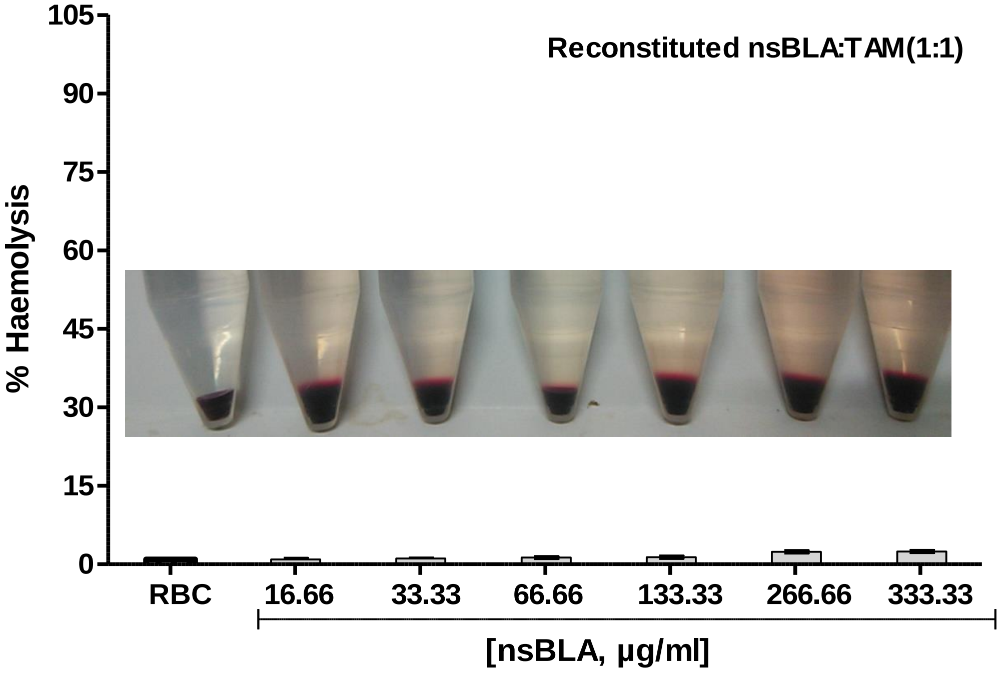
Reconstituted nsBLA:TAM(1:1)
% Haemolysis
105
90
75
60
45
30
15
0
RBC
16.66
33.33
66.66
133.33
266.66
333.33
[nsBLA, µg/ml]

(

D)

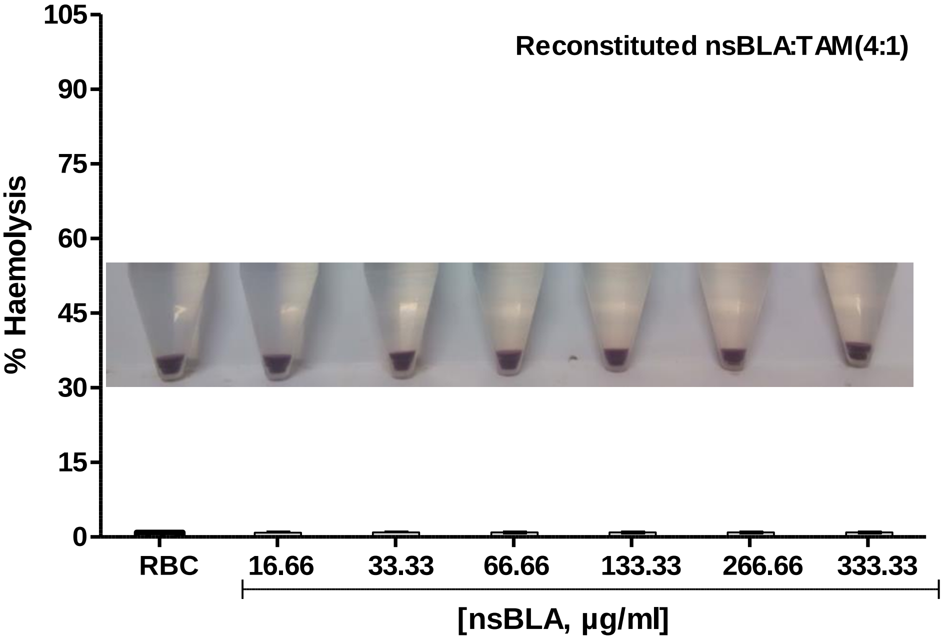
Reconstituted nsBLA:TAM(4:1)
% Haemolysis
105
90
75
60
45
30
15
0
RBC
16.66
33.33
66.66
133.33
266.66
333.33
[nsBLA, µg/ml]

(E)

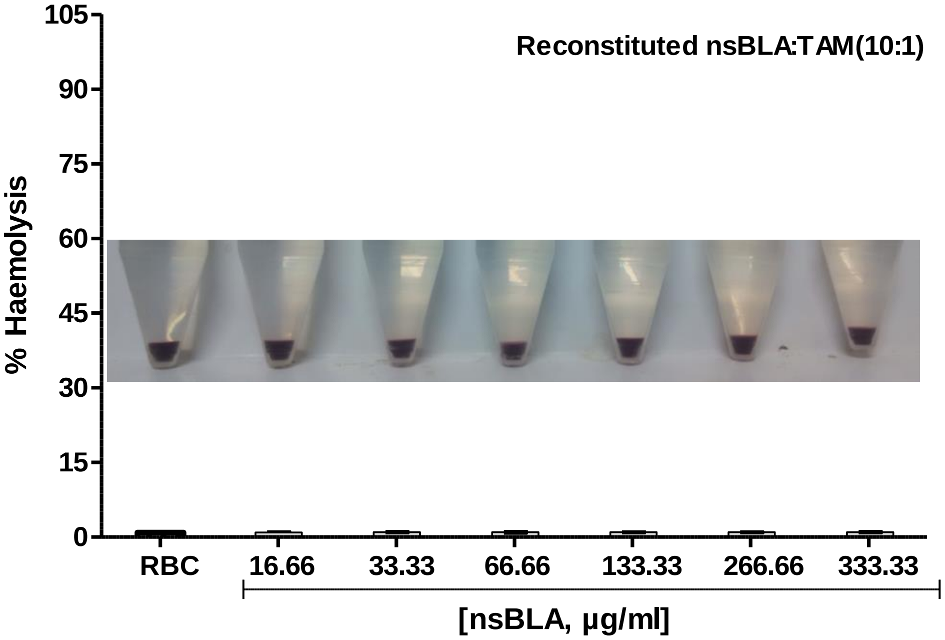

(F)

Fig.S9 Haemolysis assay of various samples (A) snBLA: TAM (1:1), (B) snBLA: TAM (4:1), (C) snBLA: TAM (10:1), (D) snBLA: TAM (1:1 reconstituted), (E) snBLA: TAM (4:1 reconstituted) and (F) snBLA: TAM (10:1 reconstituted).

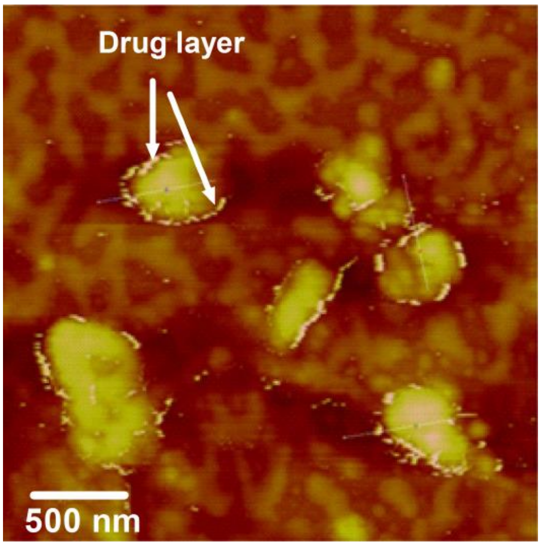

Figure S11. AFM image of sLYZ-TAM conjugate clearly showing the drug layer over the protein nanostructure snLYZ.

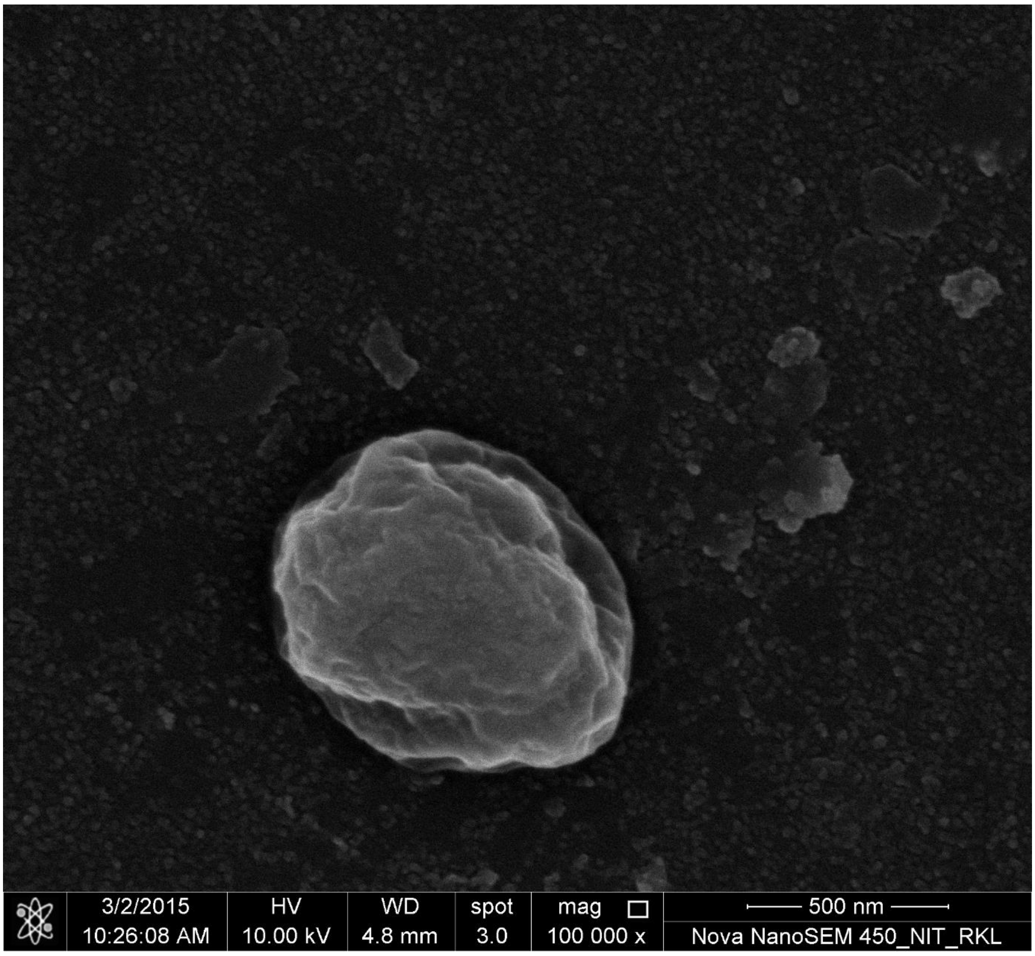

Figure S12. FESEM image of snBSA (self-assembled nanostructured bovine serum albumin) prepared using the same protocol as of snLYZ.

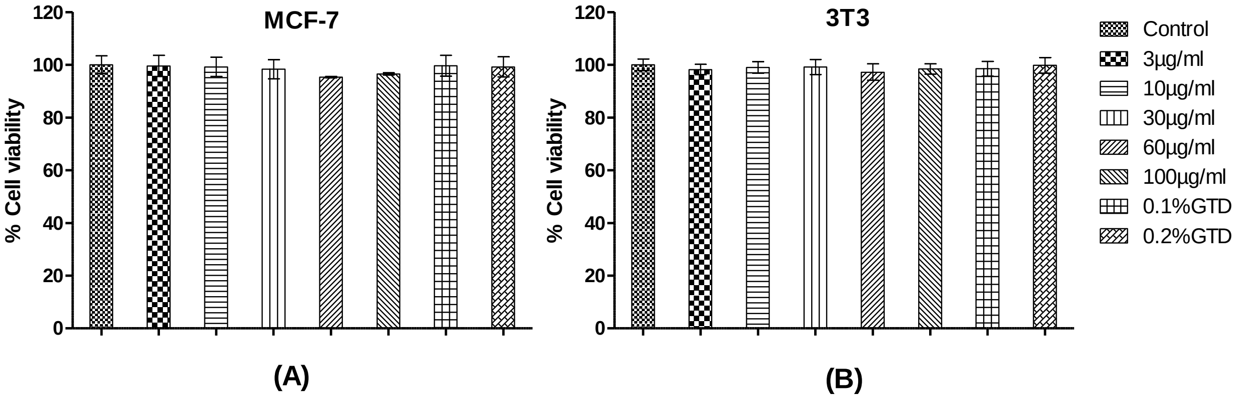

Figure S13. Cytotoxicity study of snBSA (self-assembled nanostructured BSA) by MTT assay (A) MCF-7 breast cancer cells and (B) murine fibroblast cells 3T3. Glutaraldehyde 0.1% and 0.2% was used as control. All data are expressed as Mean ± S.E.M, n =3.

REFERENCES

Adams DJ, Holtzmann K, Schneider C, et al. (2007) Self-assembly of surfactant-like peptides. Langmuir 23:12729-12736.

Aguzzi A and O'Connor T (2010) Protein aggregation diseases: pathogenicity and therapeutic perspectives. Nat Rev Drug Discov 9:237-248.

Akhavan O and Ghaderi E (2010) Toxicity of graphene and graphene oxide nanowalls against bacteria. ACS Nano 4:5731-5736.

Andey T, Sudhakar G, Marepally S, et al. (2015) Lipid nanocarriers of a lipid-conjugated estrogenic derivative inhibit tumor growth and enhance cisplatin activity against triple-negative Breast cancer: pharmacokinetic and efficacy evaluation. Mol Pharm 12:1105-1120.

Arroyo-Maya IJ, Rodiles-Lopez JO, Cornejo-Mazon M, et al. (2012) Effect of different treatments on the ability of alpha-lactalbumin to form nanoparticles. J Dairy Sci 95:6204-6214.

Avachat AM, Oswal YM, Gujar KN, et al. (2014) Preparation and characterization of rivastigmine loaded human serum albumin (HSA) nanoparticles. Curr Drug Deliv 11:359-370.

Baan R, Straif K, Grosse Y, et al. (2007) Carcinogenicity of alcoholic beverages. The Lancet Oncology 8:292-293.

Baek M, Chung H-E, Yu J, et al. (2012) Pharmacokinetics, tissue distribution, and excretion of zinc oxide nanoparticles. International journal of nanomedicine 7:3081.

Balasubramanian SK, Jittiwat J, Manikandan J, et al. (2010) Biodistribution of gold nanoparticles and gene expression changes in the liver and spleen after intravenous administration in rats. Biomaterials 31:2034-2042.

Banerjee R (2011) Trigger-responsive nanoparticles: control switches for cancer therapy. Nanomedicine 6:1657-1660.

Bareford LM and Swaan PW (2007) Endocytic mechanisms for targeted drug delivery. Advanced Drug Delivery Reviews 59:748-758.

Bhowmik A, Das N, Pal U, et al. (2013) 2,2′-Diphenyl-3,3′-Diindolylmethane: A Potent Compound Induces Apoptosis in Breast cancer Cells by Inhibiting EGFR Pathway. PLoS ONE 8:e59798.

Boerakker MJ, Hannink JM, Bomans PHH, et al. (2002) Giant amphiphiles by cofactor reconstitution. Angewandte Chemie International Edition 41:4239-4241.

Bong DT and Ghadiri MR (2001) Self assembling cyclic peptide cylinders as nuclei for crystal engineering. Angewandte Chemie 113:2221-2224.

Bramaud C, Aimar P and Daufin G (1997) Whey protein fractionation: Isoelectric precipitation of α-lactalbumin under gentle heat treatment. Biotechnology and Bioengineering 56:391-397.

Branden CI (1999) Introduction to protein structure, Garland Science.

Brar SS, Petrovich RM, Williams JG and Mason JM (2013) Phosphorylation at Serines 216 and 221 Is Important for Drosophila HeT-A Gag Protein Stability. PLoS One 8 (9).

Brea RJ, Reiriz Cs and Granja JR (2010) Towards functional bionanomaterials based on self-assembling cyclic peptide nanotubes. Chemical Society Reviews 39:1448-1456.

Brunner TJ, Wick P, Manser P, et al. (2006) In vitro cytotoxicity of oxide nanoparticles: comparison to asbestos, silica, and the effect of particle solubility. Environmental science & technology 40:4374-4381.

Burrell MM (1993) Enzymes of molecular biology, Humana Press.

Callerio-Babudieri D and Callerio C (1963) Electron microscope observations of tumour cell cultures in the presence of lysozyme. Nature 200:693-694.

Callerio C (1959) Appearance of Granules in the Cytoplasm of Tumour-Cell Cultures in Contact with Lysozyme. Nature 184:202-203.

Canfield RE (1963) The Amino Acid Sequence of Egg White Lysozyme. Journal of Biological Chemistry 238:2698-2707.

Carlson JCT, Jena SS, Flenniken M, et al. (2006) Chemically controlled self-assembly of protein nanorings. Journal of the American Chemical Society 128:7630-7638.

Carr CW (1953) Studies on the binding of small ions in protein solutions with the use of membrane electrodes. III. The binding of chloride ions in solutions of various proteins. Archives of Biochemistry and Biophysics 46:417-423.

Caseli P and Schumacher H (1955) Inhibizione dello sviluppo del sarcoma di Rous nella cornea e nel derma di pollo a mezzo di proteine basiche. Boll Ocul 34:513-533.

Cegielska-Radziejewska R, Lesnierowski G and Kijowski J (2008) Properties and application of egg white lysozyme and its modified preparations-a review. Polish Journal of Food and Nutrition Sciences 58:5-10.

Cella D, Peterman A, Hudgens S, et al. (2003) Measuring the side effects of taxane therapy in oncology. Cancer 98:822-831.

Chakraborti S, Chatterjee T, Joshi P, et al. (2009) Structure and Activity of Lysozyme on Binding to ZnO Nanoparticles. Langmuir 26:3506-3513.

Chang Y, Yang ST, Liu JH, et al. (2010) In vitro toxicity evaluation of graphene oxide on A549 cells. Toxicol Lett 200:201-210.

Chen J, Peng H, Wang X, et al. (2014) Graphene oxide exhibits broad-spectrum antimicrobial activity against bacterial phytopathogens and fungal conidia by intertwining and membrane perturbation. Nanoscale 6:1879-1889.

Cherny I and Gazit E (2008) Amyloids: not only pathological agents but also ordered nanomaterials. Angewandte Chemie International Edition 47:4062-4069.

Chou T-F, So C, White BR, et al. (2008) Enzyme nanorings. ACS Nano 2:2519-2525.

Chung W-J, Oh J-W, Kwak K, et al. (2011) Biomimetic self-templating supramolecular structures. Nature 478:364-368.

Ciryam P, Tartaglia GG, Morimoto RI, et al. (2013) Widespread aggregation and neurodegenerative diseases are associated with supersaturated proteins. Cell Rep 5:781-790.

Conn MM and Rebek J (1997) Self-assembling capsules. Chemical reviews 97:1647-1668.

Corr SJ, Raoof M, Cisneros BT, et al. (2013) Cytotoxicity and variant cellular internalization behavior of water-soluble sulfonated nanographene sheets in liver cancer cells. Nanoscale Res Lett 8:208.

Cui H, Webber MJ and Stupp SI (2010) Self assembly of peptide amphiphiles: From molecules to nanostructures to biomaterials. Peptide Science 94:1-18.

Diarrassouba F, Remondetto G, Garrait G, Alvarez P, Beyssac E and Subirade M (2015) Self-assembly of Î²-lactoglobulin and egg white lysozyme as a potential carrier for nutraceuticals. Food Chemistry 173:203-209.

Dolman ME, van Dorenmalen KM, Pieters EH, et al. (2012) Imatinib-ULS-lysozyme: a proximal tubular cell-targeted conjugate of imatinib for the treatment of renal diseases. J Control Release 157:461-468.

Dong Y, Shao J, Chen C, et al. (2012) Blue luminescent graphene quantum dots and graphene oxide prepared by tuning the carbonization degree of citric acid. Carbon 50:4738-4743.

Dreyer DR, Park S, Bielawski CW, et al. (2010) The chemistry of graphene oxide. Chemical Society Reviews 39:228-240.

Duval-Terri C, Huguet J and Muller G (2003) Self-assembly and hydrophobic clusters of amphiphilic polysaccharides. Colloids and Surfaces A: Physicochemical and Engineering Aspects 220:105-115.

Eda G, Lin YY, Mattevi C, et al. (2010) Blue photoluminescence from chemically derived graphene oxide. Adv Mater 22:505-509.

Engel MF, van Mierlo CP and Visser AJ (2002) Kinetic and structural characterization of adsorption-induced unfolding of bovine alpha -lactalbumin. J Biol Chem 277:10922-10930.

Erika N, Hirofumi M, Hiroko T, et al. (2014) Graphene oxide coating facilitates the bioactivity of scaffold material for tissue engineering. Japanese Journal of Applied Physics 53:06JD04.

Fan Z and Lu JG (2005) Zinc oxide nanostructures: synthesis and properties. Journal of nanoscience and nanotechnology 5:1561-1573.

Ferlay J, Shin HR, Bray F, et al. (2010) Estimates of worldwide burden of cancer in 2008: GLOBOCAN 2008. Int J Cancer 127:2893-2917.

Fitzmaurice C, Dicker D, Pain A, et al. (2015) The Global Burden of Cancer 2013. JAMA Oncol 1:505-527.

Fotin A, Cheng Y, Sliz P, et al. (2004) Molecular model for a complete clathrin lattice from electron cryomicroscopy. Nature 432:573-579.

Fukawa K, Nishimura N, Irino O, et al. (1982) Experimental studies on antitumor effects of lysozyme. Gan To Kagaku Ryoho 9:915-923.

Gangar A, Fegan A, Kumarapperuma SC, et al. (2013) Targeted delivery of antisense oligonucleotides by chemically self-assembled nanostructures. Mol Pharm 10:3514-3518.

Gasior-Chrzan B (1988) Clinical trial of lysozyme treatment of crural ulcers in humans. Przegl Dermatol 75:435-438.

Gaspar VM, Costa EC, Queiroz JA, et al. (2015) Folate-targeted multifunctional amino acid-chitosan nanoparticles for improved cancer therapy. Pharm Res 32:562-577.

Gazit E (2007) Self-assembled peptide nanostructures: the design of molecular building blocks and their technological utilization. Chemical Society Reviews 36:1263-1269.

Ghadiri MR, Granja JR, Milligan RA, et al. (1993) Self-assembling organic nanotubes based on a cyclic peptide architecture. Nature 366:324-327.

Gradishar WJ, Tjulandin S, Davidson N, et al. (2005) Phase III trial of nanoparticle albumin-bound paclitaxel compared with polyethylated castor oil-based paclitaxel in women with Breast cancer. J Clin Oncol 23:7794-7803.

Graveland-Bikker JF, Koning RI, Koerten HK, et al. (2009) Structural characterization of a-lactalbumin nanotubes. Soft matter 5:2020-2026.

Grill L, Dyer M, Lafferentz L, et al. (2007) Nano-architectures by covalent assembly of molecular building blocks. Nat Nano 2:687-691.

Gromiha MM, Pathak MC, Saraboji K, et al. (2013) Hydrophobic environment is a key factor for the stability of thermophilic proteins. Proteins 81:715-721.

Guo TK, Zhao X, Xie XD, et al. (2007) The anti-proliferative effects of recombinant human lysozyme on human gastric cancer cells. J Int Med Res 35:353-360.

Gupta N, Ahmed I, Steinberg H, et al. (2002) Gemcitabine-induced pulmonary toxicity: case report and review of the literature. American journal of clinical oncology 25:96-100.

Gurunathan S, Han JW, Dayem AA, et al. (2012) Oxidative stress-mediated antibacterial activity of graphene oxide and reduced graphene oxide in Pseudomonas aeruginosa. International Journal of Nanomedicine 7:5901-5914.

Hanahan D and Weinberg RA (2000) The hallmarks of cancer. Cell 100:57-70.

Hartgerink JD, Beniash E and Stupp SI (2001) Self-assembly and mineralization of peptide-amphiphile nanofibers. Science 294:1684-1688.

Hawe A, Sutter M and Jiskoot W (2008) Extrinsic fluorescent dyes as tools for protein characterization. Pharmaceutical research 25:1487-1499.

Hawkins MJ, Soon-Shiong P and Desai N (2008) Protein nanoparticles as drug carriers in clinical medicine. Adv Drug Deliv Rev 60:876-885.

Hayashi T and Hisaeda Y (2002) New functionalization of myoglobin by chemical modification of heme-propionates. Accounts of chemical research 35:35-43.

Hegyi H and Gerstein M (1999) The relationship between protein structure and function: a comprehensive survey with application to the yeast genome. J Mol Biol 288:147-164.

Heine WE, Klein PD and Reeds PJ (1991) The importance of alpha-lactalbumin in infant nutrition. J Nutr 121:277-283.

Horie M, Nishio K, Fujita K, et al. (2009) Protein adsorption of ultrafine metal oxide and its influence on cytotoxicity toward cultured cells. Chemical research in toxicology 22:543-553.

Hosseinkhani H, Hong P-D and Yu D-S (2013) Self-assembled proteins and peptides for regenerative medicine. Chemical reviews 113:4837-4861.

Hu Q, Luo T, Zhong X, et al. (2015) Application status of tamoxifen in endocrine therapy for early Breast cancer. Exp Ther Med 9:2207-2212.

Hu W, Peng C, Luo W, et al. (2010) Graphene-based antibacterial paper. ACS Nano 4:4317-4323.

Hudson SA, Ecroyd H, Kee TW, et al. (2009) The thioflavin T fluorescence assay for amyloid fibril detection can be biased by the presence of exogenous compounds. FEBS J 276:5960-5972.

Hulka BS and Moorman PG (2001) Breast cancer: hormones and other risk factors. Maturitas 38:103-113.

Ibrahim NK, Desai N, Legha S, et al. (2002) Phase I and pharmacokinetic study of ABI-007, a Cremophor-free, protein-stabilized, nanoparticle formulation of paclitaxel. Clin Cancer Res 8:1038-1044.

Iversen NK, Frische S, Thomsen K, et al. (2013) Superparamagnetic iron oxide polyacrylic acid coated gamma-Fe2O3 nanoparticles do not affect kidney function but cause acute effect on the cardiovascular function in healthy mice. Toxicol Appl Pharmacol 266:276-288.

Jabbari E (2009) Targeted delivery with peptidomimetic conjugated self-assembled nanoparticles. Pharm Res 26:612-630.

Jemal A, Bray F, Center MM, et al. (2011) Global cancer statistics. CA: A Cancer Journal for Clinicians 61:69-90.

Jemal A, Center MM, DeSantis C, et al. (2010) Global patterns of cancer incidence and mortality rates and trends. Cancer Epidemiology Biomarkers & Prevention 19:1893-1907.

Jeng HA and Swanson J (2006) Toxicity of metal oxide nanoparticles in mammalian cells. Journal of Environmental Science and Health Part A 41:2699-2711.

Jones N, Ray B, Ranjit KT, et al. (2008) Antibacterial activity of ZnO nanoparticle suspensions on a broad spectrum of microorganisms. FEMS microbiology letters 279:71-76.

Juarez J, Taboada P and Mosquera V (2009) Existence of Different Structural Intermediates on the Fibrillation Pathway of Human Serum Albumin. Biophysical Journal 96:2353-2370.

Jucker M and Walker LC (2013) Self-propagation of pathogenic protein aggregates in neurodegenerative diseases. Nature 501:45-51.

Kang S, Park JB, Lee T-J, et al. (2015) Covalent conjugation of mechanically stiff graphene oxide flakes to three-dimensional collagen scaffolds for osteogenic differentiation of human mesenchymal stem cells. Carbon 83:162-172.

Kaushik JK and Bhat R (1999) A mechanistic analysis of the increase in the thermal stability of proteins in aqueous carboxylic acid salt solutions. Protein Science : A Publication of the Protein Society 8:222-233.

Key J, Hodgson S, Omar RZ, et al. (2006) Meta-analysis of studies of alcohol and Breast cancer with consideration of the methodological issues. Cancer Causes & Control 17:759-770.

Khandelia R, Jaiswal A, Ghosh SS, et al. (2014) Polymer coated gold nanoparticle-protein agglomerates as nanocarriers for hydrophobic drug delivery. Journal of Materials Chemistry B 2:6472-6477.

Kirchhausen T and Harrison SC (1984) Structural domains of clathrin heavy chains. The Journal of cell biology 99:1725-1734.

Kitagishi H, Oohora K, Yamaguchi H, et al. (2007) Supramolecular hemoprotein linear assembly by successive interprotein heme-heme pocket interactions. Journal of the American Chemical Society 129:10326-10327.

Knyazeva EL, Grishchenko VM, Fadeev RS, et al. (2008) Who is Mr. HAMLET? Interaction of human alpha-lactalbumin with monomeric oleic acid. Biochemistry 47:13127-13137.

Koberle D and Thurlimann B (2005) Adjuvant endocrine therapy in postmenopausal Breast cancer patients. The Breast 14:446-451.

Komatsu T (2012) Protein-based nanotubes for biomedical applications. Nanoscale 4:1910-1918.

Kouchakzadeh H, Safavi MS and Shojaosadati SA (2015) Efficient delivery of therapeutic agents by using targeted albumin nanoparticles. Adv Protein Chem Struct Biol 98:121-143.

Kozawa D, Miyauchi Y, Mouri S, et al. (2013) Exploring the Origin of Blue and Ultraviolet Fluorescence in Graphene Oxide. The Journal of Physical Chemistry Letters 4:2035-2040.

Ku SH and Park CB (2013) Myoblast differentiation on graphene oxide. Biomaterials 34:2017-2023.

Kwaambwa HM and Maikokera R (2007) A fluorescence spectroscopic study of a coagulating protein extracted from Moringa oleifera seeds. Colloids and Surfaces B: Biointerfaces 60:213-220.

Kwaambwa HM and Maikokera R (2008) Infrared and circular dichroism spectroscopic characterisation of secondary structure components of a water treatment coagulant protein extracted from Moringa oleifera seeds. Colloids and Surfaces B: Biointerfaces 64:118-125.

Lai JCK, Lai MB, Jandhyam S, et al. (2008) Exposure to titanium dioxide and other metallic oxide nanoparticles induces cytotoxicity on human neural cells and fibroblasts. International Journal of Nanomedicine 3:533-545.

Lai Q, Zhu S, Luo X, et al. (2012) Ultraviolet-visible spectroscopy of graphene oxides. AIP Advances 2:1-5.

Lai Y-T, Tsai K-L, Sawaya MR, et al. (2013) Structure and flexibility of nanoscale protein cages designed by symmetric self-assembly. Journal of the American Chemical Society 135:7738-7743.

Lale SV, Kumar A, Prasad S, et al. (2015) Folic Acid and Trastuzumab Functionalized Redox Responsive Polymersomes for Intracellular Doxorubicin Delivery in Breast cancer. Biomacromolecules 16:1736-1752.

Lammel T, Boisseaux P, Fernandez-Cruz ML, et al. (2013) Internalization and cytotoxicity of graphene oxide and carboxyl graphene nanoplatelets in the human hepatocellular carcinoma cell line Hep G2. Part Fibre Toxicol 10:27.

Leamon CP and Low PS (1991) Delivery of macromolecules into living cells: a method that exploits folate receptor endocytosis. Proc Natl Acad Sci U S A 88:5572-5576.

Lee WC, Lim CH, Shi H, et al. (2011) Origin of enhanced stem cell growth and differentiation on graphene and graphene oxide. ACS Nano 5:7334-7341.

Li Q, Liu C, Zhao X, et al. (2011) Preparation, characterization and targeting of micronized 10-hydroxycamptothecin-loaded folate-conjugated human serum albumin nanoparticles to cancer cells. Int J Nanomedicine 6:397-405.

Li S, Aphale AN, Macwan IG, et al. (2012) Graphene oxide as a quencher for fluorescent assay of amino acids, peptides, and proteins. ACS Appl Mater Interfaces 4:7069-7075.

Li SD, Chen YC, Hackett MJ, et al. (2008) Tumor-targeted delivery of siRNA by self-assembled nanoparticles. Mol Ther 16:163-169.

Li Y, Wen T, Xue C, et al. (2013) RGO LBL modified biomimetic electrochemical sensor for detection of Sildenafil in herbal sexual health products. Biosens Bioelectron 42:287-292.

Liang LJ, Wang Q, Wu T, et al. (2013) Contribution of water molecules in the spontaneous release of protein by graphene sheets. Chemphyschem 14:2902-2909.

Liao K-H, Lin Y-S, Macosko CW, et al. (2011) Cytotoxicity of Graphene Oxide and Graphene in Human Erythrocytes and Skin Fibroblasts. ACS Applied Materials & Interfaces 3:2607-2615.

Lin F, Zhao X, Wang J, et al. (2014) A novel microfluidic chip electrophoresis strategy for simultaneous, label-free, multi-protein detection based on a graphene energy transfer biosensor. Analyst 139:2890-2895.

Lin IC, Su S-L and Kuo C-D (2008) Induction of cell death in RAW 264.7 cells by alpha-lactalbumin. Food and Chemical Toxicology 46:842-853.

Liu H, Zheng F, Cao Q, et al. (2006) Amelioration of oxidant stress by the defensin lysozyme. Am J Physiol Endocrinol Metab 290:E824-832.

Liu Y, Sun J, Cao W, et al. (2011) Dual targeting folate-conjugated hyaluronic acid polymeric micelles for paclitaxel delivery. Int J Pharm 421:160-169.

Liu Z, Robinson JT, Sun X, et al. (2008) PEGylated nanographene oxide for delivery of water-insoluble cancer drugs. Journal of the American Chemical Society 130:10876-10877.

Livney YD (2010) Milk proteins as vehicles for bioactives. Current Opinion in Colloid & Interface Science 15:73-83.

Lu J, Zhao W, Huang Y, et al. (2014) Targeted delivery of Doxorubicin by folic acid-decorated dual functional nanocarrier. Mol Pharm 11:4164-4178.

Lumachi F, Brunello A, Maruzzo M, et al. (2013) Treatment of estrogen receptor-positive Breast cancer. Curr Med Chem 20:596-604.

Ma SF, Nishikawa M, Hyoudou K, et al. (2007) Combining cisplatin with cationized catalase decreases nephrotoxicity while improving antitumor activity. Kidney Int 72:1474-1482.

Madhusudhan A, Reddy GB, Venkatesham M, et al. (2014) Efficient pH dependent drug delivery to target cancer cells by gold nanoparticles capped with carboxymethyl chitosan. Int J Mol Sci 15:8216-8234.

Mandelkow E and Mandelkow E-M (1994) Microtubule structure. Current Opinion in Structural Biology 4:171-179.

Martin ACR, Orengo CA, Hutchinson EG, et al. (1998) Protein folds and functions. Structure 6:875-884.

Matsuura K, Hayashi H, Murasato K, et al. (2011) Trigonal tryptophane zipper as a novel building block for pH-responsive peptide nano-assemblies. Chemical Communications 47:265-267.

Matsuura K, Murasato K and Kimizuka N (2005) Artificial peptide-nanospheres self-assembled from three-way junctions of Î²-sheet-forming peptides. Journal of the American Chemical Society 127:10148-10149.

Matsuurua K (2014) Rational design of self-assembled proteins and peptides for nano-and micro-sized architectures. RSC Advances 4:2942-2953.

Mayer M and Noble M (1994) N-acetyl-L-cysteine is a pluripotent protector against cell death and enhancer of trophic factor-mediated cell survival in vitro. Proc Natl Acad Sci U S A 91:7496-7500.

McCarty MF and Whitaker J (2010) Manipulating tumor acidification as a cancer treatment strategy. Altern Med Rev 15:264-272.

McMillan R, Meeks B, Bensebaa F, et al. (2001) Cell adhesion peptide modification of goldcoated polyurethanes for vascular endothelial cell adhesion. Journal of biomedical materials research 54:272-283.

Miele E, Spinelli GP, Tomao F, et al. (2009) Albumin-bound formulation of paclitaxel (Abraxane ABI-007) in the treatment of Breast cancer. Int J Nanomedicine 4:99-105.

Mok KH, Pettersson J, Orrenius S, et al. (2007) HAMLET, protein folding, and tumor cell death. Biochem Biophys Res Commun 354:1-7.

Morikawa M-a, Takano A, Tao S, et al. (2012) Biopolymer-Encapsulated Protein Microcapsules Spontaneously Formed at the Ionic Liquidâ€“Water Interface. Biomacromolecules 13:4075-4080.

Mu Q, Su G, Li L, et al. (2012) Size-dependent cell uptake of protein-coated graphene oxide nanosheets. ACS Appl Mater Interfaces 4:2259-2266.

Munshi A and Singh P (2008) Tamoxifen in Breast cancer: Not so easy to write off. The Breast 17:121-124.

Nair S, Sasidharan A, Divya Rani VV, et al. (2009) Role of size scale of ZnO nanoparticles and microparticles on toxicity toward bacteria and osteoblast cancer cells. Journal of Materials Science: Materials in Medicine 20:235-241.

Neklesa TK, Tae HS, Schneekloth AR, et al. (2011) Small-molecule hydrophobic tagging-induced degradation of HaloTag fusion proteins. Nat Chem Biol 7:538-543.

Ng A, Heynen M, Luensmann D, et al. (2013) Optimization of a fluorescence-based lysozyme activity assay for contact lens studies. Curr Eye Res 38:252-259.

Niece KL, Hartgerink JD, Donners JJJM, et al. (2003) Self-assembly combining two bioactive peptide-amphiphile molecules into nanofibers by electrostatic attraction. Journal of the American Chemical Society 125:7146-7147.

Niidome T, Yamauchi H, Takahashi K, et al. (2014) Hydrophobic cavity formed by oligopeptide for doxorubicin delivery based on dendritic poly(L-lysine). J Biomater Sci Polym Ed 25:1362-1373.

Olson AJ, Bricogne G and Harrison SC (1983) Structure of tomato bushy stunt virus IV: The virus particle at 2Â· 9resolution. Journal of molecular biology 171:61-93.

Pace CN, Fu H, Fryar KL, et al. (2011) Contribution of hydrophobic interactions to protein stability. J Mol Biol 408:514-528.

Padilla JE, Colovos C and Yeates TO (2001) Nanohedra: using symmetry to design self assembling protein cages, layers, crystals, and filaments. Proc Natl Acad Sci U S A 98:2217 - 2221.

Palmer LC and Stupp SI (2008) Molecular self-assembly into one-dimensional nanostructures. Accounts of chemical research 41:1674-1684.

Panda JJ, Varshney A and Chauhan VS (2013) Self-assembled nanoparticles based on modified cationic dipeptides and DNA: novel systems for gene delivery. J Nanobiotechnology 11:18.

Parodi PW (2007) A Role for Milk Proteins and their Peptides in Cancer Prevention. Current Pharmaceutical Design 13:813-828.

Permanetter W and Meister P (1984) Distribution of lysozyme (Muramidase) and a 1-antichymotrypsin in normal and neoplastic epithelial tissues: A survey. Acta histochemica 74:173-179.

Philp D and Stoddart JF (1996) Self • assembly in natural and unnatural systems. Angewandte Chemie International Edition in English 35:1154-1196.

Price WS, Tsuchiya F and Arata Y (1999) Lysozyme aggregation and solution properties studied using PGSE NMR diffusion measurements. Journal of the American Chemical Society 121:11503-11512.

Ponnusamy VK, Mani V, Chen SM, et al. (2014) Rapid microwave assisted synthesis of graphene nanosheets/polyethyleneimine/gold nanoparticle composite and its application to the selective electrochemical determination of dopamine. Talanta 120:148-157.

Prasad AS (2008) Clinical, immunological, anti-inflammatory and antioxidant roles of zinc. Experimental gerontology 43:370-377.

Purcell M, Neault JF and Tajmir-Riahi HA (2000) Interaction of taxol with human serum albumin. Biochim Biophys Acta 1478:61-68.

Qin XC, Guo ZY, Liu ZM, et al. (2013) Folic acid-conjugated graphene oxide for cancer targeted chemo-photothermal therapy. Journal of Photochemistry and Photobiology B: Biology 120:156-162.

Rammer P, Groth-Pedersen L, Kirkegaard T, et al. (2010) BAMLET activates a lysosomal cell death program in cancer cells. Mol Cancer Ther 9:24-32.

Rebek J (1996) Assembly and encapsulation with self-complementary molecules. Chemical Society Reviews 25:255-264.

Reches M and Gazit E (2003) Casting metal nanowires within discrete self-assembled peptide nanotubes. Science 300:625-627.

Reches M and Gazit E (2006) Controlled patterning of aligned self-assembled peptide nanotubes. Nature nanotechnology 1:195-200.

Ren W, Fang Y and Wang E (2011) A binary functional substrate for enrichment and ultrasensitive SERS spectroscopic detection of folic acid using graphene oxide/Ag nanoparticle hybrids. ACS Nano 5:6425-6433.

Rincker MJ, Hill GM, Link JE, et al. (2005) Effects of dietary zinc and iron supplementation on mineral excretion, body composition, and mineral status of nursery pigs. Journal of Animal Science 83:2762-2774.

Ross CA and Poirier MA (2004) Protein aggregation and neurodegenerative disease. Nat Med 10 Suppl:S10-17.

Rubio CA (2014) The natural antimicrobial enzyme lysozyme is up-regulated in gastrointestinal inflammatory conditions. Pathogens 3:73-92.

Ryoo SR, Kim YK, Kim MH, et al. (2010) Behaviors of NIH-3T3 fibroblasts on graphene/carbon nanotubes: proliferation, focal adhesion, and gene transfection studies. ACS Nano 4:6587-6598.

Sahu D, Kannan GM, Vijayaraghavan R, et al. (2013) Nanosized zinc oxide induces toxicity in human lung cells. ISRN toxicology 2013.

Saladi SV, Wong PG, Trivedi AR, et al. (2013) BRG1 promotes survival of UV-irradiated melanoma cells by cooperating with MITF to activate the melanoma inhibitor of apoptosis gene. Pigment Cell & Melanoma Research 26:377-391.

Sanders JK (1995) Supramolecular Chemistry. Concepts and Perspectives. Von J.-M. Lehn. VCH Verlagsgesellschaft, Weinheim, 1995. 271 S., geb. 128.00 DM/Broschur 58.00 DM. - ISBN 3-527-29312-4/3-527-29311-6. Angewandte Chemie 107:2617-2617.

Sava G (1989) Reduction of B16 melanoma metastases by oral administration of egg-white lysozyme. Cancer Chemother Pharmacol 25:221-222.

Sava G, Benetti A, Ceschia V, et al. (1989) Lysozyme and cancer: role of exogenous lysozyme as anticancer agent (review). Anticancer Res 9:583-591.

Sava G, Perissin L and Zorzet S (1988) Antimetastatic action of orally administered lysozyme in mice bearing Lewis lung carcinoma. Clin Exp Metastasis 6:245-253.

Sava G, Perissin L, Zorzet S, et al. (1986) Antineoplastic effects of egg-white lysozyme in mice bearing solid metastasizing tumors. Anticancer Res 6:183-186.

Scown TM, van Aerle R, Johnston BD, et al. (2009) High Doses of Intravenously Administered Titanium Dioxide Nanoparticles Accumulate in the Kidneys of Rainbow Trout but with no Observable Impairment of Renal Function. Toxicological Sciences 109:372-380.

Shen J, Shi M, Yan B, et al. (2010) Covalent attaching protein to graphene oxide via diimide-activated amidation. Colloids Surf B Biointerfaces 81:434-438.

Singh SK, Singh MK, Kulkarni PP, et al. (2012) Amine-modified graphene: thrombo-protective safer alternative to graphene oxide for biomedical applications. ACS Nano 6:2731-2740.

Sohl CD, Isin EM, Eoff RL, et al. (2008) Cooperativity in oxidation reactions catalyzed by cytochrome p450 1A2 highly cooperative pyrene hydroxylation and multiphasic kinetics of ligand binding. Journal of Biological Chemistry 283:7293-7308.

Spolaore B, Pinato O, Canton M, et al. (2010) alpha-Lactalbumin forms with oleic acid a high molecular weight complex displaying cytotoxic activity. Biochemistry 49:8658-8667.

Stehr H, Jang SH, Duarte JM, et al. (2011) The structural impact of cancer-associated missense mutations in oncogenes and tumor suppressors. Mol Cancer 10:54.

Sternhagen LG and Allen JC (2001) Growth rates of a human colon adenocarcinoma cell line are regulated by the milk protein alpha-lactalbumin, in Bioactive Components of Human Milk pp 115-120, Springer.

Strynadka NCJ and James MNG (1991) Lysozyme revisited: Crystallographic evidence for distortion of an N-acetylmuramic acid residue bound in site D. Journal of Molecular Biology 220:401-424.

Sujak A, Sanghamitra NJ, Maneg O, et al. (2007) Thermostability of proteins: role of metal binding and pH on the stability of the dinuclear CuA site of Thermus thermophilus. Biophys J 93:2845-2851.

Sun W-Y, Yoshizawa M, Kusukawa T, et al. (2002) Multicomponent metal ligand self-assembly. Current opinion in chemical biology 6:757-764.

Svensson M, Hakansson A, Mossberg AK, et al. (2000) Conversion of alpha-lactalbumin to a protein inducing apoptosis. Proc Natl Acad Sci U S A 97:4221-4226.

Tacar O, Sriamornsak P and Dass CR (2013) Doxorubicin: an update on anticancer molecular action, toxicity and novel drug delivery systems. Journal of Pharmacy and Pharmacology 65:157-170.

Takiar R, Nadayil D and Nandakumar A (2010) Projections of number of cancer cases in India (2010-2020) by cancer groups. Asian Pac J Cancer Prev 11:1045-1049.

Thompson AB, Bohling T, Payvandi F and Rennard SI (1990) Lower respiratory tract lactoferrin and lysozyme arise primarily in the airways and are elevated in association with chronic bronchitis. The Journal of Laboratory and Clinical medicine 115:148-158.

Thompson MP, Farrell Jr HM, Mohanam S, et al. (1992) Identification of human milk α-lactalbumin as a cell growth inhibitor. Protoplasma 167:134-144.

Thornton JM, Orengo CA, Todd AE, et al. (1999) Protein folds, functions and evolution. J Mol Biol 293:333-342.

Tong W, Gao C and Mahwald H (2008) pH-responsive protein microcapsules fabricated via glutaraldehyde mediated covalent layer-by-layer assembly. Colloid and Polymer Science 286:1103-1109.

Touch V, Hayakawa S and Commins T (2009) Natural antimicrobial proteins: a review of current challenges and solutions for food applications. Asian Journal of Food and Agro-Industry 2:1-16.

Ulbrich K and Subr V (2004) Polymeric anticancer drugs with pH-controlled activation. Adv Drug Deliv Rev 56:1023-1050.

Uner A (1993) Severe vascular toxicity associated with cisplatin-based chemotherapy. Cancer 72.

Unnikrishnan B, Palanisamy S and Chen SM (2013) A simple electrochemical approach to fabricate a glucose biosensor based on graphene-glucose oxidase biocomposite. Biosens Bioelectron 39:70-75.

Wang K, Keasling JD and Muller SJ (2005) Effects of the sequence and size of non-polar residues on self-assembly of amphiphilic peptides. International journal of biological macromolecules 36:232-240.

Wang X, Zhou N, Yuan J, et al. (2012) Antibacterial and anticoagulation properties of carboxylated graphene oxide and lanthanum complexes. Journal of Materials Chemistry 22:1673-1678.

Wang Y, Tang L, Li Z, et al. (2014) In situ simultaneous monitoring of ATP and GTP using a graphene oxide nanosheet-based sensing platform in living cells. Nat Protoc 9:1944-1955.

Weber C, Coester C, Kreuter J, et al. (2000) Desolvation process and surface characterisation of protein nanoparticles. Int J Pharm 194:91-102.

Whitesides GM and Grzybowski B (2002) Self-assembly at all scales. Science 295:2418-2421.

Xu F, Zhang P, Navrotsky A, et al. (2007) Hierarchically assembled porous ZnO nanoparticles: synthesis, surface energy, and photocatalytic activity. Chemistry of Materials 19:5680-5686.

Xu M, Sugiura Y, Nagaoka S, et al. (2005) IEC-6 intestinal cell death induced by bovine milk α-lactalbumin. Bioscience, biotechnology, and biochemistry 69:1082-1089.

Xu X, Jian Y, Li Y, et al. (2014) Bio-inspired supramolecular hybrid dendrimers self-assembled from low-generation Peptide dendrons for highly efficient gene delivery and biological tracking. ACS Nano 8:9255-9264.

Xu Y, Bai H, Lu G, et al. (2008) Flexible Graphene Films via the Filtration of Water-Soluble Noncovalent Functionalized Graphene Sheets. Journal of the American Chemical Society 130:5856-5857.

Yamamoto T, Fukui N, Hori A, et al. (2006) Circular dichroism and fluorescence spectroscopy studies of the effect of cyclodextrins on the thermal stability of chicken egg white lysozyme in aqueous solution. Journal of Molecular Structure 782:60-66.

Ye J, Wang C, Chen X, et al. (2008) Marine lysozyme from a marine bacterium that inhibits angiogenesis and tumor growth. Appl Microbiol Biotechnol 77:1261-1267.

Yeber MC, Rodriguez J, Freer J, et al. (2000) Photocatalytic degradation of cellulose bleaching effluent by supported TiO_2 and ZnO. Chemosphere 41:1193-1197.

Zhang M, Yang F, Jr., Yang F, et al. (2009) Cytotoxic aggregates of alpha-lactalbumin induced by unsaturated fatty acid induce apoptosis in tumor cells. Chem Biol Interact 180:131-142.

Zhang S (2003) Fabrication of novel biomaterials through molecular self-assembly. Nat Biotechnol 21:1171-1178.

Zhang S, Marini DM, Hwang W, et al. (2002) Design of nanostructured biological materials through self-assembly of peptides and proteins. Current opinion in chemical biology 6:865-871.

Zhang YM, Cao Y, Yang Y, et al. (2014a) A small-sized graphene oxide supramolecular assembly for targeted delivery of camptothecin. Chem Commun (Camb) 50:13066-13069.

Zhang Z, Liu Y, Ji X, et al. (2014b) A graphene oxide-based enzyme-free signal amplification platform for homogeneous DNA detection. Analyst 139:4806-4809.

Zhou J, Gupta K, Yao J, et al. (2002) Paclitaxel-resistant human ovarian cancer cells undergo c-Jun NH2-terminal kinase-mediated apoptosis in response to noscapine. J Biol Chem 277:39777-39785.

Zhu G, Zheng J, Song E, et al. (2013) Self-assembled, aptamer-tethered DNA nanotrains for targeted transport of molecular drugs in cancer theranostics. Proc Natl Acad Sci U S A 110:7998-8003.

CURRICULUM VITAE

SAILENDRAKUMAR MAHANTA
M.Pharm (Pharmacology), PhD (Thesis submitted)
ResearchScholar, StructuralBiology and Nanomedicine Laboratory,
Department ofBiotechnology andMedicalEngineering,
N.I.T, Rourkela-769008, Odisha, India.
Mail:sailendra04@gmail.com, Contact No.:+91-9178559530(M).
<u>Present Address:</u>
B-311, SSB Hall of Residence, N.I.T.Rourkela-769008, Odisha

Brief synopsis of Research:

Chemotherapy has been used as widely practiced therapy for the treatment of Breast cancer. However, it exposes the patient to various side effects. To avoid side effects and achieve a cheap and biocompatible therapeutics, the focus has been gradually shifting towards biomolecule-based therapeutics like peptide and proteins. In our present investigation, we have developed protein-based therapeutic approaches in Breast cancer using two proteins, bovine α-lactalbumin (BLA) and hen egg white lysozyme (LYZ).

Here, self-assembled nanostructures of both the proteins were prepared using simple desolvation process and evaluated its anti-proliferative activity in Breast cancer cells. The nanostructures were characterized using microscopy and dynamic light scattering analysis for shape and size; FTIR, Circular dichroism and Fluorescence spectroscopy for conformational change. We found the nanostructures were spherical in shape with 300 nm average size and highly stable. Moreover, they demonstrated excellent haemocompatibility as well as cytocompatibility against normal human and mouse cells. When applied to Breast cancer cells such as MCF-7 and MDA-MB231, they demonstrated more than 90% cell death at 24 h and nearly complete cell death after 48 h, which was caused by the internalization of nanostructures in cells and through reactive oxygen species (ROS) generation. Moreover, they showed efficient loading of Tamoxifen (TAM) and pH-responsive drug release in vitro.

We also developed a therapeutic approach based on ZnO nanoparticle (ZnONP) and graphene oxide (GO) nanosheets by surface functionalization with BLA to improve their biocompatibility. Although they demonstrated high anti-proliferative activity in cancer cells via ROS-based cell death, we found some limitations of ZnONP and GO nanosheets based therapeutic approach compared to protein nanostructure–based therapeutics. Therefore, our developed stable self-assembled nanostructured lysozyme and α-lactalbumin can be used as a rational therapeutic approach in Breast cancer.

Academic Qualifications:

- Pursuing PhD on the topic "**An investigation of self-assembled nanostructured protein-based therapeutic approaches in Breast cancer**" under the supervision of **Prof. Subhankar Paul**, at Department of Biotechnology and Medical Engineering, N.I.T, Rourkela-769008, Odisha. (***Thesis submitted***)

- Masters in Pharmaceutical Sciences (Pharmacology) with C.G.P.A of 9.03 from Kanak Manjari Institute of Pharmaceutical Sciences, Rourkela affiliated to Biju Pattnaik University of Technology (BPUT), Rourkela, Orissa, 2008.

- Bachelor Degree in Pharmaceutical Sciences from North Orissa University affiliated to BPUT with 72.09% in 2006.

List of Publications:

1) S. Mahanta, S. Paul. Stable self-assembly of bovine α-lactalbumin exhibits target specific anti-proliferative activity in multiple cancer cells. **ACS Applied Materials & Interfaces**, **2015**, DOI: 10.1021/acsami.5b06076.

2) **S. Mahanta**, S. Paul. Bovine α-lactalbumin functionalized graphene oxide nano-sheet exhibits enhanced biocompatibility: A rational strategy for graphene-based targeted cancer therapy. **Colloids and Surfaces B: Biointerfaces 2015**, (134), 178-187.

3) **S. Mahanta**, S. Paul, A. Srivastava, A. Pastor, B. Kundu, T.K. Chaudhuri, Stable self-assembled nanostructured hen egg white lysozyme exhibits strong anti-proliferative activity against Breast cancer cells, **Colloids and Surfaces B: Biointerfaces 2015**, (130), 237-245.

4) Tripathy, R. K.; **Mahanta, S**.; Paul, S., Artificial intelligence-based classification of Breast cancer using cellular images. **RSC Advances 2014**, 4, (18), 9349-9355.

5) Paul, S.; **Mahanta, S**., Association of heat-shock proteins in various neurodegenerative disorders: is it a master key to open the therapeutic door? **Mol Cell Biochem 2014**, 386, (1-2), 45-61.

6) Gupta, U. K.; **Mahanta, S**.; Paul, S., In silico design of small peptide-based Hsp90 inhibitor: a novel anticancer agent. **Med Hypotheses 2013**, 81, (5), 853-61.

7) **Mahanta, S**.; Pilla, S.; Paul, S., Design of novel Geldanamycin analogue hsp90 alpha-inhibitor in silico for Breast cancer therapy. **Med Hypotheses 2013**, 81, (3), 463-9.

Conference Papers:

- S Paul and **S Mahanta**, "Preparation and Characterization of Self-Assembled Graphene Oxide Supramolecular Structures," Journal of Medical and Bioengineering 2015, (4), 480-483.

- Abstract Publication on the topic "Study of Anti-inflammatory activity of *Sphaeranthus indicus*" in Souvenir and Scientific Abstracts 2008, Orissa Journal of Pharmacology.

Industrial Experience:

- 1.8 year experience (1st December 2008 – 9th July 2010) as Research Associate at Biological Research Division, Glenmark Pharmaceuticals, Navi-Mumbai, Maharashtra.

- The work profile involved routine in-vivo and in-vitro experiments involving Neuropathic Pain, Inflammatory Pain and Safety Studies in both male and female S.D.rats and mice (BABL6J).
  Various experiments with animal models of Schizophrenia and Experimental Autoimmune Encephalomyelitis (EAE) were also involved.Routine dosing, blood collection for PD-PK correlation, Cerebrospinal fluid collection, Dissection of Brain, Spinal cord and dorsal root ganglion were also performed.

Academic Experience:

Four months of teaching experience (16th July 2008 - 30th November 2008) as Lecturer in Pharmacology at Saraswati Vidya Bhawan's College of Pharmacy, Dombivili, Maharashtra, India.

Molecular Docking methods and Software skills:

- Discovery Studio 2.5
- Autodock 4.0
- Hex 6.3
- Chembiodraw Ultra13.0
- Graphpad Prism 5.0
- Origin Pro 8.0

Languages known:

English, Hindi, Oriya and Bengali

References:

1. **Dr. Subhankar Paul, Associate Professor,**

Department of Biotechnology and Medical Engineering, National Institute of Technology, Rourkela-769008, Odisha, India.
Contact No. +91-9438211334, email: spaul@nitrkl.ac.in

2. Dr. Samir Kumar Patra, Associate Professor,

Department of Life Science, National Institute of Technology Rourkela-769008, Odisha, India. Contact No. 0661-2462683, email: samirp@nitrkl.ac.in

3. Dr. Sujit Kumar Bhutia, Assistant Professor,

Department of Life Science, National Institute of Technology Rourkela-769008, Odisha, India. Contact No. 0661-2462686, email: sujitb@nitrkl.ac.in

4. Dr. Praveen Gupta, Research Scientist (In-vivo Pharmacology),

Glenmark Pharmaceuticals Limited, Biological Research Division, Glenmark Research Centre, Plot A- 607, T.T.C. Industrial area, MIDC, Mahape, Navi Mumbai, Mumbai – 400 709, India Contact No. +91-02267720242, email: praveeng@glenmarkpharma.com

5 . Dr. Bishwajit Kundu, Associate Professor

Room No.204, Kusuma School of Biological Sciences, Indian Institute of Technology Delhi (IIT Delhi), Hauz Khas, New Delhi – 110016 , INDIA, Phone : 011 2659 1037 & 2659 6104 , Fax: 011 2658 2282 ,Email : bkundu@bioschool.iitd.ac.in , kundudr@yahoo.com

6. Prof.Tapan K.Chaudhuri

Room# 207, Block IA, IBM Building, Indian Institute of Technology, Delhi, Hauz Khas, New Delhi – 110016,Phone: +91-11-2659-1012 & 2659-6104, Fax: +91-11-2659-7530, Phone: +91-11-2658-1562 & 2659-1842, Mob: +91-9971518671
Email: tkchaudhuri@bioschool.iitd.ac.in, tapanchaudhuri@hotmail.com